5-13-2022

# Covariant density functional theory: from basic features to exotic nuclei

Ahmad Taninah
*Mississippi State University*, taninah.ahmad@gmail.com

# Covariant density functional theory:

# from basic features to exotic nuclei

By

Ahmad Taninah

Approved by:

Anatoli Afanasjev (Major Professor)
Dipangkar Dutta
Lamiaa El Fassi
Gautam Rupak Lan Tai Moong
Jeffry A. Winger
Henk F. Arnoldus (Graduate Coordinator)
Rick Travis (Dean, College of Arts & Sciences)

A Dissertation
Submitted to the Faculty of
Mississippi State University
in Partial Fulfillment of the Requirements
for the Degree of Doctor of Philosophy
in Nuclear Physics
in the Department of Physics and Astronomy

Mississippi State, Mississippi

May 2022

Name: Ahmad Taninah

Date of Degree: May 13, 2022

Institution: Mississippi State University

Major Field: Nuclear Physics

Major Professor: Anatoli Afanasjev

Title of Study: Covariant density functional theory: from basic features to exotic nuclei

Pages of Study: 180

Candidate for Degree of Doctor of Philosophy

Covariant density functional theory (CDFT) is one of the modern theoretical tools for the description of finite nuclei and neutron stars. Its performance is defined by underlying covariant energy density functionals (CEDFs) which depend on a number of parameters. Several investigations within the CDFT framework using the relativistic Hartree-Bogoliubov (RHB) approach are discussed in this dissertation.

Statistical errors in ground state observables and single-particle properties of spherical even-even nuclei and their propagation to the limits of nuclear landscape have been investigated in the covariant energy density functionals with nonlinear density dependency. The parametric correlations are studied in different classes of CEDFs; the elimination of these correlations reduces the number of independent parameters to five or six without affecting the performance of CEDFs on a global scale. Moreover, this study reveals the need to include information on deformed nuclei for the improvement of fitting protocols. A new technique for incorporating deformed nuclei data

into the fitting protocol is described. Different CEDFs are optimized using this approach, resulting in a significant improvement in the nuclear mass description.

A systematic investigation of the ground state and fission properties of even-even actinides and superheavy nuclei with proton numbers $Z = 90 - 120$ located between the two-proton and two-neutron drip lines has been performed. These results provide a necessary theoretical input for the modeling of the nuclear astrophysical rapid neutron capture process (r-process) taking place in the mergers of neutron stars. The state-of-the-art CEDFs, namely, DD-PC1, DD-ME2, NL3*, and PC-PK1, are employed in this study. Theoretical systematic uncertainties in the physical observables and their evolution as a function of proton and neutron numbers have been quantified and their major sources have been identified.

The extension of the nuclear landscape to hyperheavy nuclei is investigated. The transition from ellipsoidal-like nuclear shapes to toroidal shapes is crucial for the potential expansion of the nuclear landscape to hyperheavy nuclei. The physical reasons for the stability of toroidal nuclei in the $Z \approx 134$ region are discussed.

Key words: covariant density functional theory, statistical errors, systematic uncertainties, parametric correlations, r-process, fission barriers, superheavy nuclei, hyperheavy nuclei, triaxiality.

DEDICATION

To my parents, to Saja, and to Zain

ACKNOWLEDGEMENTS

My first and most sincere gratitude goes to my advisor Prof. Anatoli Afanasjev. I am thankful for all of his ideas, suggestions, advice. I am also grateful for the time he has devoted to me all over these years. The dedication and passion he showed inspired me greatly. Also, I want to thank Prof. Dipangkar Dutta, Assoc. Prof. Lamiaa El Fassi, Prof. Gautam Rupak, and Prof. Jeffry Winger for agreeing to serve on my dissertation committee; your questions, comments, feedback, and advice have been very valuable to me. I am very grateful to Dr. El Fassi for giving me detailed and comprehensive feedback on my dissertation. I would like to express my gratitude to those who participated with me in a number of the studies in this dissertation. In addition to Prof. Afanasjev, Dr. Sylvester Agbemava deserves special recognition for his collaboration in the dissertation's majority of research. All the contributions from Prof. Peter Ring, Mr. Abhinaly Gyalawi, and Mrs. Saja Teeti are greatly appreciated. In addition, I would like to thank all past and present members of my group (Dr. Sylvester Agbemava, Dr. Debisree Ray, Abhinaya Gyawali, Saja Teeti, and Udeshika Perera). It was a pleasure to work with you all.

In addition to showing my thankfulness to the staff of the Physics and Astronomy department for their assistance and politeness, I'd like to thank the outstanding professors who taught me the physics classes along the way. Additionally, I am grateful to the Department of Physics and Astronomy for sponsoring my teaching assistantship, as well as to the funding agencies (the

Department of Energy (DOE) and the National Nuclear Security Administration (NNSA)) for supporting my research assistantship.

Furthermore, I'd want to express my gratitude to my parents, sisters, and brothers for their care, encouragement, and love. To my wife Saja for the support and patience along the long journey, and to my son Zain, I will always be there for you.

Finally, I owe it all to Allah the Almighty for granting me the wisdom, patience, health, and strength I needed to complete this long and demanding task.

TABLE OF CONTENTS

LIST OF TABLES

LIST OF FIGURES

## LIST OF SYMBOLS, ABBREVIATIONS, AND NOMENCLATURE

The following are the most frequently used acronyms in the dissertation

**CDFT** Covariant density functional theory

**CEDF** Covariant energy density functional

**DFT** Density functional theory

**EDF** Energy density functional

**LEMAS** Lowest in energy minima for axial symmetry

**PES** Potential energy surface

**PFB** Primary fission barrier

**r-process** Rapid neutron-capture process

**RS-RHB** Reflection-symmetric axial Relativistic Hartree-Bogoliubov

**RA-RHB** Reflection-asymmetric (octupole deformed) axial Relativistic Hartree-Bogoliubov

**RHB** Relativistic Hartree-Bogoliubov

**RMF** Relativistic mean field

**SHE** Superheavy element

**SNM** Symmetric nuclear matter

**TRHB** Triaxial relativistic Hartree-Bogoliubov

# CHAPTER I

# INTRODUCTION

Atomic nuclei are translationally invariant self-bound quantum many-body systems. The spin and isospin degrees of freedom of protons and neutrons play a crucial role in the nucleon-nucleon interaction. Since pairing correlations are important in open-shell nuclei, pairing should be taken into account. There is a significant evidence that the optimal description of nuclei should be relativistic [1]. As a result, at each point in the coordinate-space, the single-particle wave functions form a spinor of dimension 16 (in the relativistic case) [2] which significantly complicates theoretical description.

Despite these complications, there are many theoretical approaches for solving the nuclear many-body problem such as the ab-initio no-core shell model [3], spherical shell model [4], density functional theories [5, 6, 7, 8, 9] and others. There are significant limitations in both the 'ab-initio' and spherical shell model calculations. While the former are feasible only for very light nuclei and computationally impossible (at least currently) for medium and heavy nuclei, the applicability of the latter is restricted to a few regions in the vicinity of doubly shell closures. On the other hand, density functional models can be applied to the whole nuclear chart. No other microscopic method achieves comparable accuracy of the description of the ground-state properties and collective excitations at the same computational cost.

## 1.1 Nuclear density functional theory

Since the early seventies, density functional theory (DFT) and its models have become one of the most important tools for the description of the ground state properties and low-energy collective excitations in the nuclei across the whole nuclear chart. DFT is built on a series of theorems by Kohn and Sham [10, 11, 12] and, in principle, it is a mapping of the many-body problem into one-body problem. As a result, it is characterized by relatively small computational cost. The description of the nuclear many-body problem in DFT is enabled in terms of energy density functionals (EDFs) utilizing self-consistent mean-field models [5, 8, 13, 14]. These EDFs are universal in the sense that they do not depend on the nucleus, nor on the specific region in nuclear chart where they are applied, but only on the underlying interaction. Due to the complexity of the nuclear force with the spin and isospin degrees of freedom, it is difficult to derive the EDFs in a microscopic way directly from the Coulomb interaction as for Coulombic systems. Consequently, all the successful functionals are phenomenological in nature with their parameters adjusted to experimental data in finite nuclei and nuclear matter. Only recently there have been attempts to reduce the number of phenomenological parameters by using information from ab-initio calculations for non-relativistic [15, 16, 17] and relativistic [18, 19] functionals. Hartree-Fock (HF) and Hartree-Fock-Bogoliubov (HFB) approaches based on zero range Skyrme forces or finite range Gogny forces are self-consistent methods that are frequently used in nuclear structure calculations [5, 6]. These approaches, which are based on the Schrödinger equation for many-body nuclear problems, represent the non-relativistic branch of DFT.

Covariant density functional theory (CDFT) based on Dirac equation represents the relativistic branch of the DFT framework. It is particularly interesting because it exploits basic properties of

quantum chromodynamics (QCD) at low energies, in particular symmetries and the separation of scales [20]. The spin degrees of freedom and the spin-orbit interaction are consistently treated in CDFT [21]. In addition, it includes the complicated interplay between the large Lorentz scalar and vector self-energies induced on the QCD level by the in-medium changes of the scalar and vector quark condensates [22]. Moreover, covariant energy density functionals (CEDFs) include nuclear magnetism [23], i.e., a consistent description of currents and time-odd mean fields important in description of odd-mass nuclei [24], nuclear magnetic moments [25], and rotating nuclei [26, 27]. Because of Lorentz invariance, no new adjustable parameters are required for the time-odd parts of the mean fields.

### 1.2 Ground state observables and fission barriers

Atomic nuclei, like many other objects, can be characterized through distinct attributes. Mass, radius, and shape are some of these characteristics which define the internal structure of the nuclei and the forces that shape them. Over the years, a huge effort has been devoted to studying the basic properties of atomic nuclei both experimentally and theoretically. Experimentally, a lot of investigations at the ground state or at low excitation energies have been led to well-known characteristics of atomic nuclei near the beta stability line. Nuclear masses represent an essential property of atomic nuclei. It is used to compute binding energies, separation energies, $Q_\alpha$ values, and $\alpha$-decay half-lives. These data are vital for modeling the astrophysical rapid neutron capture process (r-process) and, ultimately, identifying its path. Near the stability line, these values are well-known experimentally. When extrapolated to neutron-rich nuclei, however, they turn out to be scarce. This makes the extrapolation to the neutron-rich side of the nuclear landscape a challenge.

In such investigations, theoretical models should be used with cautious estimates of theoretical uncertainties.

Several decay modes (such as $\beta$-decay, $\alpha$-decay, and fission) compete in the region of heavy and superheavy nuclei. Fission is a process in which a nucleus splits into two or more fragments due to the competition between the nuclear surface tension (which favors compact spherical shapes) and the Coulomb repulsion (which favors elongated shapes to decrease repulsion energy). The continuous quest for new superheavy elements (SHE) is intimately connected to the fission barrier. This is because many heavy and superheavy nuclei decay by spontaneous fission, and the magnitude of the fission barrier is a measure of a nucleus' stability, which is mirrored in their spontaneous fission lifetimes. In addition, the experimental research of SHEs is solely based on the observation of $\alpha$-decays. Consequently, only SHEs with spontaneous fission half-lives $\tau_{SF}$ longer than the half-lives $\tau_\alpha$ of the $\alpha$ decays could be observed in the experiment. It needs to be additionally noted that only $\alpha$-decays with $\tau_\alpha$ longer than 10 $\mu$s can be observed in the experiments. This implies that the study of fission barriers leads to an understanding of the limits of the existence of atomic nuclei at large values of proton number.

Fission plays an important role in the formation of elements in the r-process of nucleosynthesis in stellar environments. This is because the region of neutron-rich actinides and superheavy nuclei are characterized by low fission barriers which make fission faster than all other decay modes as well as neutron capture. Consequently, the r-process will be likely terminated, and the matter will be returned to lighter nuclei. These will rejoin the r-process flow in the intermediate-mass region and continue to capture neutrons until they reach the fission region once more, repeating the process many times. This scenario (known as fission cycling) occurs in high neutron-to-seed ratio

environments, such as neutron star mergers, and is believed to contribute to the abundance pattern between the second and third r-process peaks. In addition, fission barriers in this region define the opportunity for the formation of new SHEs in the r-process.

### 1.3 The dissertation outline

This dissertation is organized as follows: Chapter II discusses the formalism of the main classes of covariant energy density functionals, the two types of theoretical uncertainties in physical observable predictions, and the relativistic Hartree-Boglibouve framework along with the numerical calculation details. Chapter III examines the statistical errors and their propagation to the limits of the nuclear landscape in the ground-state observables and single-particle properties of spherical even-even nuclei. The investigation of parametric correlations in CEDFs is covered in chapter IV. A new methodology for optimizing CEDFs is discussed in chapter V. Chapter VI is dedicated to the study of the ground state and fission properties of even-even actinides and superheavy nuclei with $Z = 90-120$ from the two-proton up to two-neutron drip lines with proper assessment of systematic theoretical uncertainties. Chapter VII is devoted to studying the properties of hyperheavy nuclei (the nuclei with $Z > 126$) and the extension of the nuclear landscape to hyperheavy nuclei.

# CHAPTER II

## COVARIANT DENSITY FUNCTIONAL THEORY: FORMALISM

The relativistic mean field (RMF) model, in which a nucleus is considered as a system of nucleons that interact through the exchange of effective mesons, represent the origin of CDFT. In the energy density functionals, the smallest set of mesons, which includes scalar $\sigma$, vector $\omega$, and the isovector-vector $\rho$ mesons, should be considered for a proper representation of both nuclear matter and finite nuclei. Furthermore, a point-coupling density functional may be established by analogy with meson-exchange RMF models. In the point-coupling models, a contact interaction between nucleons may be used to substitute an exchanged meson in every channel (scalar, vector, and isovector) of interactions.

In this dissertation, four classes of CEDFs were employed, namely, (i) those based on meson exchange with non-linear meson-nucleon couplings (NL-ME), (ii) those based on meson exchange with density-dependent meson-nucleon couplings (DD-ME), (iii) those based on nonlinear point coupling interactions (PC), and finally (iv) those based on density-dependent point coupling interactions (DD-PC). The basic difference between them is the way in which the interaction's range and density dependence are treated. While the meson exchange classes have a finite range of interaction, the point coupling classes have a zero range. Density dependence is explicit in the DD-ME and DD-PC classes, whereas in the NL-ME class, it is introduced by the powers of $\sigma$-mesons.

Each of these classes is represented by a set of parameters that are considered to be state-of-the-art. These parameterizations were adjusted to reproduce symmetric and asymmetric nuclear matter, binding energies, charge radii, and neutron skins in finite nuclei. The state-of-the-art functionals in these classes are NL3* [28], DD-ME2 [29], PC-PK1 [30], DD-PC1 [19] in the NL-ME, DD-ME, PC, DD-PC models, respectively.

## 2.1 Major classes of covariant energy density functionals

The Lagrangians of the four different classes of functionals can be written as: $\mathcal{L} = \mathcal{L}_{common} + \mathcal{L}_{model-specific}$ where the $\mathcal{L}_{common}$ consist of the Lagrangian of the free nucleons and the electromagnetic interaction. It is identical for all classes of functionals and is written as

$$\mathcal{L}_{common} = \mathcal{L}^{free} + \mathcal{L}^{em} \tag{2.1}$$

with

$$\mathcal{L}^{free} = \bar{\psi}(i\gamma_\mu \partial^\mu - m)\psi \tag{2.2}$$

and

$$\mathcal{L}^{em} = -\frac{1}{4}F^{\mu\nu}F_{\mu\nu} - e\frac{1-\tau_3}{2}\bar{\psi}\gamma^\mu\psi A_\mu. \tag{2.3}$$

where m is the mass of the nucleon and $\psi$ is a Dirac spinor. e is the electric charge of the protons and it vanishes for neutrons. Besides the common terms, each class has its own set of terms in the Lagrangian, as illustrated below.

### 2.1.1 Density-dependent meson-exchange (DD-ME) class

For the DD-ME functionals, the specific Lagrangian is:

$$
\begin{aligned}
\mathcal{L}_{DD-ME} &= \frac{1}{2}(\partial\sigma)^2 - \frac{1}{2}m_\sigma^2\sigma^2 - \frac{1}{4}\Omega_{\mu\nu}\Omega^{\mu\nu} + \frac{1}{2}m_\omega^2\omega^2 \\
&- \frac{1}{4}\vec{R}_{\mu\nu}\vec{R}^{\mu\nu} + \frac{1}{2}m_\rho^2\vec{\rho}^2 - g_\sigma(\bar{\psi}\psi)\sigma \\
&- g_\omega(\bar{\psi}\gamma_\mu\psi)\omega^\mu - g_\rho(\bar{\psi}\vec{\tau}\gamma_\mu\psi)\vec{\rho}^\mu
\end{aligned} \tag{2.4}
$$

with the density dependence of the coupling constants given by

$$
g_i(\rho) = g_i(\rho_0) f_i(x) \quad \text{for } i = \sigma, \omega \tag{2.5}
$$

$$
g_\rho(\rho) = g_\rho(\rho_0)\exp[-a_\rho(x-1)] \tag{2.6}
$$

where $\rho_0$ denotes the saturation density of symmetric nuclear matter and $x = \rho/\rho_0$. The functions $f_i(x)$ are given by the Typel-Wolter ansatz [31]

$$
f_i(x) = a_i \frac{1 + b_i(x + d_i)}{1 + c_i(x + d_i)}. \tag{2.7}
$$

Because of the five conditions $f_i(1) = 1$, $f_i''(1) = 0$, and $f_\sigma''(1) = f_\omega''(1)$, only three of the eight parameters $a_i$, $b_i$, $c_i$, and $d_i$ are independent and we finally have the four parameters $b_\sigma$, $c_\sigma$, $c_\omega$, and $a_\rho$ characterizing the density dependence. In addition we have the four parameters of the Lagrangian $\mathcal{L}_{DDME}$ $m_\sigma$, $g_\sigma$, $g_\omega$, and $g_\rho$. As usual the masses of the $\omega$- and the $\rho$-meson are kept fixed at the values $m_\omega = 783$ MeV and $m_\rho = 763$ MeV [18, 29]. Therefore, the number of parameters $N_{par}$ in the DD-ME class of functionals is 8. These parameters are fitted using binding energies, charge radii, neutron skins, and nuclear matter properties of 12 spherical nuclei.

### 2.1.2 Nonlinear meson-exchange (NL-ME) class

The NL-ME class of the functionals generated in Ref. [32] has the same model specific Lagrangian as the DD-ME class except that the coupling constants $g_\sigma$, $g_\omega$, and $g_\rho$ are constants

and there are extra terms for a non-linear $\sigma$ meson coupling. These couplings are important for the description of surface properties of finite nuclei, especially the incompressibility [33] and for nuclear deformations [34].

$$\mathcal{L}_{NL-ME} = \mathcal{L}_{DD-ME} - \frac{1}{3}g_2\sigma^3 - \frac{1}{4}g_3\sigma^4 \tag{2.8}$$

For the NL-ME class we have $N_{par} = 6$ parameters: $m_\sigma$, $g_\sigma$, $g_\omega$, $g_\rho$, $g_2$, and $g_3$. The fitting of these parameters is conducted using the same set of spherical nuclei as for DD-ME functionals.

### 2.1.3 Nonlinear point-coupling (PC) class

The Lagrangian of the PC functionals contains three parts:

(i) the four-fermion point coupling terms:

$$\begin{aligned}\mathcal{L}^{4f} =& -\frac{1}{2}\alpha_S(\bar{\psi}\psi)(\bar{\psi}\psi) - \frac{1}{2}\alpha_V(\bar{\psi}\gamma_\mu\psi)(\bar{\psi}\gamma^\mu\psi) \\ & - \frac{1}{2}\alpha_{TS}(\bar{\psi}\vec{\tau}\psi)(\bar{\psi}\vec{\tau}\psi) - \frac{1}{2}\alpha_{TV}(\bar{\psi}\vec{\tau}\gamma_\mu\psi)(\bar{\psi}\vec{\tau}\gamma^\mu\psi),\end{aligned} \tag{2.9}$$

(ii) the gradient terms which are important to simulate the effects of finite range:

$$\begin{aligned}\mathcal{L}^{der} =& -\frac{1}{2}\delta_S\partial_\nu(\bar{\psi}\psi)\partial^\nu(\bar{\psi}\psi) \\ & - \frac{1}{2}\delta_V\partial_\nu(\bar{\psi}\gamma_\mu\psi)\partial^\nu(\bar{\psi}\gamma^\mu\psi) \\ & - \frac{1}{2}\delta_{TS}\partial_\nu(\bar{\psi}\vec{\tau}\psi)\partial^\nu(\bar{\psi}\vec{\tau}\psi) \\ & - \frac{1}{2}\delta_{TV}\partial_\nu(\bar{\psi}\vec{\tau}\gamma_\mu\psi)\partial^\nu(\bar{\psi}\vec{\tau}\gamma^\mu\psi),\end{aligned} \tag{2.10}$$

(iii) the higher order terms which are responsible for the surface properties:

$$\begin{aligned}\mathcal{L}^{hot} =& -\frac{1}{3}\beta_S(\bar{\psi}\psi)^3 - \frac{1}{4}\gamma_S(\bar{\psi}\psi)^4 \\ & - \frac{1}{4}\gamma_V[(\bar{\psi}\gamma_\mu\psi)(\bar{\psi}\gamma^\mu\psi)]^2.\end{aligned} \tag{2.11}$$

For the PC models we have $N_{par} = 9$ parameters $\alpha_S$, $\alpha_V$, $\alpha_{TV}$, $\delta_S$, $\delta_V$, $\delta_{TV}$, $\beta_S$, $\gamma_S$, and $\gamma_V$. The fitting of these parameters is based on binding energies and charge radii of 60 spherical nuclei. In these calculations, the scalar-isovector channel is neglected, i.e. we use $\alpha_{TS} = \delta_{TS} = 0$, because it has been shown in Ref. [18] that the information on masses and radii in finite nuclei does not allow to distinguish the effects of the two isovector mesons $\delta$ and $\rho$.

### 2.1.4 Density-dependent point-coupling (DD-PC) class

This class of functionals has the same specific Lagrangian of the PC class except that the higher order terms as well as the gradient terms in the isoscalar-vector (V) and isovector-vector (TV) channels are neglected. In addition, the coupling constants $\alpha_i$ are density dependent given as:

$$\alpha_i(\rho) = a_i + (b_i + c_i x)e^{-d_i x} \text{ for i = S, V, TV} \tag{2.12}$$

In the isovector channel a pure exponential dependence is used, i.e. $a_{TV} = 0$ and $c_{TV} = 0$. The remaining set of 10 constants, $a_S$, $b_S$, $c_S$, $d_S$, $a_V$ , $b_V$ , $c_V$ , $d_V$ , $b_{TV}$ , and $d_{TV}$ that control the strength and density dependence of the interaction Lagrangian, was adjusted in a multistep parameter fit exclusively to the experimental masses of 64 axially deformed nuclei.

## 2.2 Theoretical uncertainties in covariant density functional theory

Although significant progress has been achieved over the years in the development of theoretical tools for the description of low-energy nuclear phenomena, some simplifications and approximations are still necessary because of the complexity of nuclear many-body problem and the impossibility of its exact solution for the systems with large number of particles. In addition, fine details of nuclear force and its dependence on density are still not fully resolved. As a result, it

becomes necessary to estimate theoretical uncertainties in the description of physical observables [2, 35, 36]. This is especially important when one deals with the extrapolations beyond the known regions, as, for example, in particle number or deformation, since experimental data which acts as a substitute of exact solution are not available there. Such estimates are also required for the evaluation of predictive power of the models and the robustness of their predictions. The need for such estimates has been clearly recognized by nuclear theory community as illustrated by a substantial number of the studies aiming at the quantification of theoretical uncertainties in nuclear structure, nuclear reactions and nuclear astrophysics (see Refs. [2, 37, 38, 39, 40, 41, 42, 43] and references quoted therein).

Theoretical uncertainties may be classified into two types: systematic and statistical uncertainties [36, 44]. *Systematic* theoretical uncertainties emerge from underlying theoretical approximations. In the framework of DFT, there are two major sources of these approximations, namely, the range of interaction and the form of the density dependence of the effective interaction [5, 33]. This ambiguity in defining the interaction range and its density dependence leads to several major classes of CEDFs as outlined above and discussed in Ref. [2]. It is necessary to recognize that precise quantification of *systematic errors* in the regions of nuclear chart for which experimental data are not available is not possible due to a number of reasons [2, 36]. Existing functionals, for example, do not form an independent statistical ensemble (see Ref. [2]) and are affected by the human selection of the form of the functional. As a result, the systematic error cannot be described in terms of standard deviation given by an equation similar to Eq. (3.6) (see Ref. [44]). Thus, we prefer to use the notation *systematic uncertainties* (instead of *systematic errors* introduced in Ref. [36]) which has a more narrow meaning since they are defined with respect to selected set

of the functionals (see the introduction of Ref. [2]). This is the reason why systematic theoretical uncertainties are described in terms of the spreads (Refs. [2, 45, 46]) defined as

$$\Delta O(Z,N) = |O_{max}(Z,N) - O_{min}(Z,N)| \tag{2.13}$$

where $O_{max}(Z,N)$ and $O_{min}(Z,N)$ are the largest and smallest values of the physical observable $O(Z,N)$ obtained with the employed set of CEDFs for the $(Z,N)$ nucleus.

An additional source of theoretical uncertainties is related to the details of the fitting protocol such as the choice of experimental data and the selection of adopted errors. It applies only to a given functional and the related theoretical uncertainties are called *statistical errors* [36, 44]. Note that the selection of adopted errors is to a degree subjective, in particular, if one deals with quantities of different dimensions.

### 2.3 Relativistic Hartree-Bogoliubov framework

Pairing correlations play a crucial role in all open-shell nuclei. Without pairing, calculations are limited to just a few double magic nuclei or nuclei at extremely large angular momentum where the pairings is considerably suppressed [47]. There are a variety of recipes that account for pairing correlations. Throughout the following studies, they are taken into account by relativistic Hartree-Bogoliubov (RHB) theory [47, 48, 49]. It has the proper coupling to the continuum at the neutron drip line and, therefore, it allows a correct description of weakly bound nuclei close to the neutron drip line.

Nuclear energy density functionals are dependent on two densities, the normal density, and the anomalous density, or pairing tensor, both of which depend on pairing correlations. The total

energy, therefore, is the sum of both the mean field energy, which is dependent on density matrix and meson fields, as well as the pairing energy [2].

The RHB equations for the fermions are given by [49]

$$\begin{pmatrix} \hat{h}_D - \lambda & \hat{\Delta} \\ -\hat{\Delta}^* & -\hat{h}_D^* + \lambda \end{pmatrix} \begin{pmatrix} U(\boldsymbol{r}) \\ V(\boldsymbol{r}) \end{pmatrix}_k = E_k \begin{pmatrix} U(\boldsymbol{r}) \\ V(\boldsymbol{r}) \end{pmatrix}_k , \tag{2.14}$$

Here, $\hat{h}_D$ is the Dirac Hamiltonian for the nucleons with mass $m$; $\lambda$ is the chemical potential defined by the constraints on the average particle number for protons and neutrons; $U_k(\boldsymbol{r})$ and $V_k(\boldsymbol{r})$ are quasiparticle Dirac spinors [47, 48, 49] and $E_k$ denotes the quasiparticle energies. The Dirac Hamiltonian

$$\hat{h}_D = \boldsymbol{\alpha}(\boldsymbol{p} - \boldsymbol{V}) + V_0 + \beta(m + S) \tag{2.15}$$

contains an attractive scalar potential

$$S(\boldsymbol{r}) = g_\sigma \sigma(\boldsymbol{r}), \tag{2.16}$$

a repulsive vector potential

$$V_0(\boldsymbol{r}) \;=\; g_\omega \omega_0(\boldsymbol{r}) + g_\rho \tau_3 \rho_0(\boldsymbol{r}) + e A_0(\boldsymbol{r}), \tag{2.17}$$

and a magnetic potential

$$\boldsymbol{V}(\boldsymbol{r}) \;=\; g_\omega \boldsymbol{\omega}(\boldsymbol{r}) + g_\rho \tau_3 \boldsymbol{\rho}(\boldsymbol{r}) + e \boldsymbol{A}(\boldsymbol{r}). \tag{2.18}$$

The last term breaks time-reversal symmetry and induces currents. For example, time-reversal symmetry is broken when the time-reversed orbitals are not occupied pairwise; this takes place in odd-mass nuclei [24]. However, nuclear magnetism [23], i.e. currents and time-odd mean fields,

plays no role in the studies of the ground states and fission barriers in even-even nuclei. Thus, magnetic potential is neglected in the present RHB calculations.

In order to avoid the uncertainties connected with the definition of the size of the pairing window [50], we use the separable form of the finite range Gogny pairing interaction introduced by Tian et al [51]. Its matrix elements in $r$-space have the form

$$\begin{aligned} V(\boldsymbol{r}_1, \boldsymbol{r}_2, \boldsymbol{r}'_1, \boldsymbol{r}'_2) &= \\ &= -G\delta(\boldsymbol{R} - \boldsymbol{R}')P(r)P(r')\frac{1}{2}(1 - P^{\sigma}) \end{aligned} \tag{2.19}$$

with $\boldsymbol{R} = (\boldsymbol{r}_1 + \boldsymbol{r}_2)/2$ and $\boldsymbol{r} = \boldsymbol{r}_1 - \boldsymbol{r}_2$ being the center of mass and relative coordinates. The form factor $P(r)$ is of Gaussian shape

$$P(r) = \frac{1}{(4\pi a^2)^{3/2}} e^{-r^2/4a^2} \tag{2.20}$$

The two parameters $G = 728$ MeV fm$^3$ and $a = 0.644$ fm of this interaction are the same for protons and neutrons and have been derived in Ref. [51] by mapping of the $^1$S$_0$ pairing gap of infinite nuclear matter to that of the Gogny force D1S [52]. This pairing provides a reasonable description of pairing properties in the actinides (see Refs. [2, 53, 54]) and has been used in our previous studies of different phenomena in actinides, super- and hyperheavy nuclei in Refs. [2, 32, 55, 56, 57, 58].

The truncation of the basis is performed in such a way that all states belonging to the major shells up to $N_F = 20$ fermionic shells for the Dirac spinors and up to $N_B = 20$ bosonic shells for the meson fields are taken into account. Note that the latter applies only to the functionals which contain meson exchange. As follows from investigation of Refs. [2, 59] this truncation of basis provides sufficient numerical accuracy.

## 2.4 An overview on the details of the numerical calculation

Various investigations in this dissertation were carried out utilizing various theoretical frameworks. The spherical RHB framework and the spherical RHB code were used to investigate the statistical analysis and parametric correlations in the CEDFs. The axial reflection-symmetric relativistic Hartree-Bogoliubov (RHB) framework (using the parallelized code version created and described in [2]) is used to investigate nuclei with $Z = 90 - 120$ between two-proton and two-neutron drip lines. Using the reflection-asymmetric RHB framework, the OCT-RHB code of Ref. [55] was used to study the impact of octupole deformation on the outer fission barrier. The triaxial RHB (TRHB code) [60] framework has been employed to analyze fission barriers in some selected superheavy nuclei, as well as in a few hyperheavy nuclei. Note that TRHB code does not include octupole deformation.

The constrained calculations in employed codes perform the variation of the function

$$E_{RHB} + \sum_{\lambda,\mu} C_{\lambda,\mu}(\langle\hat{Q}_{\lambda,\mu}\rangle - q_{\lambda,\mu})^2. \tag{2.21}$$

Here $(\lambda,\mu) = (2,0)$, $(\lambda,\mu) = (2,0)$ and $(3,0)$ as well as $(\lambda,\mu) = (2,0)$ and $(2,2)$ in the RHB, OCT-RHB and TRHB calculations, respectively. $E_{RHB}$ is the total energy in the RHB calculations. $< Q_{\lambda,\mu} >$ stand for the expectation values of the respective multipole moments which are defined as

$$\hat{Q}_{20} = 2z^2 - x^2 - y^2, \tag{2.22}$$

$$\hat{Q}_{22} = x^2 - y^2, \tag{2.23}$$

$$\hat{Q}_{30} = z(2z^2 - 3x^2 - 3y^2). \tag{2.24}$$

$C_{\lambda,\mu}$ in Eq. (2.21) are corresponding stiffness constants [6] and $q_{\lambda,\mu}$ are constrained values of respective moments. To provide the convergence to the exact value of the desired multipole moment, we use the method suggested in Ref. [61]. Here the quantity $q_{\lambda,\mu}$ is replaced by the parameter $q^{eff}_{\lambda,\mu}$, which is automatically modified during the iteration in such a way that we obtain $\langle\hat{Q}_{\lambda,\mu}\rangle = q_{\lambda,\mu}$ for the converged solution. This method works well in our constrained calculations. In the OCT-RHB code we also fix the (average) center-of-mass of the nucleus at the origin with the constraint

$$\langle\hat{Q}_{10}\rangle = 0 \tag{2.25}$$

on the center-of-mass operator $\hat{Q}_{10}$ to avoid a spurious motion of the center of mass.

The deformation parameters $\beta_2$, $\beta_3$ and $\gamma$ are extracted from respective multipole moments:

$$Q_{20} = \int d^3r\rho(\vec{r})\,(2z^2 - x^2 - y^2), \tag{2.26}$$

$$Q_{22} = \int d^3r\rho(\vec{r})\,(x^2 - y^2), \tag{2.27}$$

$$Q_{30} = \int d^3r\rho(\vec{r})\,z(2z^2 - 3x^2 - 3y^2), \tag{2.28}$$

via

$$\beta_2 = \sqrt{\frac{5}{16\pi}}\frac{4\pi}{3ZR_0^2}\sqrt{Q_{20}^2 + 2Q_{22}^2} \tag{2.29}$$

$$\gamma = \arctan\sqrt{2}\frac{Q_{22}}{Q_{20}} \tag{2.30}$$

$$\beta_3 = \sqrt{\frac{7}{16\pi}}\frac{4\pi}{3ZR_0^3}Q_{30} \tag{2.31}$$

where $R_0 = 1.2A^{1/3}$. Note that $Q_{22} = 0$ and $\gamma = 0$ in axially symmetric RHB calculations.

The $\beta_2$ and $\gamma$ values have a standard meaning of the deformations of the ellipsoid-like density distributions only for $|\beta_2| \lesssim 1.0$ values. At higher $\beta_2$ values they should be treated as dimensionless

and particle normalized measures of the $Q_{20}$ and $Q_{22}$ moments. This is because of the presence of toroidal shapes at large negative $\beta_2$ values and of necking degree of freedom at large positive $\beta_2$ values.

Note that physical observables are frequently shown as a function of the $Q_{20}$, $Q_{30}$ and $Q_{22}$ moments. However, from our point of view such way of presentation has a disadvantage that the physical observables of different nuclei related to the shape of the density distributions (such as deformations) are difficult to compare because the $Q_{20}$, $Q_{30}$ and $Q_{22}$ moments depend on particle number(s).

# CHAPTER III

# THE PROPAGATION OF STATISTICAL ERRORS IN COVARIANT DENSITY FUNCTIONAL THEORY: GROUND STATE OBSERVABLES AND SINGLE-PARTICLE PROPERTIES

## 3.1 Introduction

Recent years have seen systematic efforts undertaken to quantify theoretical uncertainties in the description of physical observables within the CDFT framework. Systematic uncertainties, their sources and their propagation to the extremes of neutron number have been studied globally for the ground state masses, deformations, two-particle separation energies, charge radii and neutrons skins of even-even nuclei, as well as for the positions of drip lines in Refs. [2, 38, 45, 46, 55, 58]. In Ref. [58], systematic uncertainties in the predictions of the ground state properties of superheavy nuclei have been investigated. Above mentioned investigations were restricted to even-even nuclei which are either spherical or have only even-multipole deformations in the ground state. This restriction has been removed in Refs. [55, 56] in which the global studies of octupole deformed nuclei and related systematic uncertainties in their description have been performed. The investigations of systematic uncertainties have also been carried out for excited states such as inner fission barriers in superheavy nuclei (Ref. [60]), deformed one-quasiparticle states in odd-mass actinides [54, 62] and rotational states in even-even and odd-mass actinides (Ref. [53]).

Although impressive amount of data on systematic uncertainties in the description of physical observables in the CDFT has been collected within last few years, very little is known about related statistical errors. So far, they have been investigated only for potential energy curves in a single superheavy nucleus for two CEDFs in Ref. [60]. To fill this gap in our knowledge of the performance of CEDFs, we performed a systematic study of statistical errors in the description of the ground state and single-particle properties of spherical nuclei.

So far, mostly the covariance analysis has been used in the studies of statistical errors for physical observables in the DFT framework (see, for example, Refs. [36, 39, 63, 64]. However, in the calculations of the covariance matrix a linearized least-square system in the vicinity of the minimum of objective function $\chi^2_{norm}$ is usually assumed [44]. This means that the covariance analysis assumes that full information about statistical errors is contained in the derivatives taken at the optimum parametrization and ignores potential non-linear dependence of the observables on the coupling constants in the parts of the parameter hyperspace away from the optimum parametrization. However, there is no guarantee that linear approximation is valid for non-linear problems in the region of the parameter hyperspace away from the optimum parametrization (see Ref. [44]). If that is the case, the covariance matrix loses its validity [44]. A priori such non-linearities, which are present in the CDFT models, cannot be disregarded. For example, the analysis of the correlations between the $\alpha_S$ and $\alpha_V$ parameters in point coupling models performed in Ref. [65] clearly indicates their presence.

Thus, we use alternative approach based on the Monte-Carlo method in which randomly generated functionals are accepted/rejected based on the condition of Eq. (3.4) given in Sec. 3.2 below. As a result, the set of reasonable functionals is generated which is used for the calculations

of statistical errors in the physical observables of interest (see Sec. 3.2). The advantage of this method is that its outcome is defined by full parameter hyperspace used in the analysis (and not only by the neighborhood of optimum parametrization as in covariance analysis). This allows to take existing non-linearities between the parameters fully into account. Thus, the Monte-Carlo approach is free from above mentioned deficiencies of the covariance analysis. However, it is much more numerically time consuming than relatively simple covariance analysis and requires significant computational power. As a result, so far it was applied only to the analysis of statistical errors in the single-particle energies of phenomenological Woods-Saxon potential (see Ref. [66]). For this reason, we focus in the present exploratory study on the NL-ME CEDFs which are characterized by the minimum number of the parameters (and, as a consequence, by minimal dimensionality of the parameter hyperspace) among the state-of-the-art CEDFs. Their six parameters are the mass $m_\sigma$ and coupling constant $g_\sigma$ of the $\sigma$-meson, the coupling constant $g_\omega$ of the $\omega$-meson, the coupling constant $g_\rho$ of the $\rho$ meson which is responsible for the isovector channel of the functional and the coupling constants $g_2$ and $g_3$ which define the density dependence of the functional.

### 3.2 Statistical errors and the details of the calculations

The normalized objective function is defined for model having $N_{par}$ adjustable parameters $\mathbf{p} = (p_1, p_2, ..., p_{N_{par}})$ as

$$\chi^2_{norm}(\mathbf{p}) = \frac{1}{s} \sum_{i=1}^{N_{type}} \sum_{j=1}^{n_i} \left( \frac{O_{i,j}(\mathbf{p}) - O^{exp}_{i,j}}{\Delta O_{i,j}} \right)^2 \tag{3.1}$$

where

$$s = \frac{\chi^2(\mathbf{p}_0)}{N_{data} - N_{par}} \tag{3.2}$$

is global scale factor (Birge factor [67]) defined at the minimum of the penalty function (optimum parametrization $\mathbf{p}_0$[1]) which leads to the average $\chi^2(\mathbf{p}_0)$ per degree of freedom equal to one [36] and

$$N_{data} = \sum_{i=1}^{N_{type}} n_i \tag{3.3}$$

is the total number of data points of different types. Here, $N_{type}$ stands for the number of different data types. The calculated and experimental/empirical values of physical observable $j$ of the $i-$th type are represented by $O_{i,j}(\mathbf{p})$ and $O_{i,j}^{exp}$, respectively. $\Delta O_{i,j}$ is adopted error for physical observable $O_{i,j}$. These quantities for the functionals under study are summarized in Table 3.1.

The acceptable functionals are defined from the condition [36]

$$\chi^2_{norm}(\mathbf{p}) \leq \chi^2_{norm}(\mathbf{p}_0) + \Delta\chi^2_{max} \tag{3.4}$$

This condition specifies the 'physically reasonable' domain around $\mathbf{p}_0$ in which the parametrization $\mathbf{p}$ provides a reasonable fit and thus can be considered as acceptable. This domain is the $N$-dimensional parameter hyperspace $\mathbf{P_{space}} = [p_{1_{min}} - p_{1_{max}}, p_{2_{min}} - p_{2_{max}}, ..., p_{N_{min}} - p_{N_{max}}]$, where $p_{i_{min}}$ and $p_{i_{max}}$ represent the lower and upper boundaries for the variation of the $i-th$ parameter. These boundaries are defined in such a way that their further increase (for $p_{i_{max}}$) or decrease (for $p_{i_{min}}$) does not lead to additional points in parameter hyperspace which satisfy Eq. (3.4). Note that using $\Delta\chi^2_{max} = 1.0$ one could calculate statistical errors, while only parametric correlation could be extracted using higher values of $\Delta\chi^2_{max}$

The numerical calculations are performed in the following way. New parametrizations $\mathbf{p}$ are randomly generated in the $N$-dimensional parameter hyperspace and they are accepted if the

[1]Because of the experimental errors and incompleteness of the physical modelling optimum parametrizations of the models are known only up to their uncertainty probability distributions [66].

Table 3.1

Input data for fitting protocol of the NL5() CEDFs.

| | NL5(A) | NL5(B) | NL5(C) | NL5(D) | NL5(E) |
|---|---|---|---|---|---|
| 1 | 2 | 3 | 4 | 5 | 6 |
| 1. Masses $E$ (MeV) | | | | | |
| $n_1$ | 12 | | | | |
| $\Delta E$ [MeV] | $0.001E$ | | | | |
| 2. Charge radii $r_{ch}$ (fm) | | | | | |
| $n_2$ | 9 | | | | |
| $\Delta r_{ch}$ [fm] | $0.002\,r_{ch}$ | | | | |
| 3. Neutron skin $r_{skin}$ (fm) | | | | | |
| $n_3$ | 4 | | 3 [no $^{90}$Zr] | 0 | |
| $\Delta r_{skin}$ [fm] | $0.05\,r_{skin}$ | | | | see text |
| 4. Nuclear matter properties | | | | | |
| $n_4$ | 4 | | | | |
| $E/A$ [MeV] | -16.0 | | | | |
| $\Delta E/A$ [MeV] | $0.05E/A$ | | | | |
| $\rho$ [fm$^{-3}$] | 0.153 | | | | |
| $\Delta\rho$ [fm$^{-3}$] | $0.1\rho$ | | | | |
| $K_0$ [MeV] | 250.0 | | | | |
| $\Delta K_0$ [MeV] | $0.1K_0$ | $0.025K_0$ | $0.025K_0$ | $0.025K_0$ | $0.025K_0$ |
| $J$ [MeV] | 33.0 | | | | |
| $\Delta J$ [MeV] | $0.1J$ | | | | |
| Parameters of Eq. (3.1) | | | | | |
| $N_{data}$ | 29 | | 28 | 25 | |
| $N_{par}$ | 6 | | | | |
| $N_{type}$ | 4 | | | 3 | |

The number $n_i$ of experimental (empirical) data points and adopted errors $\Delta O_{i,j}$ are presented for each type of data. The binding energies of $^{16}$O, $^{40}$Ca, $^{48}$Ca, $^{72}$Ni, $^{90}$Zr, $^{116}$Sn, $^{124}$Sn, $^{132}$Sn, $^{204}$Pb, $^{208}$Pb, $^{214}$Pb and $^{210}$Po nuclei, the charge radii of $^{16}$O, $^{40}$Ca, $^{48}$Ca, $^{90}$Zr, $^{116}$Sn, $^{124}$Sn, $^{204}$Pb, $^{208}$Pb and $^{214}$Pb nuclei as well as neutron skins of the $^{90}$Zr, $^{116}$Sn, $^{124}$Sn and $^{208}$Pb nuclei are used in the fitting protocol. In addition, employed empirical values $O_{i,j}$ for the properties of symmetric nuclear matter at saturation are provided; these are the density $\rho_0$, the energy per particle $E/A$, the incompressibility $K_0$ and the symmetry energy $J$. The columns 3-6 show only the changes with respect of the values provided in column 2.

condition (3.4) is satisfied. Using the set $[\mathbf{p}_1, \mathbf{p}_2, ..., \mathbf{p}_M]$ of $M$ accepted functional variations the calculations are performed for spherical nuclei in the Ca, Ni, Sn and Pb isotope chains from proton to neutron drip lines. For each nucleus the mean values of physical observables

$$\bar{O}_{i,j} = \frac{1}{M} \sum_{k=1}^{M} O_{i,j}(\mathbf{p}_k) \tag{3.5}$$

and their standard deviations

$$\sigma_{i,j} = \sqrt{\frac{1}{M} \sum_{k=1}^{M} [O_{i,j}(\mathbf{p}_k) - \bar{O}_{i,j}]^2} \tag{3.6}$$

are calculated. The latter serves as a measure of statistical error.

### 3.3 Fitting protocols: an example of the origin of the uncertainties

Previous fits of the non-linear CEDFs have been performed in the RMF+BCS framework with simple pairing (see Refs. [28, 68, 69, 70, 71] for details). Since in the present work the RHB framework with separable pairing of finite range is used in the fitting protocol for the first time, the investigation of the dependence of the optimum parametrization on the details of the fitting protocol is performed.

The starting point is the fitting protocol of the NL3* functional (see Ref. [28]). The types of the input data for this protocol and related adopted errors are summarized in column 2 of Table 3.1. The minimization within this protocol leads to optimum functional labeled NL5(A) (see Table 3.2). When considering the quality of the functional we take into account the ranges of the nuclear matter properties recommended for relativistic functionals in Ref. [72]. These are $\rho_0 \sim 0.15$ fm$^{-3}$, $E/A \sim -16$ MeV, $K_0 = 190 - 270$, $J = 25 - 35$ MeV ($J = 20 - 35$ MeV) and $L_0 = 25 - 115$ ($L_0 = 30 - 80$) for the SET2a (SET2b) sets of the constraints on the experimental/empirical ranges

Table 3.2

Different functionals obtained in the present work.

| | NL1 | NL3* | NL5(A) | NL5(B) | NL5(C) | NL5(D) | NL5(E) |
|---|---|---|---|---|---|---|---|
| 1. Parameters | | | | | | | |
| $m_\sigma$ | 492.250 | 502.574200 | 516.993054 | 503.253177 | 502.481217 | 503.122989 | 503.298890 |
| $g_\sigma$ | 10.1377 | 10.094400 | 10.165747 | 9.896631 | 9.900244 | 10.187753 | 10.263955 |
| $g_\omega$ | 13.2846 | 12.806500 | 12.658290 | 12.457831 | 12.489590 | 12.940276 | 13.052487 |
| $g_\rho$ | 4.9757 | 4.574800 | 4.277136 | 4.202553 | 4.318575 | 4.589814 | 4.582673 |
| $g_2$ | -12.1742 | -10.809300 | -8.350509 | -10.925997 | -10.821667 | -10.858440 | -10.976703 |
| $g_3$ | -36.2646 | -30.148600 | -19.260373 | -28.502727 | -28.27378 | -30.993091 | -32.006687 |
| 2. Nuclear matter properties | | | | | | | |
| $E/A$ | -16.42 | -16.31 | -16.25 | -16.20 | -16.24 | -16.29 | -16.27 |
| $\rho_0$ | 0.152 | 0.150 | 0.146 | 0.150 | 0.150 | 0.150 | 0.150 |
| $K_0$ | 211.11 | 258.27 | 318.42 | 259.22 | 260.673 | 256.50 | 252.96 |
| $J$ | 43.46 | 38.68 | 34.92 | 34.92 | 35.925 | 38.87 | 38.93 |
| $L_0$ | 140.07 | 122.68 | 108.85 | 108.33 | 112.31 | 123.98 | 124.96 |
| 3. Penalty function contributions | | | | | | | |
| $\chi^2_{total}$ | | | 343.901 | 367.822 | 273.014 | 74.973 | 85.049 |
| $\chi^2_{total}$/degree | | | 14.95 | 15.99 | 12.41 | 3.9459 | 3.698 |
| $\chi^2_{NM}$ (%) | | | 8.120 ( 2.3 %) | 2.626 (0.5 %) | 3.842 (1.1 %) | 4.434 (5.3 %) | 3.625 (3.5 %) |
| $\chi^2_E$ ((%) | | | 128.318 (37.3 %) | 145.727 (39.6 %) | 111.550 (40.9 %) | 55.221 (73.7 %) | 51.231 (60.2 %) |
| $\chi^2_{Rch}$ (%) | | | 34.231 ( 9.9 %) | 18.363 (5.0 %) | 16.124 (5.9 %) | 15.318 (20.4 %) | 16.802 (19.7 %) |
| $\chi^2_{Nskin}$ ( %) | | | 173.235 (50.4 %) | 201.105 (54.6 %) | 141.498 (51.8 %) | 0 (0.0 %) | 13.390 (15.7 %) |
| $\chi^2_{Nskin(Zr)}$(%) | | | 76.071 (22.1 %) | 86.591 (23.5 %) | 0 (0.0 %) | 0 (0.0 %) | 1.178 (1.4 %) |

The details of the fitting protocols are discussed in the text. First part of the table shows the parameters of the functionals. Note that the masses of nucleon, $\omega$ and $\rho$ mesons are fixed at $m_N = 939.0$ MeV, $m_\omega = 782.6$ MeV and $m_\rho = 763.0$ MeV, respectively. Related nuclear matter properties are displayed in the second part of the table. In addition to those quoted in Table 3.1, they also include the slope of the symmetry energy $L_0$. Total penalty function $\chi^2_{total}$ and the contributions to it coming from nuclear matter properties ($\chi^2_{NM}$), binding energies ($\chi^2_E$), charge radii ($\chi^2_{Rch}$) and neutron skins ($\chi^2_{Nskin}$) [and, in particular, the contribution of neutron skin of $^{90}$Zr ($\chi^2_{Nskin(Zr)}$)] are presented in the last part of the table. Note that these contributions are given both in absolute values and in percentages [in parentheses] with respect to $\chi^2_{total}$. In addition, the penalty function per degree of freedom $\chi^2_{total}$/degree (Birge factor) is provided. For comparison, the NL1 [68] (which is historically the first successful CEDF) and NL3* [28] CEDFs and their nuclear matter properties are included in columns 2 and 3.

for the quantities of interest. As compared with the CEDF NL3*, the NL5(A) functional has better $J$ and $L_0$ values but much worse $K_0$ value. The analysis of the contributions of physical observables of different classes shows that $\chi^2_{total}$ is dominated by the contributions from 4 data points on neutron skins with the contribution of the single data point on the neutron skin of $^{90}$Zr providing 22.1% of $\chi^2_{total}$. These large contributions from neutron skin data to $\chi^2_{total}$ clearly illustrate that these functionals cannot accurately describe the current adopted experimental values of $r_{skin}$ obtained by means of hadronic probes.

To compensate for too large value of $K_0$ and to force it to more acceptable value, the adopted error for $K_0$ has been reduced from 10% to 2.5% in the fitting protocol of the NL5(B) functional (see column 3 of Table 3.1). This functional and related nuclear matter properties as well as penalty function contributions are shown in Table 3.2. Its $E/A$, $\rho_0$ and $K_0$ values are close to the NL3* ones, but it has better symmetry energy $J$ and the slope of symmetry energy $L_0$. However, similar to NL5(A) it suffers from too large contribution of neutron skins (and especially, the one coming from $^{90}$Zr) to $\chi^2_{total}$.

To reduce this problem, the neutron skin of $^{90}$Zr has been dropped from the fitting protocol of the NL5(C) functional (see column 4 in Table 3.1). This functional has $E/A$, $\rho_0$ and $K_0$ values similar to the ones of the NL3* and NL5(B) functionals (see Table 3.2). Its $J$ and $L_0$ values are better than those of the NL3* functional but slightly worse as compared with those of the NL5(B) one. However, the NL5(C) functional provides better description of binding energies and charge radii as compared with the NL5(A) and NL5(B) ones; these are physical observables which are precisely measured in experiment. On the other hand, it gives slightly worse description of neutron

skins in the $^{116}$Sn, $^{124}$Sn and $^{208}$Pb nuclei but as mentioned before this physical observable is characterized by substantial experimental uncertainties.

One can consider removing the neutron skins (as least reliable experimental data on finite nuclei) from the fitting protocol; this leads to the NL5(D) functional (see Table 3.2). It is characterized by a substantial reduction (by a factor of 2 as compared with the CEDF NL5(C)) of the error in the reproduction of experimental data on binding energies. However, for this functional the $J$ and $L_0$ values deviate more from recommended values as compared with the NL5(C) one.

Alternatively, one can use experimental errors (from Refs. [73, 74, 75]) as adopted errors for neutron skins which are substantially larger than adopted errors (5%) of the fitting protocol of the NL5(A-C) functionals (Table 3.1). This leads to the NL5(E) functional in which the impact of neutron skins on total $\chi^2_{total}$ is substantially reduced as compared with NL5(A-C) functionals. As a consequence, the nuclear matter properties of the NL5(D) and NL5(E) functionals are similar and they provide comparable description of binding energies and charge radii.

The results presented here clearly show that the selection of the fitting protocol (physical observables and related adopted errors) is to a degree subjective. Definitely the use of more experimental data of different types is expected to reduce this level of subjectivity but it cannot be completely eliminated. Since the Monte-Carlo analysis of statistical errors is numerically extremely time-consuming, we restrict our investigation of statistical errors of non-linear CEDFs to NL5(C) and NL5(A) functionals.

### 3.4 The ranges of the parameters in the functionals

In meson exchange models the general features of the nuclei are dominated by the properties of the $\sigma$ and $\omega$ mesons which are responsible for intermediate range attraction and short range repulsion. They lead to attractive scalar $S$ and repulsive vector $V$ potentials with magnitudes of $S \approx -400$ MeV/nucleon and $V \approx +350$ MeV/nucleon [47, 76]. Their sum defines the depth of nucleonic potential ($\sim -50$ MeV/nucleon).

Because of these large magnitudes, very small variations of the masses and coupling constants of these two mesons lead to substantial changes in binding energies (see Figs. 3.1a and d). Note that in this chapter instead of functional parameters $par_i$ we are using the ratio

$$f_i = \frac{par_i}{par_i^{opt}} \tag{3.7}$$

where $par_i^{opt}$ is the value of the parameter in the optimum functional and $i$ indicates the type of the parameter. This allows to better understand the range of the variations of the parameters and related parametric correlations in the functionals.

Coming back to Figs. 3.1a and d, one can see that ±5% change in the values of $m_\sigma$, $g_\sigma$ and $g_\omega$ leads to the changes of binding energies in the range of 2000-3000 MeV. Other physical observables used in the fitting protocols such as charge radii $r_{ch}$ also sensitively depend on $f_i$ (see Figs. 3.1b and e). However, some flexibility in acceptable ranges of these parameters is provided by the fact that binding energies and charge radii have different dependencies on $f(m_\sigma)$, $f(g_\sigma)$ and $f(g_\omega)$ (see Fig. 3.1).

Above discussed features lead to the fact that the $m_\sigma$, $g_\sigma$ and $g_\omega$ parameters are well localized in the parameter hyperspace of all meson-exchange CEDFs (see Fig. 3.2). Note that the absolute

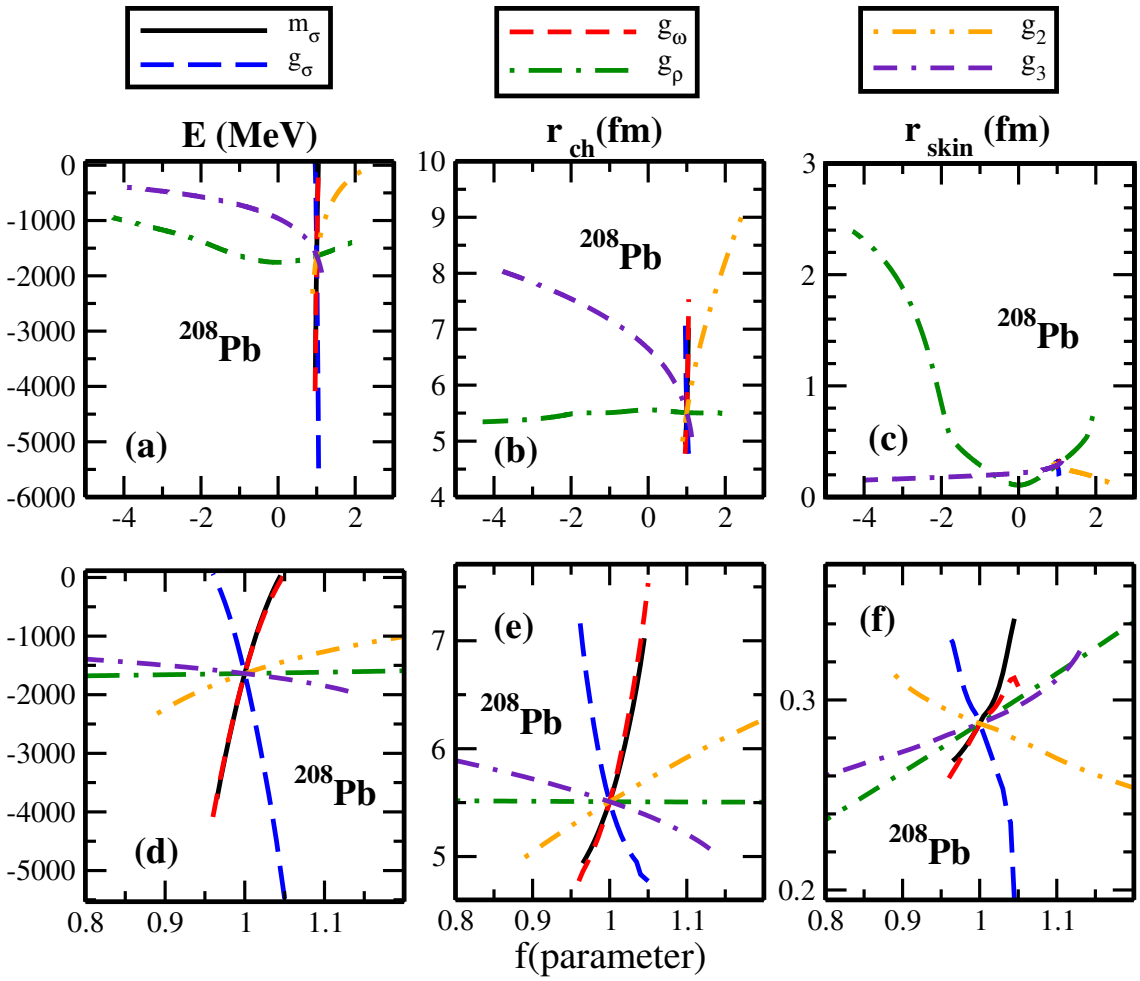


Figure 3.1

The range of the NL5(C) CEDF parameters variations and associated changes in different physical observables.

The physical observables shown are the total binding energy $E$ (left columns), charge radius $r_{ch}$ (central columns) and neutron skin $r_{skin}$ (right columns). Upper row shows the full range of the parameter variations, while the bottom panels magnify the region in the vicinity of optimum parametrization ($f_i = 1.0$). On one end, the range of parameters is limited by the condition that the total energy of the nucleus is negative. On the other end, it is defined by the collapse of numerical solution due to underlying numerical instabilities. For each line, only the indicated parameter is changing while the remaining parameters are kept at the values corresponding to optimum NL5(C) functional.

majority of these parameters are located within 5% deviation band with respect to mean value. This similarity between the functionals becomes even more striking if we consider the ratios $\frac{g_i}{m_i}$ (see Figs. 3.2c and f). In reality, many physical observables depend on such ratios in the CDFT framework. For example, the vector and scalar fields of the CDFT are proportional to $\left(\frac{g_\omega}{m_\omega}\right)^2$ and $\left(\frac{g_\sigma}{m_\sigma}\right)^2$ in the lowest order [76]. Another example is the equation of the state of nuclear matter which depends on the ratios $\frac{g_i}{m_i}$ [31]. Effective meson-nucleon coupling in nuclear matter is also determined by such ratios [29].

On the contrary, the impact of the terms which define isovector dependence, such as the $\rho$-meson, and density-dependent terms (such as $g_2$ and $g_3$) on total binding energies and charge radii is substantially smaller (see Fig. 3.1a, b, d and e). For example, to get comparable changes in binding energy of $^{208}$Pb, the changes in the $g_2$, $g_3$ and especially $g_\rho$ parameters have to be substantially larger than those for the $m_\sigma$, $g_\sigma$ and $g_\rho$ parameters (see TABLE III in Ref. [83]). In general, the $g_\rho$ parameter has significantly larger impact on neutron skin than other parameters (see Fig. 3.1c). However, in the vicinity of the optimum functional its impact is comparable with the ones of other parameters (see Fig. 3.1f). Note also that the potential range of the variations of the $g_\rho$, $g_2$ and $g_3$ parameters is substantially larger as compared with the range of variations of the $g_\sigma$, $m_\sigma$ and $g_\omega$ parameters (see Fig. 3.1).

Figure 3.3 shows that the level of localization of the $g_\rho$ parameter in the parameter hyperspace is lower as compared with the parameters of the $\sigma$ and $\omega$ mesons. The largest deviations from the mean $g_\rho$ value, defined over the set of considered functionals, are seen for the models with explicit density dependencies (Group C functionals). However, even for group A functionals, the deviations from mean values reach 10%. The level of localization is even lower for the $g_2$ and

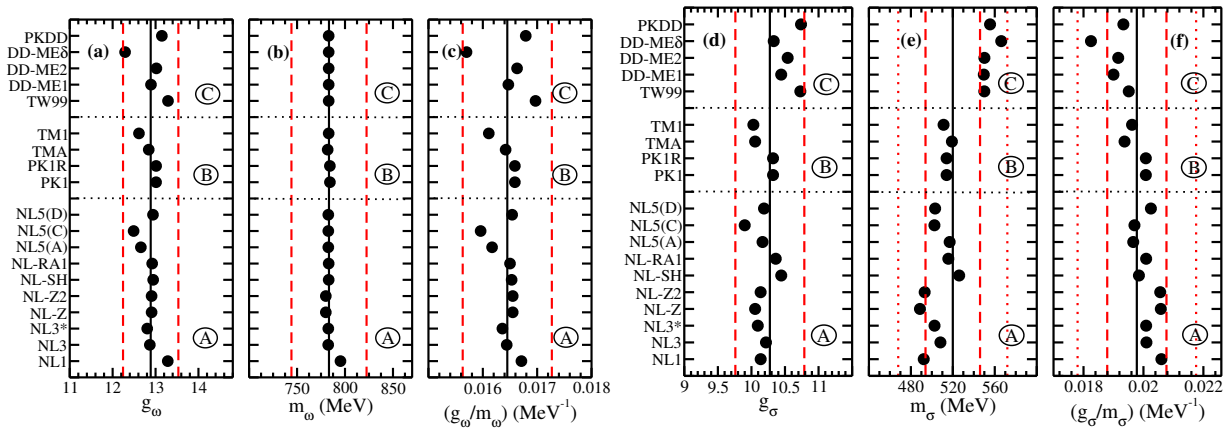


Figure 3.2

The masses and coupling constants of the $\sigma$ and $\omega$ mesons in different CEDFs which contain meson exchange.

The CEDFs are combined into three groups dependent on how self- and mixed-couplings are introduced. Group A represents the parametrizations which include non-linear self-couplings only for the $\sigma$-meson. Group B contains the parametrizations which include self-couplings for the $\sigma$- and $\omega$-mesons (and $\rho-$mesons in the case of PK1R). Group C represents the parametrizations which include density-dependent meson-nucleon couplings for the $\sigma$-, $\omega$-, and $\rho$-mesons. Note that the mass $m_\omega$ of the $\omega$-meson is fixed at indicated values in all functionals except NL3, PK1 and PK1R. The parameters are taken from Refs. [68] (NL1), [69] (NL3), [28] (NL3*), [70] (NL-Z), [77] (NL-Z2), [71] (NL-SH), [78] (NL-RA1), [79] (PK1,PK1R), [80] (TMA), [81] (TM1), [31] (TW99), [82] (DD-ME1), [29] (DD-ME2), [18] (DD-ME$\delta$), [79] (PKDD). Note that we omitted mass-dependent terms for $g_\omega$ in the TMA parametrization which is a good approximation for heavy nuclei since $g_\omega = 12.842 + 3.191A^{-0.4}$ [80]. Vertical solid lines represent the mean values of the respective parameter over the set of indicated functionals. Red dashed and dotted lines show the $\pm5\%$ and $\pm10\%$ deviation bands with respect of these mean values.

$g_3$ parameters for which the deviations from the mean values (defined for the set of considered functionals) could reach and even exceed 25% limit (see Fig. 3.4). However, it is interesting that for the considered functionals the $g_3/g_2$ ratio is very close to 2.75 (see Fig. 3.4c). Only two functionals, namely, NLSH and NL5(A), exceed 10% deviation band from the mean value for the

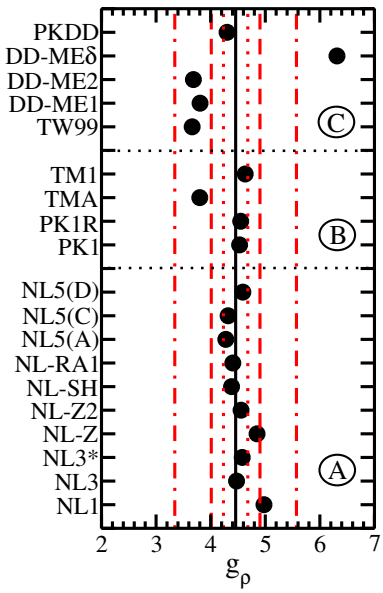


Figure 3.3

The same as Fig. 3.2 but for the $g_\rho$ parameter.

Red dotted, dashed and dash-dotted lines show the ±5%, ±10% and ±25% deviation bands with respect of mean values.

$g_3/g_2$ ratio. Considering that these two parameters define the density dependence of the non-linear meson coupling model, this consistency of the $g_3/g_2$ ratio over the studied functionals suggests hidden parametric correlations between the $g_2$ and $g_3$ parameters.

### 3.5 Statistical errors in the ground state observables of even-even nuclei.

In this section, we will investigate statistical errors in the description of the ground state properties of spherical Ca, Ni, Sn and Pb even-even isotopes. Within the isotope chain the calculations cover all nuclei between the two-proton and two-neutron drip lines. When possible the statistical errors obtained in the present study will be compared with systematic uncertainties

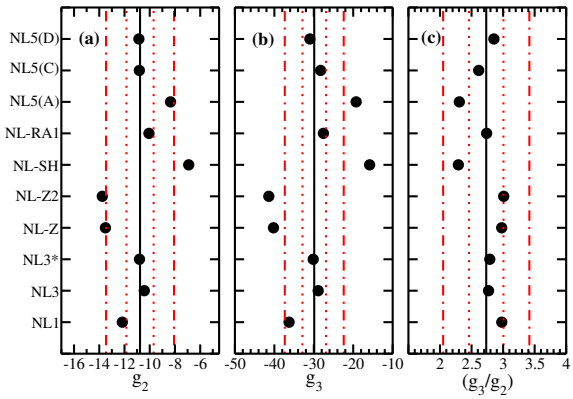


Figure 3.4

The same as Fig. 3.2 but for the $g_2$ and $g_3$ parameters.

Red dotted and dash-dotted lines show the ±10% and ±25% deviation bands with respect of the mean values. Note that only the functionals which belong to group A are considered here.

defined in Refs. [2, 46]. In addition, they will be compared with statistical errors obtained in the Skyrme DFT study with UNEDF0 functional of Ref. [39].

Statistical errors in binding energies obtained with the CEDF NL5(C) and their propagation with the neutron number are shown in Fig. 3.5a. They are close to adopted errors of the fitting protocol [0.1% of binding energy (see Table 3.1)] for the nuclei used in the fit. With increasing isospin the statistical errors in binding energies substantially increase reaching $\sim 2.6$, $\sim 2.6$, $\sim 5.0$ and $\sim 6.0$ MeV at the two-neutron drip line in the Ca, Ni, Sn and Pb isotope chains, respectively. However, they are significantly smaller at the neutron-drip line than those obtained in the Skyrme DFT studies of Ref. [39]; by factors 4.6, 3.1, 3.4 and 2.3 for the Ca, Ni, Sn and Pb isotopes, respectively. Statistical errors in binding energies of these nuclei are by a factor 2-3 smaller than systematic uncertainties in the binding energies obtained in Ref. [2] (see Fig. 8 in this reference).

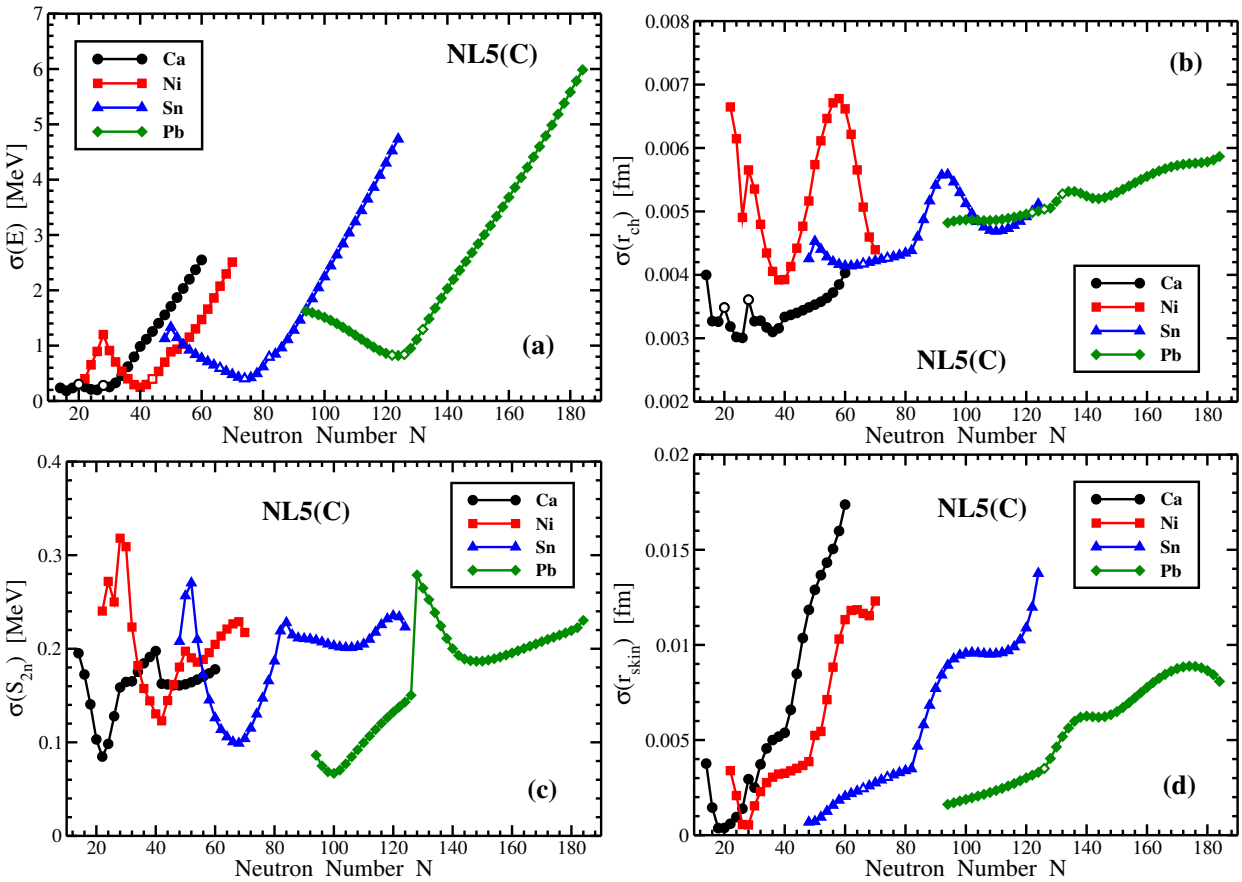


Figure 3.5

The propagation of statistical errors with neutron number.

The statistical errors are calculated for binding energies [panel (a)], charge radii [panel (b)], two-neutron separation energies [panel (c)] and neutron skins [panel (d)]. The results are presented for the Ca ($Z = 20$), Ni ($Z = 28$), Sn ($Z = 50$) and Pb ($Z = 82$) isotopes between two-proton and two-neutron drip lines. Open symbols are used to indicate the nuclei whose experimental data of the type shown on the vertical axis of the panel has been used in the fitting protocol of the NL5(C) functional.

Note that the estimate of systematic uncertainties of Ref. [2] are based only on four CEDFs, namely, NL3*, DD-PC1, DD-ME2 and DD-ME$\delta$. The investigation of Ref. [45] suggests that the addition of the PC-PK1 functional could lead to a substantial increase of systematic uncertainties in binding

energies. This is at least a case for the Yb ($Z = 70$) isotopes for which they increase by a factor of 2.1 when the PC-PK1 results are added (see Fig. 3 in Ref. [46]).

Statistical errors in charge radii $r_{ch}$ are presented in Fig. 3.5b. They are in the vicinity of 0.1% of the calculated $r_{ch}$ values shown in Fig. 23 of Ref. [2]. For the nuclei used in the fitting protocol, statistical errors are below the adopted errors of 0.2% for $r_{ch}$. Calculated statistical errors are below 25% of the rms deviations $\Delta r_{ch}^{rms}$ between calculated and experimental charge radii, which are typical for the state-of-the-art CEDFs and which are shown in Table VI of Ref. [2]. Systematic uncertainties in the predictions of charge radii of the Ca and Ni isotopes obtained from the set of the four functionals (see Fig. 24 of Ref. [2]) are substantially larger (on average, by an approximate factor of 8 and 10, respectively) than relevant statistical errors. This difference goes down with the increase of proton number. For example, the situation in the Pb isotopes depends on the neutron number $N$. Statistical errors are only somewhat smaller than systematic uncertainties in the Pb nuclei with $N \sim 110$ and $N \sim 126$. On the other hand, they are smaller than statistical uncertainties by a factor of approximately 10 for the nuclei with $N \sim 102$. On average, for the Pb nuclei the statistical errors in charge radii are by a factor of approximately 4 smaller than relevant systematic uncertainties. Similar situation is observed also in the Sn isotopes, but the average difference between statistical errors and statistical uncertainties in charge radii is of the order of 7.

Contrary to Skyrme DFT calculations with the UNEDF0 functional (see Fig. 4b in Ref. [39]), statistical errors in charge radii calculated with NL5(C) (see Fig. 3.5b in the present paper) do not show significant increase with neutron number. In reality, the $\sigma(r_{ch})$ values obtained with NL5(C) for Sn and Pb isotopes show very modest increase of approximately 20% on going from two-proton to two-neutron drip line. Note that the $\sigma(r_{ch})$ values show some fluctuations as a function of

neutron number which are due to underlying shell structure; they become especially pronounced in the Ni isotopes. While statistical errors for charge radii of the Ca, Ni and Sn isotopes are comparable for Skyrme UNEDF0 and CDFT NL5(C) calculations for the nuclei near two-proton drip line, the situation changes drastically with the increase of neutron number so that for the Ca, Ni, Sn and Pb nuclei at the two-neutron drip line the $\sigma(r_{ch})$ values obtained in Skyrme calculations are by factor of 17-33 larger than those obtained in CDFT calculations with CEDF NL5(C).

Statistical errors in two-neutron separation energies are displayed in Fig. 3.5c. They are typically in the range of 0.1 - 0.3 MeV and do not show a clear tendency of the increase on approaching two-neutron drip line. These statistical errors show substantial fluctuations as a function of neutron number with the changes in the slope of $\sigma(S_{2n})$ typically taking place in the vicinity of the shell ($N = 20, 28, 50, 82$ and 126) and subshell ($N = 40$) closures. The calculated $\sigma(S_{2n})$ values are typically by a factor of 3-4 smaller than the rms-deviations between theory and experiment for the state-of-the-art CEDF (see Table III in Ref. [2]). It is interesting to compare our results with the ones obtained in Skyrme DFT calculations of Ref. [39]. While the $\sigma(S_{2n})$ values are comparable for both models in the vicinity of the $\beta$-stability line, they increase drastically with increasing neutron number in the Skyrme DFT calculations approaching $\sim 1.4$, $\sim 1.4$, $\sim 0.8$ and $\sim 0.75$ MeV for Ca, Ni, Sn and Pb nuclei at the two-neutron drip line, respectively. This trend is contrary to the one seen in the CDFT results.

Statistical errors in the neutron skin thickness $r_{skin}$ are shown in Fig. 3.5d. They are close to zero near the $N = Z$ line but increase with increasing neutron number. This increase is rapid in the Ca, Ni and Sn isotopes but it is more moderate in the Pb isotopes. An interesting feature of the latter chain is the decrease of the $\sigma(r_{skin})$ values above $N \sim 170$ which is most likely due to

underlying shell effects. The statistical errors in the neutron skin thickness are substantially larger in the Skyrme DFT calculations with the UNEDF0 and SV-min functionals (Ref. [84]) than in the present RHB calculations with CEDF NL5(C). For example, for $^{208}$Pb the $\sigma(r_{skin})$ values are 0.058 fm, 0.037 fm and 0.0035 fm in the calculations with the UNEDF0, SV-min and NL5(C) functionals, respectively. In the neutron-rich Ca isotopes near the two-neutron drip line the $\sigma(r_{skin})$ values obtained in non-relativistic calculations are by a factor of approximately 7 larger than those obtained in the relativistic ones. The statistical errors in the neutron skin thickness shown in Fig. 3.5d are substantially smaller than systematic uncertainties shown in Fig. 25 of Ref. [2]. In the vicinity of the two-neutron drip line, the latter ones reach 0.15 fm, 0.2 fm, 0.25 fm and 0.25 fm in the neutron rich Ca, Ni, Sn and Pb nuclei, respectively.

Figure 3.6 compares statistical errors obtained for binding energies and charge radii of the Sn isotopes with systematic theoretical uncertainties given by the spreads (see Sec. 2.2 for definition). In addition, we add systematic errors defined in terms of Eq. (3.6) with keeping in mind the limitations of this definition discussed in Sec. 2.2 (that is a reason why they are labelled as "$\sigma(O)_{syst}$" versus statistical errors $\sigma$). One can see that these systematic uncertainties ($\Delta E(7)$ and $\Delta r_{ch}(7)$) and errors ("$\sigma(E)_{syst}(7)$" and "$\sigma(r_{ch})_{syst}(7)$") are typically larger than the statistical ones in the unknown region ($N \geq 84$). One should also keep in mind that they represent a lower limit of these uncertainties/errors since only very limited set of functionals is used. The increase of the number of functionals employed in the analysis will without any doubt increase these systematic uncertainties/errors.

The comparison of systematic uncertainties and systematic errors obtained with the sets of 7 and 6 functionals illustrates possible biases in model assumptions. Indeed, removing the NL5(C)

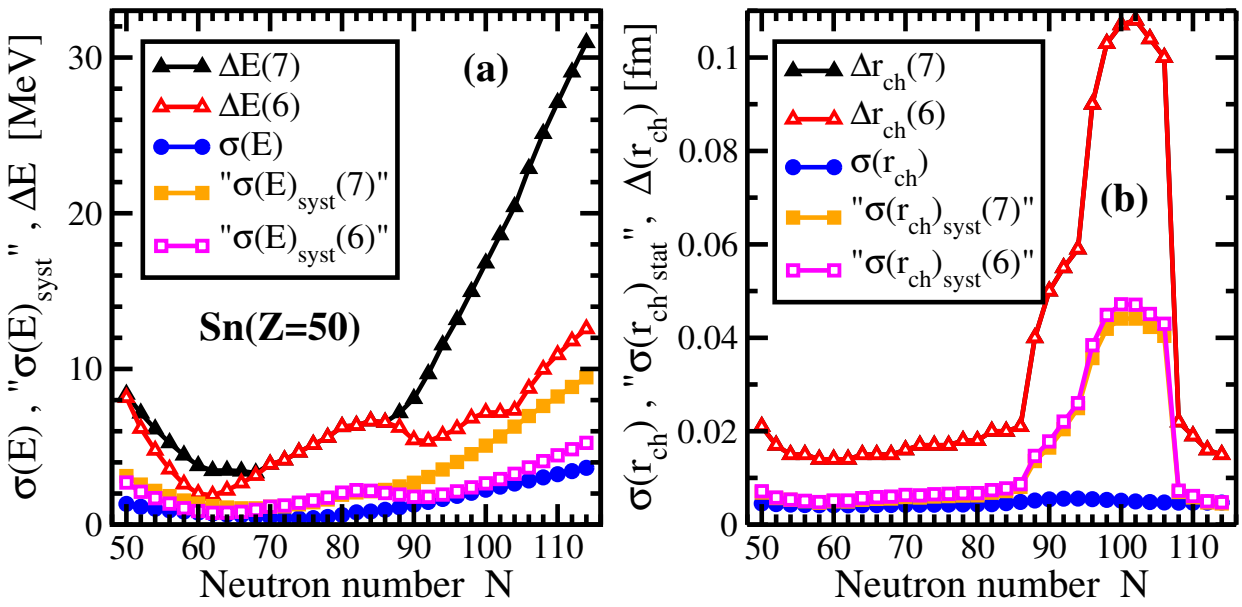


Figure 3.6

Statistical errors compared with respective theoretical systematic uncertainties (spreads) and systematic errors.

Statistical errors $\sigma(E)$ and $\sigma(r_{ch})$ in binding energies (panel (a)) and charge radii (panel (b)) compared with respective theoretical systematic uncertainties (spreads) ($\Delta E$ or $\Delta r_{ch}$) and systematic errors ("$\sigma(E)_{syst}$" or "$\sigma(r_{ch})_{syst}$). The digits '6' and '7' in the labelling of some curves indicate the number of CEDFs used in the definition of theoretical systematic uncertainties and errors. Full set of CEDFs (indicated by '7') includes NL3*, DD-ME2, DD-ME$\delta$, DD-PC1, NL5(C), NL5(D) and NL5(E) CEDFs. The label '6' is used for the set in which the results of the NL5(C) functional are dropped.

functional from the set of employed functionals does not affect so much the $\Delta(E)$ and "$\sigma(E)_{stat}$" quantities of known nuclei but drastically reduces them in unknown nuclei (see Fig. 3.6a). On the contrary, such an action has almost no effect on systematic uncertainties and systematic errors of charge radii (see Fig. 3.6b).

Based on these considerations, one can conclude that when extrapolating to unknown regions statistical errors represent only a relatively small part of total theoretical error. This result is similar

to the one obtained in the studies of 27 HFB mass models in the Skyrme DFT performed in Ref. [85]. As a consequence, statistical errors in physical observables of a given CEDF do not provide alone a meaningful estimate on how much should we trust the predictions of a given functional in experimentally unknown regions.

Our analysis also clearly illustrates the importance of the discrimination of the impact of the *stiff* and *soft* parameters of CEDFs on statistical errors. Such a separation of the parameters into two types was discussed in Ref. [86]. Even when the parameters of nuclear EDFs are adjusted to experimental/empirical/pseudo data, their predictions are sensitive to only a few combinations of parameters (*stiff* parameter combinations) and exhibit an exponential decrease of sensitivity to variations of the remaining *soft* parameters that are only approximately constrained by data. In non-linear meson coupling models, the stiff parameters are represented by $m_\sigma$, $g_\omega$ and $g_\sigma$. Their contribution to statistical errors is rather small and mostly independent of neutron number. On the contrary, the combination of soft parameters $g_2$, $g_3$ and $g_\rho$ leads to a significant increase of statistical errors for binding energies and neutron skins on approaching two-neutron drip line. They also lead to an increase of statistical errors in two-neutron separation energies. Thus, one can conclude that the presence of soft parameters in the CEDFs is the major source of statistical errors.

### 3.6 Statistical errors in the single-particle energies

The energies of the single-particle states $e_i$ represent another quantity which affects many physical observables (see Refs. [21, 45, 58, 62, 87]). In this section we investigate statistical errors in the description of the energies of the single-particle states $e_i$; they are quantified by the standard deviations $\sigma(e_i)$. We focus on two nuclei, namely, $^{208}$Pb and $^{266}$Pb. The analysis of an additional

nucleus $^{304}120$ is presented in Ref. [83]. The first one is well known doubly magic nucleus which serves as a testing ground in many theoretical studies. Second nucleus is the last bound neutron-rich Pb isotope in absolute majority of theoretical studies (see Fig. 14 in Ref. [2]); it is characterized by large $N = 184$ shell gap (see Fig. 6a in Ref. [45]).

Tables 3.3 and 3.4 show the calculated mean energies $\bar{e}_i$ of the single-particle states and related standard deviations $\sigma(e_i)$ obtained in these nuclei. The general trend, which is clearly seen in these tables, is the decrease of statistical errors on going from the bottom of nucleonic potential towards continuum. The states at the bottom of potential are characterized by $\sigma(e_i) \sim 0.35$ MeV for both proton and neutron subsystems for all nuclei under consideration. In $^{208}$Pb, the neutron and proton states are characterized by $\sigma(e_i) \sim 0.1$ MeV in the vicinity of the respective Fermi levels which have similar energies. The addition of neutrons leading to $^{266}$Pb moves the proton Fermi level to lower energies (deeper into the potential) and neutron Fermi level closer to continuum limit. As a consequence, the $\sigma(e_i)$ values for the proton states in the vicinity of the proton Fermi level increase to $\sim 0.15$ MeV (see Table 3.4). On the contrary, with the exception of the high-$j$ $\nu 1j_{15/2}$ and $\nu 1j_{13/2}$ states for which $\sigma(e_i) \sim 0.15$ MeV, the $\sigma(e_i)$ values for the neutron states in the vicinity of the neutron Fermi level is less than 0.1 MeV (see Table 3.4).

The detailed analysis of these calculations results shows that the freedom to rebalance the depths of the proton and neutron potentials is a major source of these statistical errors in the energies of the single-particle states. Indeed, it was observed that when proton potential becomes deeper as compared with the one in the optimum functional, the neutron potential becomes less deep as compared with the one in optimum functional. This leads to more/less bound proton/neutron single-particle states and allows to keep total energy of the system close to the one in the optimum

Table 3.3

The mean energies $\bar{e}_i$ and their standard deviations $\sigma(e_i)$ [in MeV] of the neutron and proton single-particle states in the $^{208}$Pb nucleus calculated with NL5(C) CEDF.

| Neutron | | | Proton | | |
|---|---|---|---|---|---|
| Orbital | $\bar{e}_\nu$ | $\sigma(e_\nu)$ | Orbital | $\bar{e}_\pi$ | $\sigma(e_\pi)$ |
| 1 | 2 | 3 | 4 | 5 | 6 |
| $1s_{1/2}$ | -58.257 | 0.424 | $1s_{1/2}$ | -47.100 | 0.401 |
| $1p_{3/2}$ | -52.142 | 0.376 | $1p_{3/2}$ | -41.573 | 0.360 |
| $1p_{1/2}$ | -51.581 | 0.363 | $1p_{1/2}$ | -40.933 | 0.345 |
| $1d_{5/2}$ | -44.809 | 0.316 | $1d_{5/2}$ | -34.691 | 0.307 |
| $1d_{3/2}$ | -43.497 | 0.282 | $1d_{3/2}$ | -33.249 | 0.270 |
| $2s_{1/2}$ | -40.566 | 0.241 | $2s_{1/2}$ | -29.725 | 0.221 |
| $1f_{7/2}$ | -36.614 | 0.252 | $1f_{7/2}$ | -26.864 | 0.251 |
| $1f_{5/2}$ | -34.228 | 0.189 | $1f_{5/2}$ | -24.320 | 0.187 |
| $2p_{3/2}$ | -30.515 | 0.149 | $2p_{3/2}$ | -20.045 | 0.150 |
| $2p_{1/2}$ | -29.526 | 0.128 | $2p_{1/2}$ | -19.054 | 0.136 |
| $1g_{9/2}$ | -27.862 | 0.191 | $1g_{9/2}$ | -18.402 | 0.199 |
| $1g_{7/2}$ | -24.177 | 0.112 | $1g_{7/2}$ | -14.556 | 0.128 |
| $2d_{5/2}$ | -20.708 | 0.098 | $2d_{5/2}$ | -10.465 | 0.122 |
| $2d_{3/2}$ | -19.127 | 0.091 | $1h_{11/2}$ | -9.544 | 0.159 |
| $1h_{11/2}$ | -18.809 | 0.141 | $2d_{3/2}$ | -8.903 | 0.121 |
| $3s_{1/2}$ | -18.301 | 0.095 | $3s_{1/2}$ | -7.729 | 0.121 |
| | | | Proton Fermi level | | |
| $1h_{9/2}$ | -13.774 | 0.108 | $1h_{9/2}$ | -4.367 | 0.134 |
| $2f_{7/2}$ | -11.320 | 0.085 | $2f_{7/2}$ | -1.107 | 0.120 |
| $1i_{13/2}$ | -9.661 | 0.104 | $1i_{13/2}$ | -0.481 | 0.133 |
| $2f_{5/2}$ | -9.390 | 0.098 | $2f_{5/2}$ | 0.802 | 0.131 |
| $3p_{3/2}$ | -8.591 | 0.087 | $3p_{3/2}$ | 2.133 | 0.121 |
| $3p_{1/2}$ | -7.895 | 0.090 | $3p_{1/2}$ | 2.828 | 0.125 |
| Neutron Fermi level | | | | | |
| $1i_{11/2}$ | -3.515 | 0.148 | | | |
| $2g_{9/2}$ | -2.688 | 0.080 | | | |
| $3d_{5/2}$ | -0.873 | 0.062 | | | |
| $2g_{7/2}$ | -0.855 | 0.090 | | | |
| $4s_{1/2}$ | -0.599 | 0.050 | | | |
| $1j_{15/2}$ | -0.597 | 0.081 | | | |
| $3d_{3/2}$ | -0.281 | 0.061 | | | |
| $4p_{3/2}$ | 2.557 | 0.018 | | | |
| $4p_{1/2}$ | 2.669 | 0.019 | | | |

Table 3.4

The same as Table 3.3 but for the $^{266}$Pb nucleus. The states in the energy range from $\sim -42$ MeV up to $\sim -20$ MeV are omitted in order to simplify the table.

| Neutron | | | Proton | | |
|---|---|---|---|---|---|
| Orbital | $\bar{e}_\nu$ | $\sigma(e_\nu)$ | Orbital | $\bar{e}_\pi$ | $\sigma(e_\pi)$ |
| 1 | 2 | 3 | 4 | 5 | 6 |
| $1s_{1/2}$ | -53.045 | 0.364 | $1s_{1/2}$ | -49.945 | 0.323 |
| $1p_{3/2}$ | -47.922 | 0.333 | $1p_{3/2}$ | -45.498 | 0.304 |
| $1p_{1/2}$ | -47.567 | 0.326 | $1p_{1/2}$ | -45.070 | 0.297 |
| —— | —— | —— | —— | —— | —— |
| $2d_{3/2}$ | -20.427 | 0.153 | $1h_{11/2}$ | -18.396 | 0.199 |
| $3s_{1/2}$ | -19.619 | 0.153 | $2d_{3/2}$ | -18.075 | 0.176 |
| $1h_{11/2}$ | -19.595 | 0.188 | $3s_{1/2}$ | -16.727 | 0.169 |
| | | | Proton Fermi level | | |
| $1h_{9/2}$ | -16.052 | 0.159 | $1h_{9/2}$ | -14.726 | 0.186 |
| $2f_{7/2}$ | -13.384 | 0.142 | $2f_{7/2}$ | -10.867 | 0.172 |
| $2f_{5/2}$ | -11.882 | 0.138 | $1i_{13/2}$ | -10.415 | 0.184 |
| $1i_{13/2}$ | -11.638 | 0.163 | $2f_{5/2}$ | -9.372 | 0.182 |
| $3p_{3/2}$ | -11.057 | 0.130 | $3p_{3/2}$ | -7.655 | 0.171 |
| $3p_{1/2}$ | -10.494 | 0.128 | $3p_{1/2}$ | -7.086 | 0.177 |
| $1i_{11/2}$ | -7.153 | 0.161 | $1i_{11/2}$ | -5.779 | 0.198 |
| $2g_{9/2}$ | -5.728 | 0.124 | $2g_{9/2}$ | -2.583 | 0.174 |
| $2g_{7/2}$ | -4.138 | 0.123 | $1j_{15/2}$ | -2.234 | 0.175 |
| $3d_{5/2}$ | -3.847 | 0.100 | $2g_{7/2}$ | -0.896 | 0.186 |
| $1j_{15/2}$ | -3.691 | 0.143 | $3d_{5/2}$ | 0.851 | 0.168 |
| $4s_{1/2}$ | -3.342 | 0.088 | $3d_{3/2}$ | 1.540 | 0.173 |
| $3d_{3/2}$ | -3.252 | 0.097 | $4s_{1/2}$ | 2.130 | 0.162 |
| Neutron Fermi level | | | | | |
| $2h_{11/2}$ | 1.038 | 0.096 | $1j_{13/2}$ | 3.185 | 0.216 |
| $4p_{3/2}$ | 1.292 | 0.034 | | | |
| $1j_{13/2}$ | 1.406 | 0.164 | | | |
| $4p_{1/2}$ | 1.460 | 0.033 | | | |
| $3f_{7/2}$ | 1.546 | 0.051 | | | |
| $3f_{5/2}$ | 1.998 | 0.045 | | | |
| $2h_{9/2}$ | 2.387 | 0.086 | | | |

functional. The opposite situation with deeper neutron and less deep proton potentials takes place with similar frequency.

In general, statistical errors in the absolute energies of the single-particle states could affect model predictions for the position of the two-neutron drip line. Indeed, as discussed in Ref. [45] its position sensitively depends on the positions (in absolute energy) and the distribution of the single-particle states (and especially high-$j$ intruder and extruder ones) located around the continuum limit. However, in the nuclei around $^{266}$Pb the standard deviations $\sigma(e_i)$ for such neutron single-particle states are safely below 0.1 MeV (see Table 3.4); the only exception is the $\nu 1j_{13/2}$ orbital for which $\sigma(e_i) = 0.164$ MeV. Thus, it is reasonable to expect that the impact of statistical errors in the energies of the single-particle states on the position of two-neutron drip line will be rather modest. Moreover, these statistical errors are substantially smaller than systematic uncertainties in the predictions of the energies of single-particle states, which for many orbitals exceed 1 MeV in nuclei near two-neutron drip line (see Figs. 11c and 6c in Ref. [45]). These facts suggest that the theoretical uncertainties in the prediction of the position of two-neutron drip line are dominated by systematic uncertainties.

While the accuracy of the prediction of the position of the neutron drip line is sensitive to calculated absolute energies of the single-particle states, the accuracy of the reproduction of the single-particle spectra depends mostly on the predictions of the relative energies of the single-particle states. Table 3.5 shows the mean relative energies $\overline{\Delta e_i}$ of the pairs of neighboring single-particle states (as defined in the NL5(C) functional) and related standard deviations $\sigma(\Delta e_i)$. One can see that the $\sigma(\Delta e_i)$ values are substantially smaller than the $\overline{\Delta e_i}$ values. They are also much smaller than the deviations between theory and experiment for one-(quasi)-particle configurations in spherical [21, 87, 88] and deformed [54, 62] nuclei. Here we assume that statistical errors in the description of the energies of deformed single-particle states are similar to spherical ones which

is a reasonable assumption considering that deformed states emerge from spherical ones. Thus, one can conclude that systematic uncertainties in the energies of the single-particle states are more important than statistical ones for the predictions of the single-particle spectra.

The results presented in Table 3.5 provide also the information on statistical errors in the description of spin-orbit splittings. Indeed, these tables contain the pairs of orbitals which form spin-orbit doublets such as $p_{3/2} - p_{1/2}$, $d_{5/2} - d_{3/2}$, $f_{7/2} - f_{5/2}$, $g_{9/2} - g_{7/2}$ and $h_{11/2} - h_{9/2}$. For the majority of the spin-orbit doublets, standard deviations $\sigma(\Delta e_i(m,j))$ are of the order of 2.7% of their mean splitting energies $\Delta e_i(m,j)$. Indeed, for 14 spin-orbit doublets of $^{208}$Pb seen in Table 3.5, the ratio $\sigma(\Delta e_i(m,j))/\Delta e_i(m,j)$ is located in the range from 0.023 up to 0.031. In $^{266}$Pb and $^{304}$120 nuclei, the standard deviations $\sigma(\Delta e_i(m,j))$ are of the order of 2.4% and 2.0% of their mean splitting energies $\Delta e_i(m,j)$, respectively (see Tables VIII and IX in Ref. [83]). Thus, statistical errors (as compared with those seen in $^{208}$Pb) in the description of spin-orbit splittings do not increase on going towards the extremes of neutron number or charge.

It is interesting to compare our CDFT results with those obtained in Skyrme DFT framework with the UNEDF0 functional presented in Table I of Ref. [39]. For the neutron/proton states of $^{208}$Pb shown in this table, the statistical errors obtained in the Skyrme DFT calculations are on average by a factor of 2.05/1.46 larger than those obtained in our CDFT calculations (compare Table 3.3 with Table I of Ref. [39]). In addition, there is one principal difference between the CDFT and Skyrme DFT results. The standard deviations $\sigma(\Delta e_i(m,j))$ for the spin-orbit splittings are very small in the CDFT calculations; they are typically on the level of 2-3% of total size of spin-orbit splitting. On the contrary, they are substantially larger (both in relative and absolute senses) in the Skyrme DFT calculations (see Table I in Ref. [39]).

Table 3.5

Relative energies $\Delta e_i(m, j) = e_i(m) - e_i(j)$ of the pairs of neutron ($i = \nu$) and proton ($i = \pi$) single-particle states in the $^{208}$Pb nucleus.

| Neutron | | | Proton | | |
|---|---|---|---|---|---|
| Orbital pairs $(m, j)$ | $\overline{\Delta e_\nu}$ | $\sigma(\Delta e_\nu)$ | Orbital pairs $(m, j)$ | $\overline{\Delta e_\pi}$ | $\sigma(\Delta e_\pi)$ |
| 1 | 2 | 3 | 4 | 5 | 6 |
| $1s_{1/2}$ - $1p_{3/2}$ | 6.115 | 0.054 | $1s_{1/2}$ - $1p_{3/2}$ | 5.527 | 0.049 |
| $1p_{3/2}$ - $1p_{1/2}$ | 0.560 | 0.013 | $1p_{3/2}$ - $1p_{1/2}$ | 0.640 | 0.016 |
| $1p_{1/2}$ - $1d_{5/2}$ | 6.772 | 0.053 | $1p_{1/2}$ - $1d_{5/2}$ | 6.242 | 0.045 |
| $1d_{5/2}$ - $1d_{3/2}$ | 1.313 | 0.037 | $1d_{5/2}$ - $1d_{3/2}$ | 1.442 | 0.042 |
| $1d_{3/2}$ - $2s_{1/2}$ | 2.931 | 0.047 | $1d_{3/2}$ - $2s_{1/2}$ | 3.524 | 0.058 |
| $2s_{1/2}$ - $1f_{7/2}$ | 3.951 | 0.033 | $2s_{1/2}$ - $1f_{7/2}$ | 2.860 | 0.049 |
| $1f_{7/2}$ - $1f_{5/2}$ | 2.386 | 0.073 | $1f_{7/2}$ - $1f_{5/2}$ | 2.545 | 0.079 |
| $1f_{5/2}$ - $2p_{3/2}$ | 3.713 | 0.055 | $1f_{5/2}$ - $2p_{3/2}$ | 4.274 | 0.063 |
| $2p_{3/2}$ - $2p_{1/2}$ | 0.989 | 0.028 | $2p_{3/2}$ - $2p_{1/2}$ | 0.991 | 0.028 |
| $2p_{1/2}$ - $1g_{9/2}$ | 1.664 | 0.090 | $2p_{1/2}$ - $1g_{9/2}$ | 0.652 | 0.106 |
| $1g_{9/2}$ - $1g_{7/2}$ | 3.685 | 0.116 | $1g_{9/2}$ - $1g_{7/2}$ | 3.846 | 0.121 |
| $1g_{7/2}$ - $2d_{5/2}$ | 3.469 | 0.051 | $1g_{7/2}$ - $2d_{5/2}$ | 4.092 | 0.058 |
| $2d_{5/2}$ - $2d_{3/2}$ | 1.581 | 0.039 | $2d_{5/2}$ - $1h_{11/2}$ | 0.920 | 0.098 |
| $2d_{3/2}$ - $1h_{11/2}$ | 0.318 | 0.122 | $1h_{11/2}$ - $2d_{3/2}$ | 0.641 | 0.133 |
| $1h_{11/2}$ - $3s_{1/2}$ | 0.507 | 0.113 | $2d_{3/2}$ - $3s_{1/2}$ | 1.174 | 0.025 |
| | | | below proton Fermi level | | |
| $3s_{1/2}$ - $1h_{9/2}$ | 4.527 | 0.094 | $3s_{1/2}$ - $1h_{9/2}$ | 3.362 | 0.095 |
| $1h_{9/2}$ - $2f_{7/2}$ | 2.455 | 0.078 | $1h_{9/2}$ - $2f_{7/2}$ | 3.260 | 0.081 |
| $2f_{7/2}$ - $1i_{13/2}$ | 1.659 | 0.094 | $2f_{7/2}$ - $1i_{13/2}$ | 0.626 | 0.103 |
| $1i_{13/2}$ - $2f_{5/2}$ | 0.271 | 0.128 | $1i_{13/2}$ - $2f_{5/2}$ | 1.283 | 0.136 |

The pairs of neighboring states $m$ and $j$ shown in columns 1 and 4 are defined from the single-particle spectra obtained with the NL5(C) CEDF. The columns 2 and 5 show their mean relative energies $\overline{\Delta e_i}(m, j)$ [in MeV] while the columns 3 and 6 show standard deviations $\sigma(\Delta e_i(m, j))$ [in MeV]. All the pairs of the states up to the label "proton/neutron Fermi level" have both members located below respective Fermi levels. Next line after this statement indicates the pair of the states one of the members of which is located below the large shell gap (either proton $Z = 82$ or neutron $N = 126$ one) and another above this gap. Subsequent lines show the pairs of the states both members of which are located above respective Fermi levels (above proton $Z = 82$ or neutron $N = 126$ shell gaps).

Table 3.5

(continued)

| Neutron | | | Proton | | |
|---|---|---|---|---|---|
| Orbital pairs $(m, j)$ | $\overline{\Delta e_\nu}$ | $\sigma(\Delta e_\nu)$ | Orbital pairs $(m, j)$ | $\overline{\Delta e_\pi}$ | $\sigma(\Delta e_\pi)$ |
| 1 | 2 | 3 | 4 | 5 | 6 |
| $2f_{5/2}$ - $3p_{3/2}$ | 0.799 | 0.033 | $2f_{5/2}$ - $3p_{3/2}$ | 1.331 | 0.031 |
| $3p_{3/2}$ - $3p_{1/2}$ | 0.696 | 0.017 | $3p_{3/2}$ - $3p_{1/2}$ | 0.695 | 0.016 |
| below neutron Fermi level | | | | | |
| $3p_{1/2}$ - $1i_{11/2}$ | 4.380 | 0.109 | | | |
| $1i_{11/2}$ - $2g_{9/2}$ | 0.827 | 0.118 | | | |
| $2g_{9/2}$ - $3d_{5/2}$ | 1.816 | 0.022 | | | |
| $3d_{5/2}$ - $2g_{7/2}$ | 0.018 | 0.036 | | | |
| $2g_{7/2}$ - $4s_{1/2}$ | 0.256 | 0.044 | | | |
| $4s_{1/2}$ - $1j_{15/2}$ | 0.003 | 0.084 | | | |
| $1j_{15/2}$ - $3d_{3/2}$ | 0.316 | 0.090 | | | |
| $3d_{3/2}$ - $4p_{3/2}$ | 2.837 | 0.044 | | | |
| $4p_{3/2}$ - $4p_{1/2}$ | 0.113 | 0.003 | | | |

### 3.7 Concluding remarks

Statistical errors in ground state observables and single-particle properties of spherical even-even nuclei and their propagation to the limits of nuclear landscape have been investigated in covariant density functional theory for the first time. The main results can be summarized as follows:

- Statistical errors in binding energies, charge radii, neutron skins and two-neutron separation energies have been studied for the Ca, Ni, Sn and Pb nuclei located between two-proton and two-neutron drip lines. While statistical errors for binding energies and neutron skins drastically increase on approaching two-neutron drip line, such a trend does not exist for statistical errors in charge radii and two-neutron separation energies. The latter is contrary to the trends seen in Skyrme density functional theory. Statistical errors obtained in the CDFT calculations are substantially smaller than related systematic uncertainties.
- The absolute energies of the single-particle states in the vicinity of the Fermi level are characterized by low statistical errors ($\sigma(e_i) \sim 0.1$ MeV). This is also true for relative energies of the single-particle states. These statistical errors are substantially smaller than

systematic uncertainties in the predictions of the absolute and relative energies of the single-particle states. Thus, they are not expected to modify in a substantial way the predictions of a given CEDF. This is true both for known nuclei and for nuclear extremes such as the vicinity of neutron-drip line and the region of superheavy elements.

- Statistical errors in the description of physical observables related to the ground state and single-particle degrees of freedom are substantially lower in CDFT as compared with Skyrme DFT. A special feature of CDFT due to which the parameters of the $\omega$ and $\sigma$ mesons, defining the basis features of the nucleus such as a nucleonic potential, are well localized in very narrow range of the parameter hyperspace, is responsible for that. Note that fixing the $g_\rho$, $g_2$ and $g_3$ parameters of the model leads to drastic reduction of statistical errors as compared with the case when all parameters of the non-linear functional are permitted to vary in Monte-Carlo procedure.

- Considering the structure of non-linear meson coupling models and typical features of existing non-linear CEDFs and their fitting protocols, it is reasonable to expect that different non-linear functionals will provide comparable statistical errors for the physical observables of interest. This was illustrated by comparison of the results for the NL5(C) and NL5(A) functionals. Note that obtained statistical errors represent in a sense their upper limit since the fitting protocol includes only limited set of nuclei and empirical data. It is expected that the increase of the size of the dataset in the fitting protocol will lead to further reduction of statistical errors [36].

# CHAPTER IV

# PARAMETRIC CORRELATIONS IN ENERGY DENSITY FUNCTIONALS

## 4.1 Introduction

Over the years, the number of phenomenological functionals has grown considerably not only for non-relativistic Skyrme DFTs, but also for CDFTs. Therefore, in recent years the question has risen about the reliability and the predictive power of such functionals [2, 36]. We investigate here whether the parameters in such CDFTs are independent. We search for correlations between such parameters. Such correlations have not been systematically studied in the CDFT framework. Their presence affects statistical errors in the description of physical observables [66]. The removal of parametric correlations leads to the reduction of the dimensionality of the parameter hyperspace and to the decrease of statistical errors. The latter was illustrated in Ref. [66] on the example of the study of statistical errors in the single-particle energies of spherical nuclei performed with Woods-Saxon potential.

Zagreb group [86, 89] has already tried to reduce the number of parameters in point-coupling model with a density dependence of exponential form (as in the functional DD-PC1 [19].) Using the manifold boundary approximation method (Ref. [86]), they showed that it is possible to reduce the number of parameters for this functional from ten to eight without sacrificing the quality of the reproduction of empirical data. This method is based on the behavior of penalty function in the

vicinity of a minimal valley. As designed this method is not completely general and it still has to be shown that it can reveal all parametric correlations in the full parameter hyperspace.

In the present investigation we go two steps further: (i) we consider all major classes CEDFs (see Sec. 2.1), and (ii) we use the methods which allow to search for such correlations in the entire parameter hyperspace. Our results are closely related to the efforts of the DFT community on the microscopic derivation of the EDFs and on the search of terms which are missing in the present generation of EDFs [14, 90]. The absence/presence of parametric dependencies between the parameters of the EDFs can indicate whether the terms added to the Hamiltonian/Lagrangian have deep roots in physics or they simply reflect additional functional dependencies, introduced either by model approximations or fitting protocol, which do not have a deep physical context. Our study employs the method discussed in Sec. 3.2 and uses the ratios defined by Eq. (3.7). The latter allows to understand the range of the variations of the parameters and related parametric correlations in the functionals. The condition of Eq. (3.4) specifies the 'physically reasonable' domain around $\mathbf{p}_0$ (the optimal parametrization) in which the parametrization $\mathbf{p}$ provides a reasonable fit and thus can be considered as acceptable [36, 44].

## 4.2 Parametric correlations in the DD-ME class and PC class: statistical analysis in full parameter hyperspace

The parametric correlations in DD-ME class and PC class will be studied in the functionals DD-MEX and PC-X respectively[1], [2]. The input data for fitting protocol of these two functionals are shown in Table 4.1.

[1]Note that parametric correlations in the NL-ME class of functionals have been studied in Ref. [83]

[2]Parameters of these two functionals as well as the total penalty function $\chi^2_{total}$ and the contributions to it coming from different observables in the fitting protocol are found in the supplementary material of Ref. [91]

Table 4.1

Input data for fitting protocols of indicated CEDFs.

| | DD-MEX | PC-X |
|---|---|---|
| 1 | 2 | 3 |
| 1. Masses $E$ (MeV) | | |
| $n_1$ | 12 | 60 |
| $\Delta E$ [MeV] | $0.001E$ | 1.0 MeV |
| 2. Charge radii $r_{ch}$ (fm) | | |
| $n_2$ | 9 | 17 |
| $\Delta r_{ch}$ [fm] | $0.002\, r_{ch}$ | 0.02 |
| 3. Neutron skin $r_{skin}$ (fm) | | |
| $n_3$ | 3 | N/A |
| $\Delta r_{skin}$ [fm] | $0.05\, r_{skin}$ | N/A |
| 4. Nuclear matter properties | | |
| $n_4$ | 4 | N/A |
| $E/A$ [MeV] | -16.0 | N/A |
| $\Delta E/A$ [MeV] | $0.05E/A$ | N/A |
| $\rho$ [fm$^-$3] | 0.153 | N/A |
| $\Delta\rho$ [fm$^-$3] | $0.1\rho$ | N/A |
| $K_0$ [MeV] | 250.0 | N/A |
| $\Delta K_0$ [MeV] | $0.1K_0$ | N/A |
| $J$ [MeV] | 33.0 | N/A |
| $\Delta J$ [MeV] | $0.1J$ | N/A |
| $N_{data}$ | 28 | 77 |
| $N_{par}$ | 8 | 9 |
| $N_{type}$ | 4 | 2 |

The number $n_i$ of experimental (empirical) data points and adopted errors are presented for each type of data. These values are taken from Refs. [29, 30]. In addition, employed empirical values for nuclear matter properties are shown.

The DD-MEX and PC-X functionals contain 8 and 9 parameters, respectively. This leads to a drastic increase of the volume of hyperspace which makes numerical calculations with $\Delta\chi^2_{max} = 1.0$ impossible. Thus, for these two classes we do not consider statistical errors but rather focus on parametric correlations. As shown in Ref. [83], these correlations between the model parameters

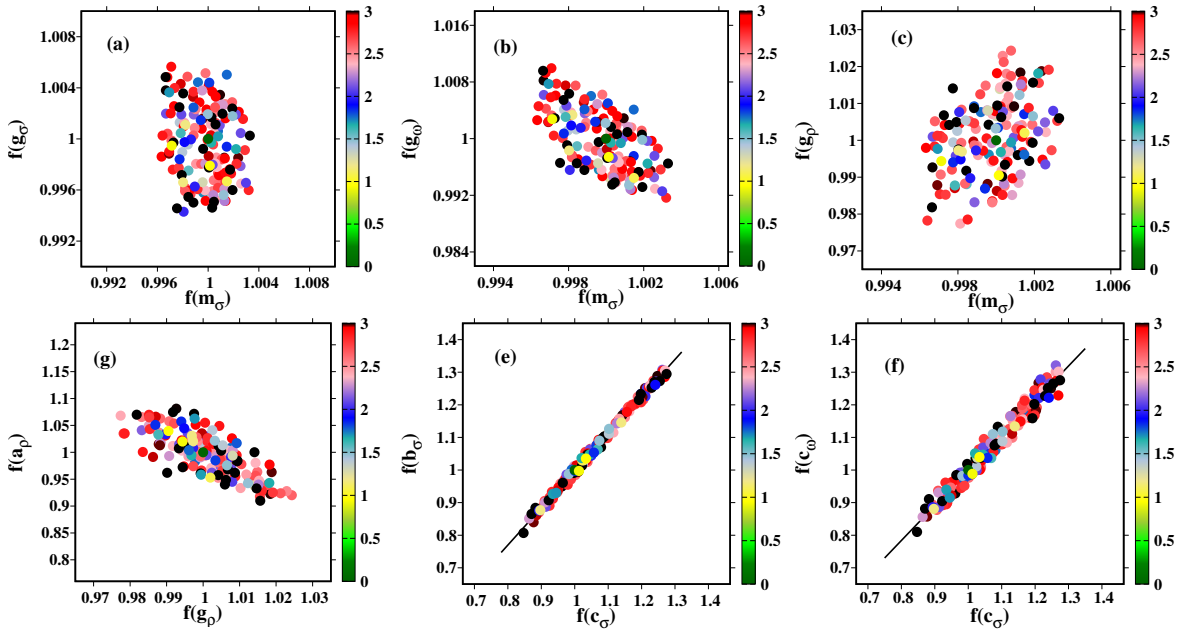


Figure 4.1

Two-dimensional projections of the distribution of the functional variations in the 8-dimensional parameter hyperspace of the DD-MEX functional.

The colors indicate the $\Delta\chi^2$ value of the $\chi^2_{norm}(\mathbf{p})$ of the functional variation where the latter is expressed as $\chi^2_{norm}(\mathbf{p}) = \chi^2_{norm}(\mathbf{p}_0) + \Delta\chi^2$. A color map is used for the functional variations with maximum value of $\Delta\chi^2$ equal to $\Delta\chi^2_{max} = 3.0$; there are 200 such variations. The optimal functional is located at the intersection of the lines $f(p_k) = 1.0$ and $f(p_j) = 1.0$. The solid lines in panels (e) and (f) display the parametric correlations between the respective parameters.

are visible even for higher values of $\Delta\chi^2_{max}$. Thus, we use $\Delta\chi^2_{max} = 3.0$ for the DD-MEX and PC-X functionals.

In Fig. 4.1, we consider the CEDF DD-MEX and show, for the randomly generated parameters obeying the condition (3.4), the 2-dimensional distributions of indicated pairs of the parameters. The parameters vary with respect of the central value of the distribution (which are typically given by the parameters of the optimal functional) by at most 0.5% for $m_\sigma$, 0.6% for $g_\sigma$, 1% for $g_\omega$, 2.5%

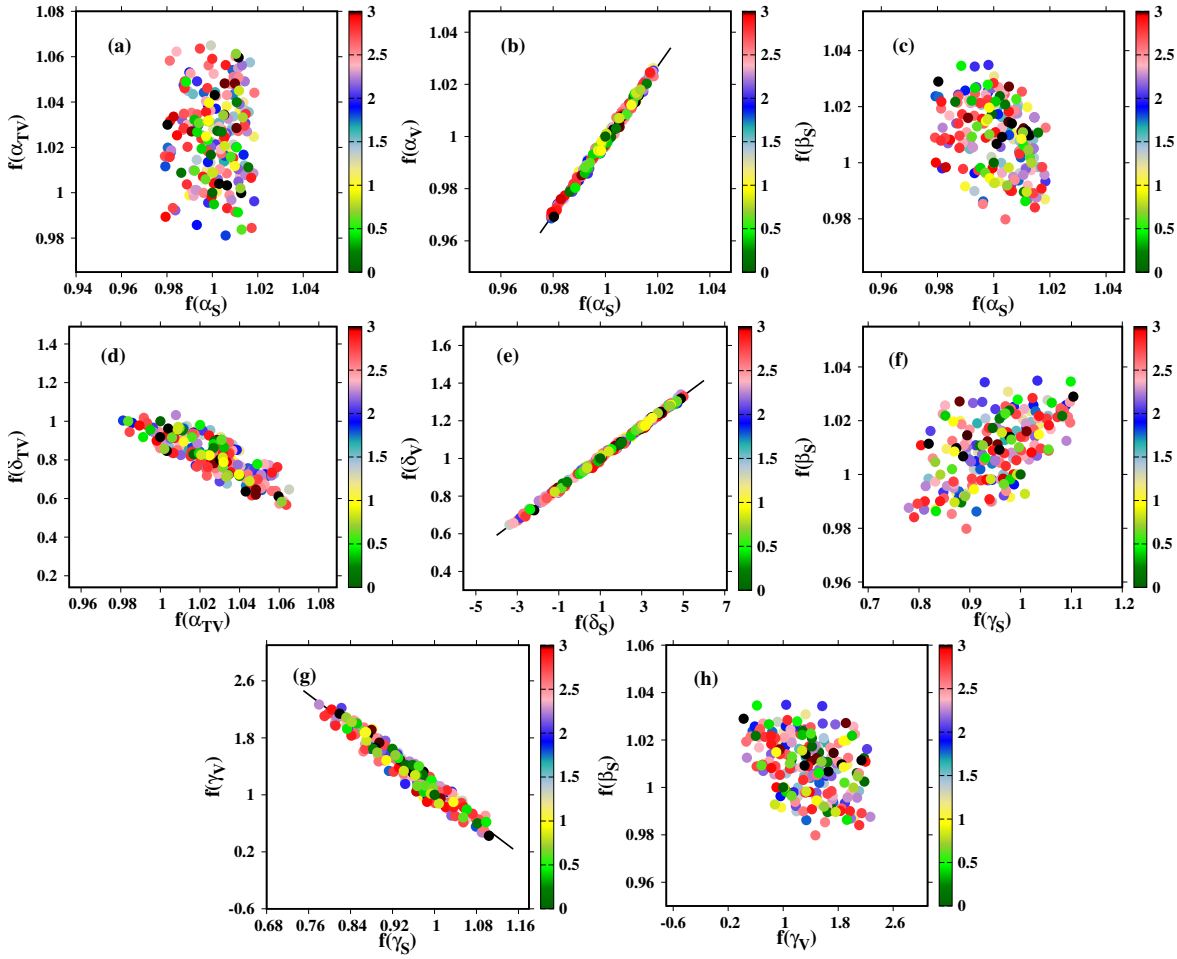


Figure 4.2

The same as Fig. 4.1 but for the functional PC-X.

for $g_\rho$, 10% for $a_\rho$, and 30% for $c_\sigma$, $b_\sigma$ and $c_\omega$. Similar plots for the PC-X functional are presented in Fig. 4.2.

One can speak about parametric correlations between these parameters when one parameter $p_k$ can, with a reasonable degree of accuracy, be expressed as a function of other parameters, for

example, as a function of the parameter $p_j$. The simplest type of the correlations is a linear form given by

$$f(p_k) = a f(p_j) + b \tag{4.1}$$

For example, the following linear relations exist between the parameters of the DD-MEX functional (shown by solid black lines in Figs. 4.1e and f)

$$\begin{aligned} f(b_\sigma) &= 1.1396 f(c_\sigma) - 0.14191 \\ f(c_\omega) &= 1.083 f(c_\sigma) - 0.08655 \end{aligned} \tag{4.2}$$

and between the parameters of the PC-X functional (shown by solid black lines in Figs.4.2b, e and g)

$$\begin{aligned} f(\alpha_v) &= 1.4203 f(\alpha_s) - 0.42178 \\ f(\delta_v) &= 0.08221 f(\delta_s) + 0.96062 \\ f(\gamma_v) &= -5.5582 f(\gamma_s) + 6.6311 \end{aligned} \tag{4.3}$$

Because of the two linear correlations (4.2) for the functionals DD-MEX and because of the three linear correlations (4.3) for the functionals PC-X the number of independent parameters can be reduced from 8 to 6 in the functional DD-MEX and from 9 to 6 in the functional PC-X. Note that the accounting of the parametric correlations in the case of non-linear meson-exchange models leaves only 5 independent parameters as shown in Ref. [83]. Thus, one can conclude that the ground state and nuclear matter properties usually used in the fitting protocols allow to define only 5-6 (dependent on the model structure) independent parameters in the case of CDFT. Models with a larger number of parameters are most likely over-parametrized.

These results are consistent for the three models. For the NL-ME model, we have only a density dependence in the isoscalar channel. Originally it is determined by 2 parameters $g_2$ and $g_3$. The parametric correlations lead to a reduction to only one parameter for the density dependence in the isoscalar channel (see Ref. [83] for details). The density dependence in the isovector channel is neglected and this obviously leads to unphysically large values of the slope of the symmetry energy $L_0$ (see Ref. [46]). In the DD-ME model, we have originally 3 parameters in the isoscalar channel and one parameter in the isovector channel. We found no parametric correlations in the isovector channel, but the number of parameters in the isoscalar channel is reduced by parametric correlations from 3 to 1. In the PC-models we have also one parameter in the isovector channel, but the number of parameters in the isoscalar channel is reduced from 4 to 1. Finally, we have in all cases one parameter in the isoscalar channel and one parameter in the isovector channel.

Additionally, this result can be qualitatively understood on a microscopic basis. Starting from the bare nucleon-nucleon interaction adjusted to the nucleon-nucleon scattering data [92] and using relativistic Brueckner-Hartree-Fock theory in symmetric and asymmetric nuclear matter at various densities, one is able to derive the relativistic self-energies of nucleons in nuclear matter without any phenomenological parameters [93, 94, 95, 96, 97]. By adjusting the self-energies obtained from CDFT in nuclear matter at the same density, it is possible to derive the density dependence of the coupling constants in a microscopic way [95]. However, in the Brueckner calculations, a number of approximations have been used and therefore this mapping is not unique. At present, the results obtained from such calculations in finite nuclei are rather different and, so far, their quality is far from that obtained with phenomenological CEDFs (see, for instance, Fig. 11 in Ref. [98]). However, they all show in the isoscalar channel a density dependence in the relevant density interval

is between 0.5 and 1.1 of the saturation density, which is close to a linear density dependence (see, for instance, Refs. [99, 100, 101]. This fact gives at least a qualitative explanation, why the parametric correlations discussed here allow a reduction to one parameter in the isoscalar channel.

### 4.3 Parametric correlations in the DD-ME class and PC class: simplex-based minimization

It is necessary to recognize that the search for parametric correlations in the multidimensional parameter hyperspace by the method described above is extremely time-consuming even with modern high performance computers. Thus, we looked for alternative methods for such a search. The simplest method we found is based on the minimization by the simplex method (see Ref. [102]). However, minimizations by the simplex method are prone to stack in local minima and that is a reason why it is not recommended for the search of global minimum. However, the drawback becomes an advantage in the context of the search of parametric correlations. Starting from different randomly defined parameter vectors we perform a number of trial minimizations with the simplex method. They lead to different local minima in the parameter hyperspace. The distributions of the parameters corresponding to these local minima are shown in Figs. 4.3 and 4.4 for the functionals DD-MEX and PC-X, respectively. One can see that the parametric correlations seen in Figs. 4.1 and 4.2 are also clearly visible in these two figures. It is important to note that the search of parametric correlations via the simplex-based minimization method is at least by an order of magnitude less time-consuming than a fully statistical search based on Eq. (3.4), which its results are shown in Figs. 4.1 and 4.2.

It is also important that the simplex-based minimization method allows to find a fine structure of such correlations which can be hidden in a fully statistical approach. This is illustrated in Fig. 4.3.

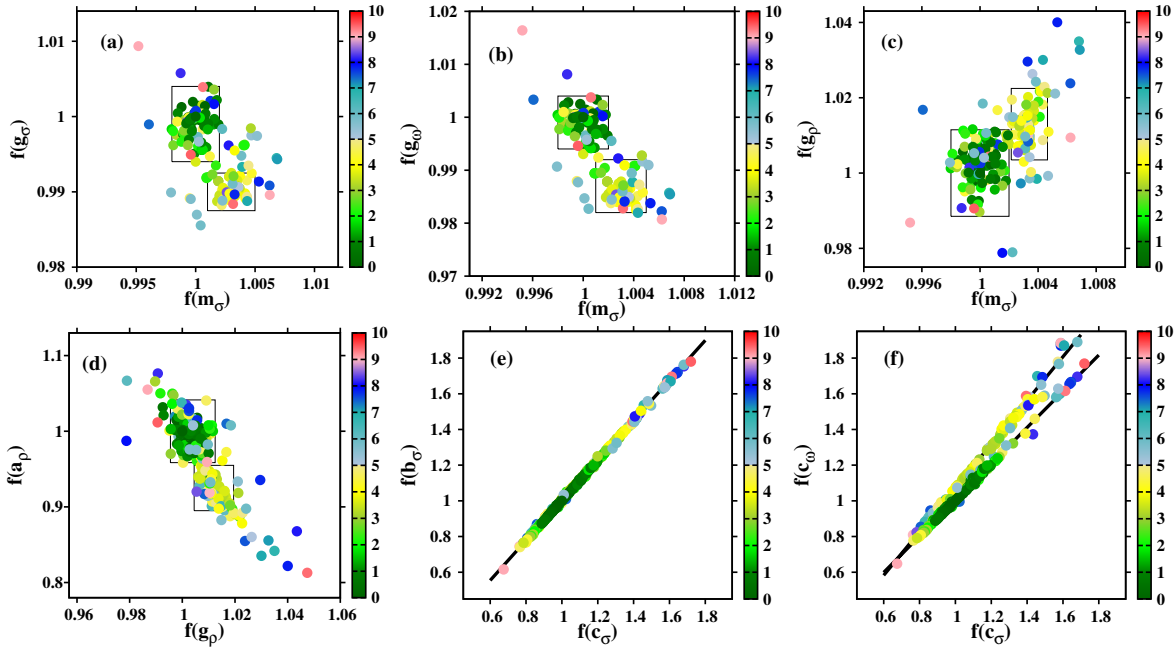


Figure 4.3

Two-dimensional projections of the distribution of the parameters corresponding to local minima obtained by simplex-based minimizations for the functional DD-MEX.

The colors indicate the $\Delta\chi^2$ value of the $\chi^2_{norm}(\mathbf{p})$ for the functionals in these local minima where the latter is expressed as $\chi^2_{norm}(\mathbf{p}) = \chi^2_{norm}(\mathbf{p}_0) + \Delta\chi^2$. Only local minima with $\Delta\chi^2 < 10.0$ are used here. There are 200 such minima. The optimal functional corresponding to global minimum is located at the intersection of the lines $f(p_k) = 1.0$ and $f(p_j) = 1.0$.

Figures 4.3a-d show the coexistence of two long-range structures corresponding to a global and a sub-global minima; the respective parameter ranges are enclosed by the rectangles in panels (a-d). While the parametric correlations between the parameters $b_\sigma$ and $c_\sigma$ are the same in both structures [which is not surprising considering that these two parameters describe the same type of meson] (see Fig. 4.3e), they are different between the $c_\omega$ and $c_\sigma$ parameters for these long-range structures (see Fig. 4.3e). This is also a reason why the correlations between the latter two parameters are broader (in width) in the fully statistical analysis presented in Fig. 4.1e; this is because $\Delta\chi^2_{max} = 3.0$

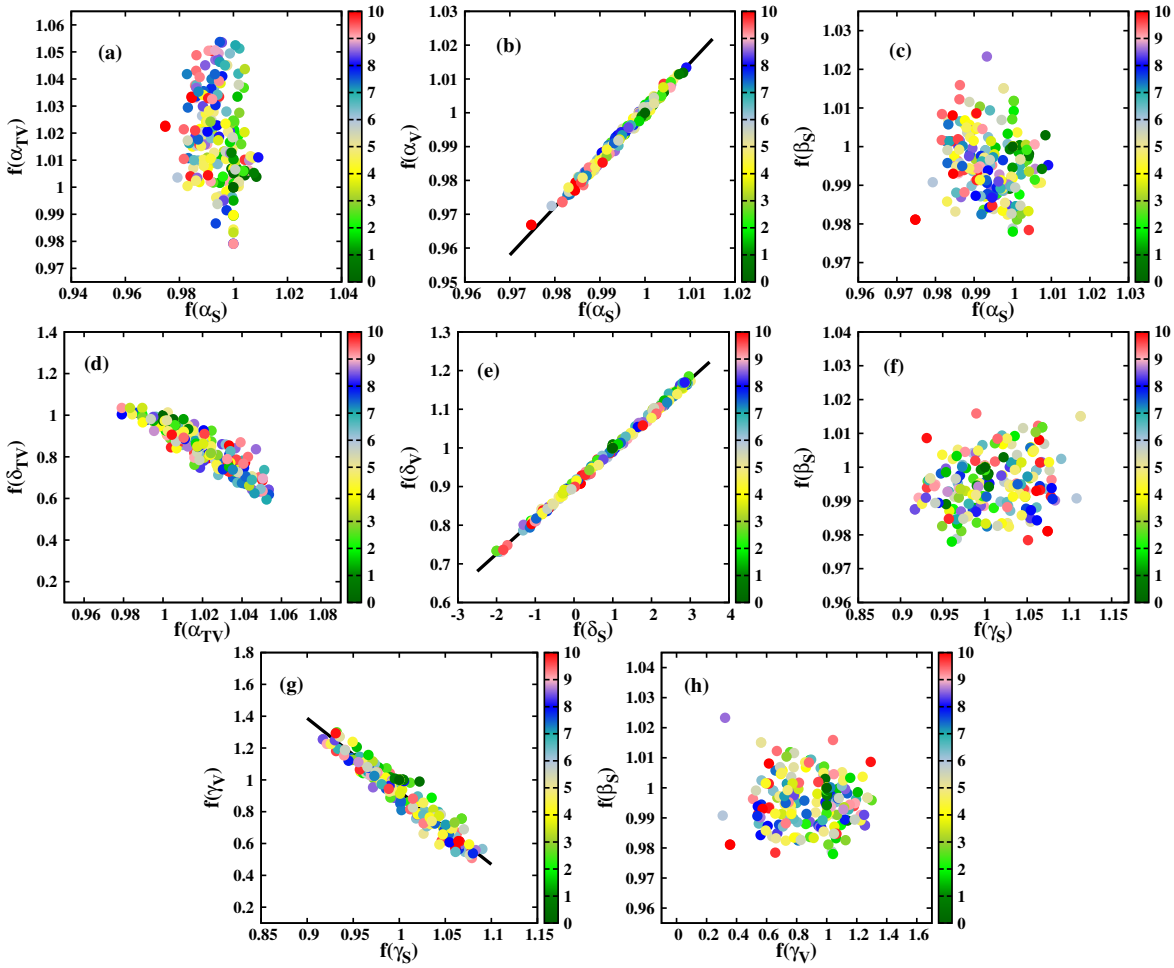


Figure 4.4

The same as Fig. 4.3 but for the PC-X functional.

used in this analysis covers both long-range structures. The linear correlations (shown by black lines in Figs. 4.3 and 4.4) defined via the simplex-based minimization method are given by

$$
\begin{aligned}
f(b_\sigma) &= 1.1212 f(c_\sigma) - 0.11845 \\
f(c_\omega) &= 1.0149 f(c_\sigma) - 0.01002 \\
f(c_\omega) &= 1.2254 f(c_\sigma) - 0.15263
\end{aligned}
\tag{4.4}
$$

for the DD-MEX functional. Note that the values given in the second and third lines of Eq. (4.4) correspond to the global and sub-global minima of the $\chi^2$ function, respectively. The equations

$$\begin{aligned} f(\alpha_v) &= 1.419 f(\alpha_s) - 0.41846 \\ f(\delta_v) &= 0.09026 f(\delta_s) + 0.90639 \\ f(\gamma_v) &= -4.5936 f(\gamma_s) + 5.9217 \end{aligned} \tag{4.5}$$

define similar correlations between the parameters of the PC-X functional. One finds an extreme similarity of the parametric correlations for PC-X obtained via the simplex-based minimization method (Eq. (4.5)) and those defined from full statistical analysis (Eq. (4.3)). The same is true for the correlations between the parameters $b_\sigma$ and $c_\sigma$ of the DD-MEX functional (compare the upper lines of Eqs. (4.2) and (4.4)). However, the results for the parametric correlations between the parameters $c_\omega$ and $c_\sigma$ of the DD-MEX functional obtained by full statistical analysis are located in between of those defined by means of simplex-based minimization method (compare Eqs. (4.2) and (4.4)). This is due to the fact that because of the selection of the $\Delta\chi^2_{max}$ value the results obtained with former method are an "envelope" of those obtained with latter method.

## 4.4 Conclusions

Density functional theories (DFT) are defined by underlying functionals. Some of those functionals depend on a substantial number of parameters. However, the parametric correlations between them have not been studied before.

Using covariant DFT as an example and statistical tools, we investigated for the first time such correlations for major classes of covariant energy density functionals. These include the non-linear

meson-exchange (NLME) functionals NL5(A) and NL5(C), the functionals DD-MEX and PC-X in DD-ME and PC models respectively.

These functionals are defined by the ground state properties of spherical nuclei and with exception of PC-X by the pseudodata on nuclear matter. It turns out that parametric correlations exist between a number of parameters in all of those functionals. For example, linear parametric correlations exist between the parameters $g_2$ and $g_3$ which are responsible for the density dependence in the NLME model. For the DD-ME functionals, the parameters $b_\sigma$ and $c_\omega$ vary linearly with $c_\sigma$. Similarly, linear correlations are visible in the parameter pairs ($\alpha_V$,$\alpha_S$), ($\delta_V$,$\delta_S$), and ($\gamma_V$,$\gamma_S$) of the PC-X functionals. The observation of correlations effectively reduces the number of independent parameters to five or six dependent on the structure and the underlying functional.

Thus, these numbers represent a limit of how many independent parameters could be defined in the CDFT using fitting protocols based on ground state and nuclear matter properties. Of course, at this stage, we cannot confirm that these correlations will show up also for other fitting protocols, in particular for those containing other types of data. However, at present, obtained results seem to be rather general.

It is reasonable to expect that similar parametric correlations exist also in non-relativistic energy density functionals. In fact, in this case one should expect even more such parametric correlations because as it is known a non-relativistic approximation of covariant functionals in terms of a $p/M$-expansion leads to a non-relativistic functionals with a large number of terms [103, 104, 105]. However, the various parameters in such functionals are not independent, but determined by Lorentz invariance. An example are the Galilean invariant terms in some Skyrme functionals [106, 107] connecting time-even and time-odd components of the functionals. They are a direct consequence

of the fact that time-even and time-odd components in relativistic functionals are determined by the same coupling constants.

# CHAPTER V

# OPTIMIZATION OF COVARIANT ENERGY DENSITY FUNCTIONALS: A NEW APPROACH

## 5.1 Introduction

Among the fundamental properties of nuclei are their masses, which reflects the binding energy of nucleons and, therefore, all their interactions. The description of nuclear masses with high precision and accuracy is a major challenge for nuclear models. Nevertheless, tremendous progress has been made over the past years, and many global nuclear mass models have been suggested. The macroscopic-microscopic models [108, 109, 110, 111] have been successful in describing nuclear masses accurately. In addition, several Hartree-Fock-Bogoliubov (HFB) mass table calculations have been created using Skyrme's [37, 112, 113] or Gogny's [114, 115] nonrelativistic DFTs, providing an accurate description of nuclear masses. The UNEDF0 [116], UNEDF1 [117], and UNEDF2 [118] EDFs were developed by fitting their parameters to large sets of experimental data involving spherical and deformed nuclei. It has been reported that the nuclear masses are described in these EDFs with an rms-accuracy of 1.428 MeV (UNEDF0), 1.912 MeV (UNEDF1), and 1.950 MeV (UNEDF2).

Although CDFT has received a wide attention and achieved a great success in describing many phenomena of both stable and exotic nuclei [8, 47, 76, 119], the description of nuclear binding energy based on the widely used CEDFs requires further improvement. Many reliable

global mass table calculations have been performed with different CEDFs. Among them are the parametrizations NL3 [69], FSUGold [120], BSR4 [121], and TM1 [81] in the RMF + BCS approach employing the constant gap approximation in Ref. [122] as well as PC-PK1 [30] in the RMF + BCS approach using density-dependent pairing in Ref. [123]. The rms errors for the masses found for these CEDFs are 3.8 MeV for NL3, 6.5 MeV for FSUGold, 2.6 MeV for BSR4, 5.9 MeV for TM1, and 2.6 MeV for PC-PK1 (at the mean-field level). The functionals NL3* [28], DD-ME2 [29], DD-ME$\delta$ [18], and DD-PC1 [19] have been employed for full mass table calculations in Ref. [2] using the RHB framework with the separable pairing interaction of finite range introduced by Tian et al. [51]. The rms deviations in the masses described in these CEDFs are 3.00 MeV for NL3*, 2.45 MeV for DD-ME2, 2.40 MeV for DD-ME$\delta$, and 2.15 MeV for DD-PC1. One can see that CEDFs NL3*, DD-ME2, DD-ME$\delta$, and DD-PC1 provide improved descriptions of masses across the nuclear chart as compared with the other CEDFs. Furthermore, they are more statistically significant than those reported in Refs. [122] and [123], since they are based on 835 (measured and estimated) even-even nuclei of AME2012 mass evaluation [124]. On the other hand, the rms deviations in binding energies for the NL3, FSUGold, BSR4, and TM1 CEDFs are only defined for 513 (575 for PC-PK1) even-even nuclei [122, 123]. It is possible that the extension of the experimental database to 835 nuclei may cause a further deterioration in mass description by these CEDFs.

The inclusion of dynamical correlations (which involve rotational correction energies obtained with the cranking approximation and quadrupole vibrational correction energies) improves the description of the masses of the 575 even-even nuclei in the CEDF PC-PK1 from 2.60 MeV to 1.24 MeV [123]. This was enhanced to 1.14 MeV by employing the triaxial RMF + BCS approach

with the incorporation of beyond mean-field dynamical correlations by solving a five-dimensional collective Hamiltonian [125]. The CEDF PC-PK1 was recently used in a mass table calculation within the triaxial RHB framework [126]. A microscopically mapped five-dimensional collective Hamiltonian with no additional free parameters was used to account for the beyond-mean-field dynamical correlation energies. With respect to the data from AME2016 mass evaluation [127], the accuracy in the description of the nuclear masses was determined to be 2.64 MeV on the mean-field level and 1.31 MeV beyond the mean-field level [126]. It is worth noting that all of the calculations performed with the CEDF PC-PK1 [123, 125, 126] employed the harmonic oscillator bases with a maximum of 16 major shells, which is a subject of concern.

The mass table calculations in this chapter have been performed in the axial RHB framework in which the equations are solved in the basis of an axially deformed harmonic oscillator potential with deformation of the basis $\beta_0$ and oscillator frequency $\hbar\omega_0 = 41A^{-\frac{1}{3}}$ MeV. The deformation of the basis $\beta_0$ influences the binding energy and convergence speed. As demonstrated in Ref. [32], $\beta_0 = 0.5\beta_2$, where $\beta_2$ is the deformation of the nucleus, provides on average the fastest convergence. As a result, this choice has been adopted in the calculation in this study. The truncation of the basis is performed in such a way that all states belonging to the shells up to $N_F$ fermionic shells and $N_B$ bosonic shells are taken into account. It has been demonstrated that the computational time grows significantly as $N_F$ increases. In addition, it has been shown that larger $N_F$ is needed when charge, deformation, and isospin increase [24, 32]. As a result, a more careful consideration should be devoted to the selection of $N_F$.

Figure 5.1 shows the difference in binding energy calculated within the DD-MEX functional for the set of even-even nuclei which have experimental data based on the AME2016 mass evaluation

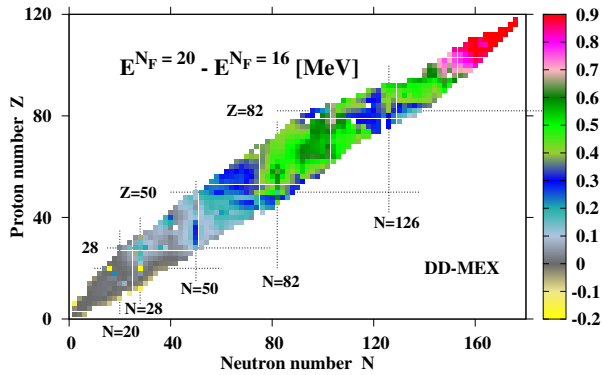


Figure 5.1

The difference between the calculated binding energies obtained with $N_F = 16$ and $N_F = 20$ fermionic shells in the calcualtion with the DD-MEX functional.

The calculations includ 855 even-even nuclei that have measured and estimated masses in Ref. [127]. Nuclei in which deformations and energies of the ground states are significantly different between the two calculations are indicated by empty squares.

[127]. This figure indicates the differences in binding energy between the calculations with $N_F = 20$ and $N_F = 16$ fermionic shells. The rise in their difference with increasing proton number Z and neutron number N is obvious. The binding energy difference ranges from 0 to 200 keV for the most of the nuclei with $Z < 50$. The difference in energy among nuclei with $50 < Z < 102$ is between 200 and 700 keV. The difference in energy for superheavy nuclei with $102 < Z < 122$ is between 700 and 900 keV. These observations confirm the view that, as Z and N increase, larger $N_F$ is required to maintain the numerical accuracy of the description of binding energy. On the basis of these observations, the use of $N_F = 16$ fermionic shells may be safe only for light ($Z < 50$) nuclei. The calculations with $N_F = 16$ fermionic shells in the other parts of the nuclear chart substantially reduce the accuracy of the calculations.

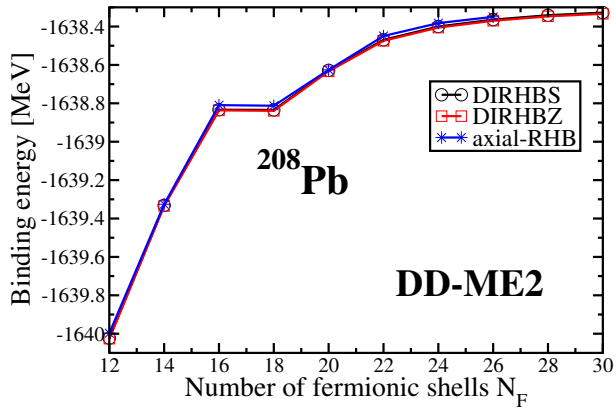


Figure 5.2

The dependence of total binding energy on the number of fermionic shells $N_F$.

The calculation was conducted within the DD-ME2 functional for the $^{208}Pb$ nucleus. The spherical DIRHBS code and the axial symmetric DIRHBZ code from Ref. [128], as well as the axial-RHB code developed in Ref. [2] were employed in these calculations.

In fact, even $N_F = 20$ fermionic shells are insufficient, and calculations of binding energy are saturated only at higher $N_F$ fermionic shells. The binding energy as a function of $N_F$ for the $^{208}Pb$ nucleus within the DD-ME2 functional is shown in Fig. 5.1. This calculation utilized the spherical DIRHBS code and the axial symmetric DIRHBZ code from Ref. [128], as well as the axial-RHB code developed in Ref. [2], and they all exhibit a similar trend in which the calculation of binding energy saturate only at $N_F \approx 26$ fermionic shells. Nevertheless, functionals fitted with $N_F = 20$ fermionic shells may be able to account partially for these errors.

## 5.2 Method

The mass table calculations in this study were conducted in the axial RHB framework with the axial-RHB code developed in Ref. [2]. The functionals optimizations were carried out using

the spherical RHB code. In order to optimize a model and identify the optimum parameters set, the penalty function $\chi 2$ defined in Eq. (3.1) must be minimized with respect to specified data of selected nuclei. This is conducted using the simplex-based minimization method described in Appendix A. A large number of CEDFs have been optimized based on the ground state and nuclear matter properties of selected spherical nuclei. However, our analysis demonstrates that too much enforcement on the spherical nuclei in the fitting protocols is not necessary to attain better global performance. The minimization of the functional DD-ME2 using 12 spherical nuclei in the fitting protocol leads to the optimal functional DD-MEX [91]. Table 2 of the supplementary material of Ref. [91] shows the parameters for the two functionals and the total penalty function along with its contributions from nuclear matter properties, binding energies, charge radii, and neutron skins. The total penalty function for the spherical nuclei has been improved from 39.25 (for DD-ME2 functional) to 24.39 (for DD-MEX functional). The penalty function of the binding energy has been improved from 25.22 for DD-ME2 to 16.18 for DD-MEX. On the global scale, however, the functional DD-MEX shows worse performance as compared with DD-ME2 functional. DD-MEX functional has an rms deviation in reproducing binding energies (masses) of 2.894 MeV compared to 2.477 MeV of DD-ME2 functional (see Table 5.2 below).

The importance of developing a fitting protocol that incorporates deformed nuclei data becomes very clear. However, adding the deformed nuclei directly to the fitting protocol will dramatically increase the computational time of the minimization. This is because solving RHB equations in deformed systems is very time-consuming. Another approach requiring less computational effort is to indirectly include deformed nuclei in the optimization process. This technique works as follows:

1. Using experimental data of spherical nuclei, we perform a minimization to determine the optimum parameters set. A full mass table calculation is then conducted using the functional with the optimum parameters set.

2. We propose a pseudo-energy equal to the binding energy of the functional plus a correction energy that depends both on mass number $A$ ($A = N + Z$) and isospin ($N - Z$):

$$E_{pseudo}(Z,N) = E_{functional}(Z,N) + E_{corr}(Z,N) \tag{5.1}$$

with,

$$E_{corr}(Z,N) = \alpha(N-Z) + \beta(N+Z) + \gamma \tag{5.2}$$

3. Following that, the optimal parameters $\alpha_0$, $\beta_0$, and $\gamma_0$ are obtained by minimizing $\Delta E_{rms}$ defined as:

$$\Delta E_{rms} = \sqrt{\frac{\sum_{i=1}^{n}(E_{pseudo}(Z,N) - E_{exp}(Z,N))^2}{n}} \tag{5.3}$$

with $i$ runs over all the even-even nuclei (deformed and spherical) that have experimental data based on AME2016 mass evaluation [127], and $n$ denoting the total number of these nuclei.

4. Then, we define the pseudo-energy of the set of spherical nuclei as follows:

$$E_{pseudo}^{spherical}(Z,N) = E_{exp}(Z,N) + E_{corr}^{optimum}(Z,N) \tag{5.4}$$

with

$$E_{corr}^{optimum}(Z,N) = \alpha_0(N-Z) + \beta_0(N+Z) + \gamma_0 \tag{5.5}$$

5. We then perform a minimization using the pseudo-data of spherical nuclei. A new functional is defined corresponding to the optimum parameter set. With the new functional, we perform a full mass table calculation and then calculate its $\Delta E_{rms}$ deviation. In the event that $\Delta E_{rms}$ is not improved satisfactorily, we repeat steps 2-5 until a satisfactory value is reached. In most calculations, however, we developed a great improvement after one round of this method.

This method will be called further the pseudo-data minimization.

## 5.3 Results

The starting point is the fitting protocol of the DD-ME2 functional [29]. The types of the input data for this protocol and related adopted errors are given in column 2 in Table 5.1. The

Table 5.1

Input data for fitting protocol of the indicated CEDFs.

| | DD-ME2 | DD-MEX | DD-MEX3 | DD-MEY1 | DD-MEY2 | NL5E | NL5E1 | DD-MEZ | DD-MEZ1 | PC-PK1 | PC-Z | PC-Z1 |
|---|---|---|---|---|---|---|---|---|---|---|---|---|
| 1 | 2 | 3 | 4 | 5 | 6 | 7 | 8 | 9 | 10 | 11 | 12 | 13 |
| 1. Masses $E$ (MeV) | | | | | | | | | | | | |
| $n_1$<br>$\Delta E$ [MeV] | 12<br>$0.001E$ | | | 12<br>1 | 12<br>1 | | 12<br>1 | 60<br>1 | | | | |
| 2. Charge radii $r_{ch}$ (fm) | | | | | | | | | | | | |
| $n_2$<br>$\Delta r_{ch}$ [fm] | 9<br>$0.002\,r_{ch}$ | | | | | | | 17<br>0.02 | | | | |
| 3. Neutron skin $r_{skin}$ (fm) | | | | | | | | | | | | |
| | YES | | | NO | NO | | NO | NO | | | | |
| 4. Nuclear matter properties | | | | | | | | | | | | |
| | YES | | | NO | NO | | NO | NO | | | | |
| 5. Pairing interaction scaling factors | | | | | | | | | | | | |
| | Ref. [2] | | | | Eqs. (5.6) and (5.7) | | Eqs. (5.6) and (5.7) | Eqs. (5.6) and (5.7) | | Ref. [2] | | |

The number $n_i$ of experimental (empirical) data points and adopted errors $\Delta O_{i,j}$ are presented binding energies and charge radii. YES/NO denotes the inclusion/removal of neutron skins and nuclear matter properties, in/from the fitting protocol. The pairing interaction scaling factors are defined either based on Ref. [2] or on Eqs. (5.6) and (5.7) below. Columns 3-8 show only the changes with respect to what is provided in column 2. Columns 10-13 show only the changes with respect to what is provided in column 9.

minimization within this protocol leads to the optimum functional DD-MEX [91]. The performance of this functional is tabulated in Table 5.2. Although this functional is considered to be the optimum for the 12 spherical nuclei employed in the fitting protocol, it performs worse in terms of binding energies and separation energies on the global scale (see Table 5.2).

When considering the quality of the functional we take into account the ranges of the nuclear matter properties recommended for relativistic functionals in Ref. [72]. These are $\rho_0 \sim 0.15$ fm$^{-3}$, $E/A \sim -16$ MeV, $K_0 = 190 - 270$, $J = 25 - 35$ MeV ($J = 30 - 35$ MeV) and $L_0 = 25 - 115$ ($L_0 = 30 - 80$) for the SET2a (SET2b) sets of the constraints on the experimental/empirical ranges for the quantities of interest. As compared with the CEDF DD-ME2, the DD-MEX functional has comparable $J$ and $L_0$ values but worse $K_0$ value (it is however within the acceptable range of experimental values). In addition, when compared to the DD-ME2 functional, this functional provides comparable values of neutron skins $r_{skin}$ of both $^{48}Ca$ and $^{208}Pb$ nuclei.

A set of pseudo-data of the spherical nuclei is identified using the pseudo-data minimization approach. Using these data, a new parametrization is achieved via minimization through DD-MEX parametrization. The DD-MEX1 functional is obtained after a few successive rounds. Compared to DD-ME2 and DD-MEX CEDFs, DD-MEX1 provides siginificant improvement in the mass description; it is on the same level of accuracy obtained with the UNDEF functionals. It also provides comparable descriptions of two proton separation energies, and neutron skins $r_{skin}$ of both $^{48}Ca$ and $^{208}Pb$ nuclei in comparison to DD-ME2 and DD-MEX functionals. Within this functional, the symmetry energy and its slope are comparable to those of DD-ME2 and DD-MEX CEDFs. The description of the two neutron separation energies within DD-MEX1 functional is better/slightly worse than the one provided by DD MEX/DD-ME2 functionals. Despite these

Table 5.2

The performance of the indicated CEDFs.

| | $\Delta E$ $rms$ | $\Delta(S_{2n})$ $rms$ | $\Delta(S_{2p})$ $rms$ | $\Delta(r_{ch})$ $rms$ | $K_0$ | $J$ | $L_0$ | $r_{skin}$ ($^{48}Ca$) | $r_{skin}$ ($^{208}Pb$) |
|---|---|---|---|---|---|---|---|---|---|
| 1 | 2 | 3 | 4 | 5 | 6 | 7 | 8 | 9 | 10 |
| | | | | | | | | | |
| DD-ME2 [29] | 2.477 | 1.046 | 0.950 | 0.0264 | 250.9 | 32.9 | 49.4 | 0.1868 | 0.1931 |
| DD-MEX [91] | 2.894 | 1.124 | 1.013 | 0.0247 | 267.0 | 32.9 | 47.8 | 0.1838 | 0.1936 |
| DD-MEX1 | 1.79 | 1.065 | 0.928 | 0.0262 | 306.7 | 32.4 | 53.5 | 0.1857 | 0.1981 |
| | | | | | | | | | |
| DD-MEY1 | 2.217 | 1.201 | 1.225 | 0.0290 | 255.8 | 35.9 | 85.3 | 0.2265 | 0.2575 |
| DD-MEY2 | 1.719 | 1.208 | 1.025 | 0.0264 | 265.8 | 32.8 | 51.8 | 0.1897 | 0.1979 |
| | | | | | | | | | |
| NL5E [83] | 2.81 | 1.232 | 1.390 | 0.0289 | 253.0 | 38.9 | 125.0 | 0.2288 | 0.2925 |
| NL5E1 | 2.36 | 1.256 | 1.222 | 0.0297 | 254.6 | 36.6 | 116.7 | 0.2209 | 0.2759 |
| | | | | | | | | | |
| DD-MEZ | 3.711 | 1.217 | 1.194 | 0.0255 | 266.5 | 35.9 | 73.6 | 0.2226 | 0.2607 |
| DD-MEZ1 | 2.200 | 1.269 | 1.277 | 0.0223 | 329.4 | 37.2 | 86.3 | 0.2270 | 0.2844 |
| | | | | | | | | | |
| PC-PK1 [30] | 2.38 | 1.283 | 1.302 | 0.0306 | | | | 0.2320 | 0.2572 |
| PC-Z | 3.08 | 1.386 | 1.213 | 0.0295 | | | | 0.2258 | 0.2619 |
| PC-Z1 | 1.93 | 1.369 | 1.156 | 0.0308 | | | | 0.2268 | 0.2607 |

The rms deviations $\Delta E_{rms}$, $\Delta(S_{2n})_{rms}$, $\Delta(S_{2p})_{rms}$, and $\Delta(r_{ch})_{rms}$ between calculated and experimental binding energies $E$, two neutron (-proton) separation energies $S_{2n}$ ($S_{2p}$), and charge radii $r_{ch}$. The first three observables are given in MeV and determined using "measured + estimated" (855 nuclei) sets of experimental masses from the AME2016 mass evaluation [127]. The values of $\Delta(r_{ch})_{rms}$ are given in fm and were calculated using experimental data from 305 even-even nuclei from Ref. [129] (see text for the discussion of exclusion of some nuclei). Columns 6-8 show the incompressibility $K_0$ in MeV, the symmetry energy $J$ in MeV, and the slope of the symmetry energy $L_0$ in MeV for the indicated CEDFs. Columns 9 and 10 shows the neutron skin $r_{skin}$ values in fm of the $^{48}Ca$ and $^{208}Pb$ nuclei for the indicated CEDFs. The fitting protocols of these functionals are given in Table 5.1. Their parameters are given Tables 5.3, 5.4, and 5.5 below.

advantages, however, this functional is considered to have a disadvantage of a high incompressibility $K_0$ (which falls outside of the acceptable limits) as compared to DD-ME2 and DD-MEX functionals.

Table 5.3

The parameters of the indicated CEDFs.

| | DD-ME2 | DD-MEX | DD-MEX1 | DD-MEY1 | DD-MEY2 | DD-MEZ | DD-MEZ1 |
|---|---|---|---|---|---|---|---|
| $m_\sigma$ | 550.123800 | 547.33272 | 555.355699 | 551.087886 | 551.321796 | 538.941984 | 538.941984 |
| $g_\sigma$ | 10.539600 | 10.70672 | 10.650805 | 10.476976 | 10.411867 | 10.629640 | 10.629640 |
| $g_\omega$ | 13.018900 | 13.33884 | 13.039170 | 12.903532 | 12.803298 | 13.466477 | 13.466477 |
| $g_\rho$ | 3.683600 | 3.61902 | 3.643546 | 4.100719 | 3.692170 | 3.947464 | 3.947464 |
| $b_s$ | 1.094300 | 1.334964 | 3.616548 | 1.506460 | 2.059712 | 1.624526 | 1.624526 |
| $c_s$ | 1.705700 | 2.067122 | 5.607824 | 2.337477 | 3.210289 | 2.597641 | 2.597641 |
| $c_o$ | 1.462000 | 1.605966 | 5.659996 | 2.100795 | 3.025356 | 1.835889 | 1.835889 |
| $a_r$ | 0.564700 | 0.620220 | 0.542229 | 0.193540 | 0.532267 | 0.340617 | 0.340617 |

The DD-ME2 and DD-MEX parameters are taken from Ref. [29] and Ref. [91] respectively.

One can consider removing the neutron skins and nuclear matter properties from the fitting protocol and changing the adopted error of binding energy to $1MeV$ (see column 5 in Table 5.1). The latter has the advantage of imposing identical constraints on all the nuclei during the fitting. Incorporating these changes and performing several rounds of pseudo-data minimization enabled the generation of the DD-MEY1 functional starting from the DD-ME2 functional. DD-MEY1 functional provides improved mass descriptions in comparison to DD-ME2 and DD-MEX CEDFs, yet its mass description is worse than that of CEDF DD-MEX1. On the other hand, the description of the two-neutron and two-proton separation energies is worse than that of the DD-ME2, DD-MEX, and DD-MEX1 functionals.

It may be worthwhile to change the form of the pairing interaction scaling factors $f_i$ from the ones of Ref. [2]. More complicated particle number dependence of scaling factors $f_i$ are allowed in general (see Refs. [2, 130]). A recent systematic investigation in Ref. [130] shows that the scaling factors $f_\nu$ of neutron pairing are isospin dependent. In the proton subsystem, however, the

situation is less certain, because both isospin-dependent and mass-dependent scaling factors $f_\pi$ may describe pairing indications with equal precision. A fitting protocol similar to that used in the CEDF DD-MEY1 was used to obtain the CEDF DD-MEY2. The only difference is that the pairing interaction scaling factors take the form of one of the optimal parameterizations derived in Ref. [130]. These formulas are:

$$f_\nu = 1.208 * e^{-0.674 * \frac{|N-Z|}{N+Z}} \tag{5.6}$$

$$f_\pi = 1.877 * (N+Z)^{-0.1072} \tag{5.7}$$

for the neutron and the proton, respectively

The functional DD-MEY2 provides a level of mass description accuracy comparable to that attained with the CEDF DD-MEX1. Despite the fact that this functional was fitted without using nuclear matter properties, it gives more reasonable values for nuclear matter properties (specifically $K_0$, which is within the allowed range of values) than the DD-MEX1 functional. In both parameterizations, the description of neutron skins of $^{48}Ca$ and $^{208}Pb$ nuclei is quite similar. The DD-MEY2 functional, on the other hand, performs poorly in reproducing the two-neutron and two-proton separation energies when compared to the DD-MEX1 functional.

The difference $E_{th} - E_{exp}$ between calculated and experimental binding energies for the CEDFs DD-MEX and DD-MEY2 is depicted in Fig. 5.3. Panels (a) and (b) represent this difference as a function of mass number $A$, while panels (c) and (d) represent it as a function of $Z$ and $N$. In comparison to the CEDF DD-MEX in panel (a), the improvement in the description of binding energies within the CEDF DD-MEY2 is extremely obvious, as the deviations in panel (b) become more clustered around the zero deviation line. Furthermore, CEDF DD-MEY2 is more accurate

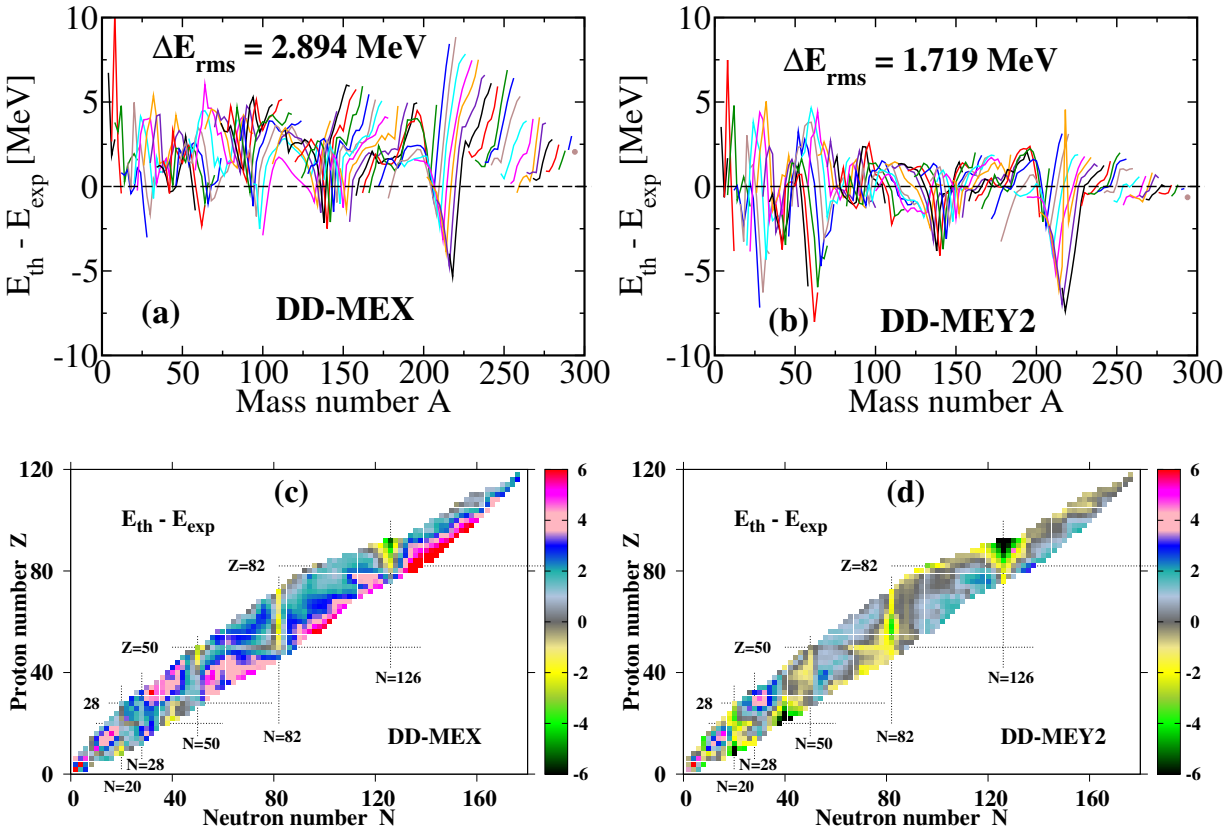


Figure 5.3

The differences $E_{th} - E_{exp}$ between calculated and experimental binding energies for the indicated CEDFs.

The experimental data are taken from Ref. [127] and all 855 even-even nuclei, for which measured and estimated masses are available, are included. If $E_{th} - E_{exp} < 0$, the nucleus is more bound in the calculations than in experiment.

in describing the masses of heavy nuclei than it is in describing the masses of medium-mass and light nuclei. The large deviation peaks that may be seen are around the double magical shell closures. Medium polarization effects associated with surface and pairing vibrations have a significant impact on the binding energies of such nuclei [131]. Furthermore, including dynamical

Table 5.4

The parameters of the indicated CEDFs.

| | NL5E | NL5E1 |
|---|---|---|
| $m_\sigma$ | 503.298890 | 508.628825 |
| $g_\sigma$ | 10.263955 | 10.274835 |
| $g_\omega$ | 13.052487 | 12.906821 |
| $g_\rho$ | 4.582673 | 4.375307 |
| $g_2$ | -10.976703 | -11.197664 |
| $g_3$ | -32.006687 | -31.996125 |

The NL5E parameters are taken from Ref. [83].

correlations is likely to improve the description of light nuclei since beyond mean-field effects may be more essential for light nuclei than for heavy ones.

It should be noted that the pseudo-data minimization approach was also applied to other classes of CEDFs and improved the description of masses across all of them. The minimization within CEDF NL5E generated the NL5E1 CEDF which offers noticeably improved mass descriptions. The functional PC-Z was developed by minimizing the functional PC-PK1 using experimental data of 60 spherical nuclei (with pairing interaction scaling factors given in Eqs. (5.6) and (5.7)). The functional PC-Z has improved descriptions of the binding energies of the spherical nuclei incorporated in the fitting protocol. However, it performs worse on the global scale. The functional PC-Z1 is obtained using the pseudo-data minimization approach executing the minimization via PC-Z functional. On the global scale, it outperforms both PC-Z and PC-PK1 CEDFs.

One could consider adding more nuclei to the fitting protocol of the DD-ME type of functionals. Using experimental data of 60 spherical nuclei, the DD-MEZ functional was generated via minimization of the DD-ME2 functional (with some changes to the fitting protocol listed in Table

Table 5.5

The parameters of the indicated CEDFs.

| | PC-PK1 | PC-Z | PC-Z1 |
|---|---|---|---|
| $\alpha_S$ | -0.39629D-03 | -0.40033D-03 | -0.40538D-03 |
| $\alpha_V$ | 0.26904D-03 | 0.27308D-03 | 0.27879D-03 |
| $\alpha_{TV}$ | 0.29502D-04 | 0.29862D-04 | 0.29052D-04 |
| $\beta_S$ | 0.86653D-10 | 0.86353D-10 | 0.83793D-10 |
| $\gamma_S$ | -0.38072D-16 | -0.37354D-16 | -0.37579D-16 |
| $\gamma_V$ | -0.36422D-17 | -0.46568D-17 | -0.38742D-17 |
| $\delta_S$ | -0.10911D-09 | -0.19130D-09 | -0.36836D-09 |
| $\delta_V$ | -0.43262D-09 | -0.36838D-09 | -0.20944D-09 |
| $\delta_{TV}$ | 0.41111D-09 | -0.28273D-09 | -0.52000D-09 |

The PC-PK1 parameters are taken from Ref. [30].

5.1). Again, putting too much restrictions on the spherical nuclei results in functionals that perform worse on the global scale. The pseudo-data minimization approach was employed to minimize the DD-MEZ functional, resulting in the DD-MEZ1 functional. In comparison to both DD-ME2 and DD-MEZ CEDFs, DD-MEZ1 functional provides a better description of masses. However, the CEDFs DD-MEX1 and DD-MEY2, which use 12 spherical nuclei in the fitting protocol, perform better in terms of mass, two-neutron and two-proton separation energies, and nuclear matter properties. This indicates that adding more spherical nuclei to the fitting protocol isn't necessary to improve it.

All CEDFs shown in Table 5.2 give comparable rms deviations for charge radii $\Delta(r_{ch})_{rms}$. The deviations are on the level of $\approx 0.025$ fm, corresponding to a high precision of $\approx 0.5\%$ in charge radii prediction. These deviations were calculated based on experimental data of 305 even-even nuclei from Ref. [129] with He ($Z = 2$) and nuclei beyond Pb ($Z = 82$) (with exception of uranium)

being eliminated. The exclusion of the He isotopes is driven by the fact that it characterized by a significant difference between calculation and experiment (see Sec. X of Ref. [2]). This could be due to the limitation of the mean-field description for light nuclei. The exclusion of nuclei with proton numbers $Z > 82$ (uranium is the exception) is based on the absence of experimental data for the absolute nuclear charge radius of those nuclei. This is because nuclear charge radii cannot be measured using muonic spectra and electronic scattering experiments in radioactive elements [129, 132].

## 5.4 Conclusions

Currently, nuclear density functional theory is one of the most widely applied microscopic approaches to studying the nuclear structure of medium and heavy nuclei. The binding energy of nuclei, or their nuclear masses, is one of the most important nuclear structure quantities to be studied rigorously through DFT. Despite the fact that the macroscopic-microscopic and non-relativistic DFT mass models achieved high accuracy in the nuclear mass description, the accuracy of the CDFT mass models needs improvement.

In this work, we present a new approach for improving CDFT mass models. The pseudo-data minimization approach discussed in Sec. 5.2 was employed to various classes of CEDFs, resulting in a better description of nuclear masses in all of them. CEDFs DD-MEX1 and DD-MEY2 are able to describe the nuclear masses with an accuracy of about 1.7 MeV, which is comparable to the accuracy of the family of the UNEDF functionals. However, the UNEDF functionals have been fitted to very large databases and explicitly include the experimental data of the deformed nuclei in the fitting protocols, resulting in extremely large computational time required for the minimization.

Our approach, on the other hand, is fast in terms of computational time, and it would be particularly useful in EDFs optimization in the beyond mean-field models, where the presence of dynamical correlations significantly increases the computational time.

The current research also shows that the inclusion of nuclear matter properties and neutron skins in the fitting protocol is not required in order to obtain CEDFs that accurately describe them. When compared to the CEDF DD-MEX1, which was fitted with the nuclear matter properties, the CEDF DD-MEY2, which was not fitted with them, is characterized by better incompressibility $K_0$. Furthermore, the neutron skins in both $^{48}Ca$ and $^{208}Pb$ nuclei are comparable in CEDFs DD-MEX1 and DD-MEY2, despite the fact that the former was fitted with neutron skins while the latter was not. Defining the pairing interaction scaling factors in the form of Eqs. (5.6) and (5.7) may, in part, compensate for the inclusion of nuclear matter properties as well as neutron skins in the fitting protocols, as CEDF DD-MEY2 possesses these characteristics as compared with CEDF DD-MEX1.

# CHAPTER VI

# COVARIANT DENSITY FUNCTIONAL THEORY INPUT FOR R-PROCESS SIMULATIONS IN ACTINIDES AND SUPERHEAVY NUCLEI: THE GROUND STATE AND FISSION PROPERTIES

## 6.1 Introduction

The majority of the nuclei found in nature are formed in the r-process. Indeed, the r-process is responsible for the synthesis of approximately half of the nuclei in nature beyond Fe [133] and it is the only process which leads to the creation of nuclei heavier than Bi [134]. It takes place at extremely high neutron densities ($N_n \geq 10^{20}$ cm$^{-3}$) which are high enough to make neutron capture faster than $\beta$-decay even for the nuclei with neutron excess between 15 to 30 units from the stability line. The production of neutron-rich nuclei located in the vicinity of the neutron dripline is enabled under these conditions via neutron capture and $(\gamma, n)$ photodisintegration during the r-process. Once the neutron source ceases, the progenitor nuclei decay either via $\beta^-$ decay or $\alpha$ emission or by fission processes (such as neutron-induced, $\beta$-delayed and spontaneous fissions) towards stability and form the stable isotopes of elements up to the heaviest species Th, U and Pu. The typical timescale of the r-process is in the seconds range [134, 135, 136].

Over the years different possible astrophysical sites have been and still are considered as possible candidates for the r-process. These include core-collapse supernovae, magneto-rotational core-collapse supernovae, accretion disk outflows from collapsars, neutron star (NS) mergers

and neutron star - black hole mergers etc [134, 135, 136, 137]. So far only the NS merger is experimentally confirmed as a site of the r-process via the observation of gravitational waves from the GW170817 neutron star merger [138] with simultaneous observation of the AT 2017gfo macronova/kilonova afterglow [139]. In NS mergers, the r-process material originates in the NS crust, and the composition of the crust and how it responds to stress caused by the merger dictates the amount of the r-process material which is ejected. NS merger produces approximately $10^{-2}$ $M_{\odot}$ of ejected r-process matter in the dynamic ejecta and similar amount in the accretion disk outflows [136, 140, 141]. Although some uncertainties still exist, at present the NS merger is considered as the major astrophysical site of the r-process providing the dominant source of heavy nuclei [134, 136, 137].

The modeling of the r-process in such neutron-rich environments depends sensitively on nuclear masses, $\alpha$- and $\beta$-decay half-lives, neutron capture and fission properties of the nuclei the majority of which will never be measured in laboratory conditions [134, 136, 137, 142]. Nuclear masses determine the flow path of the r-process, $\beta$-decay rates are responsible for the speed with which the r-process moves matter to heavier nuclei, $\alpha$-decays become important in heavy nuclei as a competing decay channel and neutron captures drive the nuclei towards neutron-rich side of nuclear landscape. Of special interest in the context of the present manuscript are fission properties. Fission needs to be considered in the r-process simulations if the neutron-to-seed ratio is large enough to produce fissioning nuclei [143, 144, 145, 146]. If the initial neutron-to-seed ratio is large ($\geq$ 100) the r-process can reach the region near and beyond neutron shell closure at $N = 184$, where fission plays a dominant role (the examples of the distribution of abundances of actinides and superheavy elements as obtained in a pair of the r-process simulations are shown in Fig. 6.1). This is exactly

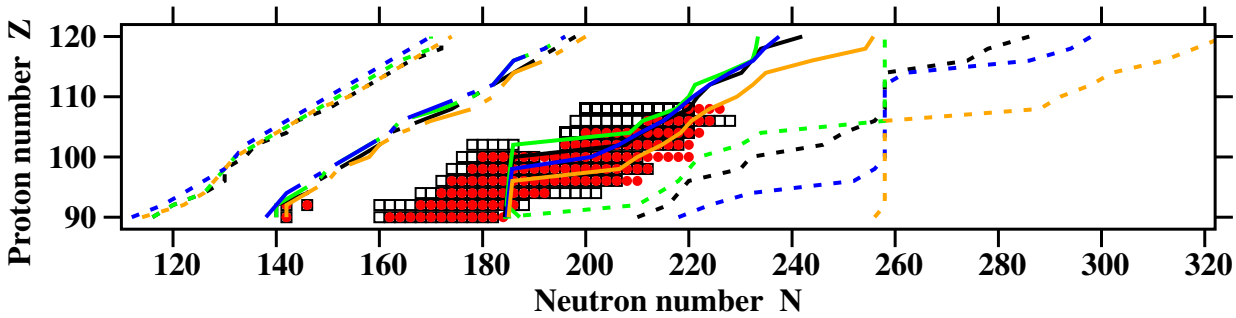


Figure 6.1

The part of nuclear chart under study.

Black, green, blue and orange lines are used for the results obtained with the DD-PC1, DD-ME2, NL3* and PC-PK1 CEDFs, respectively. Two-proton and two-neutron drip lines predicted by four CEDFs are shown by dashed lines. Two samples of the distribution of the abundances of heavy and superheavy elements in the r-process simulations are shown by open squares (based on bottom panel of Fig. 8 of Ref. [147]) and red circles (based on Fig. 3 of Ref. [148]). The former results correspond to hot r-process conditions and are based on the ETFS/ETFSI combination of fission barriers and mass predictions (see Ref. [147]). The latter results have been obtained in Ref. [148] based on fission properties obtained with the BCPM energy density functional. Note that these r-process calculations are restricted to the $Z \leq 110$ nuclei. The r-process path is shown here approximately by solid lines corresponding to two-neutron separation energy $S_{2n} = 4.0$ MeV. Dot-dashed lines show the beta-stability lines for four functionals.

the case for the NS mergers [144]. In this case, all fission channels (neutron induced, beta-delayed, neutrino induced and spontaneous fissions) need to be considered. Fission leads to the termination of hot r-process by means of fission-cycling which returns matter to lighter nuclei [142]. It also determines the strength of fission cycling, the ratio of the actinides to light and medium mass r-process nuclei and thus the shape of final element abundance pattern. In addition, it defines the possibility of the formation of neutron-rich superheavy nuclei in the r-process [147].

Thus, in the situation when experimental data are not known, the outcome of the r-process modeling sensitively depends on the quality of employed theoretical frameworks and associated theoretical uncertainties and their propagation on going to neutron-rich nuclei. By tradition, the output of different theoretical frameworks is used for different physical observables (such as masses, the rates and half-lives of different decay channels and reactions etc.) in the the r-process modeling. Existing r-process calculations, which include information on fission properties, are based on the fission barrier heights obtained in non-relativistic models [142, 146, 149]. So far fission barrier heights obtained in finite range droplet model (FRDM), Thomas-Fermi (TF) model and extended Thomas-Fermi model with Strutinsky integral approach (ETFSI-Q), Hartree-Fock-Bogoliubov (HFB) model with Skyrme HFB-14 EDF and BCPM EDF have been used in these calculations. Moreover the sets of fission barriers relevant for the r-process simulations have been generated in the FRDM in Ref. [149], in the ETFSI-Q approach with the SkSC4 functional in Ref. [150], in the HFB models with Skyrme HFB-14, SV-min, SLy6, SkI3, SV-bas EDFs [151, 152, 153], Gogny D1M* [154] and BCPM [149] functionals. Note that all these calculations assume axial symmetry of the nuclei. CDFT [8] is an approach alternative to above mentioned non-relativistic methods and so far it has not been applied for a systematic study of fission properties of the nuclei relevant for the r-process modeling.

The goal of this study is to close this gap in our knowledge and to perform first systematic investigation within the CDFT framework of the ground state and fission properties of the nuclei with proton numbers $Z = 90 - 120$ located between two-proton and two-neutron drip lines (see Fig. 6.1). This study will not only provide an input for the r-process modeling but also evaluate the extension of nuclear landscape up to two-neutron drip line as well as estimate relevant theoretical

uncertainties and their sources in the description of physical observables of interest. In addition, it will allow for the first time to compare the predictions for fission barriers in the nuclei relevant for r-process modeling obtained in relativistic and non-relativistic frameworks.

Considering the region of the nuclear chart in which the r-process is expected to take place and the fact that there are no experimental data to benchmark theoretical results, it is important to estimate theoretical uncertainties in the predictions of physical observables of interest [2, 35, 36]. Since statistical uncertainties in the physical observables are smaller than systematic ones (see Ref. [83]), we focus here on the latter ones defined by the "spreads" (see Sec. 2.2 for details).

In order to consider several possible scenarios in the evolution of physical observables as a function of proton and neutron numbers and to evaluate systematic theoretical uncertainties, the CEDFs NL3* [28], DD-ME2 [29], DD-PC1 [19] and PC-PK1 [30] are used here[1] for all $Z = 90 - 120$ even-even nuclei located between two-proton and two-neutron drip lines. These are state-of-the-art functionals representing the major classes of CDFTs (for more details see the discussion in Sect. II of Ref. [2] and the introduction to Ref. [58]). Their performance and related theoretical uncertainties have recently been analyzed globally in Refs. [2, 46, 55, 123] and in particular in superheavy nuclei in Refs. [58, 60]. They are characterized by an improved accuracy of the description of experimental data as compared with the previous generation of CEDFs. The

[1]The compilation of Ref. [72] published in 2014 indicates the existence of 263 CEDFs ranging from simplest ansatz non-linear meson exchange functionals such as NL1 [68] and NL3* [28] to more microscopically motivated CEDFs such as G1, G2 [155] and DD-ME$\delta$ [18]. In addition, a number of new functionals were fitted in the time period between 2014 and 2020 (see, for example, Refs. [83, 86, 91, 156, 157]) so at present the total number of available CEDFs is likely to be in the vicinity of 300. Because of extremely time-consuming nature of numerical calculations in this project, we use only the indicated last generation functionals. They outperform previous generation functionals in terms of the accuracy of global description of ground state observables such as binding energies and charge radii [2, 46, 58, 125], properly describe the regions of octupole deformation [55, 56] and are able to reproduce experimentally known fission barriers in actinides [158, 159, 160].

fact that the NL3*, DD-PC1 and PC-PK1 functionals reproduce empirical data on fission barrier heights in actinides [158, 159, 160, 161] is especially important in the context of the present study.

### 6.2 Theoretical framework and details of the calculation

The RHB framework discussed in Sec. 2.3 is used for a systematic study of ground state properties of all even-even actinides ($Z = 90 - 102$) and superheavy ($Z = 104 - 120$) nuclei from the proton to neutron drip line. The calculations are performed in the following way (see details in Sec. 2.4):

- Reflection-symmetric axial RHB calculations (further RS-RHB) are performed for each nucleus and the potential energy curve is defined in a large deformation range from $\beta_2 = -1.0$ up to $\beta_2 = 1.6$ in step of $\Delta\beta_2 = 0.05$.
- Reflection-asymmetric (octupole deformed) axial RHB calculations (further RA-RHB) are performed for the ground states of the nuclei not covered in previous systematic studies of octupole deformation in CDFT (see Refs. [55, 56]). We have not found any additional (as compared with those given in Refs. [55, 56]) nuclei which possess octupole deformation in the ground state. So full information on the octupole deformation of the ground states can be found in these references. The information (which follows from Refs. [55, 56]) about the gain in binding energy due to octupole deformation at the ground state and its impact on ground state quadrupole deformation and fission barrier heights is fully taken into account in the present study. In addition, RA-RHB calculations have been performed in some nuclei in order to define the heights of outer fission barriers (see the discussion below for more details).

Because of different patterns of deformation energy curves (see Figs. 6.2 and 6.3), a special care is considered when assigning a specific minimum to the ground state. A basic rule in this process is the assumption that a local minimum surrounded by the barrier, the height of which is less than 2 MeV, is considered as extremely unstable[2]. The procedure of the selection of the

[2]This low fission barrier of 2 MeV or less would translate into a high penetration probability for spontaneous fission so that such minima are expected to be extremely unstable. In addition, the inclusion of octupole deformation (or triaxial deformation in some nuclei [59]) in the case of superdeformed minima surrounded by such low fission barriers could either completely eliminate or substantially reduce them (see Refs. [32, 59, 162]).

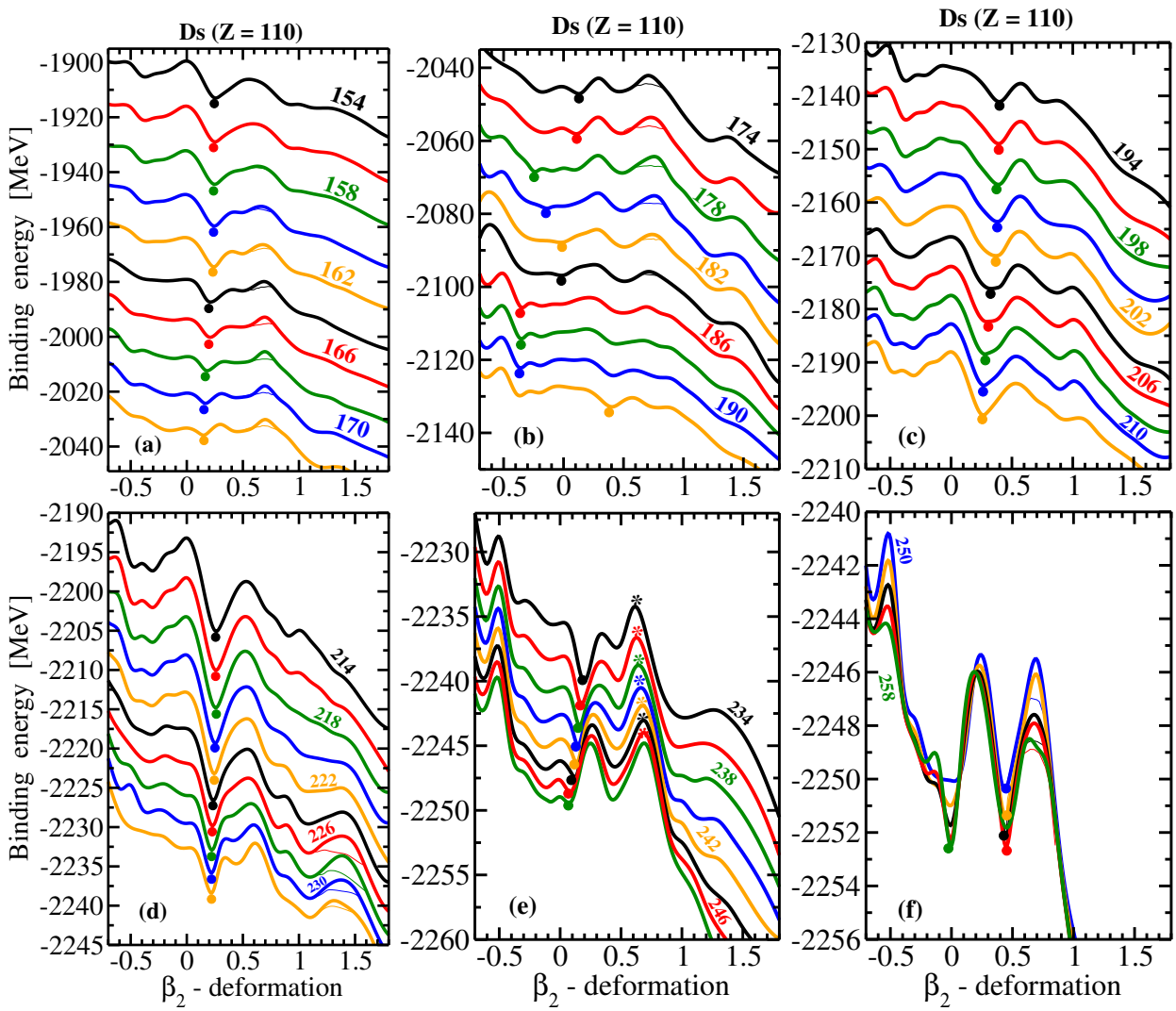


Figure 6.2

Deformation energy curves obtained in axial RHB calculations with DDPC1 functional for the Ds isotopes.

The isotopes are indicated by respective neutron numbers. Thick and thin solid lines are used for the RS-RHB and RA-RHB results, respectively. The results of the RA-RHB calculations are shown only in the deformation range in which they are lower in energy than the RS-RHB ones. Solid circles indicate the ground states and the asterisks denote the saddles of outer fission barriers which are not affected by octupole deformation. Blue, orange, black, red and green lines are used to indicate neutron numbers the last digits of which are 0, 2, 4, 6, and 8, respectively. Note that the energy on the vertical axis spans different ranges in different panels.

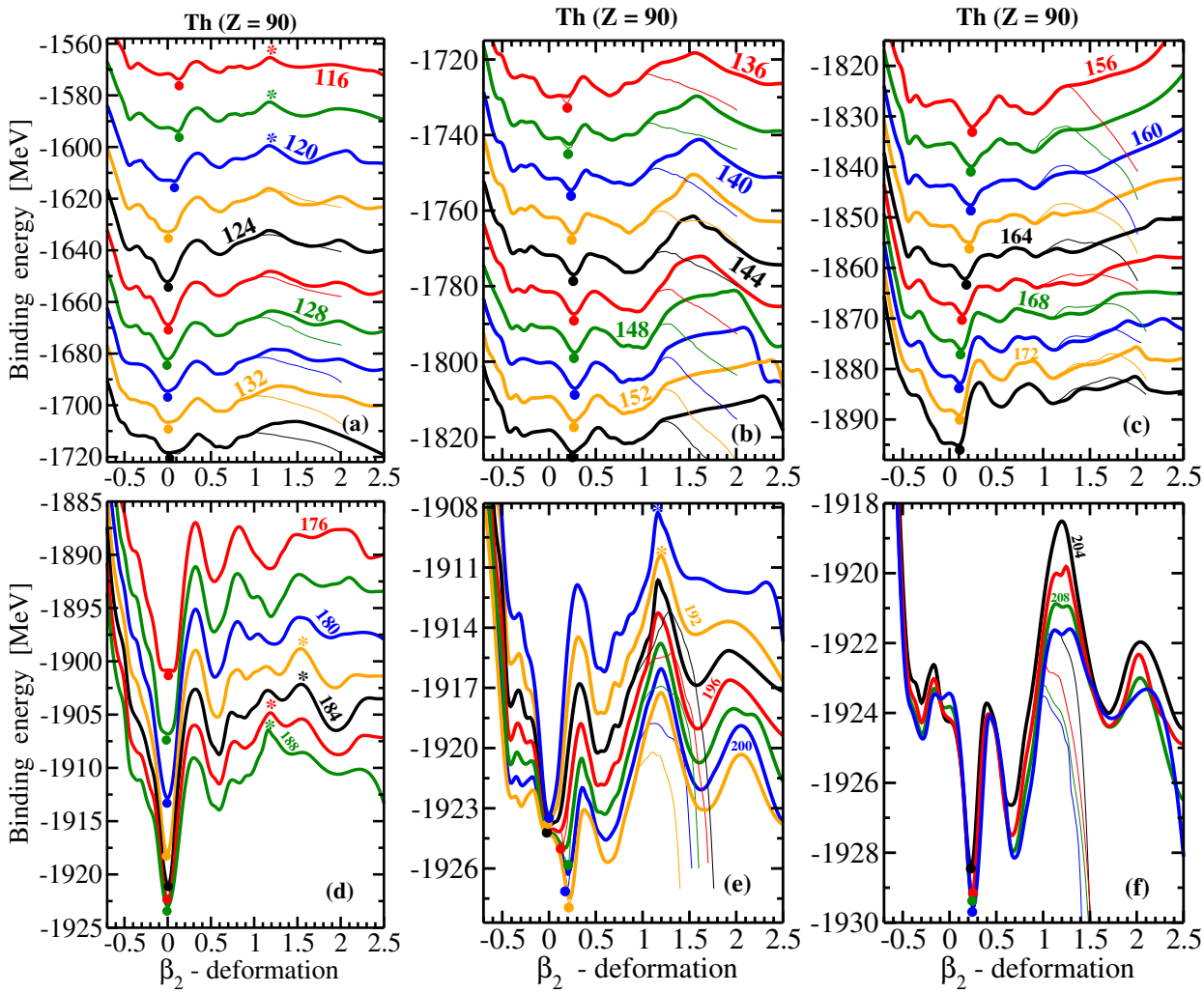


Figure 6.3

The same as Fig. 6.2 but for the Th isotopes.

Note that the deformation range has been extended on horizontal axis as compared with Fig. 6.2. In order to save computational time the RA-RHB calculations have been carried out only up to $\beta_2 = 2.0$.

ground state is discussed below. The situation shown in Fig. 6.4a is the simplest one: single-humped (inner) fission barrier acts against the fission into two fragments and when $B_{in} > 2$ MeV the assignment of the normal-deformed prolate minimum to the ground state is straightforward. It

changes if the height of this fission barrier decreases and becomes smaller than 2 MeV (see Fig. 6.4b). Then highly-deformed oblate minimum B becomes a ground state; it has larger and broader fission barrier as compared with minimum A. Thus, it is expected that this ground state will live significantly longer than the state associated with minimum A.

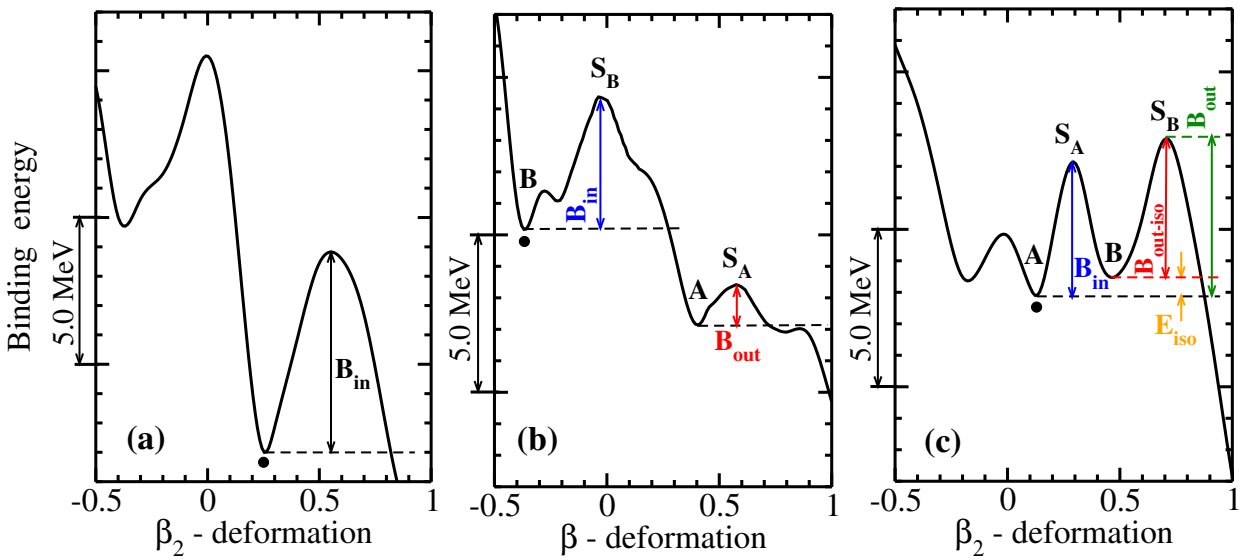


Figure 6.4

Schematic illustration of different types of deformation energy curves and the selection of respective ground states (see text for details).

Local minima are labelled by the letters A and B and the saddle points of respective fission barriers by $S_A$ and $S_B$. Solid circles indicate the minima selected as the ground states. The heights of inner and outer fission barriers with respect of corresponding minima (shown by dashed lines) are indicated by $B_{in}$ and $B_{out}$. $B_{out-iso}$ is the height of outer fission barrier with respect of fission isomer.

More complex situation involving two humped fission barrier is shown in Fig. 6.4(c). If $B_{out-iso} < 2$ MeV, then the minimum B corresponding to the fission isomer is considered extremely unstable and the minimum A is associated with the ground state. Note that in some cases the

minimum B can be lower in energy than minimum A. If that is the case and if $B_{out-iso} > 2$ MeV then the minimum B is considered as the ground state. Note that the heights of outer fission barriers are frequently lowered when octupole deformation is included in the calculations [59, 159, 161, 162, 163, 164]. Thus, if $B_{out-iso} > 2$ MeV in RS-RHB calculations, we perform RA-RHB calculations in the region of the $(\beta_2, \beta_3)$ plane covering the minimum B and the saddle of outer fission barrier on the grid with the steps of $\Delta\beta_2 = \Delta\beta_3 = 0.05$. This allows to establish whether minimum B could be considered as relatively stable or unstable. Similar calculations are also performed in the cases when $B_{in} < B_{out}$ in the RS-RHB calculations. This is because we consider only the height of the primary (highest) fission barrier (PFB) in Sec. 6.5 in the case of doubly-humped structure of the barrier to minimize the computational cost. Note that the calculations leading to the definition of the fission path and the saddle point in the RA-RHB code are by roughly two orders of magnitude more time consuming than those in the RS-RHB code.

The procedure outlined above takes into account potential stability of the nuclei in respective energy minima with respect of fission and it is especially important in superheavy nuclei some local minima of which are characterized by small fission barriers (see Fig. 6.2). Note that after defining the minimum corresponding to the ground state, the RS-RHB and RA-RHB calculations without constraint are performed and precise binding energy and equilibrium of the ground state is determined. In addition, the height(s) of the fission barrier(s) is(are) defined.

In the calculations with the PC-PK1 and NL3* functionals there are two small islands of the nuclei located in the $Z \approx 114 - 118, N \approx 238 - 240$ and $Z \approx 106 - 110, N \approx 190 - 194$ regions in which calculated deformation energy curves reveal several local minima (somewhat similar to the deformation energy curves shown at the bottom of Fig. 6.2b). However, all these minima are

surrounded by very low fission barriers with the heights smaller than 2.0 MeV. Moreover, many of these minima have even lower heights of respective fission barriers (on the level of 1.0 MeV or smaller). These nuclei are expected to be unstable against fission and in principle it does not matter which of the calculated fission barriers is used. For these nuclei, we select the ground state guided by the flow of the $\beta$-decays in the r-process: the selected local minimum (and thus the corresponding ground state deformation and fission barrier height) in the $(Z, N)$ nucleus has the deformation closest to the one of the well established ground state in the $(Z-2, N+2)$ nucleus.

So far all existing global calculations of the fission barriers for the r-process simulations have been performed in non-relativistic models. These include the calculations within the FRDM [149, 165], the TF and ETFSI-Q approaches [147, 150], the HFB approaches with different Skyrme functionals [152, 153, 166], Gogny D1M* [154] and BCPM [149] EDFs. Because of their global character, all these calculations are restricted to axial symmetry. We also assume axial symmetry in our calculations because triaxial RMF+BCS and RHB calculations (see Refs. [32, 59, 60, 158, 167]) are too time consuming to be performed on a global scale. Note also that dynamical correlations are not taken into account in our calculations of fission barriers because of the reasons discussed Ref. [168].

### 6.3 Ground state properties

The distributions of calculated proton deformations $\beta_2$ in the $(Z, N)$ plane obtained with four employed CEDFs are shown in Fig. 6.5. The width of the gray region (the gray color corresponds to spherical and near-spherical shapes) along a specific magic number corresponding to a shell closure indicates the impact of this shell closure on the structure of neighboring nuclei. Note that proton

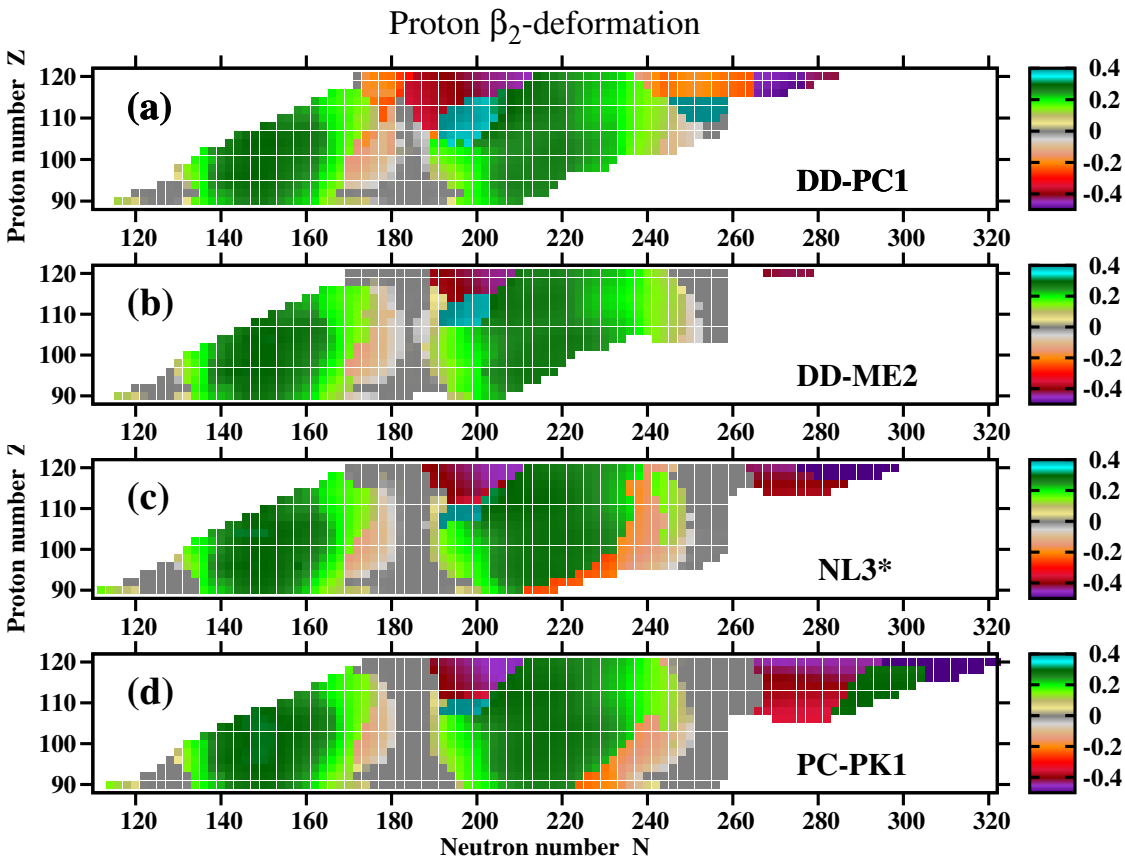


Figure 6.5

Proton quadrupole deformations $\beta_2$ obtained in the RS-RHB and RA-RHB calculations with indicated CEDFs.

The details of the regions of octupole deformation are discussed in Refs. [55, 56]. Note that last bound $Z = 120$ nucleus appears at $N = 324$ in the calculations with the CEDF PC-PK1 (see Table 6.3 below); for simplicity it is not shown in panel (d).

and neutron shell gaps act simultaneously in the vicinity of doubly magic spherical nuclei. Thus, the effect of a single gap is more quantifiable away from these nuclei. One can see that neutron $N = 184$ and $N = 258$ spherical shell gaps have a pronounced impact on calculated deformations while the impact of the proton $Z = 120$ spherical shell closure is limited to the $N \sim 170 - 184$ nuclei (see Refs. [45, 58] for examples of their size dependence on the functional). In addition, as

illustrated in Ref. [167] on the example of the PC-PK1 functional, the inclusion of the correlations beyond mean field washes out the impact of the $Z = 120$ shell closure and leads to oblate deformed ground states in the majority of the $Z = 120$ nuclei with $N = 172 - 186$. The predictions of the DD-PC1 functional differs substantially from other CEDFs: the impact of above mentioned shell closures are substantially reduced in it and as a consequence the regions with $Z \sim 120, N \sim 184$ and $Z \sim 120, N \sim 258$ are dominated by oblate ground states contrary to spherical states in other functionals. Note that this functional provides the best global description of experimental binding energies (see Ref. [2]). This, however, does not guarantee that it will outperform other functionals in the description of physical observables of interest in the region of superheavy nuclei (see Table I in Ref. [58]).

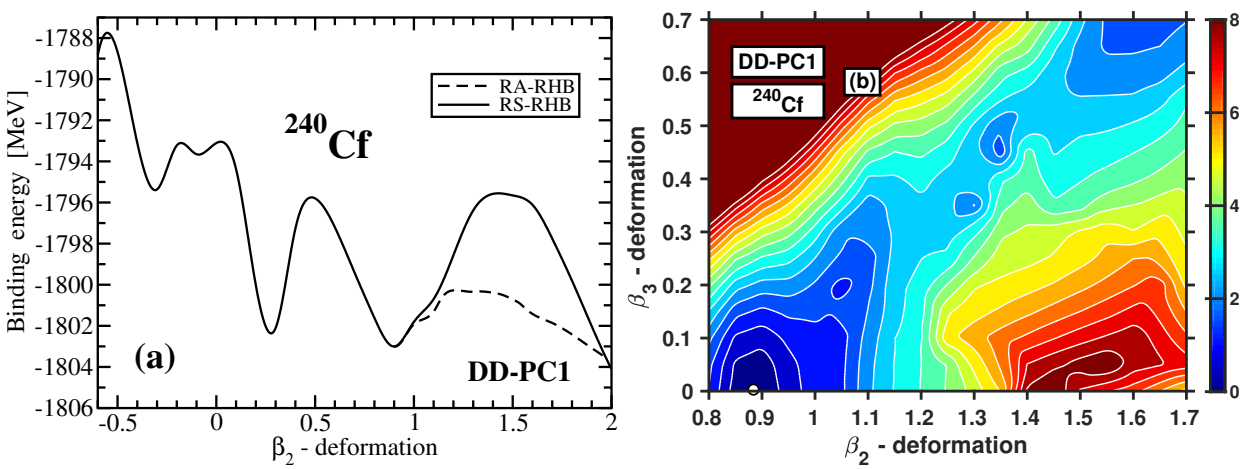


Figure 6.6

Deformation energy curves and potential energy surface obtained in calculations with the CEDF DD-PC1 for the $^{240}$Cf nucleus.

(a) Deformation energy curves obtained in axial RS-RHB calculations. (b) Potential energy surface in the $(\beta_2, \beta_3)$ plane obtained in the RA-RHB calculations. Extremely superdeformed minimum is indicated by open white circle.

Table 6.1

The nuclei in which extremely superdeformed minimum is the lowest in energy in the calculations with CEDF DD-PC1.

| Z | N | $E_{N-S}$ [MeV] | $\beta_2^{min}$ | $\beta_2^{saddle}, \beta_3^{saddle}$ | $E_B^{II}$[MeV] (RS-RHB) | $E_B^{II}$ [MeV] (RA-RHB) |
|---|---|---|---|---|---|---|
| 1 | 2 | 3 | 4 | 5 | 6 | 7 |
| 98 | 142 | 0.603 | 0.88 | 1.21, 0.33 | 7.207 | 2.625 |
| 98 | 144 | 0.306 | 0.90 | 1.34, 0.46 | 7.373 | 3.503 |
| 98 | 228 | 2.341 | 1.01 | 1.29, 0.34 | 6.622 | 2.906 |
| 98 | 230 | 2.083 | 1.01 | 1.30, 0.35 | 5.072 | 3.203 |
| 100 | 146 | 0.876 | 0.97 | 1.32, 0.37 | 5.890 | 2.985 |
| 100 | 230 | 2.431 | 1.01 | 1.30, 0.35 | 5.750 | 3.270 |
| 100 | 232 | 2.336 | 1.01 | 1.30, 0.37 | 4.060 | 2.739 |
| 102 | 146 | 2.038 | 0.99 | 1.32, 0.34 | 4.813 | 2.749 |
| 102 | 148 | 0.629 | 0.98 | 1.28, 0.31 | 4.093 | 2.250 |
| 102 | 232 | 2.591 | 1.02 | 1.29, 0.36 | 3.476 | 2.840 |
| 102 | 234 | 3.567 | 1.03 | 1.31, 0.31 | 2.674 | 2.304 |
| 104 | 146 | 3.435 | 0.99 | 1.33, 0.28 | 6.042 | 2.410 |
| 104 | 148 | 1.921 | 1.00 | 1.31, 0.27 | 5.579 | 2.204 |
| 104 | 150 | 0.924 | 1.00 | 1.29, 0.27 | 5.370 | 2.505 |
| 106 | 148 | 3.638 | 1.08 | 1.32, 0.26 | 4.112 | 2.340 |
| 106 | 150 | 2.374 | 1.10 | 1.30, 0.23 | 3.753 | 2.345 |

The columns 1 and 2 show the proton and neutron numbers of the nuclei. Third column displays the energy $E_{N-S}$ [in MeV] by which the ESD minimum is lower than the normal-deformed minimum. The deformations of the ESD minimum $\beta_2^{min}$ and the saddle of second fission barrier $\beta_2^{saddle}$, $\beta_3^{saddle}$ are presented in the columns 4 and 5, respectively. The energies [in MeV] of the second fission barrier with respect of the ESD minimum, obtained in the RS-RHB and RA-RHB calculations, are shown in the columns 6 and 7. Note that the values presented in the columns 5-7 are obtained in the calculations with $N_F = 26$; this is done in order to have a comparable numerical accuracy with the one obtained at normal deformed minimum.

The calculations reveal a number of nuclei scattered across the part of nuclear chart under study which have extremely superdeformed (ESD) minimum with $\beta_2 \sim 1.0$ located at lower energy than

normal-deformed minimum (see Fig. 6.6a and Table 6.1). In these nuclei the ESD minimum is surrounded by outer fission barrier the height of which exceeds 2.0 MeV (being typically in the range of 2.0 − 3.0 MeV) in the RA-RHB calculations (see Fig. 6.6b and Table 6.1). Although the fission barrier is low, some of these ESD minima could be potentially stabilized against fission for physically sufficient time because of broad fission barrier in the $(\beta_2, \beta_3)$ plane. If that would be the case, they would represent the ground states. However, they are not included into Fig. 6.5 because of the following reasons. First, there are significant theoretical uncertainties in the predictions of fission barriers (see current chapter and Refs. [59, 60]) as well as in relative energies of the minima with different deformations [50]. Second, only few nuclei in the $Z \approx 100, N \approx 230$ region could be potentially extremely supedeformed in the ground states (see Table 6.1). However, the flow of matter in the r-process between two nuclei with drastically different deformations of the ground states will be most likely significantly suppressed because of considerable differences in the wave functions of these ground states. Thus, it will proceed mostly along the dominant deformation of the ground states in the region, namely, normal deformation, even if such states are excited in energy in a few nuclei. Third, the majority of the nuclei in Table 6.1 are neutron poor $Z \approx 102$ nuclei which do not play a role in the r-process. There are experimental data on the $^{240,242}$Cf, $^{246}$Fm and $^{254}$Rf nuclei but only for their ground states [169]. At present, these data do not allow to define the deformations of the ground states. However, since it has been obtained in the reactions (such as $\alpha$-decay, $\beta$-decay, electron capture and the reactions on spherical Pb isotopes) which do not favor significant shape changes, these ground states are most likely normal-deformed. More detailed and focused experimental studies are needed in order to see whether ESD states exist in such nuclei.

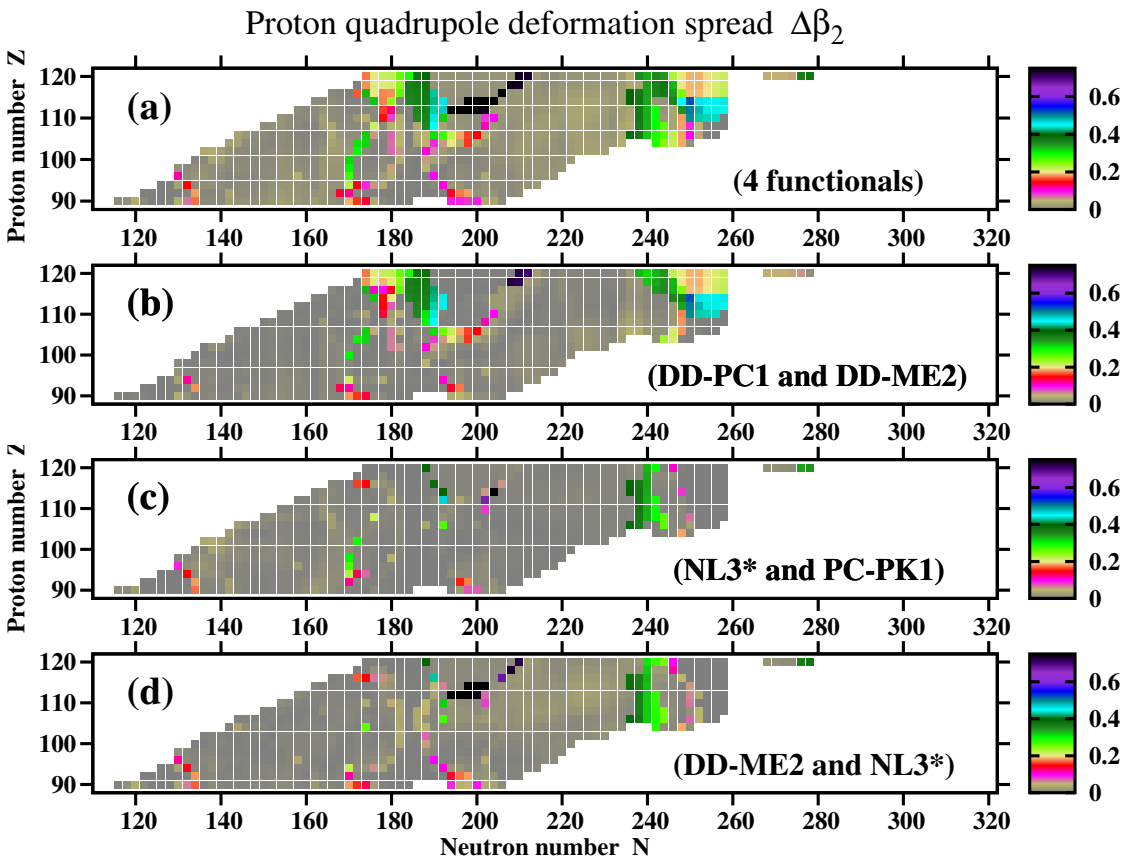


Figure 6.7

Proton quadrupole deformation spreads $\Delta\beta_2(Z,N)$ as a function of proton and neutron number.

$\Delta\beta_2(Z,N) = |\beta_2^{\max}(Z,N) - \beta_2^{\min}(Z,N)|$, where $\beta_2^{\max}(Z,N)$ and $\beta_2^{\min}(Z,N)$ are the largest and smallest proton quadrupole deformations obtained with four employed CEDF for the $(Z,N)$ nucleus.

The spreads of theoretical predictions in quadrupole deformations $\beta_2$ obtained with four employed functionals are summarized in Fig. 6.7(a). The largest spread of $\Delta\beta_2 \approx 0.7$ is visible along the line of $N/Z \approx 1.81$ which starts at $Z = 104$. This corresponds to the boundary of the transition from oblate to prolate shapes the exact position of which in the $(Z,N)$ plane is functional dependent (see Fig. 6.5). It is defined by the underlying single-particle structure at prolate and oblate shapes

as well as to a degree by the heights of outer fission barriers (see the rules for the definition of the ground states described in Sec. 6.2). Second region of the largest spreads in $\Delta\beta_2$ is located along the $N \approx 184$ line starting from $Z \approx 100$ and extending up to $Z = 120$. Third region is located along the $Z = 120$ line from proton-drip line up to $N \approx 188$. These two regions of large spreads in calculated quadrupole deformation emerge from the differences in the predictions of ground state deformations (see Fig. 6.5) which in turn can be traced back to the sizes of the $Z = 120$ and $N = 184$ spherical shell closures and the densities of the single-particle states in their vicinities (see Ref. [58]). The last region of large theoretical uncertainties is located between $N \approx 236$ and $N = 258$. In the region around $N \approx 236$ these theoretical uncertainties are mostly due to the uncertainties in the predictions of the boundary of the transition from prolate to oblate shapes. For higher $N$ values, large $\Delta\beta_2$ values emerge from the transition from prolate or oblate shapes to spherical ones and to a large degree are defined by the uncertainties in the prediction of the size of the $N = 258$ spherical shell closure (see Fig. 6d in Ref. [45]) and single-particle densities in its vicinity. With few exceptions theoretical uncertainties in the predictions of ground state deformations in the part of nuclear chart outside of above discussed regions are very small (see Fig. 6.7(a)).

It is important to understand to what extent the predictions of the ground state deformations and related theoretical uncertainties in these predictions are dependent on nuclear matter properties of employed CEDFs. All employed CEDFs have the density $\rho_0$ and the energy per particle $E/A$ at the saturation of symmetric nuclear matter (SNM) which are very close to each other and to empirical estimates (see Table III in Ref. [46]). Thus, the impact of only selected SNM properties listed in Table 6.2 on the ground state deformations are discussed below. Let start from the consideration of the predictions by the pair of the functionals DD-PC1 and DD-ME2. Their SNM properties such

as incompressibility $K_0$, the symmetry energy $J$ and its slope $L_0$ are close to each other and are located within the SET2b constraints on experimental/empirical ranges for physical observables of interest (see Table 6.2). Despite that this pair of the functionals gives the largest contribution into the spreads $\Delta\beta_2$ (compare panels (b) and (a) of Fig. 6.7). On the contrary, the pairs of the functionals PC-PK1 and NL3* (which have $J$ and $L_0$ values located outside the SET2b constraint range [see Table 6.2]) as well as NL3* and DD-ME2 (which have drastically different values of the $J$ and $L_0$ parameters [see Table 6.2]) have (with very few exceptions) very similar predictions for the ground state deformations across the part of nuclear chart under study. These exceptions are related to some differences in the predictions of the boundaries between oblate and prolate shapes as well as between prolate and spherical shapes.

Table 6.2

Selected properties of symmetric nuclear matter at saturation: the incompressibility $K_0$, the symmetry energy $J$ and its slope $L_0$.

| CEDF | $K_0$ [MeV] | $J$ [MeV] | $L_0$ [MeV] |
|---|---|---|---|
| 1 | 2 | 3 | 4 |
| NL3* [28] | 258 | **38.68** | **122.6** |
| DD-ME2 [29] | 251 | 32.40 | 49.4 |
| DD-PC1 [19] | 230 | 33.00 | 68.4 |
| PC-PK1 [30] | 238 | **35.6** | **113** |
| SET2a | 190-270 | 25-35 | 25-115 |
| SET2b | 190-270 | 30-35 | 30-80 |

Top four lines show the values for indicated CEDFs, while bottom two lines show two sets (SET2a and SET2b) of the constraints on the experimental/empirical ranges for the quantities of interest defined in Ref. [72]. The CEDF values which are located outside the limits of the SET2b constraint set are shown in bold.

These results for ground state deformations together with the analysis of the results for binding energies and charge radii of the $Z \leq 104$ nuclei presented in Ref. [46] strongly indicate that

- the major source of the uncertainties in the predictions of ground state deformations is related to local differences in underlying single-particle structure and, in particular, to the size of spherical $Z = 120$ and $N = 184$ and 258 shell closures and the densities of the single-particle states in their vicinities,
- strict enforcement of the limits on the nuclear matter properties defined in Ref. [72] will not necessary lead to the functionals with good description of ground and excited state properties and will not reduce theoretical uncertainties in the description of physical observables of interest in high-$Z$ and/or neutron-rich nuclei.

Table 6.3 compares the positions of the two-proton and two-neutron drip lines obtained in the RHB calculations with the NL3* and PC-PK1 functionals; the results for the DD-PC1 and DD-ME2 functionals could be found in Table IV of Ref. [2]. One can see that the two-proton drip lines are very similar in these two functionals; they differ by no more than four neutrons. This is in line with earlier observations that theoretical uncertainties in the predictions of the position of two-proton drip line are relatively small (see Ref. [38] and Sec. VII in Ref. [2]). Note that two-proton drip lines in the isotopic chains of interest obtained with PC-PK1 are very close to those obtained with DD-PC1 (compare Table 6.3 in the present study with Table IV of Ref. [2]).

Among the considered CEDFs the PC-PK1 functional provides the most neutron-rich two-neutron drip line and the NL3* provides the second most neutron-rich two-neutron drip lines (compare Table 6.3 in the present study with Table IV of Ref. [2] and see Sec. VIII in Ref. [2]). All employed functionals reveal the presence of the shell closure at $N = 258$ (see Fig. 6d in Ref. [45]). The size of this gap is almost the same in the NL3* and PC-PK1 functionals, but (i) it is shifted down in energy by $\approx 400$ keV for PC-PK1 as compared with NL3* and (ii) high-$j$ intruder orbitals $1k_{15/2}$ and $2i_{13/2}$, which have a significant impact on the position of neutron drip line (see

Table 6.3

Two-proton and two-neutron drip lines predicted by the NL3* and PC-PK1 functionals (see Fig. 6.1 for graphical representation of drip lines).

| Proton | Two-proton drip line | | Two-neutron drip line | |
|---|---|---|---|---|
| number $Z$ | NL3* | PCPK1 | NL3* | PCPK1 |
| 1 | 2 | 3 | 4 | 5 |
| 90 | 112 | 114 | 218 | 256 |
| 92 | 118 | 122 | 224 | 258 |
| 94 | 122 | 126 | 232 | 258 |
| 96 | 126 | 128 | 252 | 258 |
| 98 | 130 | 130 | 256 | 258 |
| 100 | 132 | 132 | 258 | 258 |
| 102 | 134 | 136 | 258 | 258 |
| 104 | 138 | 140 | 258 | 258 |
| 106 | 142 | 144 | 258 | 258* |
| 108 | 146 | 148 | 258 | 288 |
| 110 | 150 | 154 | 258 | 292 |
| 112 | 154 | 158 | 258 | 298 |
| 114 | 158 | 162 | 262* | 302 |
| 116 | 162 | 166 | 286 | 312 |
| 118 | 166 | 170 | 294 | 318 |
| 120 | 170 | 174 | 298 | 324 |

Neutron numbers (columns 2-5) corresponding to these drip lines are given for each even proton number $Z$ (column 1). An asterisk at a neutron number at the two-neutron drip line indicates isotope chains with additional two-neutron binding at higher $N$ values (peninsulas).

discussion in Ref. [45]), are located at lower energies in the PC-PK1 functional as compared with the NL3* one. These features lead to the shift of the two-neutron drip line to substantially higher neutron numbers in the PC-PK1 CEDF as compared with NL3*. The sizes of the $N = 258$ shell gaps are smaller by $\approx$ 10% and 20% in the DD-ME2 and DD-PC1 functionals as compared with the ones in the PC-PK1 and NL3*. In addition, above mentioned high-$j$ intruder orbitals in the

calculations with the DD-ME2 and DD-PC1 functionals are located at higher energies as compared with the ones in NL3*. As a consequence, their two-neutron drip lines are located at lower neutron numbers as compared with the NL3*. These features are clearly seen in Fig. 6.5.

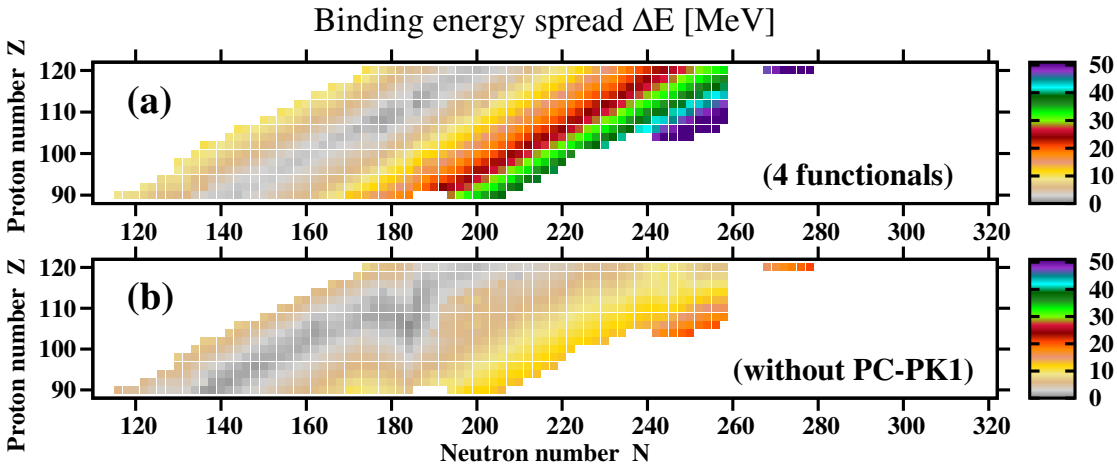


Figure 6.8

The binding energy spreads $\Delta E(Z,N)$ as a function of proton and neutron number.

$\Delta E(Z,N) = |E_{\rm max}(Z,N) - E_{\rm min}(Z,N)|$, where $E_{\rm max}(Z,N)$ and $E_{\rm min}(Z,N)$ are the largest and smallest binding energies obtained with employed set of CEDFs for the $(Z,N)$ nucleus. Upper panel shows the binding energy spreads for four employed functionals, while the bottom one the spreads for a set of functionals in which PC-PK1 is excluded.

Figure 6.8 shows the map of theoretical uncertainties $\Delta E(Z,N)$ in binding energies. These uncertainties increase drastically when approaching the neutron-drip line and in some nuclei they reach 50 MeV. Poorly defined isovector properties of CEDFs is the major reason for that (see Ref. [2]). Note that the $\Delta E(Z,N)$ spreads for the NL3*, DD-PC1 and DD-ME2 functionals are relatively modest [see Fig. 6.8(b)] and the major contribution to $\Delta E(Z,N)$ is coming from the

PC-PK1 functional (compare panels (a) and (b) in Fig. 6.8). The fact that isovector properties of the PC-PK1 functional are significantly different from those of NL3*, DD-PC1, DD-ME2 and DD-ME$\delta$ is also confirmed by the analysis of binding energies in the Yb ($Z = 70$) isotopic chain (see Fig. 3 in Ref. [46]). As follows from the analysis of parametric correlations in different classes of CEDFs performed in Chapter IV and in Ref. [91], a possible reason for that could be related to over-parametrization of the isoscalar channel in this class of CEDFs. This, in turn, may lead to a somewhat wrong balance of the isoscalar and isovector channels in known nuclei which reveals itself in a more pronounced way via different (as compared with other functionals) isovector dependence of binding energies in neutron-rich one.

Figure 6.9 presents the summary of two-neutron separation energies $S_{2n}(Z, N)$ obtained with four employed CEDFs. Note that some discontinuities in smooth trends of the $S_{2n}(Z, N)$ distributions as a function of neutron number are either due to the presence of substantial spherical shell gaps at $N = 184$ or $N = 258$ or due to the crossing of the boundaries between prolate and oblate shapes. For example, the impact of the $N = 184$ spherical shell gap on the $S_{2n}(Z, N)$ distributions is clearly visible in Figs. 6.9(b), (c) and (d) (see also Figs. 6.5 (b), (c) and (d) for deformation distributions). On the contrary, its impact is substantially suppressed in superheavy nuclei in the calculations with CEDF DD-PC1 [see Fig. 6.9(a)] because of the reduced role of the $N = 184$ spherical shell gap in this functional.

Finally, the spreads $\Delta S_{2n}(Z, N)$ in two-neutron separation energies are presented in Fig. 6.10. They are the lowest in known nuclei but in general increase with increasing neutron number. The $\Delta S_{2n}(Z, N)$ values are quite large ($\Delta S_{2n}(Z, N) \approx 2.2$ MeV) in the vicinity of two-neutron drip lines and the $N = 184$ and $N = 258$ spherical shell gaps. However, they become extremely

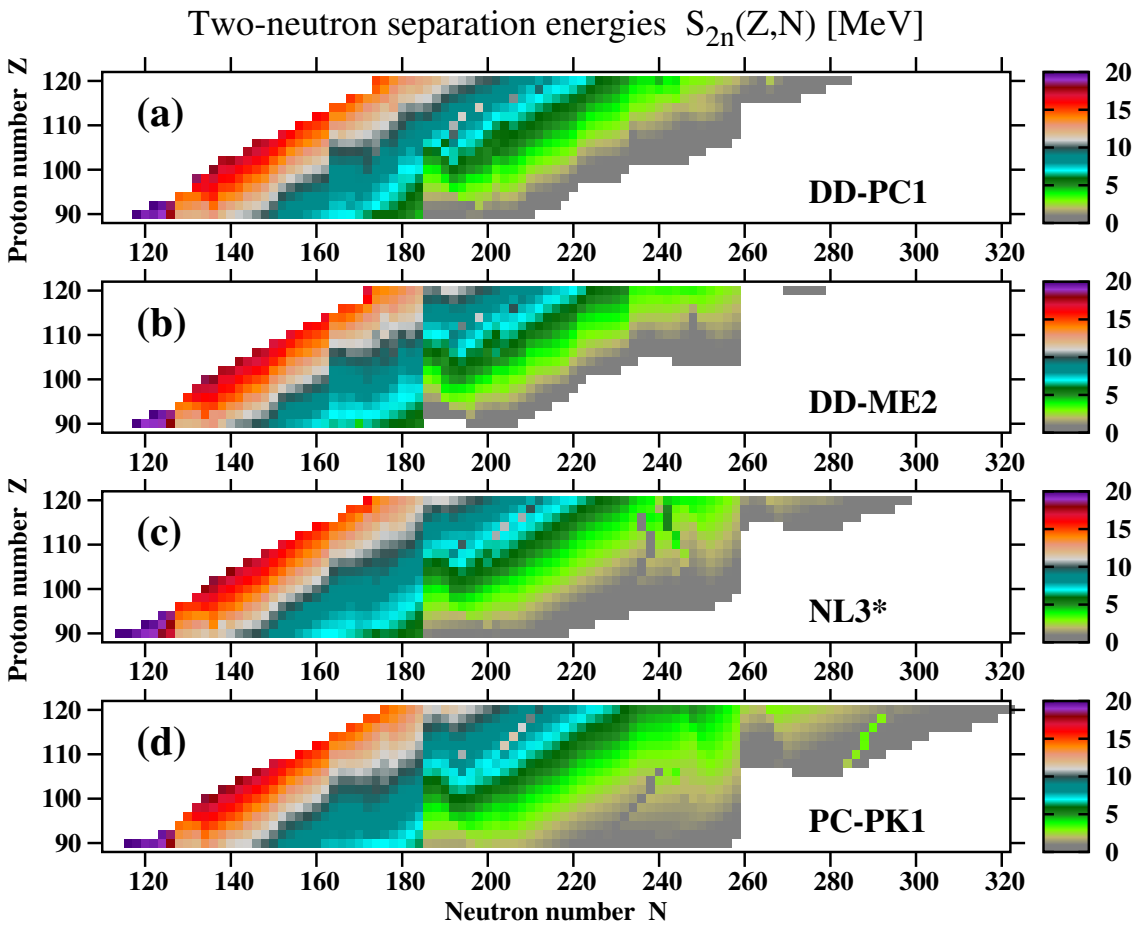


Figure 6.9

Two-neutron separation energies $S_{2n}(Z,N)$ obtained in the RHB calculations with indicated CEDFs.

large ($\Delta S_{2n}(Z,N) \approx 4.0$ MeV) at the boundaries between prolate and oblate shapes. Similar to the spreads in binding energies (see discussion of Fig. 6.8 above), the largest contribution to the $\Delta S_{2n}(Z,N)$ values comes from the CEDF PC-PK1. If the PC-PK1 functional is excluded from consideration these values on average decrease by a factor of 2 (compare panels (b) and (a) in Fig. 6.10). It is interesting that in neutron-rich deformed $N \approx 190 - 236$ region the $\Delta S_{2n}(Z,N)$ values

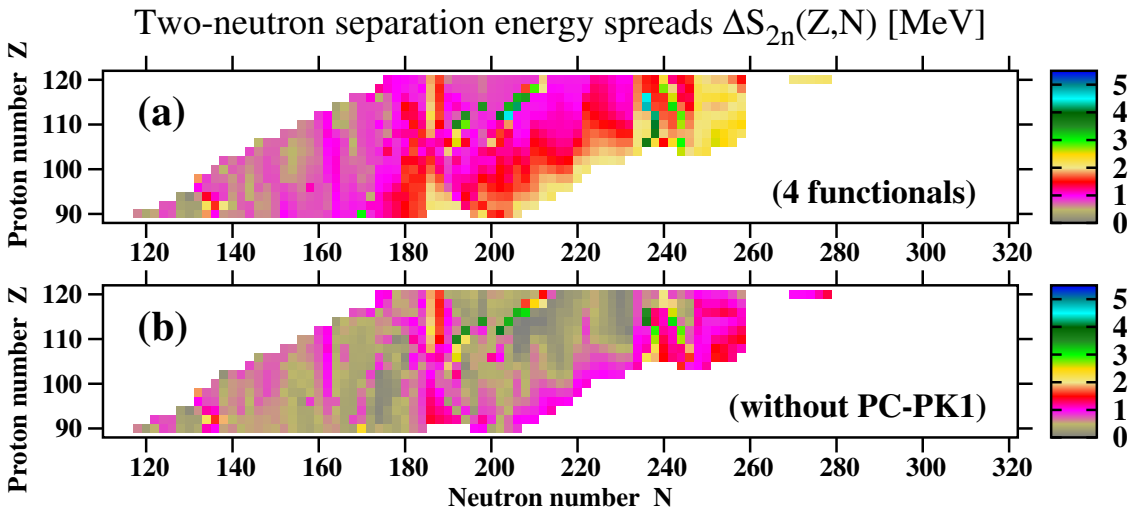


Figure 6.10

The $S_{2n}$ spreads $\Delta S_{2n}(Z,N)$ as a function of proton and neutron number.

$\Delta S_{2n}(Z,N) = |S_{2n}^{\max}(Z,N) - S_{2n}^{\min}(Z,N)|$, where $S_{2n}^{\max}(Z,N)$ and $S_{2n}^{\min}(Z,N)$ are the largest and smallest $S_{2n}$ values obtained with four employed CEDFs for the $(Z,N)$ nucleus.

are on average comparable with those in known nuclei (see Fig. 6.10(b). However, they still show increased magnitudes at above discussed locations of nuclear chart.

## 6.4 $\alpha$-decay properties

In actinides and superheavy nuclei spontaneous fission and $\alpha$ emission compete and the shortest half-life determines the dominant decay channel and the total half-life. Only in the cases where the spontaneous fission half-life is longer than the half-life of $\alpha$ emission can superheavy nuclei be observed in experiment. In addition, only nuclei with half-lives longer than $\tau = 10\ \mu$s are observed in experiments.

The $\alpha$ decay half-live depends on the $Q_\alpha$ values which are calculated according to

$$Q_\alpha = E(Z,N) - E(Z-2,N-2) - E(2,2) \tag{6.1}$$

with $E(2,2) = -28.295674$ MeV [124] and $Z$ and $N$ representing the parent nucleus.

To estimate theoretical uncertainties in the predictions of the $\alpha$-decay half-lives, they were calculated using three phenomenological expressions, namely,

- the Viola-Seaborg semiempirical formula [170]

$$log_{10}\tau_\alpha = \frac{aZ+b}{\sqrt{Q_\alpha}} + cZ + d \tag{6.2}$$

  employing two sets of parametrizations. The first one with the parameters $a = 1.66175$, $b = -8.5166$, $c = -0.20228$ and $d = -33.9069$ has been fitted in Ref. [171]. This set and the results obtained with it are labelled further as VSS-1989. Another set has been defined in Ref. [172] and its parameters are: $a = 1.64062$, $b = -8.54399$, $c = -0.19430$ and $d = -33.9054$. The label VSS-2005 is used for it and its results.

- phenomenological first modified Brown fit (mB1) [173]

$$log_{10}\tau_\alpha = \frac{a(Z-2)^b}{\sqrt{Q_\alpha}} + c \tag{6.3}$$

  with the parameters $a = 13.0705$, $b = 0.5182$, $c = -47.8867$. This set and its results are labeled further as MB-2016.

- phenomenological Royer model [174]

$$log_{10}\tau_\alpha = \frac{aZ}{\sqrt{Q_\alpha}} + bA^{\frac{1}{6}}\sqrt{Z} + c \tag{6.4}$$

  with the parameters $a = 1.5864$, $b = -1.1629$ and $c = -25.31$ of Ref. [174]. Its results are labeled further as Royer-2000.

These phenomenological expressions employ different functional dependencies (in particular, they show different dependencies on proton and mass numbers) and are fitted to different sets of experimental data. This is expected to lead to different predictions for $\tau_\alpha$ in high-$Z$ and neutron-rich nuclei.

The $Q_\alpha$ values calculated with the DD-PC1, DD-ME2, NL3* and PC-PK1 functionals are presented in Fig. 6.11. One can see that for a fixed value of $Z$ with increasing neutron number the $Q_\alpha$ values in general decrease. They are positive in proton-rich nuclei as well as in the nuclei located close to the $\beta$-stability line. The $Q_\alpha$ values experience a substantial increase at shell closure with $N = 184$ (see Fig. 6.11 below as well as Fig. 14 in Ref. [58]); note that the effect of this shell closure is washed out in the $Z > 110$ nuclei for the DD-PC1 functional. With subsequent increase of neutron number the $Q_\alpha$ values become first smaller, then they become close (or equal) to zero and with further increase of $N$ they get more and more negative. Note that $\alpha$-decay is energetically not possible for $Q_\alpha \leq 0$ MeV. Thus, very neutron-rich nuclei cannot decay by $\alpha$-emission.

Note that general trends in the development of the $Q_\alpha$ values as a function of proton and neutron number are similar in all functionals. The major differences are related to the location of the two-neutron drip line, the impact of the $N = 184$ and $N = 258$ shell closures and the location of the boundaries between prolate and oblate nuclear shapes. These differences between the functionals are summarized in Fig. 6.12 which shows the $Q_\alpha$ spreads $\Delta Q_\alpha(Z, N)$ as a function of proton and neutron number. The largest spread in the predictions exists in the island centered around $Z \sim 110, N \sim 198$ in which $\Delta Q_\alpha(Z, N) > 3$ MeV. This spread emerges from different predictions of the boundaries in the $(Z, N)$ plane between prolate and oblate shapes (see Fig. 6.5) and coincides with the largest spread in calculated ground state deformations (see Fig. 6.7). The next region with the largest differences in the predictions is located between neutron numbers N=236 and N=258 (see Fig. 6.12). However, these differences are not critical because (i) this region is not expected to play a role in the r-process, (b) expected $\alpha$-decay half-lives exceed $10^{20}$ s (see Fig. 6.13) and (c) many of the nuclei in this region are not expected to decay by $\alpha$-emission.

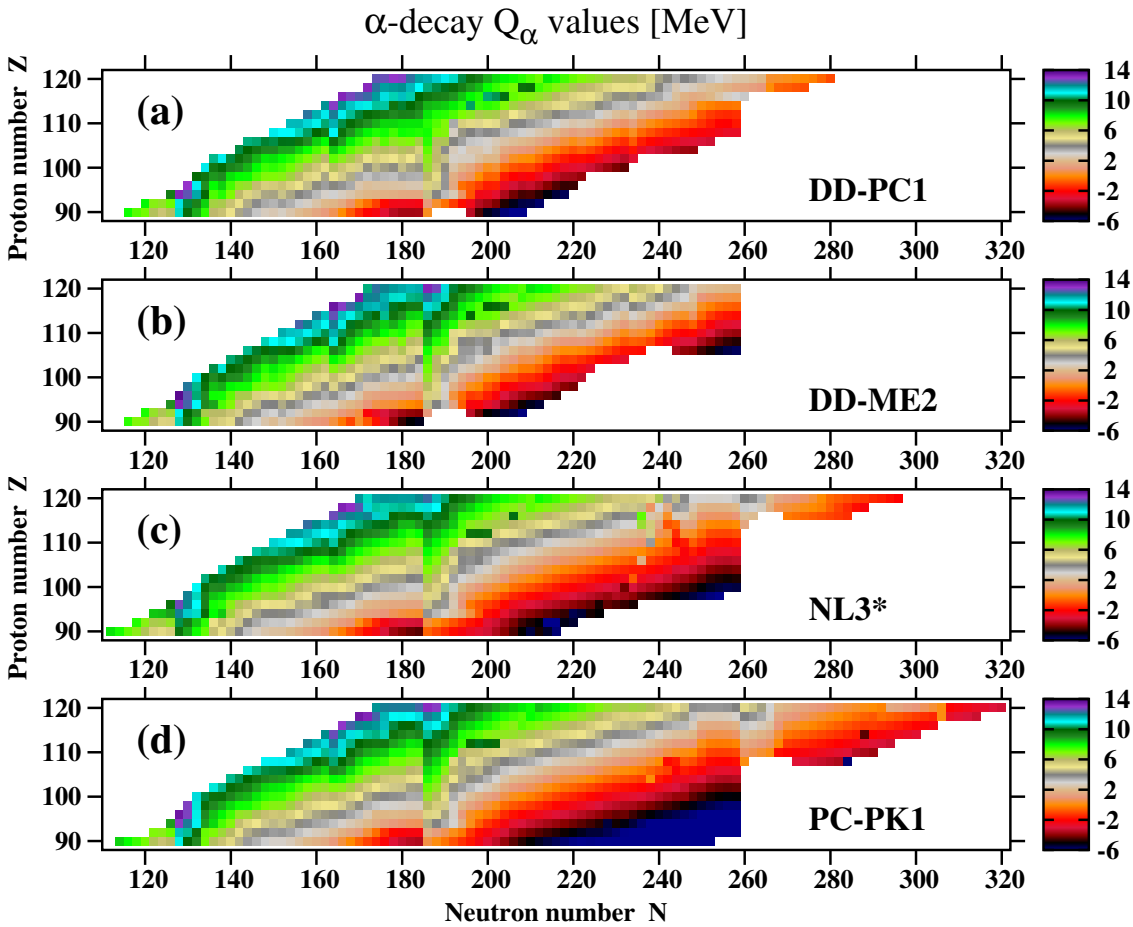


Figure 6.11

The $Q_\alpha$ values for even-even actinides and superheavy nuclei calculated with indicated CEDFs.

High $\Delta Q_\alpha$ values ($\Delta Q_\alpha(Z,N) \approx 1.5$ MeV) are observed near shell closure at $N = 184$ and in very neutron-rich nuclei near two-neutron drip line. This is a consequence of the difference in the predictions of the ground state properties such as deformations in the nuclei near $N = 184$ (see Ref. [58]) and general deterioration of predictive power of nuclear models on approaching neutron drip line (see Ref. [2]). In other regions of nuclear chart, $\Delta Q_\alpha(Z,N) \leq 1.0$ MeV with smallest spreads seen in the $N < 180$ nuclei.

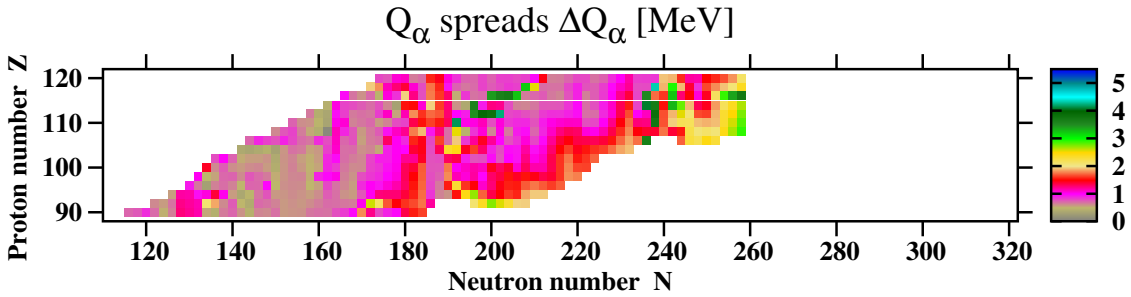


Figure 6.12

The $Q_\alpha$ spreads $\Delta Q_\alpha(Z,N)$ as a function of proton and neutron number.

$\Delta Q_\alpha(Z,N) = |Q_\alpha^{\max}(Z,N) - Q_\alpha^{\min}(Z,N)|$, where $Q_\alpha^{\max}(Z,N)$ and $Q_\alpha^{\min}(Z,N)$ are the largest and smallest $Q_\alpha$ values obtained with four employed CEDFs for the $(Z,N)$ nucleus.

Note that the inclusion of dynamical correlations (for example, by means of 5 dimensional collective Hamiltonian) can locally modify the binding energies and $Q_\alpha$ values [123, 159, 167] but they have the largest impact on transitional nuclei which represent only minor part of the nuclei under study. For well deformed nuclei, the impact of dynamical correlations on $Q_\alpha$ values is rather modest [159]. Thus, their inclusion is not expected to change drastically global picture for the behavior of $Q_\alpha$.

Calculated $\alpha$-decay half-lives $\tau_\alpha$ (in logarithmic scale) obtained with the VSS-2005 empirical formula for four CEDFs are shown in Fig. 6.13. Other phenomenological formulas such as VSS-1989, MB-2016 and Royer-2000 give similar results; thus, they are not shown. For a given isotope chain the calculated half-lives generally increase with increasing neutron number. This trend is interrupted only at the $N = 184$ and $N = 258$ shell closures. The consequence of this feature is the fact that traditional experimental technique of detecting superheavy nuclei by $\alpha$-decay will not work in neutron-rich nuclei because they can decay faster by spontaneous fission. Note that

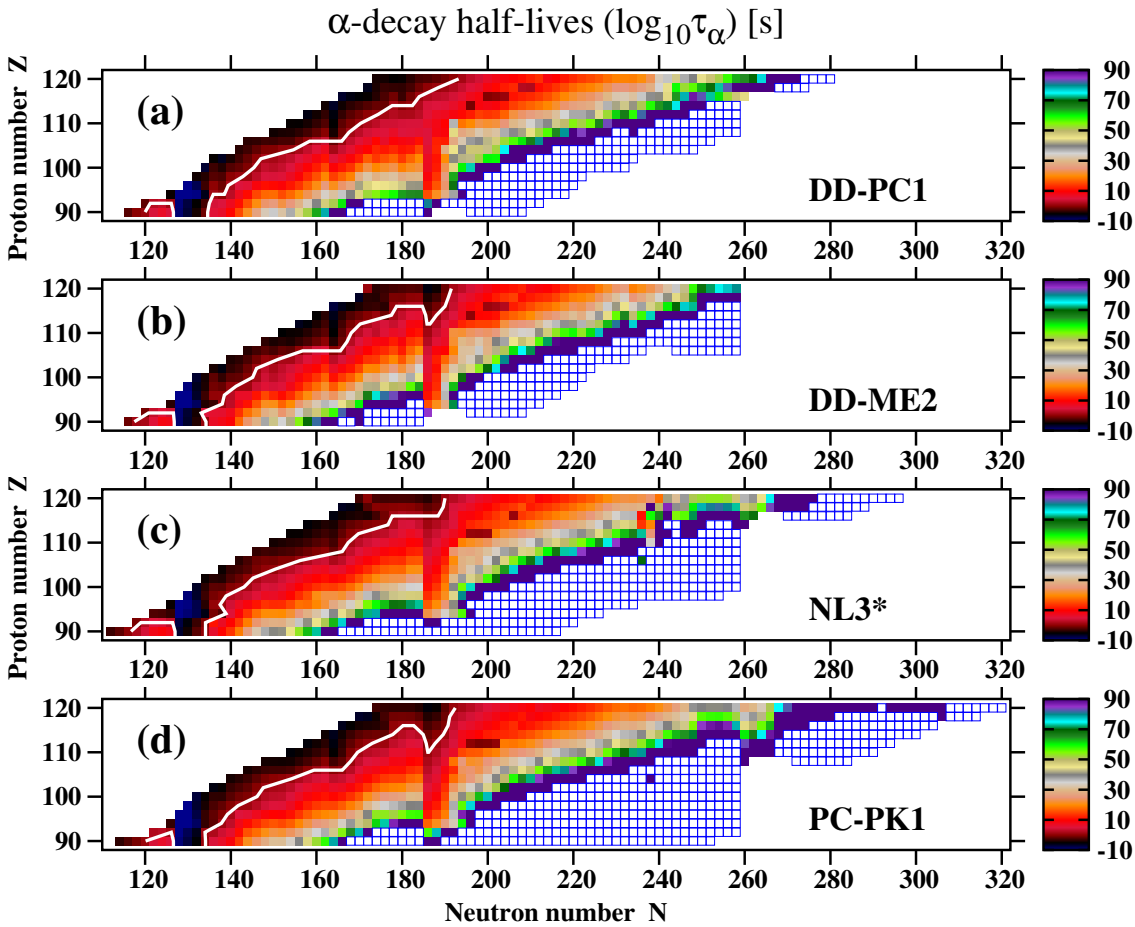


Figure 6.13

Calculated $log_{10}(\tau_\alpha)$ values of the $\alpha$-decays for even-even superheavy nuclei obtained with the VSS-2005 version of Viola-Seaborg semi-empirical formula for four indicated CEDFs.

Open squares are used for the nuclei in which $\alpha$-decay is energetically forbidden. The white line corresponding to $log_{10}(\tau_\alpha) = 1.0$ outlines the region of nuclei in which the alpha-decay half-live is smaller than 10 s.

$\alpha$-decay is energetically forbidden for a large group of very neutron-rich nuclei located in the vicinity of neutron-drip line. In such nuclei as well as in those which have very large $\tau_\alpha$ values, the competition of spontaneous fission, neutron induced fission, $\beta$-decay, and neutron emission will define the leading channel of decay in the r-process calculations.

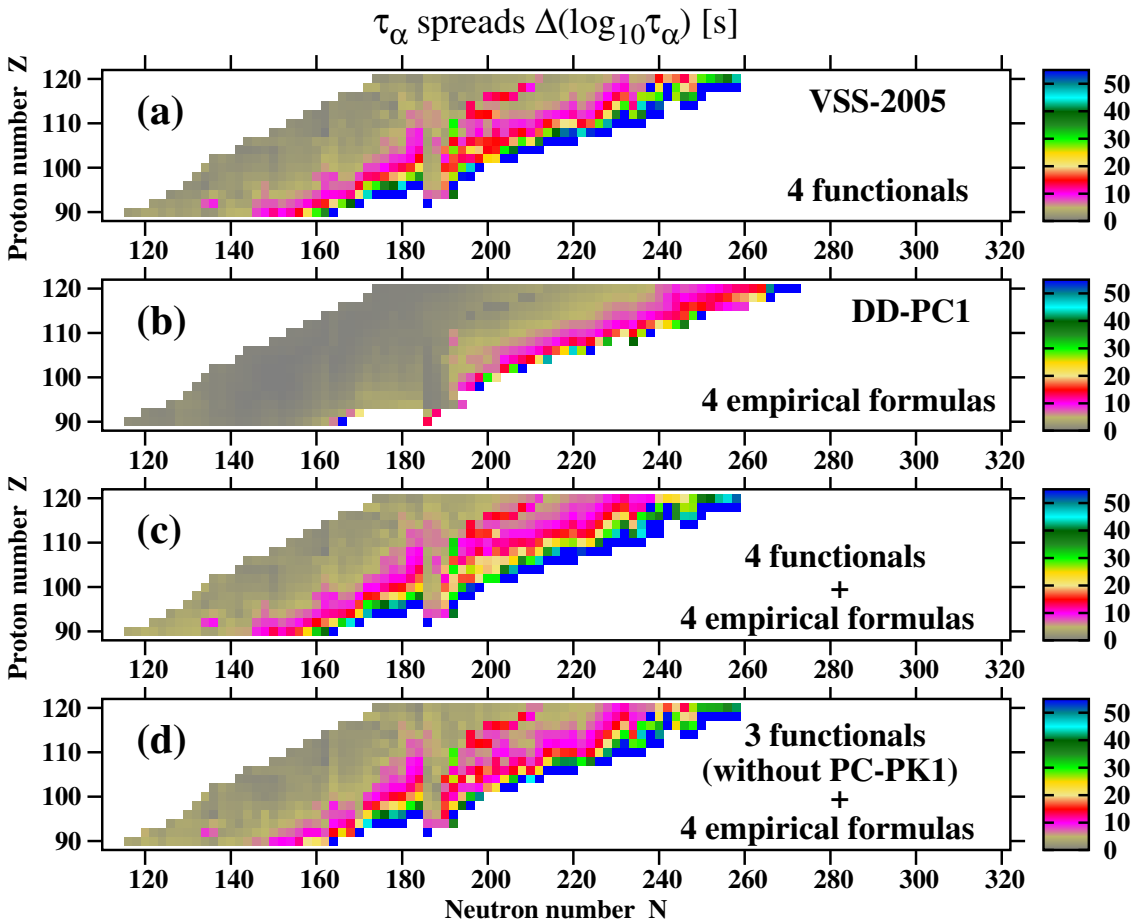


Figure 6.14

The $\tau_\alpha$ spreads $\Delta\tau_\alpha(Z,N)$ as a function of proton and neutron number.

$\Delta\tau_\alpha(Z,N) = |\tau_\alpha^{\max}(Z,N) - \tau_\alpha^{\min}(Z,N)|$, where $\tau_\alpha^{\max}(Z,N)$ and $\tau_\alpha^{\min}(Z,N)$ are the largest and smallest $\tau_\alpha$ values obtained with selected set of functionals and empirical formulas. Panel (a) shows these spreads obtained with four employed CEDFs and VSS-2005 empirical formula. DD-PC1 CEDF and four empirical formulas are used in panel (b). Panel (c) presents combined spread of $\tau_\alpha$ obtained with four CEDFs and four empirical formulas. Panel (d) is the subversion of panel (c) in which the PC-PK1 functional is excluded.

It is important to remember that the typical timescale of the r-process is in the seconds range [134, 135, 136]. Figure 6.13 clearly illustrates that with few exceptions the nuclei located to the right of white lines have $\alpha$-decay half-lives exceeding 10 s. Thus, $\alpha$-decay half-lives of these nuclei

are longer than the typical timescale of the r-process and, as a consequence, their alpha-decays will not affect the r-process simulations. These white lines in Fig. 6.13 also outline the region of nuclear chart in which traditional experimental measurements of superheavy nuclei based on the $\alpha$-decays are possible: these are the regions located near and to the left of these white lines.

Theoretical uncertainties in the predictions of $\alpha$-decay half-lives given via the $\Delta(log_{10}(\tau_\alpha))$ spreads are summarized in Fig. 6.14. The comparison of the panels (a) and (b) clearly shows that these uncertainties mostly emerge from the differences in the predictions of the $Q_\alpha$ values by different functionals. These uncertainties exceed 50 orders of magnitude in the nuclei located in the vicinity of two-neutron drip line and in some nuclei around $Z \approx 108, N \approx 198$ (see Fig. 6.14). The uncertainties in $\tau_\alpha$ originating from different empirical formulas [see Eqs. (6.2), (6.3) and (6.4)] are significantly smaller [see Fig. 6.14(b)]. For absolute majority of the nuclei they are smaller than 5 orders of magnitude and for proton-rich nuclei and the nuclei located close to the beta-stability they are very small. They are larger than 10 orders of magnitude only in neutron-rich nuclei located in close vicinity of two-neutron drip line. Combined theoretical uncertainties in $\tau_\alpha$ emerging from the use of four empirical formulas and four CEDFs are summarized in Fig. 6.14(c). One can see that for almost half of nuclei they exceed 10 orders of magnitude; these nuclei are located on neutron-rich side of the nuclear chart. However, these uncertainties are not very critical since the $\alpha$-decay lifetimes become extremely large in such nuclei (see Fig. 6.13) so $\alpha$-decay can compete neither with fission nor with $\beta$-decay. Note also that the removing of the PC-PK1 functional from consideration does not appreciably change the theoretical uncertainties in the predictions of $\alpha$-decay half-lives (compare Figs. 6.14 (c) and (d)).

## 6.5 Fission properties

### 6.5.1 Primary fission barriers

The distributions of primary fission barriers[3] (PFB) heights in the $(Z, N)$ plane obtained with employed functionals are shown in Fig. 6.15. Figure 6.16 presents the maps of the nuclei in the region under study in which outer fission barriers are higher than the inner ones in the RS-RHB calculations (see Figs. 6.2 and 6.3 for more details). It also illustrates that the importance of outer fission barriers in stabilization of nuclei in general decreases on going from light actinides to superheavy nuclei because of increased importance of Coulomb interaction (compare Figs. 6.3 and 6.2). Figure 6.16 also demonstrates the impact of octupole deformation (as obtained in RA-RHB calculations) on the outer fission barriers and on their heights with respect to inner ones. The lowering of outer fission barrier due to octupole deformation indicates that asymmetric fission becomes dominant, while the absence of the impact of octupole deformation on outer fission barrier height tells that fission will be symmetric.

Figure 6.16 shows that similar regions in the $(Z, N)$ plane, in which the outer fission barriers are higher in energy than inner ones in the RS-RHB calculations, appear in the calculations with all employed functionals. However, these regions are substantially larger in the density dependent functionals (such as DD-PC1 and DD-ME2) as compared with CEDFs NL3* and PC-PK1. Octupole deformation does not affect outer fission barriers in the nuclei located in the $Z \sim 110, N \sim 240$ region, in the $N \leq 120$ nuclei as well as in the nuclei located not so far away from $N \approx 180$. By moving away from the latter two regions, octupole deformation first starts to reduce the heights of outer fission barriers but they still remain higher in energy than inner ones.

[3]The highest in energy fission barrier (among inner and outer ones) is called primary and it plays an important role in the r-process modeling (see Ref. [166]).

Further transition away from these regions leads to the reduction of the heights of outer fission barriers below the inner ones due to the impact of octupole deformation.

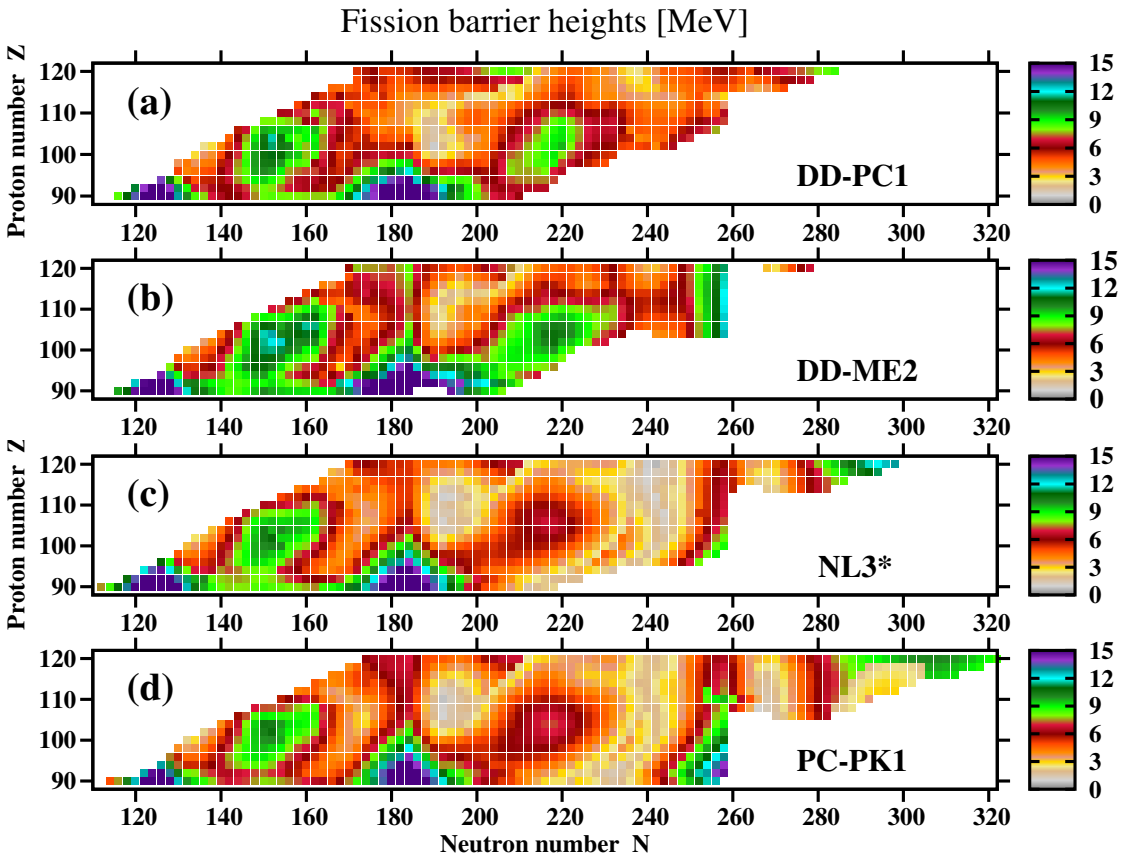


Figure 6.15

The heights of primary fission barriers (in MeV) obtained in axial RS-RHB and RA-RHB calculations as a function of proton and neutron numbers.

Figure 6.15 reveals a lot of similarities in the predictions of the global structure of the maps of fission barrier heights obtained with employed functionals. The highest PFBs are predicted in the islands of low-$Z$ nuclei centered around spherical shell closures with $N = 126$ and $N = 184$ (and $N = 258$ in the case of the PC-PK1 functional). Fission barriers reach 15 MeV in the centers

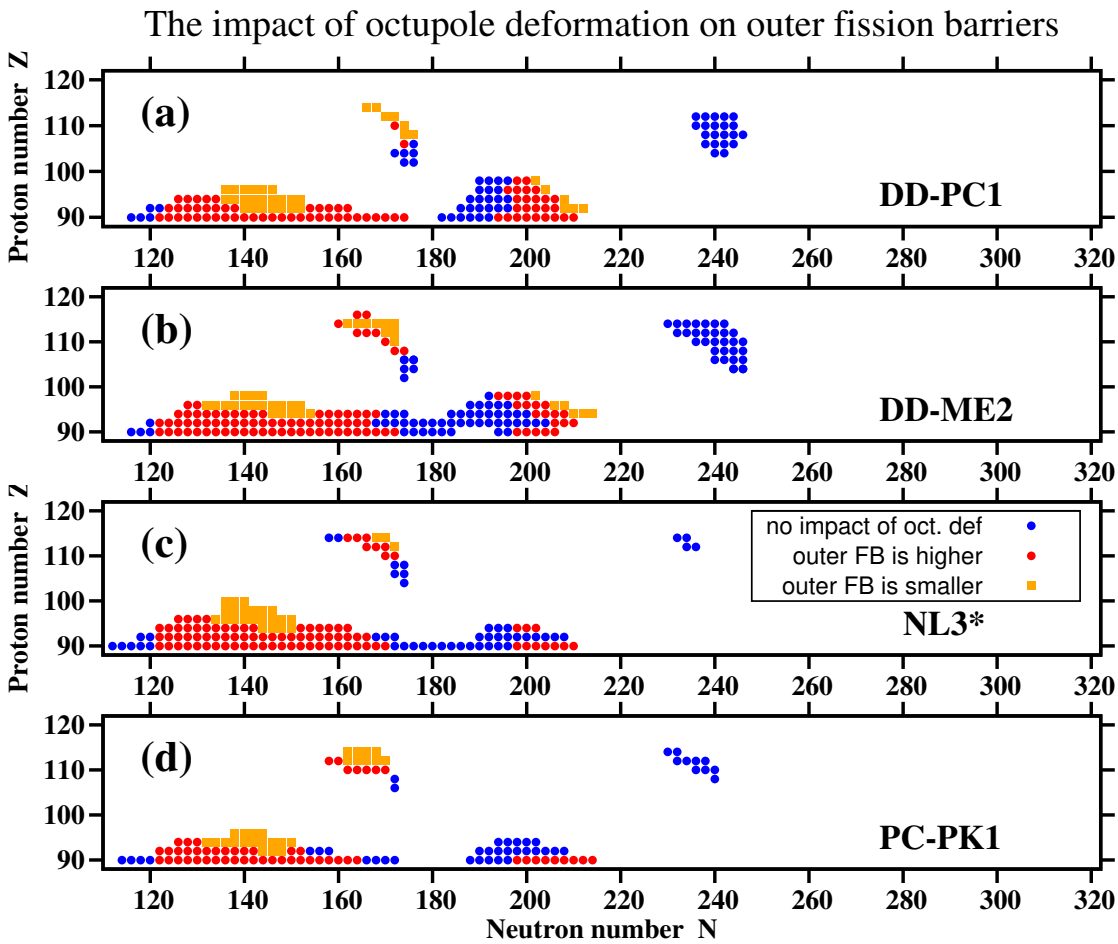


Figure 6.16

The distributions of the nuclei, in which the outer fission barrier is higher than inner one in the RS-RHB calculations, in the $(Z, N)$ plane for four employed CEDFs.

Different types of symbols are used to indicate the impact of octupole deformation on outer fission barriers of these nuclei. Blue solid circles are used for the nuclei of which the heights of outer fission barriers are not affected by the inclusion of octupole deformation. Solid red circles/orange squares are used for the nuclei in which outer fission barrier is affected by octupole deformation in the RA-RHB calculations and is higher/lower than inner fission barrier.

of these islands. Next island with high fission barriers exists around $Z \approx 100, N \approx 150$. Left bottom part of this island coincides with the region of actinides (see, for example, Fig. 7 in Ref.

[158]) in which the heights of fission barriers have been experimentally measured. Relativistic mean field calculations with the NL3*, PC-PK1 and DD-PC1 functionals performed by different groups rather well describe inner and outer fission barriers in actinides [158, 159, 160, 161]. Note also that the spreads of the heights of inner fission barriers obtained with these three functionals in the $Z \approx 100, N \approx 150$ island are relatively small (approximately 1 MeV or less) for the majority of nuclei in this island (see Fig. 3b in Ref. [60]). On the contrary, the DD-ME2 functional predicts somewhat higher fission barriers in this island (see Fig. 6.15b) which leads to somewhat higher spreads $\Delta E^B$ in the heights of primary fission barriers (see Fig. 6.17a). The island of low fission barriers is seen near $Z \approx 108, N \approx 192$ in all functionals. Then another island of high fission barriers centered around $Z \approx 104, N \approx 216$ is formed. The highest fission barriers reaching $10 - 11$ MeV in the center of this island are predicted by the DD-ME2 functional (see Fig. 6.15b). Somewhat lower fission barriers (with approximately 9 MeV height in the center of the island) are predicted by the DD-PC1 functional (see Fig. 6.15a). Fission barriers with height of approximately 6 MeV appear in broad region of this island in the calculations with the NL3* and PC-PK1 CEDFs (see Figs. 6.15c and d).

With increasing neutron number the predictions start to differ substantially. The NL3* and PC-PK1 functionals predict extremely low fission barriers with heights of around 2 MeV or less for the band of nuclei around $N \approx 240$ (see Figs. 6.15c and d). No such band is formed in the calculations with DD-ME2 and DD-PC1 functionals (see Figs. 6.15a and b). This could have a drastic impact on the creation of superheavy elements in the r-process because the nuclear flow during most of neutron irradiation step of the r-process follows the neutron drip line and produces in tens of ms the heaviest drip line nuclei (see the discussion in Sec. 4 of Ref. [144]). However, this nuclear flow

will most likely be terminated at $N \approx 240$ nuclei in the calculations with NL3* and PC-PK1 since fission will be much faster than neutron capture. Thus, no superheavy nuclei are expected to be formed in the r-process calculations based on fission barriers obtained with these two functionals. This is similar to the results of the r-process simulations based on non-relativistic models (such as Skyrme DFT with HFB-14 functional, Thomas-Fermi (TF) model and Finite Range Droplet Model (FRDM)) with low fission barriers in the vicinity of neutron drip line [144, 147]. On the contrary, the formation of superheavy elements in the r-process is more likely in the calculations based on the DD-ME2 and DD-PC1 functionals since the $(Z, N)$ region near neutron drip line is characterized by relatively high fission barriers (see Figs. 6.15a and b). As a consequence, neutron capture is expected to proceed faster than fission and nuclear flow during neutron irradiation step of the r-process could extend to higher proton numbers [144, 147]. To a degree this is similar to the r-process simulations based on the models (such as Extended Thomas Fermi (ETFSI) model) with high fission barriers near neutron drip line (see Ref. [147]).

Further increase of neutron number leads to a rise of the heights of primary fission barriers (PFBs) and the formation of the band of nuclei near shell closure at $N = 258$ with the heights of PFBs exceeding 6 MeV (see Fig. 6.15b, c and d). In some nuclei they even reach 12-15 MeV in the calculations with PC-PK1 and NL3* CEDFs (see Fig. 6.15c and d). Note that this process is suppressed in the calculations with CEDF DD-PC1 (see Fig. 6.15a) because of reduced impact of the $N = 258$ spherical shell gap on the ground state deformations (see Fig. 6.5a). Nuclear landscape extends substantially beyond $N = 258$ in the calculations with NL3* and PC-PK1 (see Fig. 6.15c and d). In this region, we again see the alteration of the regions of low (near $N \approx 268$) and high (near $N \approx 280$ and above) PFBs. Note that in the $N > 258$ region, toroidal shapes [57, 175] could

become the lowest in energy solutions. This has been verified in the calculations with DD-PC1 functional in Ref. [32] but has not been checked for other functionals.

### 6.5.2 Theoretical uncertainties in primary fission barriers and their sources

The spreads $\Delta E^B$ of the heights of primary fission barriers as a function of proton and neutron numbers for four employed functionals are shown in Fig. 6.17(a). One can see that on the average they are moderate (on the level of 1.0-1.5 MeV) in the neutron poor region of actinides centered around ($Z \sim 100, N \sim 140$). Then the spreads start to increase with a small island of high $\Delta E^B \approx 4.0$ MeV values seen in superheavy nuclei around $Z \approx 110, N \approx 164$. Further increase of neutron number leads to the band of high $\Delta E^B \approx 4.0$ MeV values for the nuclei with $N \approx 184$. The sources of these uncertainties are directly related to the differences in the predictions of the ground state properties of these nuclei: spherical ground states are predicted in these nuclei in the calculations with PCPK1, DD-ME2 and NL3* functionals [see Figs. 6.5(b),(c) and (d)] while the DD-PC1 functional prefers oblate ground states in superheavy $N \approx 184$ nuclei (see Fig. 6.5(a)). After crossing this band, theoretical uncertainties in the heights of primary fission barriers substantially decrease and for the majority of the nuclei located inside the triangle with the sides $N = 188$ [for $Z = 96 - 120$], $Z = 120$ [for $N = 188 - 240$] and [$Z = 96, N = 188$ to $Z = 120, N = 240$] they are in general better than 2.5 MeV and in many nuclei they are even better than 1.5 MeV. However, the $\Delta E^B$ spreads start to increase again on approaching two-neutron drip line. They form here quite wide band of the nuclei parallel to two-neutron drip line in which $\Delta E^B$ is close to 4.0 MeV. Even higher spreads reaching 5.5 MeV are seen near shell closure at $N = 258$.

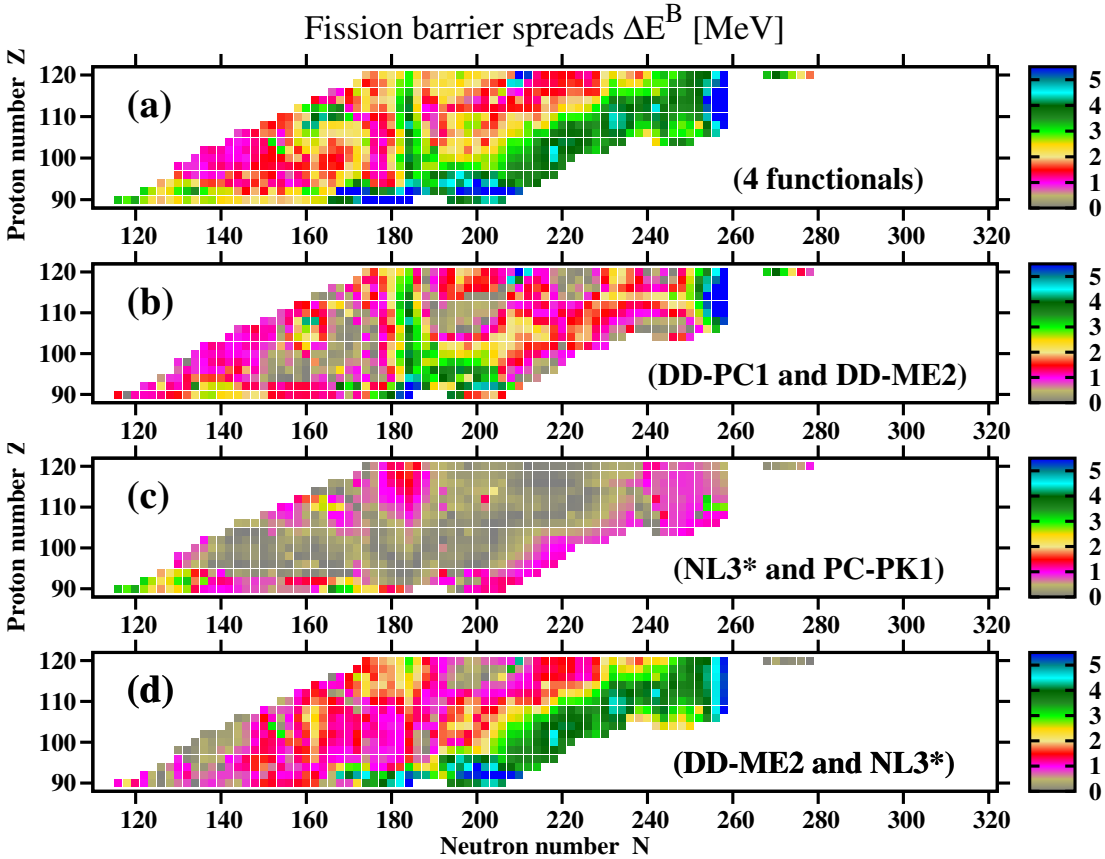


Figure 6.17

The spreads $\Delta E^B$ of the heights of primary fission barriers as a function of proton and neutron numbers.

The spreads $\Delta E^B(Z,N) = |E^B_{max}(Z,N) - E^B_{min}(Z,N)|$, where, for given $Z$ and $N$ values, $E^B_{max}(Z,N)$ and $E^B_{min}(Z,N)$ are the largest and smallest heights of inner fission barriers obtained with employed set of functionals. Panel (a) shows the spreads obtained with four employed CEDFs. Panels (b-d) show the spreads obtained for indicated pairs of the functionals.

The analysis of the spreads $\Delta E^B$ allows to identify major sources of theoretical uncertainties in the predictions of the heights of PFBs. These could be reduces to two major contributors, namely, underlying single-particle structure mostly affecting the ground state properties and nuclear matter

properties of employed CEDFs. To facilitate the discussion we will consider the $\Delta E^B$ spreads for the pairs of selected functionals.

The lowest spreads exist for the pair of the NL3* and PC-PK1 functionals (see Fig. 6.17c): $\Delta E^B \leq 0.5$ MeV for absolute majority of the nuclei and only in specific regions of nuclear chart it is higher. Even in those regions, it is higher than 1 MeV only for limited set of the nuclei. These regions are: (i) the actinides around $N = 126$, (ii) the $Z = 90$ and 92 actinides with $N \approx 170$, (iii) superheavy nuclei in the vicinity of the $Z = 120$ and $N = 184$ lines, (iv) very neutron-rich nuclei in the vicinity of two-neutron drip line and (v) the band of the nuclei around $N \approx 246$. The differences in the predictions of the heights of outer fission barriers are responsible for the spreads in the region (i). At present, their source is not clear. The spreads $\Delta E^B$ seen in the region (ii) are due both to different proton and neutron dependencies of the impact of octupole deformation on outer fission barriers in the NL3* and PC-PK1 functionals (compare panels (c) and (d) of Fig. 6.16) and the fact that in some nuclei we compare the heights of outer and inner fission barriers. In the region (iii), the large $\Delta E^B$ values are due to the differences in the predictions of the spherical shell closures at $Z = 120$ and $N = 184$ and the densities of the single-particle states in their vicinities (see Fig. 1 in Ref. [58] and the discussion in this reference). Slightly different isovector properties of the NL3* and PC-PK1 functionals (see Table 6.2) may be responsible for the divergence of their predictions in the region (iv). The large $\Delta E^B$ values in the region (v) are due to prolate-oblate-spherical shape coexistence which takes place in slightly different regions of the $(Z, N)$ chart in these two functionals [compare Figs. 6.5 (c) and (d)].

The comparison of the predictions of the NL3* and PC-PK1 functionals for the fission barriers is quite illuminating since it shows in a global way a number of important features. First, apart of

the regions (i)-(v) the comparable (typically within 0.5 MeV) predictions for the heights of PFBs are obtained on a global scale by these two functionals despite the fact that they differ substantially in the predictions of the ground states energies in neutron-rich nuclei (see the discussion of Fig. 6.8). Thus, the description of the ground state energies is to a degree decoupled from the description of fission barriers; the latter depends on the relative energies of the saddle and the ground state. As a consequence, good description of the ground state energies does not guarantee good description of the fission barriers and vice versa. Second, the differences in the predictions of the PFB heights seen in the regions (iii) and (v) are related to the differences in the predictions of the ground states properties, which in turn are defined by the differences in the underlying single-particle structure. Third, the exclusion of the regions (i)-(v) from consideration has clearly shown that some differences in nuclear matter properties such as the symmetry energy $J$ and its slope $L_0$ (see Table 6.2) do not lead to important differences in the predictions for PFBs. Fourth, comparable global predictions for the PFBs are obtained despite underlying differences in the basic structure of the functionals and their fitting protocols. The NL3* functional includes meson exchange of finite range, while PC-PK1 CEDF does not have mesons and thus it has zero range interactions (see Ref. [91]). The fitting protocol of the CEDF NL3* is based on 12 spherical nuclei and includes empirical data on nuclear matter properties (see Ref. [28]), while the one for PC-PK1 includes only data on binding energies (60 spherical nuclei) and charge radii (17 spherical nuclei) [30]. Note that the NL3* and PC-PK1 functionals have 6 and 9 parameters, respectively. However, the analysis of parametric correlations shows that in reality there are only 5 and 6 independent parameters in these two functionals [83, 91].

Next we consider the spreads $\Delta E^B$ obtained with the NL3*/DD-ME2 pair of functionals (see Fig. 6.17d). These two functionals have almost identical fitting protocols (see Refs. [28, 29]). The only difference is the fact that DD-ME2 fitting protocol uses 3 experimental data points on neutron skins as compared with 4 in NL3* but the impact of this difference is expected to be small. Thus, larger values of the $\Delta E^B$ spreads in the NL3*/DD-ME2 pair as compared with the ones in the NL3*/PC-PK1 pair are related to the basic difference of these two functionals due to the implementation of density dependence. The DD-ME2 functional has explicit dependence of the meson-nucleon coupling on the nucleonic density, while NL3* employs cubic and quartic powers of the $\sigma$ meson for density dependence (see Sect. II of Ref. [2] for details). In addition, the nuclear matter properties (in particular, the symmetry energy $J$ and its slope $L_0$) of these two functionals differ substantially (see Table 6.2) and this difference is expected to contribute into the increase of the spreads $\Delta E^B$ obtained for the NL3*/DD-ME2 pair as compared with those for the NL3*/PC-PK1 pair.

Finally, the $\Delta E^B$ spreads for the DD-PC1/DD-ME2 pair of the functionals are presented in Fig. 6.17b. Nuclear matter properties of these two functionals are close to each other and they are located within the limits of the SET2b constraint set on the experimental/empirical ranges for the quantities of interest derived in Ref. [72] (see Table 6.2). However, fitting protocols of these two functionals are drastically different: CEDF DD-ME2 is fitted to the properties of 12 spherical nuclei (see Ref. [28]) while DD-PC1 is defined by the properties of 64 deformed rare-earth nuclei and actinides (see Ref. [19]). As a result of this difference in fitting protocols, the largest $\Delta E^B$ spreads appear in the vicinity of spherical shell closures at $N = 184$ (with $\Delta E^B$ reaching 4.0 MeV) and $N = 258$ (with $\Delta E^B$ reaching 5.5 MeV) [see Fig. 6.17b]. Indeed, the impact of these shell

closures on the equilibrium deformation differs substantially in these two functionals (compare Figs. 6.5(a) and (b) and see Fig. 6.7(b)) and this is a reason for increased $\Delta E^B$ spreads.

### 6.5.3 The comparison with the results obtained in non-relativistic calculations

It is interesting to compare the global trends of the heights of PFB in the $(Z, N)$ plane obtained in the RHB calculations (see Fig. 6.15) with those obtained in earlier non-relativistic calculations for which the maps similar to those presented in Fig. 6.15 are available. Note that similar to our calculations all these non-relativistic calculations have been performed only for axial nuclear shapes.

Fission barriers obtained in Gogny DFT calculations with D1M* functional are presented in Fig. 12 of Ref. [154]. These calculations cover the region from two-proton drip line up to the nuclei with two-neutron separation energies of $S_{2n} = 4.0$ MeV. In these calculations, the fission barriers of the $N \leq 186$ nuclei typically exceed 6 MeV and in a number of these nuclei their heights are close to 12 MeV. Then fission barriers in the $N \approx 190 - 210$ nuclei are lower than 4 MeV but they increase to approximately 8 MeV on approaching $S_{2n} = 4.0$ MeV line. The differences in the predictions of the heights of PFB obtained in the CDFT and Gogny DFT calculations (compare Fig. 6.15 with Fig. 12 of Ref. [154]) are in part related to the differences in the predictions of ground state properties (compare Fig. 6.5 in the present paper with Fig. 5 in Ref. [154]).

Our results for fission barriers (Fig. 6.15) could also be compared with those obtained in non-relativistic DFTs with the BCPM and HFB14 functionals and FRLDM (see Fig. 7 in Ref. [149]). The calculations with HFB14 predict very low fission barriers (with $E^B < 4$ MeV) for the $Z \geq 110$ nuclei with exceptionally low fission barriers ($E^B < 2$ MeV) in many nuclei located in

the $N \approx 184 - 210$ region (see middle panel of Fig. 7 in Ref. [149] and Fig. 13 in Ref. [166]). The RHB calculations predict in general higher fission barriers (as compared with HFB14 ones), but similar island of low fission barriers is seen near $Z \approx 108, N \approx 192$ in all functionals (see Fig. 6.15). However, this island is narrower as compared with the HFB14 one. Fission barriers obtained with the BCPM functional and FRLDM are somewhat higher than those obtained with HFB14 (compare top and bottom panel with middle panel of Fig. 7 in Ref. [149]). However, they share the same general structure in the $(Z, N)$ plane.

Fission barriers calculated in the DFT framework with Skyrme SLy6, SkI3, SV-min and SV-bas functionals are presented in Fig. 5 of Ref. [152]. Unfortunately, the colormap used in this figure does not allow to extract the details in the most interesting energy range of 6 – 10 MeV[4]. However, the region of low fission barriers (with $E^B < 4$ MeV) similar to that discussed above appear in all functionals for $N \approx 190 - 210, Z \approx 94 - 120$. Fission barriers obtained in the TF and ETFSI models for the $(Z = 84 - 120, N = 140 - 236)$ and $(Z = 84 - 115, N = 140 - 216)$ regions of nuclear chart are presented in Fig. 2 of Ref. [147]. Both of these models show the island of low fission barriers centered around $Z \approx 110, N \approx 192$. In general, the ETFSI results are close to above mentioned results obtained with Skyrme EDFs.

### 6.6 Possible impact of triaxiality on inner fission barriers

The restriction to axial symmetry is one of the approximations used in the present study which is a consequence of the global character of the study (see detailed discussion presented in the end of Sect. 6.2 and in APPENDIX A of Ref. [168]). In order to better understand for which nuclei

[4]Better colormap for the fission barrier height distribution in the $(Z, N)$ plane obtained with the Skyrme SV-min functional is used in Fig. 4 of Ref. [153].

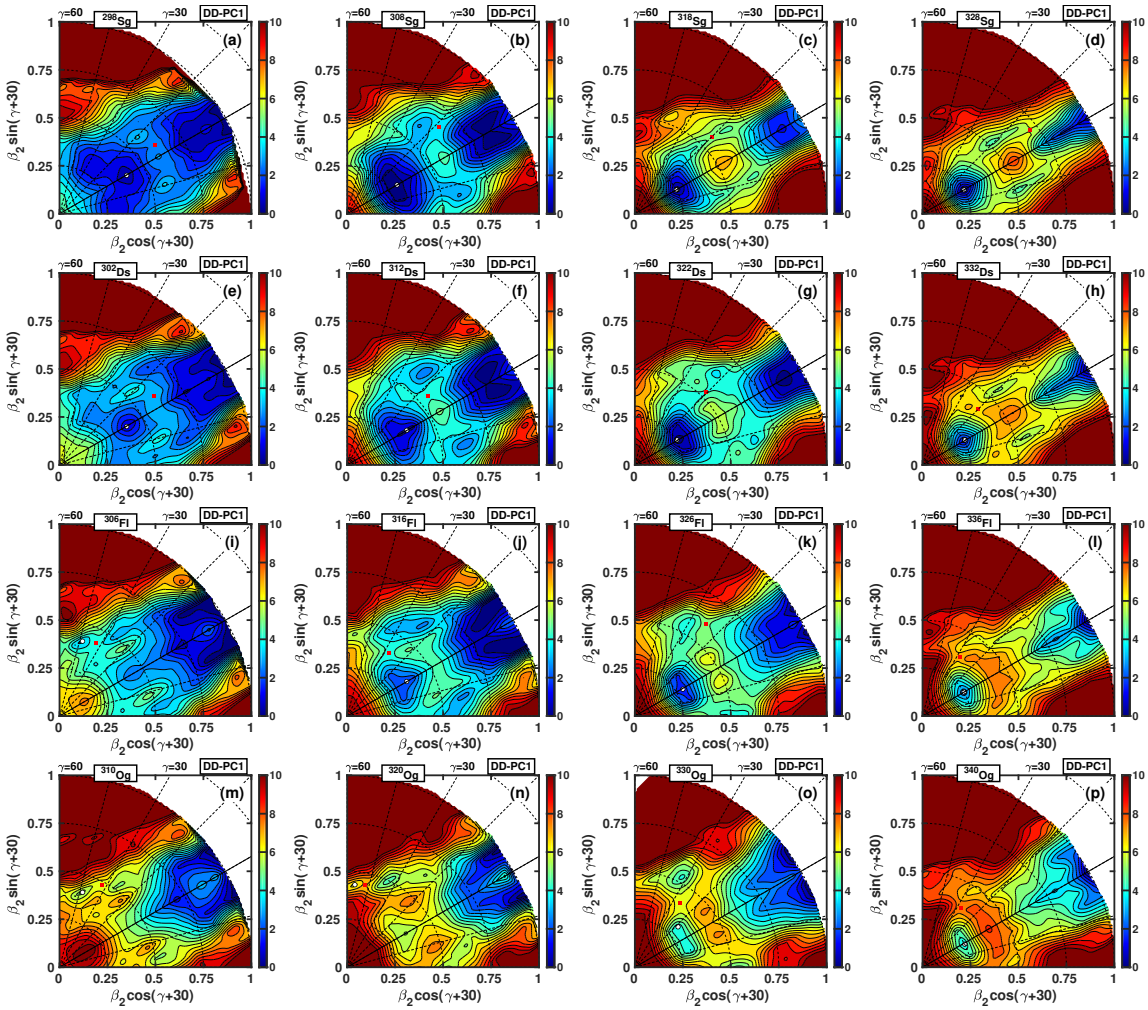


Figure 6.18

Potential energy surfaces of the indicated nuclei obtained in the triaxial RHB calculations with the DD-PC1 functional.

The calculations cover the Sg ($Z = 106$), Ds ($Z = 110$), Fl ($Z = 114$) and Og ($Z = 118$) isotopes with neutron numbers $N = 192, 202, 212$ and 222. Neutron number is increasing on going from left to right. The energy difference between two neighboring equipotential lines is equal to 0.5 MeV. The ground state minima and saddle points are shown by white circles and red solid squares, respectively.

this approximation may be violated (even in least-action calculations with pairing fluctuations included such as those presented in Refs. [176, 177]), we consider the examples of potential energy

surfaces obtained in triaxial RHB calculations with the DD-PC1 functional. These PES calculated for the Sg ($Z = 106$), Ds ($Z = 110$), Fl ($Z = 114$) and Og ($Z = 118$) isotopes with neutron numbers $N = 192, 202, 212$ and 222 are presented in Fig. 6.18. They represent the extension of the calculations, executed in a more limited deformation space, the results of which are discussed in Sect. XI of Ref. [32]. The summary of the heights $E^B_{triax}$ of triaxial inner fission barriers and the decreases of the fission barrier heights due to triaxiality $\Delta E^{gain}$ are presented in Fig. 21 and Table II of this reference. Note that these superheavy nuclei are selected in such a way that they cover the part of nuclear chart characterized by both oblate and prolate ground states (see Fig. 6.5a).

The review of existing literature suggests two possible scenarios in which the least-action fission path will most likely be characterized by triaxiality. In the first one, the decrease of the fission barrier by triaxiality in static calculations is substantial, being on the order of $3 - 4$ MeV [176, 178]. Such decreases are observed in $^{328}$Sg ($\Delta E^{gain} = 4.04$ MeV), $^{310}$Og ($\Delta E^{gain} = 3.42$ MeV), and $^{320}$Og ($\Delta E^{gain} = 4.93$ MeV) (see Figs. 6.18(d), (m) and (n) and Table II in Ref. [32]). In the second scenario, the ground state is oblate (or possibly soft in oblate-prolate direction [167]) so that the fission path across the $\gamma$-plane is shorter then the one along the $\gamma = 0^\circ$ line [178]. This condition is satisfied only in the $^{306}$Fl (see Fig. 6.18(i)) and $^{310,320}$Og (see Fig. 6.18(m) and (n)) nuclei. Based on general features discussed in Refs. [176, 177], the analysis of PES of remaining nuclei (see Figs. 6.18 a, b, c, e, f, g, h, j, k, l, o and p) suggests that least-action fission pathway will be axial in these nuclei when pairing fluctuations are taken into account.

Whether one or another scenario takes place depends on the underlying shell structure (both at the ground state and saddle) defining the topology of potential energy surfaces in the $(\beta_2, \gamma)$ plane. Figure 6.18 shows that the $N = 192$ isotones are extremely soft in the $\gamma$-plane with clear

tendency for the formation of near-oblate triaxial ground state minimum in the Fl and Og nuclei. However, static fission pathes from these minima are characterized by low fission barriers so these nuclei are expected to be unstable. Similar (but slightly less pronounced) situation is also seen for the $N = 202$ isotones. The increase of neutron number to $N = 212$ and 222 leads to a better localization of the ground state minimum at prolate shape and to an increase of fission barrier heights.

## 6.7 Conclusions

The systematic investigation of the ground state and fission properties of even-even actinides and superheavy nuclei with $Z = 90 - 120$ from the two-proton up to two-neutron drip lines has been performed for the first time in the framework of covariant density functional theory. Four state-of-the-art CEDFs such as DD-PC1, DD-ME2, NL3* and PC-PK1 are used in this study. They represent the major classes of the CDFT models which differ by basic assumptions and fitting protocols. This allows a proper assessment of systematic theoretical uncertainties for physical observables of interest. Obtained results provide a necessary theoretical input for the r-process modeling in heavy nuclei and, in particular, for the study of fission recycling. The main results can be summarized as follows:

- Quadrupole deformations of calculated ground states and related theoretical uncertainties have been investigated. It turns out that four employed functionals predict very similar deformations for the majority of the nuclei. However, large theoretical uncertainties in quadrupole deformation exist for some nuclei but they are well localized in the $(Z, N)$ plane. These uncertainties are mostly due to the uncertainties in the predictions of the underlying single-particle structure. They are dominated by the uncertainties in the predictions of both spherical shell closures at $N = 184$, $N = 258$ and $Z = 120$ (for the $N < 190$ nuclei) and deformed single-particle structures leading to somewhat different boundaries in the $(Z, N)$ plane between the regions with oblate and prolate shapes. The differences in nuclear matter properties of employed functionals have only marginal impact on theoretical uncertainties related to calculated quadrupole deformations.

- Theoretical uncertainties $\Delta E(Z,N)$ in binding energies, emerging from poorly defined isovector properties of CEDFs, increase drastically when approaching the neutron drip line and in some nuclei they reach 50 MeV. However, they reduce substantially (down to maximum value of $\Delta E(Z,N) \approx 21$ MeV) when PC-PK1 functional is removed from consideration. Two-neutron drip line of this functional is also located at substantially higher neutron numbers as compared with the ones obtained with other functionals. In addition, this functional is the major source of theoretical uncertainties in two-neutron separation energies. Parametric correlations leading to an over-parametrization of the isoscalar channel is a possible reason for such a unique behavior of the CEDF PC-PK1. Theoretical uncertainties in two-neutron separation energies reveal clear importance of the uncertainties in the $N = 184$ and $N = 258$ spherical shell closures and in the location of the boundaries between the regions of prolate and oblate shapes.

- $\alpha$-decay properties, such as the $Q_\alpha$ values and the lifetimes $\tau_\alpha$, and related theoretical uncertainties have been investigated employing four empirical formulas and four CEDFs. While the predictive power of the models is relatively high on proton-rich side of nuclear chart, it starts to deteriorate on approaching $N = 184$. It is especially low in the nuclei around $Z \approx 108, N \approx 198$ [the region of the transition from prolate to oblate ground states] and in very neutron-rich nuclei located in the vicinity of two-proton drip line. However, the uncertainties in the latter region are not very important since the $\alpha$-decay in these nuclei is not expected to play any role in the r-process because of extremely large lifetimes.

- The distributions of the primary fission barriers in the $(Z,N)$ plane have been investigated with four employed CEDFs. Globally, the highest fission barriers are produced by the CEDF DD-ME2, and the lowest ones by the NL3* and PC-PK1 functionals. The results obtained with DD-PC1 are located between these two extremes but closer to the DD-ME2 ones. The presence of the band of nuclei with $N \approx 240$ in the $(Z,N)$ plane with low fission barriers, obtained in the calculations with the NL3* and PC-PK1 functionals, could have a drastic impact on the creation of superheavy elements in the r-process. The nuclear flow during most of neutron irradiation step of the r-process follows the neutron drip line and produces in tens of ms the heaviest drip line nuclei. However, this nuclear flow will most likely be terminated at $N \approx 240$ nuclei since fission will be much faster than neutron capture. On the contrary, the formation of superheavy elements in the r-process is more likely in the calculations based on the DD-ME2 and DD-PC1 functionals since the $(Z,N)$ region near neutron drip line is characterized by relatively high fission barriers and the band of nuclei with low fission barriers (similar to the one at $N \approx 240$ in the NL3* and PC-PK1 functionals) is absent.

- There are two major sources of theoretical uncertainties in the predictions of the heights of PFBs, namely, underlying single-particle structure mostly affecting the ground state properties and nuclear matter properties of employed CEDFs. For example, the increase of theoretical uncertainties for the ground states of the nuclei in the vicinity of the $N = 184$ and $N = 258$ spherical shell closures leads to an increase of theoretical uncertainties for their fission barriers. The functionals with nuclear matter properties located in the vicinity

of empirical SET2b estimates [72] tend to produce higher fission barriers as compared with the predictions of the functionals the nuclear matter properties of which are located outside the limits of the SET2b constraint set. The problem of finding the best functional for the description of fission barriers is further complicated by the fact that the description of the ground state energies is to a degree decoupled from the description of fission barriers; the latter depends on the relative energies of the saddle and the ground state. As a consequence, good description of the ground state energies does not guarantee good description of the fission barriers and vice versa.

This is first ever systematic attempt within the covariant density functional theory to provide both the input for the r-process calculations which includes the ground state and fission properties of actinides and superheavy nuclei and the assessment of systematic theoretical uncertainties in the physical quantities of interest. As such it follows the ideology of all previous non-relativistic calculations of relevance for the r-process of heavy and superheavy nuclei, which depend also on the fission processes, and assumes the axial symmetry of nuclei. This is a reasonable approximation for the ground state properties of the majority of nuclei; the only exception is transitional nuclei which are soft in $\gamma$-deformation. However, the restriction to axial symmetry leads to the fact that the calculated inner and outer fission barriers represent the upper limits and can be potentially lowered when the triaxiality is taken into account. The r-process simulations with the data obtained in this study will allow to limit the region of the $(Z, N)$ plane which has an impact on this process. The hope is that for this limited set of nuclei, systematic refined calculations taking into account the dynamical correlations and the triaxiality in the calculations of the part of the $(\beta_2, \gamma)$-plane covering ground state, inner fission barrier and second minimum as well as triaixiality and octupole deformation in the calculations of the part of the $(\beta_2, \beta_3, \gamma)$ plane covering second minimum, outer fission barrier and the region beyond that will be possible in the era of exascale computing.

Underlying single-particle structure and nuclear matter properties of CEDFs emerge as the major sources of theoretical uncertainties. However, they affect different physical observables in a different way. For example, theoretical uncertainties in the ground state quadrupole deformations are defined mostly by the uncertainties in the underlying single-particle structure. On the contrary, both factors contribute into theoretical uncertainties for fission barriers. The existence of appreciable theoretical uncertainties in the ground state and fission properties calls for a better covariant energy density functionals. The reduction of parametric correlations between the parameters of CEDFs is one possible way in that direction [86, 91]. In addition, experimental studies of superheavy elements in the vicinity of the $Z = 120$ and $N = 184$ lines, planned at new facilities such as SHE factory [179], will hopefully provide critical data which will allow to discriminate the predictions of different models. Such information could be used for a better constraint of the CEDFs and thus to the reduction of substantial theoretical uncertainties in this region of nuclear chart which affect all physical observables of interest and have a direct impact on the modeling of the r-process.

# CHAPTER VII

# EXTENSION OF NUCLEAR LANDSCAPE TO HYPERHEAVY NUCLEI

## 7.1 Introduction

One of the main focuses of modern low-energy physics is the limits of the existence of finite nuclei. New generation of facilities such as FRIB, FAIR, RIKEN, and GANIL will explore such limits in neutron-rich nuclei. SHE-factory and similar facilities will attempt to extend the limits of our knowledge on superheavy nuclei. However, already now it is clear that there are significant restrictions on what could be achieved by these new facilities: many neutron-rich medium mass, heavy and superheavy nuclei will be beyond their experimental reach [46]. In such a situation, theoretical predictions became the only tool to investigate such limits. Indeed, a significant progress has been achieved in understanding the limits of nuclear landscape for the $Z < 120$ nuclei (see Refs. [2, 37, 38]) and more or less consistent picture has been obtained using the combination of different theoretical tools. In addition, systematic theoretical uncertainties [2, 37, 45] and statistical errors [39, 84, 83] in the predictions of the properties of neutron-rich nuclei and the positions of two-proton and two neutron-drip lines have been evaluated.

However, the nuclear landscape is not restricted to the $Z < 120$ nuclei. Although there were some attempts to investigate higher $Z$ nuclei [180, 181, 182, 183, 184, 185], these systematic studies were restricted to spherical symmetry. Recent study (Ref. [57]) based on systematic axial RHB calculations and triaxial RHB as well as triaxial (RMF+BCS) calculations for a reasonable large

set of selected nuclei has invalidated many conclusions of these studies[1]. In addition, it provided a new vision on the properties of hyperheavy nuclei and on the extension of nuclear landscape to the $Z > 120$ region. These results are briefly summarized below. The increase of proton number beyond $Z = 120$ leads to the dominance of highly deformed and superdeformed oblate ground states. However, these states with ellipsoidal-like shapes become unstable with respect of fission in the $Z \approx 130$ region (see also Ref. [189] for the results obtained for fission barriers in non-relativistic theories). This triggers the transition to the states with toroidal shapes; the lowest in energy solutions in the $Z = 140 - 180$ nuclei have such shapes in axial RHB calculations. It was illustrated that some of such states could be stable against fission. In addition, some regions of stability of spherical hyperheavy nuclei have been predicted for the first time in Ref. [57]. Although these states are highly excited with respect of the lowest in energy states with toroidal shapes (as obtained in axial RHB calculations), they will become the ground states if toroidal states are not stable with respect of multifragmentation (which according to present understanding (see Ref. [175]) is quite likely scenario).

Note that only in hyperheavy nuclei the states with toroidal shapes could become the lowest in energy. The toroidal shapes in atomic nuclei have been investigated in a number of the papers [187, 188, 190, 191, 192, 193]. However, in absolute majority of the cases such shapes correspond to highly excited states either at spin zero [188, 192] or at extreme values of angular momentum [190, 191, 194]. In the former case, such states are unstable against returning to the shape of sphere-like geometry (Ref. [192]). In the latter case, calculated angular momenta at which toroidal

[1]The effects of axial and triaxial deformations have also been studied for a few hyperheavy nuclei in Refs. [186, 187] and Ref. [188], respectively. Somewhat larger set of the nuclei was studied with triaxiality included in Ref. [189], but according to Ref. [57] the deformation range employed in this work is not sufficient for $Z \geq 130$ nuclei.

shapes appear substantially exceed the values of angular momentum presently achievable at the state-of-art experimental facilities [195].

This chapter will summarize some of the recent work on the properties of hyperheavy nuclei and on the extension of nuclear landscape to hyperheavy nuclei. This work has been started in Ref. [57] and it was extended with more details in Ref. [32]. The stability of toroidal shapes in selected nuclei and the evolution of such shapes along their fission path are considered in Sec. 7.2. Section 7.3 is devoted to the analysis of the impact of triaxial deformation on the fission barriers of neutron-rich superheavy nuclei. The extension of nuclear landscape to hyperheavy nuclei is discussed in Sec. 7.4. Finally, Sec. 7.5 summarizes the main concluding remarks.

## 7.2 Toroidal shapes: stability and shape evolution along the fission path.

The investigations of Ref. [57] showed that some toroidal shapes could be stable with respect of triaxial distortions. Figure 7.1 shows potential energy surfaces of the $^{354}134$ and $^{348}138$ nuclei around minima of such configurations located at $\beta_2 \approx 2.3, \beta_4 \approx +1.5, \gamma = 60^\circ$. The saddle points of the first fission barriers of these configurations are located at 4.4 and 8.54 MeV, respectively. However, physical reasons for such stability of toroidal shapes have not been discussed in Ref. [57].

To understand these reasons, the evolution of toroidal shapes along the fission path of the configuration in the $^{354}134$ nucleus (shown in Fig. 7.1) is displayed in Fig. 7.2. The toroid and its tube are fully symmetric at the minimum (Fig. 7.2a-c). The deviations from axial symmetry lead to the distortions which are already seen at $\gamma = 50^\circ$; the toroid is stretched out in the direction of the axis of symmetry and squeezed in perpendicular direction (Fig. 7.2f)). However, the tubes of the toroid still remain cylindrical (Fig. 7.2d,e)). Figures 7.2g,h,i show the density distributions at

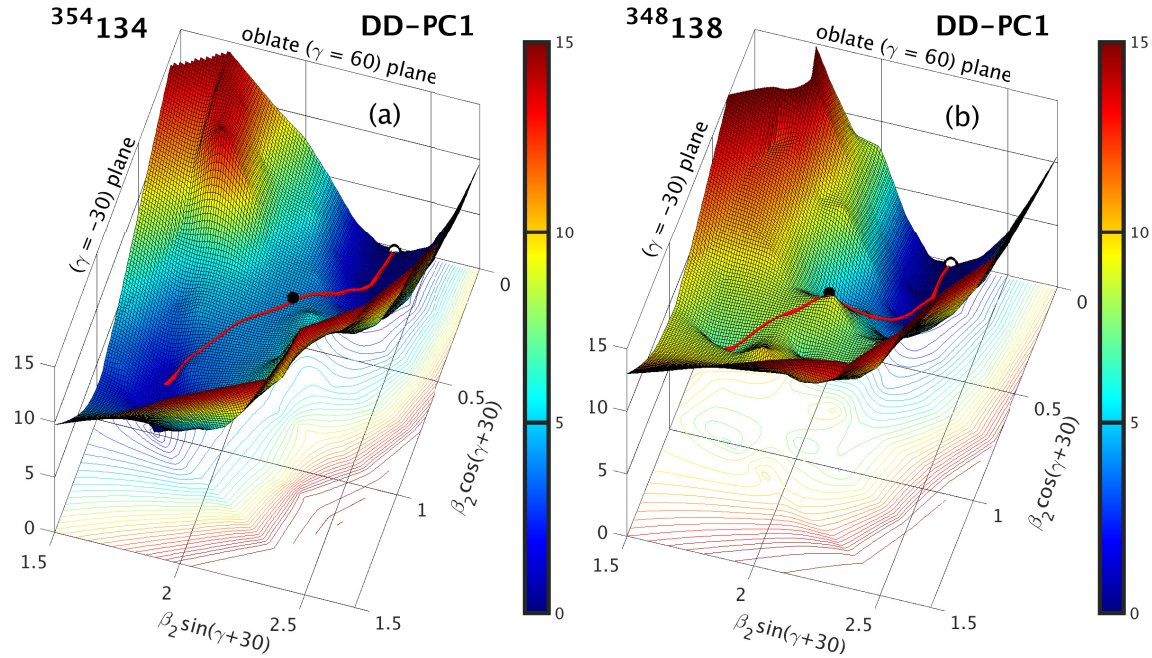


Figure 7.1

Three-dimensional potential energy surfaces with their two-dimensional projections for the solutions with minimum at $\beta_2 \approx 2.3, \beta_4 \approx +1.5, \gamma = 60°$ in indicated nuclei.

Note that based on the results of the TRMF+BCS calculations of Ref. [57], these solutions are excited ones in axial calculations, but they are the lowest in energy stable solutions in triaxial calculations. The red line shows static fission path from the minimum indicated by open white circle; the saddle point is shown by black solid circle. The energy difference between two neighboring equipotential lines in contour plot is 0.5 MeV.

the deformations corresponding to the saddle point. One can see further increase of the asymmetry of torus and the decrease of the area of toroid hole. Thus, one can conclude that the barrier against fission emerges because these deviations from symmetrical shape of toroid cost the energy.

Further decrease of the $\gamma$- and $\beta_2$ deformations leads to increasing distortion of the geometry of toroid ((Fig. 7.2l)) the outer shape of which looks now similar to parallelogram and the shape of toroid hole comes closer to square. In addition, Figs. 7.2j,k reveal visible deviations from

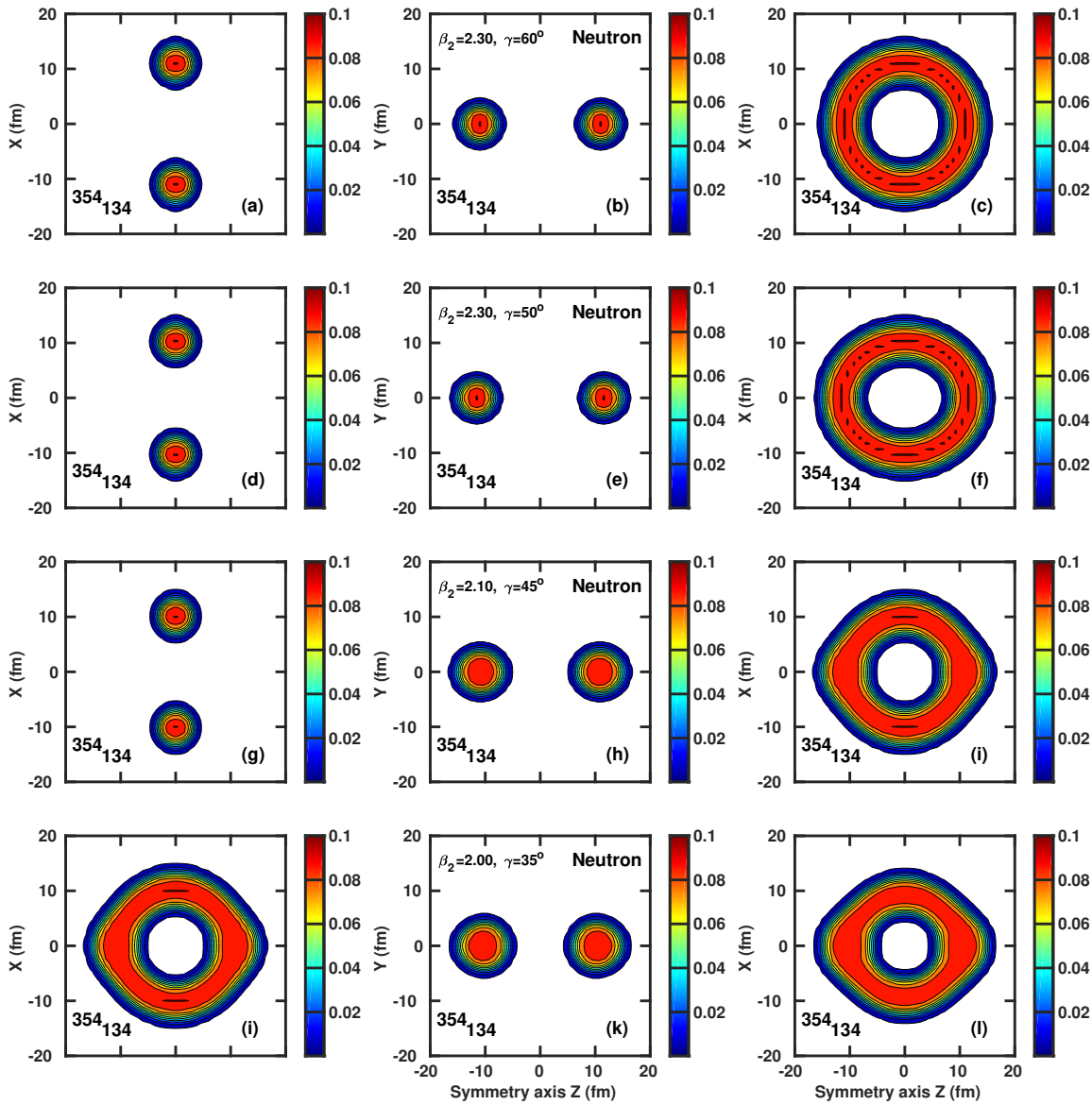


Figure 7.2

The evolution of toroidal shapes along the fission path in the $^{354}134$ nucleus shown on left panel of Fig. 7.1.

Neutron density distributions are shown at indicated $(\beta_2, \gamma)$-deformations along this fission path. To give a full three-dimensional representation of the density distributions, they are plotted in the $xy$, $yz$ and $xz$ planes at the positions of the Gauss-Hermite integration points in the $z$, $x$ and $y$ directions closest to zero, respectively. The density colormap starts at $\rho_n = 0.005$ fm$^{-3}$ and shows the densities in fm$^{-3}$.

cylindrical shape of the tube of toroid. However, these changes reduce the total energy of the configuration as compared with the one at the saddle point.

Above discussed changes in shapes and total energies along the fission path are the consequences of a delicate balance of liquid drip and shell correction energy contributions.

### 7.3 The impact of triaxial deformation on the fission barriers of neutron-rich superheavy nuclei

Although oblate minima of high-$Z$ ($Z > 120$) superheavy and low-$Z$ hyperheavy nuclei are relatively stable with respect of axial reflection symmetric and asymmetric deformations (see Refs. [32, 57]), that is not necessary the case with respect of triaxial deformation. The impact of triaxiality on the fission paths and the differences in the stability of super- and hyperheavy elements is illustrated in Fig. 7.3 on the example of superheavy $^{268}$Sg and $^{332}$Ds nuclei and hyperheavy $^{360}$130 and $^{432}$134 nuclei.

Both in super- and hyperheavy nuclei the potential energy surfaces (PES) represent the canyon in which some local valleys and hills are located. However, there are two principal differences between super- and hyperheavy nuclei. The canyon is quite narrow in superheavy nuclei which prevents the formation of local minima at large oblate deformation and limits the role of triaxial deformation. One can see that normal deformed minima are prolate in superheavy $^{268}$Sg and $^{332}$Ds nuclei and fission paths from these minima is located not far away from the $\gamma = 0^\circ$ axis. In addition, the bottoms of the canyons in PES are on average flat.

On the contrary, in hyperheavy nuclei the walls of the canyon with very rapid raise of energy with deformation are located at larger separation (so only right wall is seen in the bottom panels of Fig. 7.3) as compared with superheavy nuclei and the mountain centered around $\beta_2 \approx 0$ is formed

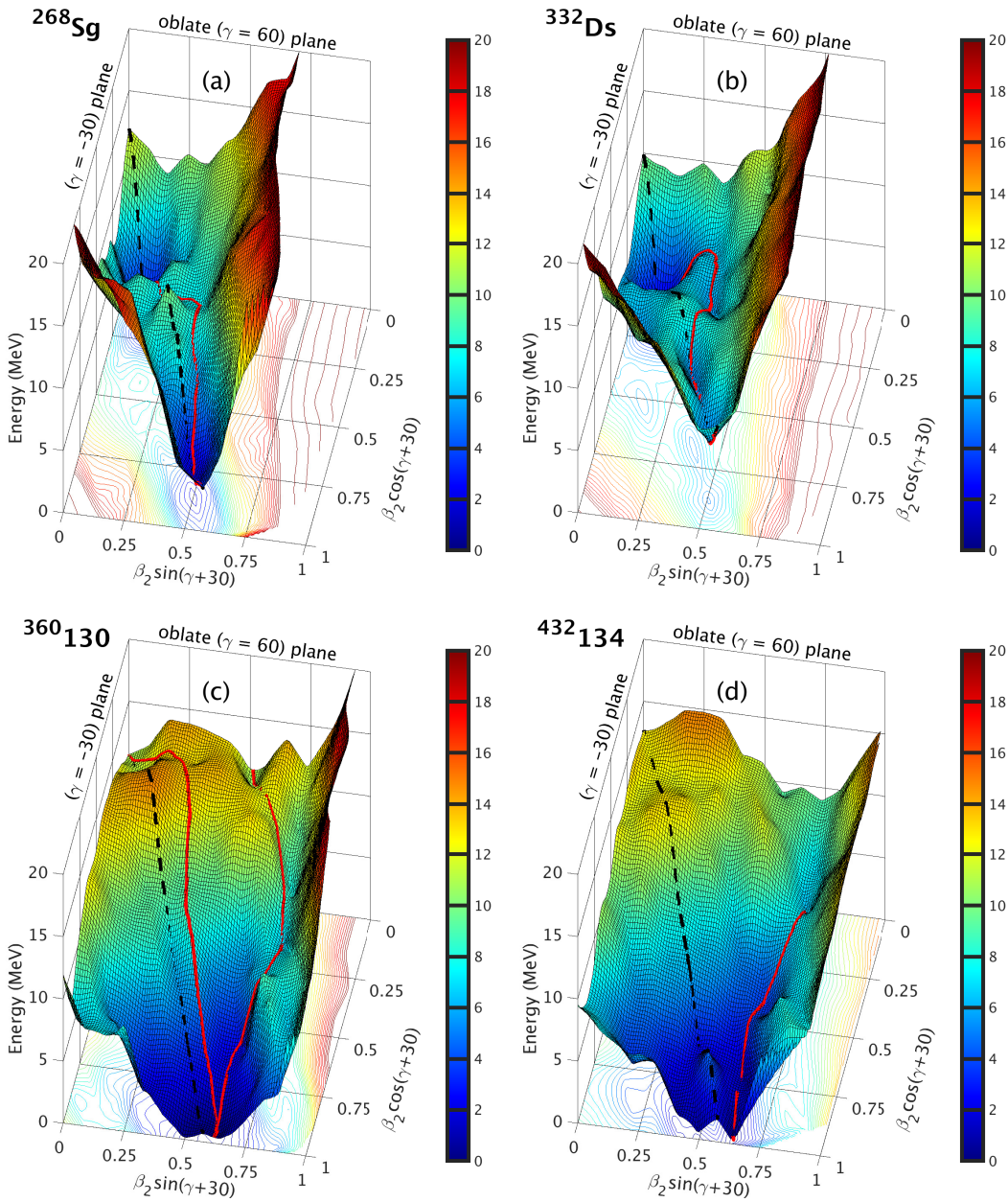


Figure 7.3

Three-dimensional potential energy surfaces with their two-dimensional projections (contour plots) for the nuclei with the ground states having ellipsoidal shape.

These results have been obtained in the TRHB calculations with $N_F = 18$. The red line shows static fission path from respective minimum, while black dashed line the $\gamma = 0°$ axis. The energy difference between two neighboring equipotential lines in contour plot is 0.5 MeV.

in this canyon. The slope of the mountain in the direction of the $\beta_2$-deformation at $\gamma = 0^\circ$ is very high. This indicates higher instability of hyperheavy nuclei against fission as compared with superheavy ones. The larger separation of the canyon walls leads to an increased role of triaxiality in hyperheavy nuclei: local minima are formed either at oblate superdeformation (see example of the $^{360}130$ nucleus in Fig. 7.3) or at very large $\gamma$-deformation (see example of the $^{432}134$ nucleus in Fig. 7.3). In addition, the fission paths from these minima proceed at larger $\gamma$-deformations as compared with superheavy nuclei. Not only the fission through the $\gamma$-plane gets more energetically favored, but also the fission path through $\gamma$-plane becomes much shorter than the one through the $\gamma = 0^\circ$ axis (see also the discussion in Ref. [57]).

The general conclusion is that the barriers along the fission paths emerging from the oblate minima located within the $-1.0 < \beta_2 \leq 0.0$ range decrease with increasing proton number (see Ref. [57]). As a result (see discussion in Sect. 7.4 below), the fission barriers for oblate ellipsoidal shapes become consistently lower than 2 MeV above some $(Z, N)$ line in nuclear landscape so the nuclei in ellipsoidal shapes cease to exist for these particle numbers.

However, in order to delineate this borderline additional information on the impact of triaxiality on the fission barrier heights of the superheavy $Z = 106 - 118$ nuclei located between two-proton and two-neutron drip lines is needed. So far, such information is available only for actinides and superheavy nuclei with $Z \leq 120$ and $N \leq 184$ [59, 158, 163, 164, 196, 197] . These nuclei are either prolate or spherical in their ground states and thus the impact of triaxiality is limited: the lowering of inner fission barriers in actinides due to triaxiality is typically on the level of 1-3 MeV. This reduction is substantially smaller as compared with the one typically seen in hyperheavy nuclei [57].

Table 7.1

The heights of the fission barriers along the fission paths from different minima obtained in axial and triaxial RHB calculations.

| | | Axial RHB | | | Triaxial RHB | | | |
|---|---|---|---|---|---|---|---|---|
| $Z$ | $N$ | $\beta_{min}$ | $\beta_{saddle}$ | $E^B_{ax}$ | $(\beta,\gamma)_{min}$ | $(\beta,\gamma)_{saddle}$ | $E^B_{triax}$ | $\Delta E^{gain}$ |
| 1 | 2 | 3 | 4 | 5 | 6 | 7 | 8 | 9 |
| 106 (Sg) | 152 | 0.29 | 0.57 | 10.09 | 0.29, 0 | 0.62, 12.4 | 7.04 | 3.05 |
| | 162 | 0.26 | 0.65 | 10.70 | 0.26, 0 | 0.68, 8.4 | 7.48 | 3.32 |
| | 172 | 0.14 | 0.69 | 5.31 | 0.14, 0 | 0.71, 3.5 | 2.95 | 2.36 |
| | 182 | -0.05 | 0.27 | 4.25 | 0.05, 60.0 | 0.47, 23.6 | 3.70 | 0.55 |
| | | (0.49) | (0.73) | (3.42) | (0.49, 0) | (0.81, 8.0) | (2.47) | (0.95) |
| | 192 | 0.39 | 0.59 | 2.42 | 0.40, 0 | 0.61, 6.3 | 2.20 | 0.22 |
| | 202 | 0.28 | 0.59 | 4.27 | 0.29, 9.5 | 0.66, 13.2 | 3.73 | 0.54 |
| | 212 | 0.25 | 0.54 | 7.23 | 0.25, 0 | 0.69, 10.3 | 4.99 | 2.24 |
| | 222 | 0.25 | 0.55 | 8.53 | 0.250, 0 | 0.70, 8.7 | 4.49 | 4.04 |
| | 232 | 0.23 | 0.65 | 6.73 | 0.23, 0 | 0.62, 10.4 | 4.63 | 2.10 |
| | 242 | 0.13 | 0.25 | 3.77 | 0.13, 0 | 0.25, 0 | 3.77 | 0.0 |
| | | (0.45) | (0.65) | (5.08) | (0.45, 0) | (0.60, 6.9) | (2.37) | (2.71) |
| | 252 | -0.06 | 0.25 | 6.40 | 0.06, 59.1 | 0.42, 26.7 | 3.86 | 2.54 |
| | | (0.45) | (0.69) | (5.68) | (0.45, 0) | (0.69,10.3) | (3.20) | (2.48) |
| 110 (Ds) | 162 | 0.24 | 0.66 | 8.98 | 0.242,0 | 0.65, 6.9 | 6.20 | 2.78 |

The columns $3-5$ show the results of the axial RHB calculations. Here $\beta_{min}$, $\beta_{saddle}$ and $E^B_{ax}$ are the equilibrium quadrupole deformation of the global minimum, the quadrupole deformation and the energy of the saddle along respective fission path. The results of the triaxial RHB calculations are provided in the columns $6-8$. Note that the allowance of triaxial deformation could shift the position of the local minimum in the deformation plane and in absolute majority of the cases shifts the positions of the saddle points. Thus, $(\beta,\gamma)_{min}$, $(\beta,\gamma)_{saddle}$ and $E^B_{triax}$ show the deformations of the minima, the deformations of saddle points and their energies obtained in triaxial RHB calculations. The neutron numbers of the nuclei in which superdeformed minimum with $\beta_2 \approx 0.5$ is lower than normal-deformed or spherical ones are marked by an asterisk. With exception of these nuclei, the values in parentheses show either the deformation of superdeformed minimum or the deformation of the saddle of outer fission barrier or the height of outer fission barrier. Note that these values are shown only when the lowest height of the outer fission barrier obtained in the TRHB and RHB+OCT calculations is higher than 2 MeV. The column 3 shows the $\Delta E^{gain} = E^B_{ax} - E^B_{triax}$ quantity which is the decrease of the height of respective fission barrier due to triaxiality

Table 7.1

(continued)

| | | Axial RHB | | | Triaxial RHB | | | |
|---|---|---|---|---|---|---|---|---|
| $Z$ | $N$ | $\beta_{min}$ | $\beta_{saddle}$ | $E^B_{ax}$ | $(\beta,\gamma)_{min}$ | $(\beta,\gamma)_{saddle}$ | $E^B_{triax}$ | $\Delta E^{gain}$ |
| 1 | 2 | 3 | 4 | 5 | 6 | 7 | 8 | 9 |
| 110 (Ds) | 172 | 0.15<br>(0.46) | 0.30<br>(0.70) | 3.97<br>(5.75) | 0.15, 0<br>(0.45, 0) | 0.30, 0.0<br>(0.74, 5.6) | 3.92<br>(3.24) | 0.05<br>(2.51) |
| | 182 | -0.14 | 0.26 | 3.92 | 0.139, 60 | 0.36, 35.6 | 2.54 | 1.38 |
| | 192 | 0.41 | 0.58 | 2.52 | 0.417,0 | 0.62, 5.8 | 2.52 | 0.0 |
| | 202 | 0.38 | 0.56 | 4.56 | 0.385,0 | 0.73, 14.4 | 2.90 | 1.66 |
| | 212 | 0.26 | 0.51 | 5.95 | 0.262,0 | 0.54, 15.7 | 4.28 | 1.67 |
| | 222 | 0.24 | 0.54 | 7.02 | 0.243,0 | 0.36, 28.5 | 5.90 | 1.12 |
| | 232 | 0.22 | 0.60 | 6.27 | 0.220,0 | 0.61, 7.0 | 4.51 | 1.76 |
| | 242 | 0.14<br>(0.47) | 0.27<br>(0.66) | 3.92<br>(5.06) | 0.17, 0<br>(0.46, 0) | 0.27, 0<br>(0.68, 6.0) | 3.92<br>(2.51) | 0.0<br>(2.55) |
| | 252 | 0.44 | 0.70 | 4.79 | 0.444,0 | 0.72, 11.6 | 2.27 | 2.52 |
| 114 (Fl) | 162 | 0.23<br>(0.52) | 0.40<br>(0.66) | 5.95<br>(6.00) | 0.23, 0<br>(0.54, 0) | 0.40, 0<br>(0.57, 5.1) | 5.95<br>(3.85) | 0.0<br>(2.15) |
| | 172 | 0.15<br>(0.50) | 0.32<br>(0.73) | 5.22<br>(4.76) | 0.15, 0<br>(0.51, 0) | 0.32,0<br>(0.73, 6.0) | 5.22<br>(3.33) | 0.0<br>(1.43) |
| | 182 | -0.14 | 0.26 | 4.26 | 0.14, 60 | 0.41, 38.5 | 2.72 | 1.54 |
| | 192 | -0.38 | 0.15 | 3.79 | 0.40, 42 | 0.42, 33.4 | 1.35 | 2.44 |
| | 202 | 0.38 | 0.54 | 2.79 | 0.38, 0 | 0.54, 3.7 | 2.71 | 0.08 |
| | 212 | 0.27 | 0.49 | 4.27 | 0.28, 0 | 0.40, 23.1 | 3.31 | 0.96 |
| | 222 | 0.24 | 0.41 | 5.56 | 0.24, 0 | 0.36, 26.3 | 4.95 | 0.61 |
| | 232 | 0.21 | 0.35 | 4.68 | 0.21, 0 | 0.35, 0 | 4.68 | 0.0 |
| | 242 | 0.14 | 0.27 | 3.73 | 0.142,0 | 0.27,0 | 3.73 | 0.0 |
| | 252* | 0.458 | 0.72 | 3.31 | 0.459,0 | 0.63, 8.0 | 2.27 | 1.04 |
| | | (0.0) | (0.23) | (4.68) | (0.0, 0) | (0.46, 23.9) | (1.40) | (3.28) |
| 118 (Og) | 172 | 0.0 | 0.34 | 5.11 | 0.000,0 | 0.49, 28.2 | 4.47 | 0.64 |
| | 182* | 0.57<br>(-0.27) | 0.84<br>(0.26) | 4.02<br>(5.32) | 0.58,0<br>(0.27, 60) | 0.66, 9.5<br>(0.42, 36.4) | 2.41<br>(3.57) | 1.61<br>(1.75) |
| | 192 | -0.39 | 0.15 | 5.79 | 0.40, 74 | 0.33, 43.3 | 2.37 | 3.42 |
| | 202 | -0.43 | 0.07 | 6.24 | 0.43, 60 | 0.46, 45.0 | 1.31 | 4.93 |
| | 212 | 0.29 | 0.44 | 3.03 | 0.30, 11 | 0.64, 21.3 | 2.45 | 0.58 |
| | 222 | 0.24 | 0.39 | 5.19 | 0.24, 0 | 0.37, 27.2 | 4.18 | 1.01 |
| | 232 | 0.22 | 0.35 | 4.89 | 0.22, 0 | 0.35, 0 | 4.56 | 0.33 |
| | 242 | -0.20 | 0.31 | 3.70 | 0.21, 60.0 | 0.47, 32.4 | 2.88 | 0.82 |
| | 252 | -0.19 | 0.19 | 5.06 | 0.20, 60 | 0.41, 38.5 | 2.98 | 2.08 |
| | 262 | -0.23 | 0.15 | 4.95 | 0.24, 59.9 | 0.32, 41.6 | 0.80 | 4.15 |
| | 272 | -0.49 | -0.01 | 5.98 | 0.49, 59.6 | 0.48, 51.7 | 0.44 | 5.54 |

Unfortunately, even nowadays fully systematic triaxial RHB calculations are extremely computationally demanding. Thus, in order to get at least rough outline of the impact of low fission barriers on potential topology of nuclear landscape, we have performed triaxial RHB calculations for selected nuclei with $Z = 106, 110, 114$ and 118 and with $N = 152 + \Delta N$, where $\Delta N = 0, 10, 20, ...$ and only the nuclei between two-proton and two-neutron drip lines are considered here. Note that in some nuclei there are two fission barriers. If the outer fission barrier is lower than 2 MeV in axial RHB calculations, it is ignored and the TRHB calculations are focused on the inner fission barrier. If the outer fission barrier is higher than 2 MeV, then we first perform TRHB calculations in order to see whether triaxiality lowers outer fission barrier below 2 MeV. If that is no a case, we carry out RHB-OCT calculations in order to see whether octupole deformation lowers outer fission barrier below 2 MeV. The results of such calculations, which provide information on the highest fission barrier in the nuclei under consideration, are summarized in Table 7.1. Together with the results of the TRHB calculations presented in Refs. [57, 60] for superheavy $Z = 122$ and hyperheavy $Z = 126, 130$ and 134 nuclei they allow in an approximate way to delineate the impact of fission on the boundaries of nuclear landscape[2] in Sec. 7.4 below.

Note that these are first ever triaxial calculations for fission barriers in neutron-rich ($N > 200$) superheavy nuclei and as such they can be very useful for understanding the role of the fission in the r-process calculations. The fission of heavy systems affects this process via fission recycling

[2]The boundaries of nuclear landscape in heavy nuclei with ellipsoidal shapes in the ground states are defined by spontaneous fission and not by the particle emission as in lower $Z$ nuclei (see Ref. [57] and the discussion in Sec. 7.4). This fact has been ignored in many studies of nuclear landscape in neutron-rich actinides and superheavy nuclei (such as Refs. [2, 37]) since the boundaries of nuclear landscape were defined via two-neutron and two-proton separation energies. The reasons for such a choice are obvious: such calculations require only binding energies of the ground states which are relatively easy to compute. On the contrary, the calculations of fission barriers in triaxial DFT codes are by approximately three orders of magnitude more numerically time-consuming.

[198, 199]. However, so far the fission barriers for such nuclei were calculated only in theoretical frameworks restricted to axial symmetry [151, 152, 200].

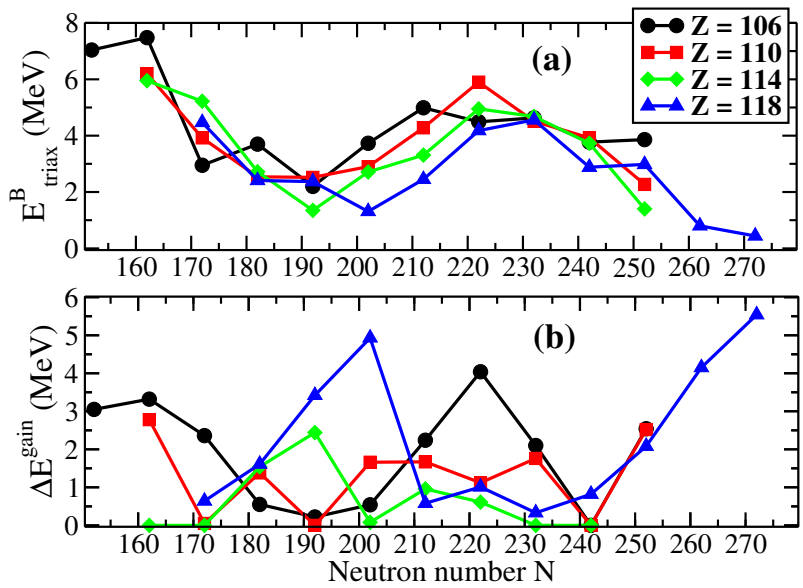


Figure 7.4

Inner fission barrier heights $E^B_{triax}$ (panel (a)) and its decrease due to triaxiality $\Delta E^{gain}$ (panel (b)) as a function of neutron number $N$.

The results for inner fission barrier heights $E^B_{triax}$ and the decrease of the height of inner fission barrier due to triaxiality $\Delta E^{gain}$, presented in Table 7.1, are summarized in Fig. 7.4. The $E^B_{triax}$ values show oscillatory behavior as a function of neutron number $N$ with maxima seen at $N \approx 162$ and $N \approx 222$ (at $N = 172$ and 232 in the $Z = 118$ nuclei) and minima at $N = 192$ and $N \approx 252$ (at $N = 202$ and 272 in the $Z = 118$ nuclei). More erratic behavior is seen for the $\Delta E^{gain}$ values; note that the triaxiality has no effect on the heights of inner fission barriers for $\Delta E^{gain} = 0$ MeV. In some nuclei the triaxiality lowers inner fission barrier by more than 4 MeV. These features seen in

$E^B_{triax}$ and $\Delta E^{gain}$ curves are the consequences of underlying shell structure and its evolution with proton and neutron numbers (see discussion in Ref. [158]). A general trend of the lowering of the height of inner fission barrier with the increase of proton number is clearly seen in Table 7.1 and Fig. 7.4a.

Table 7.1 clearly indicates three regions of instability based on the fission barrier heights; in these regions the height of the highest fission barrier is below 2 MeV. These are two islands of instability centered around ($Z \approx 114$, $N \approx 192$) and ($Z \approx 118$, $N \approx 202$) which are shown in Fig. 7.5b. In addition, very neutron rich nuclei near and above $N = 252$ in the $Z = 114$ isotopic chain as well as near and above $N = 262$ in the $Z = 118$ isotopic chain are unstable with respect of fission. Such instability against fission is also seen in very neutron rich hyperheavy nuclei (see supplemental material to Ref. [57]). These factors together lead to a substantial reduction of the region of potentially stable elliposoidal-like nuclei in the $N \geq 258$ region (compare panels (a) and (b) in Fig. 7.5 below).

## 7.4 Extension of nuclear landscape to hyperheavy nuclei

One of the important goals of our studies is the extension of nuclear landscape to the limits of extreme $Z$ values. There are numerous studies of the limits of nuclear landscape at the neutron and proton drip lines for the $Z < 120$ nuclei carried out in different theoretical frameworks (see Refs. [2, 37, 38, 115, 201, 202] and, in particular, the compilation presented in Sec. VIII of Ref. [2]). The studies of Refs. [2, 37, 38] also define systematic theoretical uncertainties in the position of two-proton and two-neutron drip lines. On the contrary, nothing was known about the nuclear landscape in hyperheavy nuclei and its limits before our previous publication in Ref. [57]. The

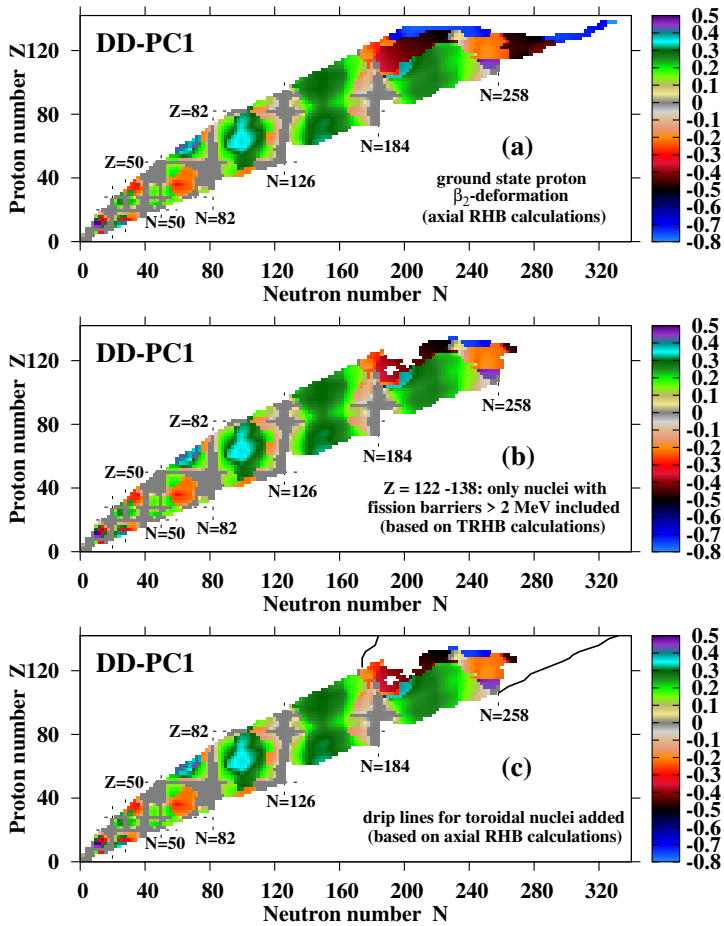


Figure 7.5

The distribution of nuclear shapes in the nuclear landscape.

(a) Proton quadrupole deformations $\beta_2$ of the lowest in energy minima for axial symmetry (LEMAS) obtained in axial RHB calculations with the DD-PC1 functional. Based on the results presented in Fig. 17c of Ref. [2] and Fig. 3 of Ref. [57], only the nuclei whose LEMAS have ellipsoidal-like shapes are included here; those who have toroidal shapes in LEMAS (see Fig. 3 in Ref. [57]) are neglected. The colormap in the $\beta_2 = -0.4 - 0.5$ range is equivalent to the one of Fig. 17c of Ref. [2] for consistency with previous results. (b) The same as panel (a) but with the nuclei, in which neither inner nor outer (if exist) fission barrier(s) have the height(s) higher than 2 MeV, excluded. Here the results of the calculations for fission barriers presented in Table 1 of supplemental material to Ref. [57] and in Table 7.1 of the present manuscript are used for approximate delineation of the boundaries of the region of nuclear chart in which fission barriers satisfy above mentioned condition. (c) The same as panel (b) but with two-proton and two-neutron drip lines (shown by solid lines), defined from separation energies, for toroidal nuclei added. They are based on the results of axial RHB calculations with $N_F = 26$.

goal of this section is to present a comprehensive summary on the structure and limits of nuclear landscape with special emphasis on the region of hyperheavy nuclei.

The results of Refs. [32, 57] clearly show that critical distinction between the parts of nuclear chart are related to the dominance of two different types of shapes: ellipsoidal-like and toroidal ones. Note that concave disk shapes, appearing at large oblate deformation, belong to ellipsoidal-like shapes. Fig. 7.5a shows the region of nuclear chart which is dominated by ellipsoidal-like shapes. Note that for $Z < 120$ LEMAS obtained in reflection-symmetric RHB calculations typically correspond to the ground states since only few nuclei in their ground states are affected by $\gamma$-deformation (see Ref. [203] for the results obtained in microscopic+macroscopic method) and octupole deformation shows up in the ground states of the nuclei in few localized regions [55, 56, 203].

The situation changes in the $Z > 120$ nuclei which are typically soft with respect of triaxial deformation up to the point that many ground states possess triaxial deformation (see Table 1 in supplemental material of Ref. [57] and Table 7.1 in this chapter). This softness also leads to a substantial reduction of the heights of the fission barriers in many nuclei. If the barrier height is less than 2 MeV, the nucleus is typically considered unstable against fission (see discussion in Ref. [59]). If we take this fact into account, the region of nuclear chart with ellipsoidal-like shapes will be considerably reduced at high-$Z$ values; this is illustrated in Fig. 7.5b. Note that in some nuclei eliminated on transition from panel (a) to panel (b) the local minima (which are otherwise excited ones) with toroidal shapes could become the lowest in energy solutions if ellipsoidal-like shapes are unstable with respect of fission. Finally, two-proton and two-neutron drip lines for toroidal shapes are added in Fig. 7.5c.

While there is the coexistence of ellipsoidal-like and toroidal shapes in the $Z = 120 - 140$ part of nuclear chart (see Fig. 7.5 above and Fig. 3 in Ref. [57]), with increasing proton number beyond $Z = 140$, the LEMAS always have toroidal shapes (see discussion in Ref. [57] and in Sec. III. of Ref. [32]). The nuclear chart extended up to $Z = 180$ displays the two-proton and two-neutron drip lines for toroidal nuclei outlining the potential limits of nuclear landscape (Fig. 7.6).

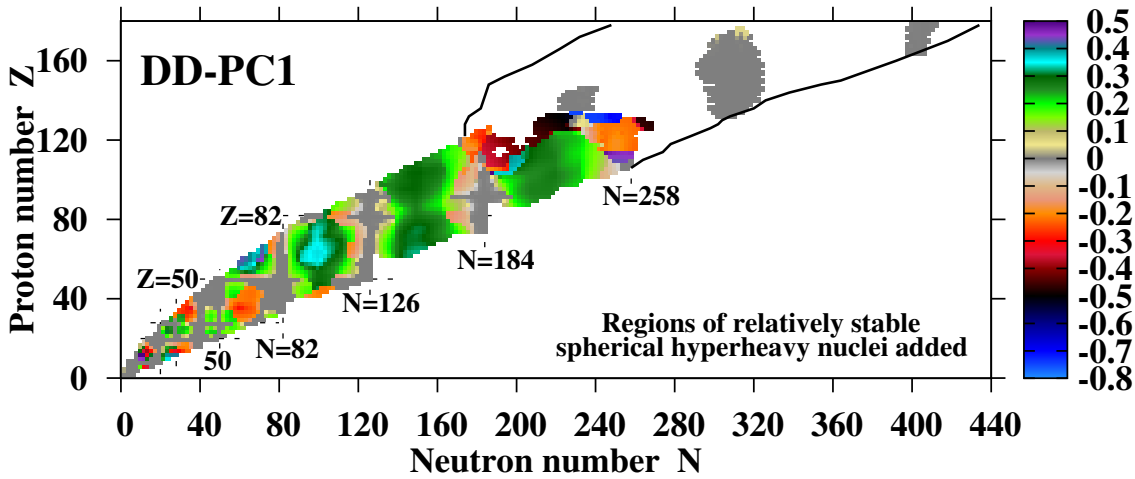


Figure 7.6

The same as Fig. 7.5 but with extended proton and neutron ranges and added regions of relatively stable spherical hyperheavy nuclei shown in gray.

Note that in the same nucleus two-neutron drip lines for spherical and toroidal shapes are different. This is a reason why some regions of stability of spherical nuclei extend beyond two-neutron drip line for toroidal shapes.

It is clear that nuclear landscape shown in Fig. 7.6 is not complete because it does not take into account the potential instabilities of toroidal shapes with respect of different types of distortions. Although it was shown in Ref. [57] that some toroidal nuclei are potentially stable with respect of triaxial distortions, this was illustrated only for two nuclei. The underlying mechanism of their

stability is discussed in Sec. 7.2. The problem is that with increasing proton number the extreme sizes of fermionic basis (up to $N_F = 30$ for nuclei at $Z = 156$ and beyond, see discussion in Sec. III of Ref. [32]) are required for the description of toroidal nuclei. Neither triaxial nor axial reflection asymmetric calculations are possible nowadays for such sizes of basises.

The investigations of Ref. [175] suggest that toroidal shapes are expected to be unstable with respect of the so-called sausage deformations which make a torus thicker in one section(s) and thinner in another section(s). They are expected to lead to multifragmentation[3]. However, these investigations are performed in the liquid drop model which neglects potential stabilizing role of the shell effects. In addition, they do not extend beyond the region of superheavy nuclei. It is expected that all of the nuclei located between neutron and proton drip lines in $Z \approx 130 - 180$ region will be stable with respect to breathing deformations [205]. The question of their stability with regard to sausage deformations is much more complicated due to numerical difficulties. In spite of this, the analysis of theoretical and experimental studies on toroidal liquid droplets as well as the results on the stability of the $^{354}134$ and $^{348}138$ nuclei (see Sec. 7.2) with respect to even-multipole sausage deformations suggests that fat toroidal nuclei located in the $Z \approx 136$, $N \approx 210$ region are potentially more stable with respect to sausage deformations than thin toroidal nuclei located outside this region [205]. Nonetheless, further fully quantum mechanical calculations based on DFT will be required to determine the stability of certain toroidal nuclei, this is because quantum shell effects can counterbalance instabilities in with respect of sausage deformations. If the toroidal shapes are unstable, then the spherical shapes become the ground states in the islands

[3]There are also some experimental indications of the role of multifragmentation in toroidal nuclei, but they are restricted to a single $^{86}\mathrm{Kr} + ^{93}\mathrm{Nb}$ reaction [204].

of potential stability of spherical hyperheavy nuclei (see Ref. [57]). These islands centered around ($Z \approx 138, N \approx 230$), ($Z \approx 156, N \approx 310$) and ($Z \approx 174, N \approx 410$) are shown in Fig. 7.6.

The analysis of Figs. 7.5 and 7.6 clearly indicates that the classical structure of the nuclear landscape in which spherical shell closures at different particle numbers play a defining role disappears in the $Z > 120$ nuclei. This is because the ground states are either oblate or toroidal in axial RHB calculations.

The extrapolation to unknown regions is definitely associated with theoretical uncertainties [36] which are especially large for the position of two-neutron drip line [2, 37, 38, 45, 46] and fission barriers [60, 206]. In the CDFT framework, systematic theoretical uncertainties due to the form of the CEDF are substantially larger than statistical errors [83]. So far, such systematic uncertainties have been estimated only for fission barriers in the regions of potentially stable spherical hyperheavy nuclei and for the sizes of these regions (see Fig. 6 in Ref. [57]). Their more global evaluation is extremely time consuming and at this stage, when we try to understand the general features of hyperheavy nuclei, is not necessary. These uncertainties will definitely affect the stability of ellipsoidal shapes with respect of fission and, as a consequence, the boundary of the transition from ellipsoidal to toroidal shapes and the two-proton and two-neutron drip lines for toroidal nuclei. However, they will not affect the general features.

## 7.5 Concluding remarks

In conclusion, the detailed investigation of the properties of hyperheavy nuclei has been performed in the framework of covariant density functional theory. The following conclusions have been obtained:

- The shape evolution of toroidal shapes along the fission path and the stability of such shapes with respect of fission have been studied. In considered cases, the analysis shows the transition from symmetrical toroid (at the local minimum) to the asymmetric one (at the saddle point). This transition cost the energy which is a physical reason for the formation of fission barrier and, thus, for the stability of such shapes.
- The topology of potential energy surfaces for ellipsoidal shapes of the super- and hyperheavy nuclei has been compared. In both types of the nuclei the PES has the form of the canyon in which some local valleys and hills are located. The canyon is quite narrow in superheavy nuclei which prevents the formation of local minima at large oblate deformation and limits the role of triaxial deformation. On the contrary, this canyon is much wider in hyperheavy nuclei with a mountain, centered at $\beta_2 \approx 0$, formed in it. This leads to the formation of local minima at oblate superdeformation, increased role of triaxiality and higher instability of hyperheavy nuclei against fission as compared with superheavy ones.
- The extension of nuclear landscape to hyperheavy nuclei with proton numbers up to $Z = 180$ has been performed. With increasing proton number beyond $Z \approx 130$ the transition from ellipsoidal-like nuclear shapes to toroidal shapes takes place in axial RHB calculations. The ellipsoidal ground states are affected by above-mentioned increased instability against fission. Many hyperheavy nuclei with toroidal shapes (as the lowest in energy solutions in axial RHB calculations) are expected to be unstable towards multi-fragmentation. However, it is difficult to quantify their stability or instability since the description of toroidal shapes requires the basis which is typically significantly larger than the one employed for the description of ellipsoidal-like shapes. This makes the calculations with octupole or triaxial deformation included impossible for toroidal shapes with extreme $\beta_2$ values. Nevertheless, three islands of stability of spherical hyperheavy nuclei are predicted. The nuclei in these islands will become the ground states in the case of instability of relevant toroidal states.

Detailed investigation of possible mechanisms of the creation of spherical and toroidal hyperheavy nuclei represents an interesting topic but goes beyond the scope of the present study. The nuclei in the ($Z \approx 138, N \approx 230$), ($Z \approx 156, N \approx 310$) and ($Z \approx 174, N \approx 410$) islands of stability of spherical hyperheavy nuclei have neutron to proton ratios of $N/Z \approx 1.67$, $N/Z \approx 1.99$ and $N/Z \approx 2.36$, respectively. Thus, they cannot be formed in laboratory conditions and the only possible environment in which they can be produced is the ejecta of the mergers of neutron stars [138]. In a similar fashion, the regions of neutron stars with nuclear pasta phases [207, 208, 209] may be a breading ground for the formation of toroidal nuclei in the ejecta of the merger of neutron

stars. The two-proton drip line for toroidal nuclei is characterized by neutron to proton ratio of $N/Z \approx 1.25$. Thus, the stability and/or multi-fragmentation of toroidal nuclei located in the vicinity of two-proton drip line could possibly be studied in nucleus-nucleus collisions of stable nuclei or the nuclei located close to the beta-stability line. This is similar to what has already been done in the $^{86}$Kr + $^{93}$Nb reaction at incident energies ranging from 35 to 95 MeV/nucleon in Ref. [204].

# CHAPTER VIII

# CONCLUSIONS AND OUTLOOKS

## 8.1 Conclusions

Covariant density functional theory (CDFT) was employed for several investigations in this dissertation. The following are the summaries and main conclusions of these studies:

- The statistical errors and their propagation to the limits of nuclear landscape in ground-state observables and single-particle properties of spherical even-even nuclei have been analyzed in chapter III. The calculations were performed in the spherical RHB framework for the NL-ME class of the functionals. It was shown that statistical errors for binding energies and neutron skins drastically increase on approaching the two-neutron drip line. In contrast, such a trend does not exist for statistical errors in charge radii and two-neutron separation energies. It has also been demonstrated that statistical errors in the energies of the single-particle states, their relative energies, and spin-orbit splittings are small. This study revealed that within the CDFT framework the statistical errors for physical observables of interest are substantially smaller than systematic uncertainties. It also demonstrated that they are smaller than those in non-relativistic Skyrme DFT.

- The parametric correlations in CEDFs have been investigated in chapter IV. It was concluded that parametric correlations exist in all major classes of CEDFs when the functionals are fitted to the ground state properties of finite nuclei and to nuclear matter properties. It was also demonstrated that by removing parametric correlations, the number of independent parameters in the functionals may be reduced to 5 or 6 depending on the structure and underlying functional. The elimination of parametric correlations has the obvious benefit of reducing the dimension of the parameter hyperspace, which leads to a reduction of theoretical statistical errors.

- A new approach for optimizing CEDFs is discussed in chapter V. The CEDFs resulting from this new technique are characterized by an improved description of nuclear masses. For instance, CEDFs DD-MEX1 and DD-MEY2 describe nuclear masses at the same level of accuracy as the UNEDF functionals of non-relativistic DFT. In addition, this study raises the question of whether the CEDFs fitting protocols should include data of the nuclear matter properties and neutron skins. Additionally, it raises the question of whether isospin-dependent pairing is important for simultaneous description of masses, nuclear matter properties, and charge radii.

- The ground state and fission properties of even-even actinides and superheavy nuclei with $Z = 90 - 120$ from the two-proton up to two-neutron drip lines with proper assessment of systematic theoretical uncertainties were systematically investigated in chapter VI. These results provide essential theoretical input for the r-process modeling in heavy nuclei and, in particular, for the study of fission cycling. Four state-of-the-art globally tested CEDFs, namely, DD-PC1, DD-ME2, NL3*, and PC-PK1, representing the major classes of the CDFT models were employed in this study. All these nuclei have had their ground state deformations, binding energies, two neutron separation energies, $\alpha$-decay $Q_\alpha$ values and half-lives, and fission barrier heights evaluated. Theoretical systematic uncertainties in these physical observables have been quantified, and their evolution as a function of proton and neutron numbers has been identified. The structure of single-particle (particularly high-$j$) states in the vicinity of spherical shell closures at $Z = 120$, $N = 184$, and $N = 258$, as well as nuclear matter properties of employed CEDFs, were shown to be two main factors contributing to theoretical uncertainties. The impact of octupole deformation on the outer fission barriers and the impact of the triaxiality on the inner fission barriers have been analyzed in the axial-asymmetric RHB and triaxial RHB frameworks respectively.

- The extension of the nuclear landscape to hyperheavy nuclei was investigated in chapter VII. With increasing proton number beyond $Z \approx 130$ the transition from ellipsoidal-like nuclear shapes to toroidal shapes takes place in the axial RHB calculations. This transition is crucial for potential expansion of the nuclear landscape to hyperheavy nuclei. Many hyperheavy nuclei with toroidal shapes (as the lowest in energy solutions in axial RHB calculations) are expected to be unstable toward multifragmentation. Nevertheless, three islands of stability of spherical hyperheavy nuclei are anticipated. These nuclei are relatively stable against both octupole and triaxial distortions. The nuclei in these islands will become the ground states in the case of instability of relevant toroidal states. Toroidal nuclei in the region near $Z \approx 134$ are expected to be relatively stable. The transition from the symmetrical toroid (at the local minimum) to the asymmetric one (at the saddle point) cost the energy which is a physical reason for the formation of fission barrier and, thus, for the stability of these nuclei.

## 8.2 Outlooks

Nuclear DFT is a very good starting point when looking into physical phenomena that can be investigated experimentally with facilities like the Facility for Rare Isotope Beams (FRIB). In addition, FRIB will provide new data which will be helpful in improving nuclear DFT models. For these reasons, this framework provides inspiration for further research. Listed below are some examples of ongoing or future research that can be accomplished within CDFT framework.

- Studying the global consequences of removing parametric correlations: A new set of functionals is obtained by fitting the CEDFs while taking into account the parametric correlations. On a global scale, the removal of these parametric correlations has little effect on the performance of CEDFs.

- Rotation in the proton-rich nuclei: This study is performed in the framework of cranking relativistic mean-field (CRMF) theory. It was shown that with increasing angular momentum some of the unbound configurations at spin-zero become bound at higher spins [210]. This allows extending the nuclear landscape beyond the spin-zero limits. The physical mechanism behind the development of extreme proton halos generated by rotation in light very proton-rich nuclei was also explored. The development of a proton halo in rotating proton-rich nuclei is based either on a significant excess of protons over neutrons or on the occupation of intruder strongly mixed orbitals. A follow-up study with extra in-depth analysis is now being prepared.

- Investigation of the ground state and fission properties of odd-mass and odd-odd nuclei: The calculations of the ground state properties and fission barriers of these nuclei require time reverse symmetry breaking, which involves blocking one-quasiparticle states. The Equal Filling Approximation (EFA) method, which is an alternative to the numerically unstable standard blocking procedure, is currently being implemented and tested in RHB codes.

- Gathering of nuclear input of even-even, odd-mass, and odd-odd nuclei and performing real r-process simulations.

- Investigation of the ground state and fission properties of the nuclei relevant for r-process in the models which go beyond the mean-field approximation, such as the five-dimensional collective Hamiltonian.

- Improving the performance of the covariant energy density functionals and reducing the related theoretical uncertainties. With FRIB's ability to study and provide information on very neutron-rich nuclei, the isovector dependence of the functionals can be better defined.

REFERENCES


[1] P. Ring. Energy density functional theory in nuclei: does it have to be relativistic? *Phys. Scr. T*, 150:014035, 2012.

[2] S. E. Agbemava, A. V. Afanasjev, D. Ray, and P. Ring. Global performance of covariant energy density functionals: Ground state observables of even-even nuclei and the estimate of theoretical uncertainties. *Phys. Rev. C*, 89:054320, 2014.

[3] Bruce R. Barrett, Petr Navrátil, and James P. Vary. Ab initio no core shell model. *Progress in Particle and Nuclear Physics*, 69(1):131–181, March 2013.

[4] E. Caurier, G. Martinez-Pinedo, F. Nowacki, A. Poves, and A.P. Zuker. The shell model as a unified view of nuclear structure. *Reviews of Modern Physics*, 77, April 2005.

[5] M. Bender, P.-H. Heenen, and P.-G. Reinhard. Self-consistent mean-field models for nuclear structure. *Rev. Mod. Phys.*, 75:121, 2003.

[6] P. Ring and P. Schuck. The Nuclear Many-Body Problem *(Springer-Verlag, Berlin)*, 1980.

[7] Extended density functionals in nuclear structure physics. *Extended Density Functionals in Nuclear Structure Physics,* Lecture Notes in Physics, edited by G. A. Lalazissis, P. Ring, and D. Vretenar (Springer-Verlag, Heidelberg, 2004), Vol. 641, 2004.

[8] D. Vretenar, A. V. Afanasjev, G. A. Lalazissis, and P. Ring. Relativistic hartree-bogoliubov theory: Static and dynamic aspects of exotic nuclear structure. *Phys. Rep.*, 409:101, 2005.

[9] T. Nikšić, D. Vretenar, and P. Ring. Relativistic nuclear energy density functionals: Mean-field and beyond. *Prog. Part. Nucl. Phys.*, 66:519, 2011.

[10] P. Hohenberg and W. Kohn. Inhomogeneous electron gas. *Phys. Rev.*, 136:B864, Nov 1964.

[11] W. Kohn and L. J. Sham. Self-consistent equations including exchange and correlation effects. *Phys. Rev.*, 140:A1133, 1965.

[12] W. Kohn. Nobel lecture: Electronic structure of matter - wave functions and density functionals. *Rev. Mod. Phys.*, 71:1253–1266, 1999.

[13] B. D. Serot and J. D. Walecka. Recent progress in quantum hadrodynamics. *Int. J. Mod. Phys.*, E6, 1997.

[14] B. G. Carlsson, J. Dobaczewski, and M. Kortelainen. Local nuclear energy density functional at next-to-next-to-next-to-leading order. *Phys. Rev. C*, 78:044326, 2008.

[15] S. Fayans. Towards a universal nuclear density functional. *JETP Lett.*, 68:169–174, 1998.

[16] M. Baldo, P. Schuck, and X. Viñas. Kohn-sham density functional inspired approach to nuclear binding. *Phys. Lett. B*, 663(5):390 – 394, 2008.

[17] J. E. Drut, R. J. Furnstahl, and L. Platter. Toward ab initio density functional theory for nuclei. *Prog. Part. Nucl. Phys.*, 64(1):120, 2010.

[18] X. Roca-Maza, X. Viñas, M. Centelles, P. Ring, and P. Schuck. Relativistic mean-field interaction with density-dependent meson-nucleon vertices based on microscopical calculations. *Phys. Rev. C*, 84:054309, 2011.

[19] T. Nikšić, D. Vretenar, and P. Ring. Relativistic nuclear energy density functionals: adjusting parameters to binding energies. *Phys. Rev. C*, 78:034318, 2008.

[20] G.A. Lalazissis, P. Ring, and D. Vretenar. *Extended Density Functionals in Nuclear Structure Physics*. Lecture Notes in Physics. Springer Berlin Heidelberg, 2004.

[21] E. V. Litvinova and A. V. Afanasjev. Dynamics of nuclear single-particle structure in covariant theory of particle-vibration coupling: From light to superheavy nuclei. *Phys. Rev. C*, 84:014305, 2011.

[22] T. D. Cohen, R. J. Furnstahl, and K. Griegel. Quark and gluon condensates in nuclear matter. *Phys. Rev. C*, 45:1881, 1992.

[23] W. Koepf and P. Ring. A relativistic description of rotating nuclei: the yrast line of $^{20}$ne. *Nucl. Phys. A*, 493:61, 1989.

[24] A. V. Afanasjev and H. Abusara. Time-odd mean fields in covariant density functional theory: nonrotating systems. *Phys. Rev. C*, 81:014309, 2010.

[25] U. Hofmann and P. Ring. A new method to calculate magnetic moments of relativistic mean field theories. *Phys. Lett. B*, 214:307, 1988.

[26] A. V. Afanasjev and P. Ring. Time-odd mean fields in the rotating frame: Microscopic nature of nuclear magnetism. *Phys. Rev. C*, 62:031302(R), 2000.

[27] A. V. Afanasjev and H. Abusara. Time-odd mean fields in covariant density functional theory: Rotating systems. *Phys. Rev. C*, 82:034329, 2010.

[28] G. A. Lalazissis, S. Karatzikos, R. Fossion, D. Peña Arteaga, A. V. Afanasjev, and P. Ring. The effective force nl3 revisited. *Phys. Lett.*, B671:36, 2009.

[29] G. A. Lalazissis, T. Nikšić, D. Vretenar, and P. Ring. New relativistic mean-field interaction with density-dependent meson-nucleon couplings. *Phys. Rev. C*, 71:024312, 2005.

[30] P. W. Zhao, Z. P. Li, J. M. Yao, and J. Meng. New parametrization for the nuclear covariant energy density functional with a point-coupling interaction. *Phys. Rev. C*, 82:054319, 2010.

[31] S. Typel and H.H̃. Wolter. *Nucl. Phys.*, A656:331, 1999.

[32] S. E. Agbemava, A. V. Afanasjev, A. Taninah, and A. Gyawali. Extension of the nuclear landscape to hyperheavy nuclei. *Phys. Rev. C*, 99:034316, Mar 2019.

[33] J. Boguta and R. Bodmer. *Nucl. Phys.*, A292:413, 1977.

[34] Y.K̃. Gambhir, P. Ring, and A. Thimet. *Ann. Phys. (N.Y.)*, 198:132, 1990.

[35] P. G. Reinhard and W. Nazarewicz. Information content of a new observable: The case of the nuclear neutron skin. *Phys. Rev. C*, 81:051303(R), 2010.

[36] J. Dobaczewski, W. Nazarewicz, and P.-G. Reinhard. Error estimates of theoretical models: a guide. *J. Phys. G*, 41:074001, 2014.

[37] J. Erler, N. Birge, M. Kortelainen, W. Nazarewicz, E. Olsen, A. M. Perhac, and M. Stoitsov. The limits of the nuclear landscape. *Nature*, 486:509, 2012.

[38] A. V. Afanasjev, S. E. Agbemava, D. Ray, and P. Ring. Nuclear landscape in covariant density functional theory. *Phys. Lett. B*, 726:680, 2013.

[39] Y. Gao, J. Dobaczewski, M. Kortelainen, J. Toivanen, and D. Tarpanov. Propagation of uncertainties in the skyrme energy-density-functional model. *Phys. Rev. C*, 87:034324, 2013.

[40] J. D. McDonnell, N. Schunck, D. Higdon, J. Sarich, S. M. Wild, and W. Nazarewicz. Uncertainty quantification for nuclear density functional theory and information content of new measurements. *Phys. Rev. Lett.*, 114:122501, 2015.

[41] D. Martin, A. Arcones, W. Nazarewicz, and E. Olsen. Impact of nuclear mass uncertainties on the *r* process. *Phys. Rev. Lett.*, 116:121101, 2016.

[42] M. R. Mumpower, R. Surman, G. C. McLaughlin, and A. Aprahamian. The impact of individual nuclear properties on r-process nucleosynthesis. *Prog. Part. Nucl. Phys.*, 86:86 – 126, 2016.

[43] A. E. Lovell, F. M. Nunes, J. Sarich, and S. M. Wild. Uncertainty quantification for optical model parameters. *Phys. Rev. C*, 95:024611, Feb 2017.

[44] S. Brandt. *Data analysis. Statistical and Computational Methods for Scientists and Engineers.* Springer International Publishing, Switzerland, 2014.

[45] A. V. Afanasjev, S. E. Agbemava, D. Ray, and P. Ring. Neutron drip line: Single-particle degrees of freedom and pairing properties as sources of theoretical uncertainties. *Phys. Rev. C*, 91:014324, 2015.

[46] A. V. Afanasjev and S. E. Agbemava. Covariant energy density functionals: Nuclear matter constraints and global ground state properties. *Phys. Rev. C*, 93:054310, 2016.

[47] P. Ring. Relativistic mean field theory in finite nuclei. *Prog. Part. Nucl. Phys.*, 37, 1996.

[48] H. Kucharek and P. Ring. Relativistic field theory of superfluidity in nuclei. *Z. Phys. A*, 339(1):23–35, March 1991.

[49] A. V. Afanasjev, P. Ring, and J. König. Cranked relativistic hartree-bogoliubov theory: formalism and application to the superdeformed bands in the $a \sim 190$ region. *Nucl. Phys.*, A676:196, 2000.

[50] S. Karatzikos, A. V. Afanasjev, G. A. Lalazissis, and P. Ring. The fission barriers in actinides and superheavy nuclei in covariant density functional theory. *Phys. Lett. B*, 689:72, 2010.

[51] Y. Tian, Z. Y. Ma, and P. Ring. A finite range pairing force for density functional theory in superfluid nuclei. *Phys. Lett. B*, 676:44, 2009.

[52] J. F. Berger, M. Girod, and D. Gogny. *Comp. Phys. Comm.*, 63:365, 1991.

[53] A. V. Afanasjev and O. Abdurazakov. Pairing and rotational properties of actinides and superheavy nuclei in covariant density functional theory. *Phys. Rev. C*, 88:014320, 2013.

[54] J. Dobaczewski, A. V. Afanasjev, M. Bender, L. M. Robledo, and Yue Shi. Properties of nuclei in the nobelium region studied within the covariant, skyrme, and gogny energy density functionals. *Nucl. Phys. A*, 944:388 – 414, 2015.

[55] S. E. Agbemava, A. V. Afanasjev, and P. Ring. Octupole deformation in the ground states of even-even nuclei: a global analysis within the covariant density functional theory. *Phys. Rev. C*, 93:044304, 2016.

[56] S. E. Agbemava and A. V. Afanasjev. Octupole deformation in the ground states of even-even $z \sim 96, n \sim 196$ actinides and superheavy nuclei. *Phys. Rev. C*, 96:024301, Aug 2017.

[57] A. V. Afanasjev, S. E. Agbemava, and A. Gyawali. Hyperheavy nuclei: Existence and stability. *Phys. Lett. B*, 782:533, 2018.

[58] S. E. Agbemava, A. V. Afanasjev, T. Nakatsukasa, and P. Ring. Covariant density functional theory: Reexamining the structure of superheavy nuclei. *Phys. Rev. C*, 92:054310, 2015.

[59] H. Abusara, A. V. Afanasjev, and P. Ring. Fission barriers in covariant density functional theory: extrapolation to superheavy nuclei. *Phys. Rev. C*, 85:024314, 2012.

[60] S. E. Agbemava, A. V. Afanasjev, D. Ray, and P. Ring. Assessing theoretical uncertainties in fission barriers of superheavy nuclei. *Phys. Rev. C*, 95:054324, May 2017.

[61] P. Bonche, H. Flocard, and P.H̃. Heenen. Solution of the skyrme hf+bcs equation on a 3d mesh. *Comp. Phys. Comm.*, 171:49, 2005.

[62] A. V. Afanasjev and S. Shawaqfeh. Deformed one-quasiparticle states in covariant density functional theory. *Phys. Lett. B*, 706:177, 2011.

[63] T. Niksic, N. Paar, P.-G. Reinhard, and D. Vretenar. Optimizing relativistic energy density functionals: covariance analysis. *J. Phys. G*, 42:034008, 2015.

[64] T. Haverinen and M. Kortelainen. Uncertainty propagation within the unedf models. *J. Phys. G*, 44:044008, 2017.

[65] T.J. Bürvenich, D.G. Madland, and P.-G. Reinhard. Adjustment studies in self-consistent relativistic mean-field models. *Nucl. Phys. A*, 744:92 – 107, 2004.

[66] I. Debes and J. Dudek. Narrowing the confidence intervals in nuclear structure predictions through elimination of parametric correlations. *Acta Phys. Polonica*, B10:51, 2017.

[67] Raymond T. Birge. The calculation of errors by the method of least squares. *Phys. Rev.*, 40:207–227, Apr 1932.

[68] P.-G. Reinhard, M. Rufa, J. Maruhn, W. Greiner, and J. Friedrich. Nuclear ground state properties in a relativistic meson field model. *Z. Phys. A*, 323:13, 1986.

[69] G.Ã. Lalazissis, J. König, and P. Ring. *Phys. Rev. C*, 55:540, 1997.

[70] M. Rufa, P.-G. Reinhard, J. A. Maruhn, W. Greiner, and M. R. Strayer. Optimal parametrization for the relativistic mean-field model of the nucleus. *Phys. Rev. C*, 38:390–409, Jul 1988.

[71] M.M. Sharma, M.A. Nagarajan, and P. Ring. Rho meson coupling in the relativistic mean field theory and description of exotic nuclei. *Phys. Lett. B*, 312(4):377 – 381, 1993.

[72] M. Dutra, O. Lourenco, S. S. Avancini, B. V. Carlson, A. Delfino, D. P. Menezes, C. Providencia, S. Typel, and J. R. Stone. Relativistic mean-field hadronic models under nuclear matter constraints. *Phys. Rev. C*, 90:055203, 2014.

[73] A. Krasznahorkay, M. Fujiwara, P. van Aarle, H. Akimune, I. Daito, H. Fujimura, Y. Fujita, M. N. Harakeh, T. Inomata, J. Jänecke, S. Nakayama, A. Tamii, M. Tanaka, H. Toyokawa, W. Uijen, and M. Yosoi. Excitation of isovector spin-dipole resonances and neutron skin of nuclei. *Phys. Rev. Lett.*, 82:3216–3219, Apr 1999.

[74] K. Yako, H. Sagawa, and H. Sakai. Neutron skin thickness of $^{90}$Zr determined by charge exchange reactions. *Phys. Rev. C*, 74:051303, Nov 2006.

[75] C. M. Tarbert, D. P. Watts, D. I. Glazier, P. Aguar, J. Ahrens, J. R. M. Annand, H. J. Arends, R. Beck, V. Bekrenev, B. Boillat, A. Braghieri, D. Branford, W. J. Briscoe, J. Brudvik, S. Cherepnya, R. Codling, E. J. Downie, K. Foehl, P. Grabmayr, R. Gregor, E. Heid, D. Hornidge, O. Jahn, V. L. Kashevarov, A. Knezevic, R. Kondratiev, M. Korolija, M. Kotulla, D. Krambrich, B. Krusche, M. Lang, V. Lisin, K. Livingston, S. Lugert, I. J. D. MacGregor, D. M. Manley, M. Martinez, J. C. McGeorge, D. Mekterovic, V. Metag, B. M. K. Nefkens, A. Nikolaev, R. Novotny, R. O. Owens, P. Pedroni, A. Polonski, S. N. Prakhov, J. W. Price, G. Rosner, M. Rost, T. Rostomyan, S. Schadmand, S. Schumann, D. Sober, A. Starostin, I. Supek, A. Thomas, M. Unverzagt, Th. Walcher, L. Zana, and F. Zehr. Neutron skin of $^{208}$Pb from coherent pion photoproduction. *Phys. Rev. Lett.*, 112:242502, Jun 2014.

[76] P.-G. Reinhard. The relativistic mean-field description of nuclei and nuclear dynamics. *Rep. Prog. Phys.*, 52:439, 1989.

[77] M. Bender, K. Rutz, P.-G. Reinhard, J. A. Maruhn, and W. Greiner. Shell structure of superheavy nuclei in self-consistent mean-field models. *Phys. Rev. C*, 60:034304, 1999.

[78] M. Rashdan. Structure of exotic nuclei and superheavy elements in a relativistic shell model. *Phys. Rev. C*, 63:044303, Mar 2001.

[79] Wenhui Long, Jie Meng, Nguyen Van Giai, and Shan-Gui Zhou. New effective interactions in relativistic mean field theory with nonlinear terms and density-dependent meson-nucleon coupling. *Phys. Rev. C*, 69:034319, Mar 2004.

[80] Zhongzhou Ren and Hiroshi Toki. Superdeformation in the newly discovered superheavy elements. *Nucl. Phys. A*, 689(3â4):691 – 706, 2001.

[81] Y. Sugahara and H. Toki. Relativistic mean-field theory for unstable nuclei with non-linear sigma and omega terms. *Nucl. Phys. A*, 579:557 – 572, 1994.

[82] T. Nikšić, D. Vretenar, P. Finelli, and P. Ring. Relativistic hartree-bogoliubov model with density-dependent meson-nucleon couplings. *Phys. Rev. C*, 66:024306, Aug 2002.

[83] S. E. Agbemava, A. V. Afanasjev, and A. Taninah. Propagation of statistical uncertainties in covariant density functional theory: Ground state observables and single-particle properties. *Phys. Rev. C*, 99:014318, 2019.

[84] M. Kortelainen, J. Erler, W. Nazarewicz, N. Birge, Y. Gao, and E. Olsen. Neutron-skin uncertainties of skyrme energy density functionals. *Phys. Rev. C*, 88:031305(R), 2013.

[85] S. Goriely and R. Capote. Uncertainties of mass extrapolations in hartree-fock-bogoliubov mass models. *Phys. Rev. C*, 89:054318, May 2014.

[86] T. Nikšić, M. Imbrišak, and D. Vretenar. "sloppy" nuclear energy density functionals. ii. finite nuclei. *Phys. Rev. C*, 95:054304, May 2017.

[87] A. V. Afanasjev and E. Litvinova. Impact of collective vibrations on quasiparticle states of open-shell odd-mass nuclei and possible interference with the tensor force. *Phys. Rev. C*, 92:044317, 2015.

[88] A. V. Afanasjev. Addressing spectroscopic quality of covariant density functional theory. *J. Phys. G*, 42:034002, 2015.

[89] Tamara Nikšić and Dario Vretenar. "sloppy" nuclear energy density functionals: Effective model reduction. *Phys. Rev. C*, 94:024333, Aug 2016.

[90] S. Shen, H. Z. Liang, W. H. Long, J. Meng, and P. Ring. Towards an *ab initio* covariant density functional for nuclear structure. *Prog. Nucl. Part. Phys.*, 109:103713, 2019.

[91] A. Taninah, S. E. Agbemava, A. V. Afanasjev, and P. Ring. Parametric correlations in energy density functionals. *Phys. Lett. B*, 800:135065, 2020.

[92] R. Machleidt, K. Holinde, and C. Elster. The bonn meson-exchange model for the nucleon-nucleon interaction. *Phys. Rep.*, 149(1):1–89, 1987.

[93] S. Marcos, R. Niembro, M. López-Quelle, Nguyen Van Giai, and R. Malfliet. Parametrization of the relativistic Dirac-Brueckner G matrix. *Phys. Rev. C*, 39(3):1134–1141, 1989.

[94] L. Sehn and H.H. Wolter. Effective interactions and the equation of state in heavy ion collisions. *Nucl. Phys. A*, 519(1):289 – 302, 1990.

[95] R. Brockmann and H. Toki. Relativistic density-dependent hartree approach for finite nuclei. *Phys. Rev. Lett.*, 68:3408, 1992.

[96] S. Haddad and M. K. Weigel. Finite nuclear systems in a relativistic extended Thomas-Fermi approach with density-dependent coupling parameters. *Phys. Rev. C*, 48(6):2740–2745, 1993.

[97] R. Fritz and H. Müther. Nn correlations and relativistic hartree fock in finite nuclei. *Phys. Rev. C*, 49:633–644, 1994.

[98] Shihang Shen, Haozhao Liang, Wen Hui Long, Jie Meng, and Peter Ring. Towards an ab initio covariant density functional for nuclear structure. *arXiv [nucl-th]*, page 1904.04977, 2019.

[99] Bernard ter Haar and R. Malfliet. Nucleons, mesons and deltas in nuclear matter a relativistic dirac-brueckner approach. *Phys. Rep.*, 149(4):207 – 286, 1987.

[100] R. Brockmann and R. Machleidt. Relativistic nuclear structure. i. nuclear matter. *Phys. Rev. C*, 42:1965–1980, Nov 1990.

[101] M. Serra, T. Otsuka, Y. Akaishi, P. Ring, and S. Hirose. Relativisitic mean field models and nucleon-nucleon interactions. *Prog. Theor. Phys.*, 113:1009, 2005.

[102] W. H. Press, S. A. Teukolsky, W. T. Vetterling, and B. P. Flannery. *Numerical recipies in Fortran 77. The art of scientific computing*. 2d Edition, Cambridge University Press, Cambridge, 2007.

[103] M. Thies. New interpretation of the dirac approach to proton-nucleus scattering. *Phys. Lett. B*, 162:255 – 259, 1985.

[104] M. Thies. On the relation between relativistic and non-relativistic mean-field theories. *Phys. Lett. B*, 166(1):23 – 26, 1986.

[105] Josef König. *Superdeformation im Rahmen des Relativistischen Mean-Field Modells*. Phd thesis, Technical University of Munich (unpublished), 1996.

[106] Y. M. Engel, D. M. Brink, K. Geoke, S. J. Krieger, and D. Vauterin. Time-dependent hartree-fock theory with skyrme's interaction. *Nucl. Phys. A*, 249:215, 1975.

[107] J. Dobaczewski and J. Dudek. Time-odd components in the mean field of rotating superdeformed nuclei. *Phys. Rev. C*, 52:1827, 1995.

[108] Ning Wang, Min Liu, Xizhen Wu, and Jie Meng. Surface diffuseness correction in global mass formula. *Physics Letters B*, 734:215–219, 2014.

[109] P. Möller, A.J. Sierk, T. Ichikawa, and H. Sagawa. Nuclear ground-state masses and deformations: Frdm(2012). *Atomic Data and Nuclear Data Tables*, 109-110:1–204, 2016.

[110] Y. Aboussir, J.M. Pearson, A.K. Dutta, and F. Tondeur. Nuclear mass formula via an approximation to the hartree—fock method. *Atomic Data and Nuclear Data Tables*, 61(1):127–176, 1995.

[111] Haifei Zhang, Jianmin Dong, Nana Ma, G. Royer, Junqing Li, and Hongfei Zhang. An improved nuclear mass formula with a unified prescription for the shell and pairing corrections. *Nuclear Physics A*, 929:38–53, 2014.

[112] S. Goriely, N. Chamel, and J. M. Pearson. Skyrme-hartree-fock-bogoliubov nuclear mass formulas: crossing the 0.6 mev accuracy threshold with microscopically deduced pairing. *Phys. Rev. Lett.*, 102:152503, 2009.

[113] S. Goriely, N. Chamel, and J. M. Pearson. Hartree-fock-bogoliubov nuclear mass model with 0.50 mev accuracy based on standard forms of skyrme and pairing functionals. *Phys. Rev. C*, 88:061302, 2013.

[114] S. Goriely, S. Hilaire, M. Girod, and S. Péru. First gogny-hartree-fock-bogoliubov nuclear mass model. *Phys. Rev. Lett.*, 102:242501, 2009.

[115] J.-P. Delaroche, M. Girod, J. Libert, H. Goutte, S. Hilaire, S. Peru, N. Pillet, and G. F. Bertsch. Structure of even-even nuclei using a mapped collective hamiltonian and the d1s gogny interaction. *Phys. Rev. C*, 81:014303, 2010.

[116] M. Kortelainen, T. Lesinski, J. Moré, W. Nazarewicz, J. Sarich, N. Schunck, M. V. Stoitsov, and S. Wild. Nuclear energy density optimization. *Phys. Rev. C*, 82:024313, Aug 2010.

[117] M. Kortelainen, J. McDonnell, W. Nazarewicz, P.-G. Reinhard, J. Sarich, N. Schunck, M. V. Stoitsov, and S. M. Wild. Nuclear energy density optimization: Large deformations. *Phys. Rev. C*, 85:024304, 2012.

[118] M. Kortelainen, J. McDonnell, W. Nazarewicz, E. Olsen, P.-G. Reinhard, J. Sarich, N. Schunck, S. M. Wild, D. Davesne, J. Erler, and A. Pastore. Nuclear energy density optimization: Shell structure. *Phys. Rev. C*, 89:054314, May 2014.

[119] J. Meng, H. Toki, S. G. Zhou, S. Q. Zhang, W. H. Long, and L. S. Geng. Relativistic continuum hartree-bogoliubov theory for ground state properties of exotic nuclei. *Prog. Part. Nucl. Phys.*, 57:470–563, 2006.

[120] B.G̃. Todd-Rutel and J. Piekarewicz. Neutron-rich nuclei and neutron stars: a new accurately calibrated interaction for the study of neutron-rich matter. *Phys. Rev. Lett.*, 95:122501, 2005.

[121] B. K. Agrawal. Asymmetric nuclear matter and neutron skin in an extended relativistic mean-field model. *Phys. Rev. C*, 81:034323, 2010.

[122] P.-G. Reinhard and B. K. Agrawal. Energy systematics of heavy nuclei - mean field models in comparison. *Int. Jour. Mod. Phys.*, E20:1379, 2011.

[123] Q. S. Zhang, Z. M. Niu, Z. P. Li, J. M. Yao, and J. Meng. Global dynamical correlation energies in covariant density functional theory: cranking approximation. *Frontiers of Physics*, 9:529, 2014.

[124] M. Wang, G. Audi, A. H. Wapstra, F. G. Kondev, M. MacCormick, X. Xu, and B. Pfeiffer. *Chinese Physics*, C36:1603, 2012.

[125] K. Q. Lu, Z. X. Li, Z. P. Li, J. M. Yao, and J. Meng. Global study of beyond-mean-field correlation energies in covariant energy density functional theory using a collective hamiltonian method. *Phys. Rev. C*, 91:027304, 2015.

[126] Y. L. Yang, Y. K. Wang, P. W. Zhao, and Z. P. Li. Nuclear landscape in a mapped collective hamiltonian from covariant density functional theory. *Phys. Rev. C*, 104:054312, Nov 2021.

[127] Meng Wang, G. Audi, F. G. Kondev, W.J. Huang, S. Naimi, and Xing Xu. The AME2016 atomic mass evaluation (II). tables, graphs and references. *Chinese Physics C*, 41(3):030003, mar 2017.

[128] T. Nikšić, N. Paar, D. Vretenar, and P. Ring. Dirhb - a relativistic self-consistent mean-field framework for atomic nuclei. *Comp. Phys. Comm.*, 185(6):1808 – 1821, 2014.

[129] I. Angeli and K. P. Marinova. Table of experimental nuclear ground state charge radii: An update. *At. Data Nucl. Data Tables*, 99:69, 2013.

[130] S. Teeti and A. V. Afanasjev. Global study of separable pairing interaction in covariant density functional theory. *Phys. Rev. C*, 103:034310, Mar 2021.

[131] S. Baroni, F. Barranco, P. F. Bortignon, R. A. Broglia, G. Coló, and E. Vigezzi. Medium polarization isotopic effects on nuclear binding energies. *Phys. Rev. C*, 74:024305, 2006.

[132] P. Campbell, I.D. Moore, and M.R. Pearson. Laser spectroscopy for nuclear structure physics. *Prog. Part. Nucl. Phys.*, 86:127, 2016.

[133] Martínez-Pinedo. Selected topics in nuclear astrophysics. *Eur. Phys. J. Spec. Topics*, 156:123, 2008.

[134] V. Liccardo, M. Malheiro, M. S. Hussein, B. V. Carlson, and T. Frederico. Nuclear processes in astrophysics: recent progress. *Eur. Phys. J.*, A54:221, 2018.

[135] D. Kasen, B. Metzger, J. Barnes, E. Quataert, and E. Ramirez-Ruiz. Origin of the heavy elements in binary neutron-star mergers from a gravitational-wave event. *Nature*, 551:80, 2017.

[136] J. J. Cowan, C. Sneden, J. E. Lawler, A. Aprahamian, M. Wiescher, K. Langangke, G. Martínez-Pinedo, and F.-K. Thielemann. Making the heaviest elements in the universe: A review of the rapid neutron capture process. *arkhiv: 1901.014110v1 [astro-ph.HE], subm. to Rev. Mod. Phys.*

[137] F. K. Thielemann, M. Eichler, I. V. Panov, and B. Wehmeyer. Neutron star mergers and nucleosynthesis of heavy elements. *Ann. Rev. Nucl. Part. Sci.*, 67:253, 2017.

[138] B. P. Abbott et al. Gw170817: Observation of gravitational waves from a binary neutron star inspiral. *Phys. Rev. Lett.*, 119:161101, 2017.

[139] B. P. Abbott et al. Multi-messenger observations of a binary neutron star merger. *Astrophys. J. Lett.*, 848:L12.

[140] O. Just, A. Bauswein, R. Ardevol Pulpillo, S. Goriely, and H.-T. Janka. Comprehensive nucleosynthesis analysis for ejecta of compact binary mergers. *Mont. Not. R. Astr. Soc.*, 448(1):541, 2015.

[141] Yuichiro Sekiguchi, Kenta Kiuchi, Koutarou Kyutoku, and Masaru Shibata. Dynamical mass ejection from binary neutron star mergers: Radiation-hydrodynamics study in general relativity. *Phys. Rev. D*, 91:064059, 2015.

[142] Joel de Jesús Mendoza-Temis, Meng-Ru Wu, Karlheinz Langanke, Gabriel Martínez-Pinedo, Andreas Bauswein, and Hans-Thomas Janka. Nuclear robustness of the *r* process in neutron-star mergers. *Phys. Rev. C*, 92:055805, Nov 2015.

[143] G. Martínez-Pinedo, D. Mocelj, N.T. Zinner, A. Kelić, K. Langanke, I. Panov, B. Pfeiffer, T. Rauscher, K.-H. Schmidt, and F.-K. Thielemann. The role of fission in the r-process. *Prog. Part. Nucl. Phys.*, 59(1):199 – 205, 2007.

[144] S. Goriely. The fundamental role of fission during r-process nucleosynthesis in neutron star mergers. *Eur. Phys. J*, A51:22, 2015.

[145] S. Goriely, J.-L. Sida, J.-F. Lemaître, S. Panebianco, N. Dubray, S. Hilaire, A. Bauswein, and H.-T. Janka. New fission fragment distributions and $r$-process origin of the rare-earth elements. *Phys. Rev. Lett.*, 111:242502, Dec 2013.

[146] M. Eichler, A. Arcones, A. Kelic, O. Korobkin, K. Langanke, T. Marketin, G. Martinez-Pinedo, I. Panov, T. Rauscher, S. Rosswog, C. Winteler, N. T. Zinner, and F.-K. Thielemann. The role of fission in neutron star mergers and its impact on the r-process peaks. *Astrophys. J.*, 808(1):30, jul 2015.

[147] I. Petermann, K. Langanke, G. MartÃnez-Pinedo, I.V. Panov, P.-G. Reinhard, and F.-K. Thielemann. Have superheavy elements been produced in nature? *Eur. Phys. J. A*, 48(9), 2012.

[148] S. A. Giuliani, G. Martínez-Pinedo, L. M. Robledo, and M.-R. Wu. r-process calculations with a microsocpic description of the fission process. *Acta Phys. Polonica B*, 48:299, 2017.

[149] Samuel A. Giuliani, Gabriel Martínez-Pinedo, and Luis M. Robledo. Fission properties of superheavy nuclei for $r$-process calculations. *Phys. Rev. C*, 97:034323, Mar 2018.

[150] A. Mamdouh, J.M. Pearson, M. Rayet, and F. Tondeur. Large-scale fission-barrier calculations with the etfsi method. *Nucl. Phys. A*, 644(4):389 – 414, 1998.

[151] S. Goriely, M. Samyn, and J. M. Pearson. Further explorations of skyrme-hartree-fock-bogoliubov mass formulas. vii. simultaneous fits to masses and fission barriers. *Phys. Rev. C*, 75:064312, Jun 2007.

[152] J. Erler, K. Langanke, H. P. Loens, G. Martinez-Pinedo, and P.-G. Reinhard. Fission properties for $r-$process nuclei. *Phys. Rev. C*, 85:025802, 2012.

[153] P.-G. Reinhard. Nuclear density-functional theory and fission of super-heavy elements. *Eur. Phys. J*, 312(54):13, 2018.

[154] R. Rodríguez-Guzman, Y. M. Humadi, and L. M. Robledo. Microscopic description of fission in superheavy nuclei with the parametrization d1m* of the gogny energy density functional. *Eur. Phys. J.*, A56:43, 2020.

[155] R. Furnstahl, B. D. Serot, and H.-B. Tang. A chiral effective lagrangian for nuclei. *Nucl. Phys. A*, 615:441, 1997.

[156] Bharat Kumar, S.K. Singh, B.K. Agrawal, and S.K. Patra. New parameterization of the effective field theory motivated relativistic mean field model. *Nucl. Phys. A*, 966:197 – 207, 2017.

[157] E. Yüksel, T. Marketin, and N. Paar. Optimizing the relativistic energy density functional with nuclear ground state and collective excitation properties. *Phys. Rev. C*, 99:034318, 2019.

[158] H. Abusara, A. V. Afanasjev, and P. Ring. Fission barriers in actinides in covariant density functional theory: the role of triaxiality. *Phys. Rev. C*, 82:044303, 2010.

[159] V. Prassa, T. Nikšić, G. A. Lalazissis, and D. Vretenar. Relativistic energy density functional description of shape transitions in superheavy nuclei. *Phys. Rev. C*, 86:024317, 2012.

[160] Bing-Nan Lu, Jie Zhao, En-Guang Zhao, and Shan-Gui Zhou. Multidimensionally-constrained relativistic mean-field models and potential-energy surfaces of actinide nuclei. *Phys. Rev. C*, 89:014323, Jan 2014.

[161] B.-N. Lu, E.-G. Zhao, and S.-G. Zhou. Potential energy surfaces of actinide nuclei from a multidimensional constrained covariant density functional theory: Barrier heights and saddle point shapes. *Phys. Rev. C*, 85:011301, 2012.

[162] T. Bürvenich, M. Bender, J. A. Maruhn, and P.-G. Reinhard. Systematics of fission barriers in superheavy elements. *Phys. Rev. C*, 69:014307, 2004.

[163] A. Staszczak, A. Baran, J. Dobaczewski, and W. Nazarewicz. Microscopic description of complex nuclear decay: Multimodal fission. *Phys. Rev. C*, 80:014309, Jul 2009.

[164] P. Möller, A. J. Sierk, T. Ichikawa, A. Iwamoto, R. Bengtsson, H. Uhrenholt, and S. Åberg. Heavy-element fission barriers. *Phys. Rev. C*, 79:064304, Jun 2009.

[165] W. D. Myers and W. J. Świątecki. Thomas-fermi fission barriers. *Phys. Rev. C*, 60:014606, Jun 1999.

[166] M. Arnould and S. Goriely. Astronuclear physics: a tale of the atomic nuclei in the skies. *arXiv:2001.11228v1 [astro-ph.SR*, 2020.

[167] Z. Shi, A. V. Afanasjev, Z. P. Li, and J. Meng. Superheavy nuclei in a microscopic collective hamiltonian approach: The impact of beyond-mean-field correlations on ground state and fission properties. *Phys. Rev. C*, 99:064316, 2019.

[168] A. Taninah, S. E. Agbemava, and A. V. Afanasjev. Covariant density functional theory input for $r$-process simulations in actinides and superheavy nuclei: The ground state and fission properties. *Phys. Rev. C*, 102:054330, Nov 2020.

[169] *Evaluated Nuclear Structure Data File (ENSDF) located at the website (http://www.nndc.bnl.gov/ensdf/) of Brookhaven National Laboratory. ENSDF is based on the publications presented in Nuclear Data Sheets (NDS) which is a standard for evaluated nuclear data.*, 2015.

[170] Jr. V. E. Viola and G. T. Seaborg. *J. Inorg. Nucl. Chem.*, 28:741, 1966.

[171] A. Sobiczewski, Z. Patyk, and S. Äwiok. Deformed superheavy nuclei. *Physics Letters B*, 224(1):1 – 4, 1989.

[172] T. Dong and Z. Ren. New calculations of Î±-decay half-lives by the viola-seaborg formula. *Eur. Phys. J.*, A26:69 – 72, 2005.

[173] A.I. Budaca, R. Budaca, and I. Silisteanu. Extended systematics of alpha decay half lives for exotic superheavy nuclei. *Nuclear Physics A*, 951:60 – 74, 2016.

[174] G Royer. Alpha emission and spontaneous fission through quasi-molecular shapes. *Journal of Physics G: Nuclear and Particle Physics*, 26(8):1149, 2000.

[175] C. Y. Wong. Toroidal and spherical bubble nuclei. *Annals of Physics*, 77:279, 1973.

[176] J. Sadhukhan, J. Dobaczewski, W. Nazarewicz, J. A. Sheikh, and A. Baran. Pairing-induced speedup of nuclear spontaneous fission. *Phys. Rev. C*, 90:061304(R), 2014.

[177] J. Zhao, B.-N. Lu, T. Nikšić, D. Vretenar, and S.-G. Zhou. Multidimensionally-constrained relativistic mean-field study of spontaneous fission: Coupling between shape and pairing degrees of freedom. *Phys. Rev. C*, 93:044315, 2016.

[178] R.A. Gherghescu, J. Skalski, Z. Patyk, and A. Sobiczewski. Non-axial shapes in spontaneous fission of superheavy nuclei. *Nucl. Phys. A*, 651(3):237, 1999.

[179] Y. Ts. Oganessian and S. N. Dmitriev. Synthesis and study of properties of superheavy atoms. factory of superheavy elements. *Rus. Chem. Rev.*, 85(9):901, 2016.

[180] K. Dietrich and K. Pomorski. Stability of bubble nuclei through shell effects. *Phys. Rev. Lett.*, 80:37–40, 1998.

[181] J. Dechargé, J.-F. Berger, K. Dietrich, and M.S. Weiss. Superheavy and hyperheavy nuclei in the form of bubbles or semi-bubbles. *Phys. Lett. B*, 451(3â4):275 – 282, 1999.

[182] M. Bender, W. Nazarewicz, and P.-G. Reinhard. Shell stabilization of super- and hyperheavy nuclei without magic gaps. *Phys. Lett. B*, 515(1â2):42 – 48, 2001.

[183] V. Yu. Denisov. Magic numbers of ultraheavy nuclei. *Phys. At. Nuclei*, 68:1133, 2005.

[184] Y. K. Gambhir, A. Bhagwat, and M. Gupta. The highest limiting $z$ in the extended periodic table. *J. Phys. G*, 42(12):125105, 2015.

[185] M. Ismail, A. Y. Ellithi, A. Adel, and H. Anwer. On magic numbers for super- and ultraheavy systems and hypothetical spherical double-magic nuclei. *J. Phys. G*, 43:015101, 2016.

[186] J.F̃. Berger, L. Bitaud, J. Decharg'e, M. Girod, and K. Dietrich. Superheavy, hyperheavy and bubble nuclei. *Nucl. Phys. A*, 685:1c, 2001.

[187] M. Warda. Toroidal structure of super-heavy nuclei in the hfb theory. *Int. J. Mod. Phys. E*, 16:452, 2007.

[188] A. Staszczak and C. Y. Wong. Toroidal super-heavy nuclei in skyrme hartree-fock approach. *Acta Phys. Pol.*, 40:753, 2009.

[189] W. Brodziński and J. Skalski. Predictions for superheavy elements beyond $z = 126$. *Phys. Rev. C*, 88:044307, Oct 2013.

[190] Andrzej Staszczak and Cheuk-Yin Wong. A region of high-spin toroidal isomers. *Phys. Lett. B*, 738(Supplement C):401 – 404, 2014.

[191] T. Ichikawa, K. Matsuyanagi, J. A. Maruhn, and N. Itagaki. High-spin torus isomers and their precession motions. *Phys. Rev. C*, 90:034314, Sep 2014.

[192] A. Kosior, A. Staszczak, and C.-Y. Wong. Toroidal nuclear matter distributions of superheavy nuclei from constrained skyrmeâhfb calculations. *Acta Phys. Pol.*, 10:249, 2017.

[193] W. Nazarewicz, M. Bender, S. Cwiok, P. H. Heenen, A. T. Kruppa, P.-G. Reinhard, and T. Vertse. Theoretical description of superheavy elements. *Nucl. Phys. A*, 701:165c, 2002.

[194] A. Staszczak, Cheuk-Yin Wong, and A. Kosior. Toroidal high-spin isomers in the nucleus $^{304}120$. *Phys. Rev. C*, 95:054315, May 2017.

[195] A. V. Afanasjev, D. B. Fossan, G. J. Lane, and I. Ragnarsson. Termination of rotational bands: Disappearance of quantum many-body collectivity. *Phys. Rep.*, 322:1, 1999.

[196] M. Warda, J. L. Egido, L. M. Robledo, and K. Pomorski. Self-consistent calculations of fission barriers in the fm region. *Phys. Rev. C*, 66:014310, 2002.

[197] N. Schunck and L. M. Robledo. Microscopic theory of nuclear fission: A review. *Rep. Prog. Phys.*, 79:116301, 2016.

[198] M. Arnould, S. Goriely, and K. Takahashi. The r-process of stellar nucleosynthesis: Astrophysics and nuclear physics achievements and mysteries. *Phys. Rep.*, 450:97–213, 2007.

[199] G. Martínez-Pinedo, D. Mocelj, N. T. Zinner, A. Kelić, K. Langanke, I. Panov, B. Pfeiffer, T. Rauscher, K.-H. Schmidt, and F.-K. Thielemann. The role of fission in the r-process. *Prog. Part. Nucl. Phys.*, 59:199–205, 2007.

[200] Samuel A. Giuliani, Gabriel Martínez-Pinedo, and Luis M. Robledo. Fission properties of superheavy nuclei for $r$-process calculations. *Phys. Rev. C*, 97:034323, Mar 2018.

[201] P. Möller, J. R. Nix, W. D. Myers, and W. J. Swiatecki. Nuclear ground-state masses and deformations. *At. Data Nucl. Data Tables*, 59:185, 1995.

[202] J. Erler, C.J̃. Horowitz, W. Nazarewicz, M. Rafalski, and P.-G. Reinhard. *Phys. Rev. C*, 87:044320, 2013.

[203] P. Möller, R. Bengtsson, B.G. Carlsson, P. Olivius, T. Ichikawa, H. Sagawa, and A. Iwamoto. Axial and reflection asymmetry of the nuclear ground state. *At. Data and Nucl. Data Tables*, 94(5):758–780, 2008.

[204] N. T. B. Stone, O. Bjarki, E. E. Gualtieri, S. A. Hannuschke, R. Lacey, J. Lauret, W. J. Llope, D. J. Magestro, R. Pak, A. M. Vander Molen, G. D. Westfall, and J. Yee. Evidence for the decay of nuclear matter toroidal geometries in nucleus-nucleus collision. *Phys. Rev. Lett.*, 78:2084, 1997.

[205] S. E. Agbemava and A. V. Afanasjev. Hyperheavy spherical and toroidal nuclei: The role of shell structure. *Phys. Rev. C*, 103:034323, Mar 2021.

[206] P. Jachimowicz, M. Kowal, and J. Skalski. Adiabatic fission barriers in superheavy nuclei. *Phys. Rev. C*, 95:014303, Jan 2017.

[207] M. E. Caplan, A. S. Schneider, C. J. Horowitz, and D. K. Berry. Pasta nucleosynthesis: Molecular dynamics simulations of nuclear statistical equilibrium. *Phys. Rev. C*, 91:065802, Jun 2015.

[208] F. J. Fattoyev, C. J. Horowitz, and B. Schuetrumpf. Quantum nuclear pasta and nuclear symmetry energy. *Phys. Rev. C*, 95:055804, May 2017.

[209] Radosław A. Kycia, Sebastian Kubis, and Włodzimierz Wójcik. Topological analysis of nuclear pasta phases. *Phys. Rev. C*, 96:025803, Aug 2017.

[210] A. V. Afanasjev, S. E. Agbemava, and A. Taninah. Exploring nuclear exotica at the limits. *Acta Phys. Polonica B*, 13:347, 2020.

[211] J. Nelder and R. Mead. A simplex method for function minimization. *Comput. J.*, 7:308–313, 1965.

[212] John Burkardt. Nelder-mead minimization algorithm. `https://people.sc.fsu.edu/~jburkardt/f77_src/asa047/asa047.html`, 2008.

[213] `https://www.hpc.msstate.edu/computing/hpc.php`.

# APPENDIX A

# SIMPLEX-BASED MINIMIZATION

Simplex-based minimization based on the Nelder-Mead algorithm [211] is very useful in the context of looking at parametric correlations (see discussion in Sec. 4.3). An efficient minimization code based on this method was written by John Burkardt and it is available free at the online library ASA047 [212]. The code seeks the minimum value of a specified function of the N variables. The user provides in the input the function to be minimized, the number of variables, and the initial values (initial guess) of the variables. The code does a series of reflections, extensions, and contractions till the convergence to a local minimum is reached. A detailed description of the method is given in Ref. [102]. After the convergence, the code gives in the output the minimum value of the function, and the variables correspond to the minimum (the optimum variables).

This code has been merged into the spherical RHB code. It has been modified in such a way that the code is minimizing the normalized objective function $\chi^2$ defined in Eq. (3.1). The variables of the function are the parameters used in the fitting protocol or more precisely the factors $f_i$ defined in Eq. (3.7). A flow chart representing the procedure is shown in Fig. A.1

The increase in the number of variables results in a growth of the computational time of the minimization. Also, the evaluation of the function $\chi^2$ is computationally time-consuming. Note that all the calculations of the discussed studies in this dissertation were performed on the High-Performance Computing Collaboratory ($HPC^2$) [213] supercomputers at Mississippi State University. The $HPC^2$ supercomputers provide a large number of processors (up to 400 processors on the very recent cluster called "ORION") where one can run the calculations in parallel with the allocation time for each processor of up to 48 hours. The minimization of the NL-ME class of functionals with 6 parameters (variables) and experimental data of 12 nuclei in the fitting protocol is possible on one processor (using the sequential version of the spherical RHB code). The same

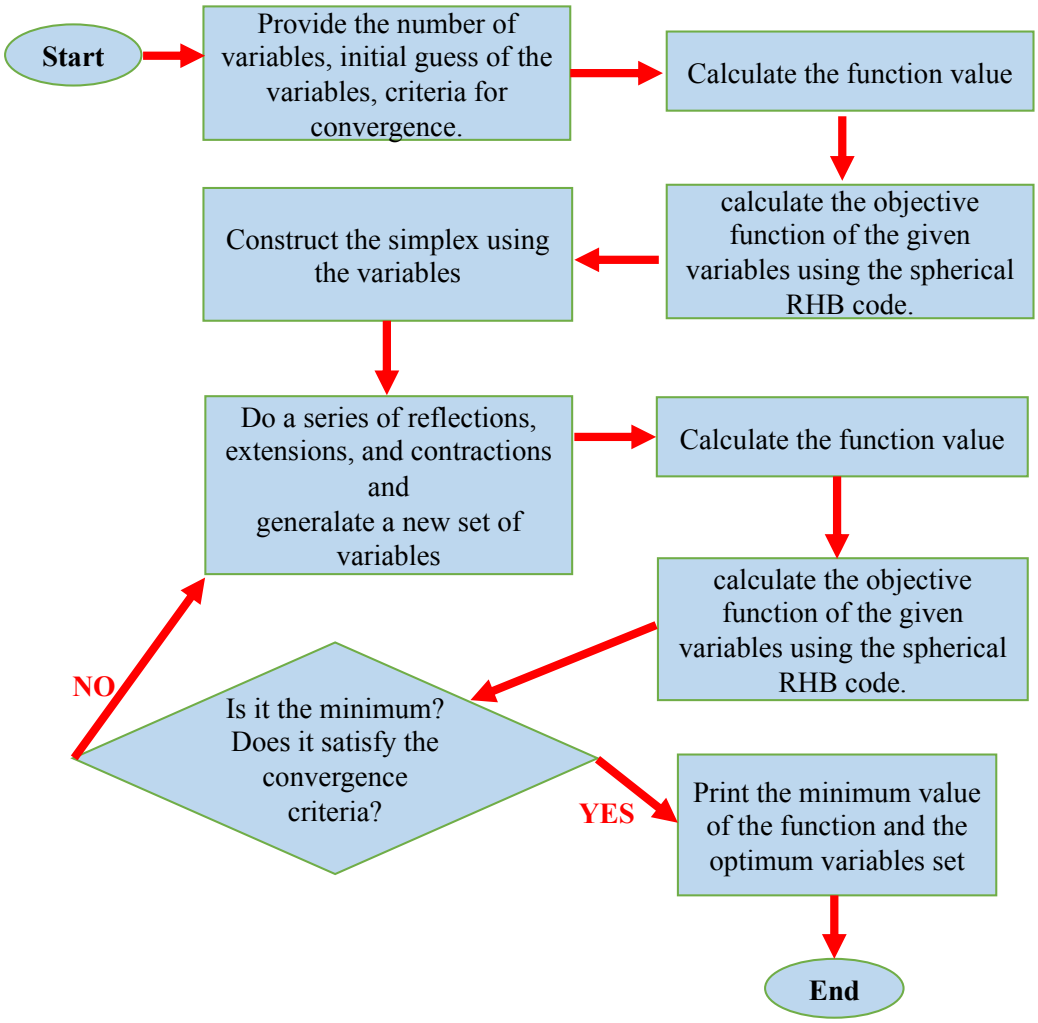


Figure A.1

A flow chart representing the simplex minimization procedure for the function $\chi^2$ defined in Eq. (3.1)

is true for the DD-ME class of functionals with 8 parameters (variables) and experimental data of the same nuclei in the fitting protocol. However, the increase in the number of variables from 6 to 8 results in raising the time needed for the minimization. On the other hand, the minimization of the PC class of functionals with 9 parameters (variables) and experimental data of 60 nuclei in the

fitting protocol on one processor of the computer is impossible within the limited computational time (48 hours) available at the HPC$^2$ supercomputers.

The use of Message Passing Interface (MPI) libraries to parallelize the spherical RHB code was the ideal way to speed up the procedure. The code was modified in such a way that the calculation of $\chi^2$ of each nucleus in the fitting protocol is performed on one processor of the computer. The contributions to the total $\chi^2$ from the individual nuclei are computed concurrently on the different processors by executing the computations with a number of processors equal to the number of nuclei used in the fitting protocol. After that, the total $\chi^2$ is computed by adding all of these contributions together. The parallel version of the code saves enormous amounts of computational time. These benefits apply to all classes of functionals. However, this efficiency is more pronounced in the PC class of functionals due to the large number of nuclei used in its fitting protocol. In the parallel version of the code, the calculation of the total $\chi^2$ for a given variation of the parameters is by factor $\approx 20$ faster than in the sequential version. Depending on the type of functional or more precisely based on the number of nuclei used in the fitting protocol, this number may vary. For the NL-ME and DD-ME classes, where 12 nuclei are used in the fitting protocol, the parallel version is by a factor of $\approx 10$ faster than the sequential version.

Figures A.2, A.3, A, A.5, and A.6 present several screenshots where important modifications took place in the sample calling program of the minimization code and in the spherical RHB code. The *italic* font will be used in the following discussion to denote the phrases and symbols used in the code. Furthermore, the discussion will be centered on the PC-PK1 functional model. It is, nevertheless, applicable to all functional classes. Starting from the sample calling program *main.f* (Fig. A.2), we specify a parameter *ifun* which identify for which functional we preform the

```
c       ifun = 1                    ! (set NL3* )
c       ifun = 2                    ! (set DDME2)
        ifun = 3                    ! (set PC-PK1)

      if (ifun .eq. 1) n = 6
      if (ifun .eq. 2) n = 8
      if (ifun .eq. 3) n = 9

c     initialize MPI
      call MPI_INIT (ierr)
c     Get this process's ID
      call MPI_Comm_rank (mpi_comm_world, my_id,ierr)
c     Get the number of processes
      call MPI_Comm_size (MPI_COMM_WORLD,num_procs,ierr)
```

Figure A.2

Screen shots from *main.f* subroutine (the main program) after the parallelization of the spherical RHB code and the merging of the minimization code

minimization. Based on the choice of the functional we need to define the number of variables $n$ (the number of parameters in the fitting protocol). The initialization of the parallelization should be written at the beginning of this subroutine since this subroutine serves as the main program. One should keep in mind that the total number of processors given in the job file and accessed by *call MPI_Comm_size* (*num_procs*) should be equal to the total number of the nuclei used in the fitting protocol of each class of functionals. For example, the minimization of the functional PC-PK1 from the PC class requires reserving 60 processors in the job file. After that, we need to define the initial guess of the variables *start(n)* (Fig. A.3). Considering that each parameter has a specific range in which the calculations do not diverge, one should choose the initial values of the parameters within their acceptable ranges. Manually choosing these initial parameters is, however,

```
if (ifun .eq. 3) then

   start(1) = 1.01383
   start(2) = 1.02164
   start(3) = 0.97668
   start(4) = 0.98465
   start(5) = 0.92559
   start(6) = 1.69228
   start(7) =-1.19235
   start(8) = 1.54528
   start(9) = 1.18468

   reqmin = 1.0E-06

   step(1) = 0.001
   step(2) = 0.001
   step(3) = 0.001
   step(4) = 0.001
   step(5) = 0.001
   step(6) = 0.001
   step(7) = 0.001
   step(8) = 0.001
   step(9) = 0.001
endif
```

Figure A.3

The same as A.2 but for different part of the *main.f* subroutine

inefficient. A random generator program could be used in which one specifies the possible ranges of parameters, and the program will generate the values randomly within these ranges. We also need to define the step size of the variables *step(n)* (Fig. A.3) as it is needed in the first *n* iterations to build the initial simplex. The choice of the *step(n)* is not critical to the minimization but one

should choose it very small to prevent the divergence in the first steps (building the simplex) before real minimization starts. The dimension of the arrays *start(n)* and *step(n)* varies depending on the number of the parameters (variables) in the fitting protocol of the functional. One also needs to define criteria for the convergence (*reqmin*) (Fig. A.3). The convergence to the local minima is reached when the difference between the successive iterations is less than *reqmin*.

```
konvge = 10
kcount = 50000

ynewlo = chi ( start )
call MPI_Barrier(MPI_Comm_world,ierr)


call nelmin ( chi, n, start, xmin, ynewlo, reqmin, step,
&  konvge, kcount, icount, numres, ifault )
call MPI_Barrier(MPI_Comm_world,ierr)



function chi ( x )

if (ipr_flag .eq. 0) call chi_square(x,chi2,.false.)
if (ipr_flag .eq. 1) call chi_square(x,chi2,.true.)
call MPI_Barrier(MPI_Comm_world,ierr)

chi = chi2

return
end
```

Figure A.4

The same as A.2 but for different part of the *main.f* subroutine

The maximum number of iterations *Kcount* should also be defined in the sample calling program. Besides, it is important to define the parameter *Konvge* which defines how frequently the convergence needs to be checked (see Fig. A). After defining these parameters one needs to calculate the function value. Considering that our function to be minimized is the penalty function $\chi^2$, we define a function in the main program named *chi(X)* which calculates the function value of a given variables set *X*. From this function we call the *chi-square.f* subroutine which calculates the $\chi^2$ of the given variables and returns the function value (Fig. A). After calculating the function value of the initial guess we call the subroutine *nelmin* which does the real minimization with all the details explained in Ref. [102] and returns the minimum value of the function with the optimum variables set. One should note that at each iteration of the minimization the subroutine *chi-square.f* will be called to evaluate the function value of the variables (parameters) variation.

Figure A.5 shows a few screenshots from *chi-square.f* subroutine. One of the main changes in this subroutine is the parallelization over the nuclei. In the sequential version of the code, we calculate the total $\chi^2$ by going over all the nuclei sequentially through a *"do"* loop. The calculation of $\chi^2$ of each nucleus is performed before moving to the next nucleus and the total $\chi^2$ is calculated by accumulating the $\chi^2$ of each nucleus. In the parallel version of the code we remove this *"do"* loop, we define a parameter *i_nuc* which takes values from 1 to the total number of nuclei. This could be done by relating it to the *my_id* of each processor (note that *my_id* takes the values 0, 1, 2, ..., *num_procs*-1). Each nucleus is assigned a specific *i_nuc* so its calculation is performed on a specific processor. The calculations of the different nuclei are performed simultaneously on different processors. For each nucleus, the calculation of the contributions to $\chi^2$ from the different observables (different data types in the fitting protocol) is performed. After that, the total $\chi^2$ of

```
        i_nuc = my_id + 1
c        do i_nuc=1,n_nuc_tot

         chi_dEx(i_nuc) =  ((E_exp(i_nuc) - etot)
*        /Ad_err_E)**2.0

      chi_drch1x(i_nuc) =   ((Rch_exp(i_nuc) - rc)/
*         Ad_err_rch)**2.0




if (i_fun.eq.3) then     ! PC-PK1
   chi_tot1(i_nuc) = chi_dEx(i_nuc) + chi_drch1x(i_nuc)
endif




  chii =chi_tot1(i_nuc)

  call MPI_Allreduce(chii, chisum, 1, MPI_REAL, MPI_SUM,
&      MPI_COMM_WORLD, ierr)
  call MPI_Barrier(MPI_Comm_world,ierr)

  chitotal = chisum
```

Figure A.5

The same as A.2 but for a *chi-square.f* subroutine

each nucleus is calculated by summing up these contributions from the different observables. Note that the screenshots of this calculation in Fig. A.5 are the portions of the subroutine specified for the functional PC-PK1 of the PC class of functionals. In this functional only data of binding energy and charge radius are used in the fitting protocol. For other classes of functionals, the contributions from the neutron skin and the nuclear matter properties are taken into account. Using

*call MPI_Allreduce*, the contributions to the total $\chi^2$ from different nuclei are combined to a single value called *chitotal*. This value is returned to the main program as the function value. The expression *call MPI_barrier* is written in many places in the subroutines to ensure that we do not move beyond the barrier until all processors finish their tasks. The fact that the variables we are using in the minimization are the factors defined as $f(p_k) = \frac{p_k}{p_k^{opt}}$ leads to a change in the *x_forces_new.f* subroutine. Each parameter used in the fitting protocol should be equal to the original value of the parameter multiplied by the variation of the variable which is transferred to this subroutine as a *factor* (see Fig. A.6). There are no changes in the rest of the subroutines and the calculations are done self-consistently.

```
c================================================
      if (parname.eq.'PC-PK1') then

c----  quadratic term                    ! MeV^-2
         alfs   =  -3.96291d-4*factor(1)
         alfv   =  +2.69040d-4*factor(2)
         alfts  =  0.d0
         alftv  =  +2.95018d-5*factor(3)
c
c----- to cubic term                     ! MeV^-5
         bets   =  +8.66530d-11*factor(4)
c
c----- quartic term                      ! MeV^-8
         gams   =  -3.80724d-17*factor(5)
         gamv   =  -3.64219d-18 *factor(6)
c
c----- derivative terms                  ! MeV^-4
         dels   =  -1.09108d-10*factor(7)
         delv   =  -4.32619d-10*factor(8)
         delts =   0.d0
         deltv =  -4.11112d-10*factor(9)
```

Figure A.6

The same as A.2 but from *x-forces-new.f* subroutine

The simplex method is known to be prone to stack in the local minima in the region close to the initial parameters (this drawback is a benefit in the context of looking at parametric correlations, see the discussion in Sec. 4.3). The minimization was performed in two stages. In the first stage, hundreds of the minimization trials were performed with randomly initial variables (parameters). In the second stage, the simplex minimization was applied several times with initial variables (parameters) equals to those corresponding to the local minima. In this way, one can confirm that the minimization converges to the real local minima. Besides, one can define the global minimum as the lowest minimum among the local minima (see the discussion in the following paragraphs for using the simulated annealing method as another confirmation of the global minimum).

It is worth to note that the simulated annealing method was used to confirm the global minimum we got from the numerous applications of the simplex method. In brief, the method is working as follows (see Ref. [102] for detailed description). At each iteration of the simulated annealing minimization, a new point is randomly generated. The distance of the new point from the current point as well as the range of the search are controlled by a probability distribution with a scale proportional to the temperature. All new points that lower the function value are accepted. In addition, the points which increase the function value will be accepted with a certain probability. This probability is decreasing with the decrease of temperature. By accepting those points which increase the function value, the method avoids being trapped in local minima, and it will be able to explore globally for more possible solutions. As the minimization proceeds, the temperature will systematically decrease based on a specific schedule. As the temperature decreases, the extent of the search is reduced and the convergence to the global minimum is eventually achieved.

The use of this method in the minimization of the penalty function defined in Eq. (3.1) for the different classes of functionals with the possible ranges of the variables (parameters) (see figures 4.1,4.2) has some problems. This method requires a huge number of iterations in order to converge to the global minimum. This number is increasing with the increase of the number as well as the range of variables (parameters). Considering the computational time needed for the evaluation of $\chi^2$ (the function value), it is impossible to perform all of these iterations within the limited computational time available at the HPC$^2$ supercomputers even with the parallel version of the code discussed above. In addition, the possibility of the divergence during the minimization is quite high since the variables are randomly generated in the full parameters hyperspace. Moreover, this method is not helpful in looking at the parametric correlations since it will always converge (if so) to the global minimum (see the discussion in Sec. 4.3 which explains why the simplex method is the best in this regard). In order to confirm that the global minimum we got from the numerous applications of the simplex method is the real one, the simulated annealing method was used with the following trick to avoid these problems. It was applied several times at different regions in the parameters hyperspace. The ranges of the variables (parameters) were picked very small but containing the local minima we got from the simplex method in different regions. The global minima we got in all classes of the functionals were consistent in the two methods.

# APPENDIX B

# IMPROVING THE CONVERGENCE OF THE CALCULATIONS BY READING FROM THE CONVERGED FIELDS

The calculation of the potential energy surfaces (PES) in the ($\beta_2$,$\beta_3$) and ($\beta_2$,$\gamma$) deformation planes was one of the most challenging aspects of the research presented in this dissertation. The PES in these planes are essential for investigating the fission paths and fission barriers. Consequently, the study of the impact of the triaxial deformation on the inner fission barriers, and the impact of the octupole deformation on the outer fission barriers. With such calculations, one can study how stable nuclei are against such deformations.

To get a clear picture of the fission path and fission barrier in the ($\beta_2$,$\gamma$) plane one needs at least 180 deformation points. The situation in the ($\beta_2$,$\beta_3$) plane is even more complicated and one could need more than 350 deformation points to study the impact of octupole deformation on the outer fission barrier. The fact that these calculations are performed using the Message Passing Interface (MPI) version of the code is very useful and very efficient. The calculations of the different deformation points are performed simultaneously on the different processors of the HPC$^2$ supercomputers. This would save months of computational time as compared to perform the calculations sequentially on one processor. However, there are still some challenges in getting converged solutions. This is due to the limited allocation time (48 hours) of running the calculations on each processor of the HPC$^2$ supercomputers clusters, the impossibility of getting converged solutions by starting the calculations from Wood-Saxon potential, or both.

Our typical solution for deformation points with non-converged solutions is to repeat their calculations starting from the fields of the nearest grid points in deformation space that have converged solutions. This approach has shown to be quite effective, and after a few rounds of calculations, converged solutions for all of the desired deformation points may be obtained. It's

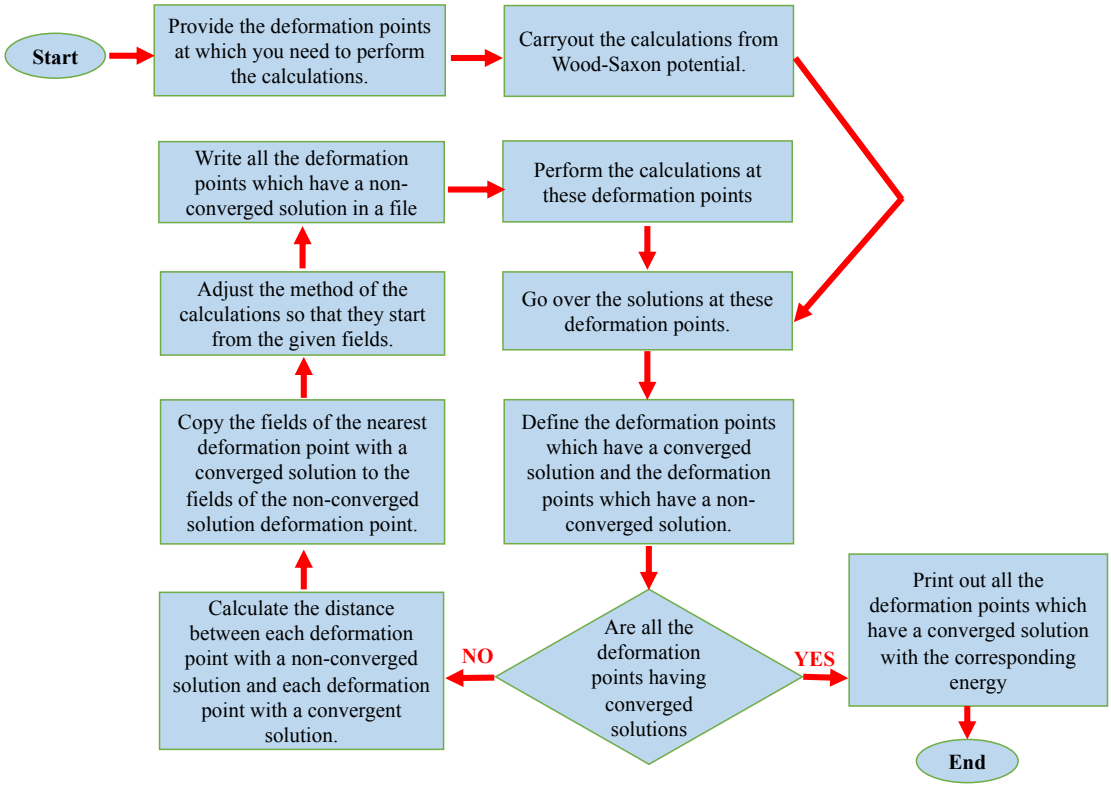


Figure B.1

A flow chart represents the strategy of performing the calculations the ($\beta_2$,$\beta_3$) and ($\beta_2$,$\gamma$) deformation planes.

also worth noting that performing this procedure manually would take a long time because it entails a number of steps, which are depicted in Fig. B.1 as a chart flow and detailed below:

- One needs to define the deformation points which have a converged solution and the deformation points which have a non-converged solution.
- One needs to calculate the distance in the grid (deformation space) between the deformation points which have a converged solution and each deformation point having a non-converged solution
- For each deformation point with a non-converged solution, one needs to copy the fields of the closest deformation point which has a converged solution to the fields of this deformation point which has a non-converged solution.

- One needs to repeat the calculations for the deformation points which have a non-converged solution by starting from the fields of those closest deformation points which have a converged solution.

In order to reduce the amount of manual work, a simple code in Fortran was added to the existing file that was analyzing the results of the calculation. The new commands in the file execute the first three items listed above automatically and in a very short time. The efficiency of this method in improving the convergence of the calculations is shown in Fig. B.2 for the reflection-symmetric triaxial RHB (TRHB) calculations. This method was also implemented and showed great efficiency in the reflection-asymmetric (octupole deformed) axial RHB (RA-RHB) calculations.

TRHB calculations in the ($\beta_2$,$\gamma$) plane require huge computational time even with fermionic bases including up to $N_F = 18$ fermionic shells. By performing the calculations starting from Wood-Saxon potential, one never get converged solutions for all the desired deformation points within the 48 hours allocation time of the HPC$^2$ supercomputers nodes (see Fig. B.2a, b). Performing the calculations for the deformation points with non-converged solutions from the fields of closest deformation points with converged solutions results in many new deformation points with converged solutions (see Fig. B.2c). Repeating the process a few more times results in getting converged solutions of almost all the desired deformation points (see Fig. B.2d, e). Figure B.2f) shows the potential energy surfaces obtained from the deformation points which have a converged solution. The global minimum and the saddle point of the fission barrier are represented by an open circle and red square, respectively.

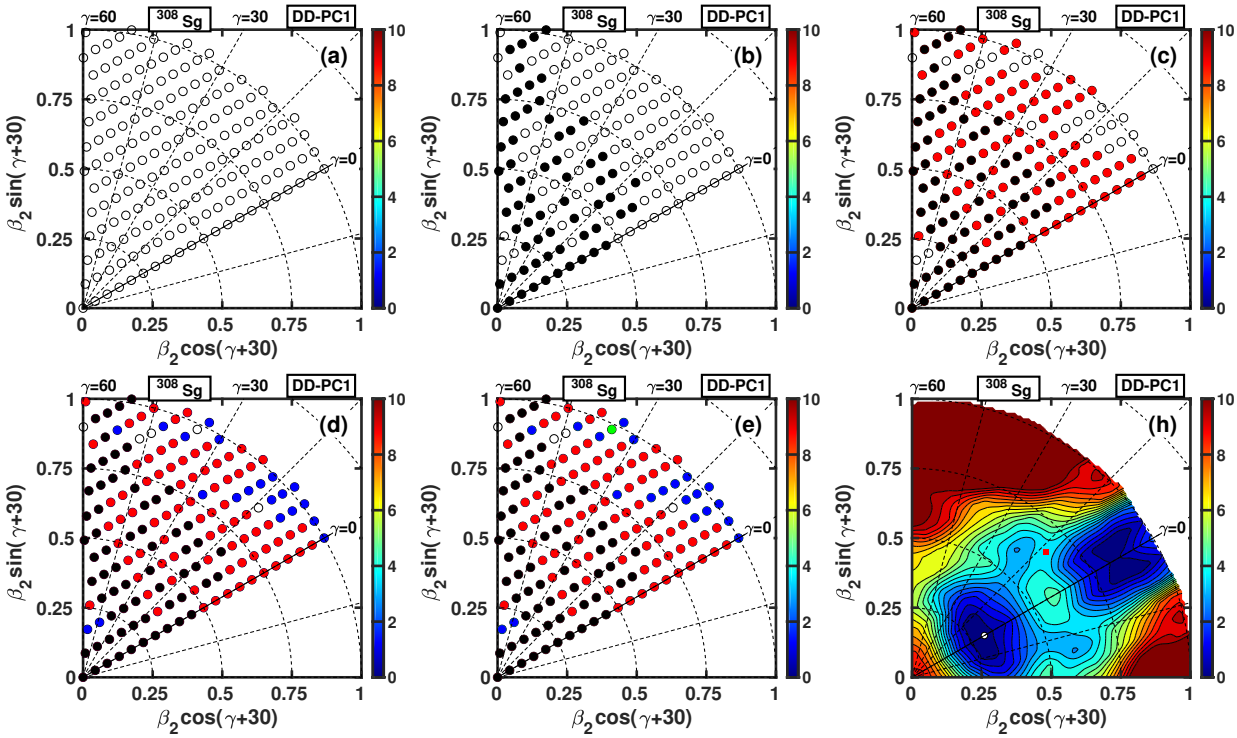


Figure B.2

The distribution of the deformation points in the ($\beta_2$,$\gamma$) plane obtained in the reflection-symmetric triaxial RHB framework calculations with the DD-PC1 functional for the nucleus $^{308}$Sg.

The open circles in panel (a) represent all the desired deformation points needs to be calculated. Solid black circles in panel (b) represent the deformation points which achieved a converged solution with the calculations started from Wood-Saxon potential. Performing the calculations of the deformation points which have non-converged solutions by reading from the fields of the closest deformation points that achieved converged solutions are shown in panels (c), (d), and (e) with solid red, blue, and green circles respectively. The PES obtained from the deformation points which achieved convergence is shown in panel (f). Note that the PES for $\gamma < 0$ is plotted by performing reflection of the PES with $\gamma > 0$ around $\gamma = 0$.